Modelling Chromospheric Evaporation in Response to Coronal Heating

Craig David Johnston

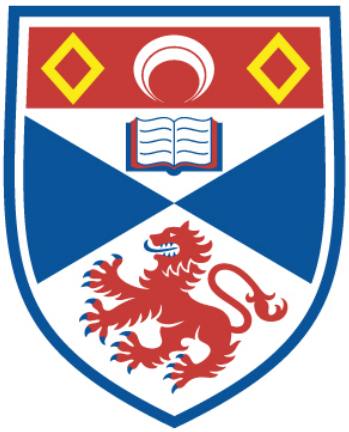

University of
St Andrews

This thesis is submitted in partial fulfilment for the degree of
Doctor of Philosophy (PhD)
at the University of St Andrews

March 2018

Abstract

This thesis presents a new computationally efficient method for modelling the response of the solar corona to the release of energy. During impulsive heating events, the coronal temperature increases which leads to a downward heat flux into the transition region (TR). The plasma is unable to radiate this excess conductive heating and so the gas pressure increases locally. The resulting pressure gradient drives an upflow of dense material, creating an increase in the coronal density. This density increase is often called chromospheric evaporation. A process which is highly sensitive to the TR resolution in numerical simulations. If the resolution is not adequate, then the downward heat flux jumps over the TR and deposits the heat in the chromosphere, where it is radiated away. The outcome is that with an under-resolved TR, major errors occur in simulating the coronal density evolution. We address this problem by treating the lower transition region as a discontinuity that responds to changing coronal conditions through the imposition of a jump condition that is derived from an integrated form of energy conservation. In this thesis, it is shown that this method permits fast and accurate numerical solutions in both one-dimensional and multi-dimensional simulations. By modelling the TR with this appropriate jump condition, we remove the influence of poor numerical resolution and obtain the correct evaporative response to coronal heating, even when using resolutions that are compatible with multi-dimensional magnetohydrodynamic simulations.

Candidate's declaration

I, Craig David Johnston, do hereby certify that this thesis, submitted for the degree of PhD, which is approximately 30,000 words in length, has been written by me, and that it is the record of work carried out by me, or principally by myself in collaboration with others as acknowledged, and that it has not been submitted in any previous application for any degree.

I was admitted as a research student at the University of St Andrews in September 2014.

I received funding from an organisation or institution and have acknowledged the funder(s) in the full text of my thesis.

Date: ..... Signature of candidate: .....

Supervisor's declaration

I hereby certify that the candidate has fulfilled the conditions of the Resolution and Regulations appropriate for the degree of PhD in the University of St Andrews and that the candidate is qualified to submit this thesis in application for that degree.

Date: ..... Signature of supervisor: .....

Permission for publication

In submitting this thesis to the University of St Andrews we understand that we are giving permission for it to be made available for use in accordance with the regulations of the University Library for the time being in force, subject to any copyright vested in the work not being affected thereby. We also understand, unless exempt by an award of an embargo as requested below, that the title and the abstract will be published, and that a copy of the work may be made and supplied to any bona fide library or research worker, that this thesis will be electronically accessible for personal or research use and that the library has the right to migrate this thesis into new electronic forms as required to ensure continued access to the thesis.

I, Craig David Johnston, confirm that my thesis does not contain any third-party material that requires copyright clearance.

The following is an agreed request by candidate and supervisor regarding the publication of this thesis:

Printed copy

Embargo on all of print copy for a period of 1 year on the following ground(s):

- Publication would be commercially damaging to the researcher, or to the supervisor, or the University.

Supporting statement for printed embargo request

Part of this thesis contains unpublished material, which could be used by fellow researchers before publication, which would be damaging for the researcher, supervisor and University.

Electronic copy

Embargo on all of electronic copy for a period of 1 year on the following ground(s):

- Publication would be commercially damaging to the researcher, or to the supervisor, or the University.

Supporting statement for electronic embargo request

Part of this thesis contains unpublished material, which could be used by fellow researchers before publication, which would be damaging for the researcher, supervisor and University.

Title and Abstract

- I agree to the title and abstract being published.

Date: ..... Signature of candidate: .....

Date: ..... Signature of supervisor: .....

Underpinning Research Data or Digital Outputs

Candidate's declaration

I, Craig David Johnston, hereby certify that no requirements to deposit original research data or digital outputs apply to this thesis and that, where appropriate, secondary data used have been referenced in the full text of my thesis.

Date: ..... Signature of candidate: .....

Acknowledgements

Many people have shaped my time spent in St Andrews over the last three and a half years. I am grateful for the support and friendship of all those who have shared the journey with me and have made this time so enjoyable.

Firstly, I would like to thank my supervisors, Alan and Ineke, for their help and guidance throughout my PhD. It has been a pleasure to work with both of you. Your enthusiasm and advice, even when I started to explore tangent projects (e.g. Chapter 5), has been pivotal both in making this work possible and in developing my confidence as a researcher. I would also like to extend my thanks to Peter for the many helpful discussions we have had during my PhD and for your useful suggestions – in many ways you became my third supervisor.

Secondly, I would like to thank all the staff and students in the Maths department who have made St Andrews such a fun place to study throughout my time here. A special 'thanks' goes to the PhD students that I have shared many long lunch breaks, late nights and enjoyable trips with, and to Ben in particular for allowing me to sleep on his sofa whenever I missed the last bus back to Dundee or the bridge was closed.

Finally and most of all, thank you to my family for all your love and support throughout my studies. Especially to my mum and dad for always believing in me and being so supportive through the highs and lows. Likewise, to my brothers, Scott and Derek, for making me laugh and keeping me grounded.

This is for all of you.

Funding

This work was supported by the Carnegie Trust for the Universities of Scotland.

Publications

This thesis contains work which has been adapted from the following publications:

1. C. D. Johnston, A. W. Hood, P. J. Cargill, & I. De Moortel. A new approach for modelling chromospheric evaporation in response to enhanced coronal heating: I The method. A&A, 597:A81, January 2017. doi: 10.1051/0004-6361/201629153.

2. C. D. Johnston, A. W. Hood, P. J. Cargill, & I. De Moortel. A new approach for modelling chromospheric evaporation in response to enhanced coronal heating: II Non-uniform heating. A&A, 605:A8, August 2017b. doi: 10.1051/0004-6361/201730486.

3. C. D. Johnston, A. W. Hood, P. J. Cargill, I. De Moortel & P. Antolin. The effect of numerical resolution and background heating on limit cycles in coronal loop models of thermal non-equilibrium, ApJ (*in prep.*).

4. C. D. Johnston, A. W. Hood, P. J. Cargill, & I. De Moortel. A fast multi–dimensional approach to modelling chromospheric evaporation: 2D applications, A&A (*in prep.*).

Collaboration Statement

The numerical simulations presented in this thesis were carried out by myself under the supervision of Prof Alan Hood and Prof Ineke De Moortel and in collaboration with Prof Peter Cargill. The implementation of super time stepping methods to treat thermal conduction, which is work presented in Chapter 2, was completed in collaboration with Prof Tony Arber. The HYDRAD code was provided to us by Prof Stephen Bradshaw and used in Chapters 3 & 4 as a benchmark solution. The work in Chapter 5 was completed in collaboration with Dr Patrick Antolin, who collaborated on the publication upon which the chapter is based.

Contents

Chapter 1

Introduction

1.1 The Sun

Positioned at the centre of our solar system, the Sun is our nearest star and source of light. It is very hot, reaching temperatures of over one million degrees in its outer atmosphere. This facilitates the ionisation of atoms into a positively charged ion and free electrons. Therefore, the Sun can be considered to be a giant ball of hot plasma. In particular, the property of having free electric charges means that the plasma is electrically conductive and, thus, its dynamic evolution involves interactions with electric and magnetic fields.

1.1.1 The Solar Atmosphere

The solar atmosphere consists of four main layers: the photosphere, chromosphere, transition region and corona (see Figure 1.1). Emitting most of the Sun's visible light, the photosphere is the visible surface of the Sun. At a few 100km thick, it is a thin layer of dense plasma. Moving outwards from the observable surface (where the optical depth is 1), i.e. base of the photosphere, the temperature drops down to the temperature minimum (from 10000 to 4500 K) and the density drops continually from the photospheric base through the chromosphere and into the corona.

Separating the hot corona from the much cooler chromosphere is a very thin layer called the transition region (TR). The temperature increases rapidly with height, by two orders of magnitude to a value of around 1MK at the TR/corona interface while the density falls off by a similar factor. The top of the TR is defined as the location where conduction changes sign from an energy loss in the corona to an energy gain below (e.g. Vesecky et al., 1979; Bradshaw and Cargill, 2010a,b). Although the width of the TR is

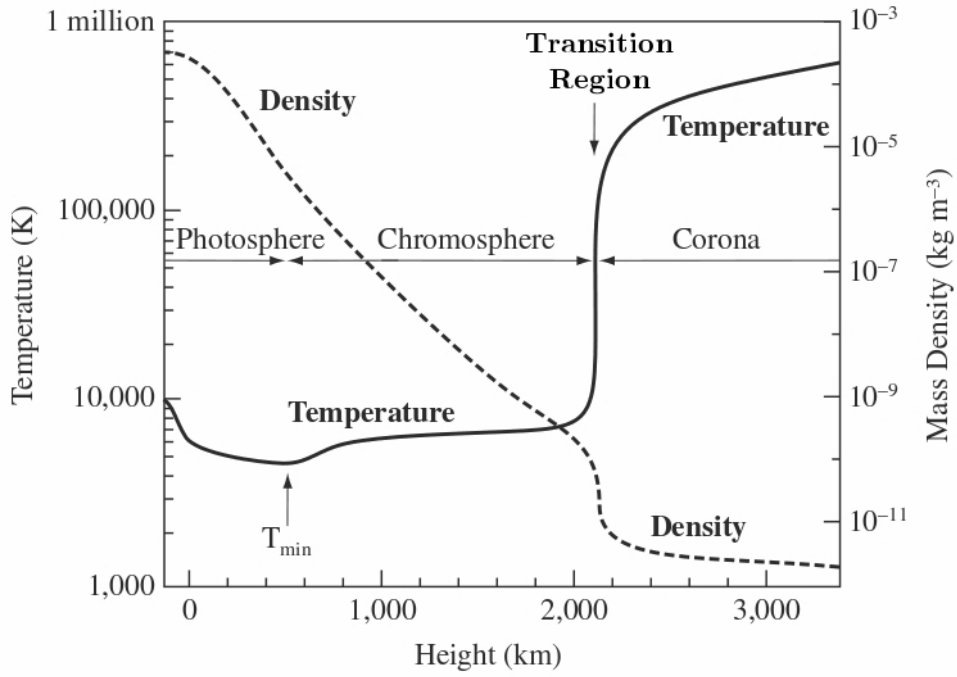

Figure 1.1: A schematic representation of the temperature (left-hand axis) and density (right-hand axis) variation with height in the solar atmosphere, starting at the photosphere and then moving upwards through the chromosphere and TR, up into the corona, based on Priest (2014).

much smaller than the total loop length for a typical coronal loop, the TR is very important because (i) the TR radiative losses are always more significant than the coronal losses, and (ii) the energy balance in the TR controls the mass exchange that takes place between the corona and chromosphere.

Characterised by very high temperatures and low densities, the corona is the outer layer of the Sun's atmosphere. Typical temperatures exceed 1 MK with densities ranging between 10^{-12} and 10^{-11} kg m^{-3}. In the corona the plasma is predominantly hydrogen, but there are also other elements present, and at the extremely hot temperatures the plasma is highly ionised. Identifying and understanding the physical mechanism responsible for heating the corona to these multi-million degree temperatures, which are orders of magnitude hotter than the photosphere, is known as the coronal heating problem (for a comprehensive review, see e.g. Klimchuk, 2006; Parnell and De Moortel, 2012; Reale, 2014). To maintain its high temperature the corona requires a heat source that at least balances the energy losses due to thermal conduction and optically thin radiation.

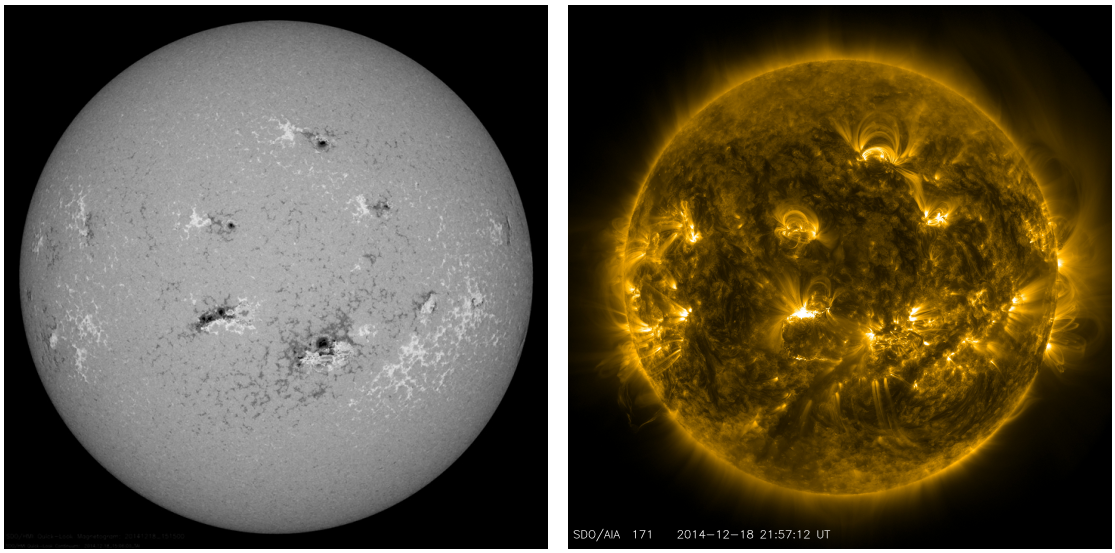

Figure 1.2: Images of the magnetic field configuration on the photosphere (LHS) from the Helioseismic and Magnetic Imager (HMI) magnetogram, and the solar corona at 171Å (RHS) from the Atmospheric Imaging Assembly (AIA) on the Solar Dynamics Observatory (SDO), taken on 18th December 2014 (NASA).

1.1.2 Common Visible Solar Features

Sunspots and Active regions

Sunspots are regions of strong magnetic field, which are observed as dark features on the photosphere. Associated with sunspots are large scale regions of strong magnetic flux that are known as active regions. This link between sunspots and active regions can be seen clearly by comparing the magnetic field map with the coronal emission image in Figure 1.2. The average field strength of an active region can range from 10^{-2} to 5×10^{-2} T (100 to 500 G).

Coronal Loops

Coronal loops are a common feature observed in the solar corona in soft X-rays. Anchored in the photosphere in regions of strong magnetic field of opposite polarity, these structures outline the complex magnetic field that extends from the photosphere upwards into the corona (e.g. see Figure 1.3). The brightness of the emission depends on the density and temperature of the confined plasma. The temperatures of coronal loops can vary from 1 to 10 MK and similarly a range of densities are observed from 10^{-12} to 10^{-10} kg m^{-3}, where the highest values are typically seen only in active region and flaring loops (Reale, 2014). The lengths of typical active region loops range between 10 to 100Mm. This

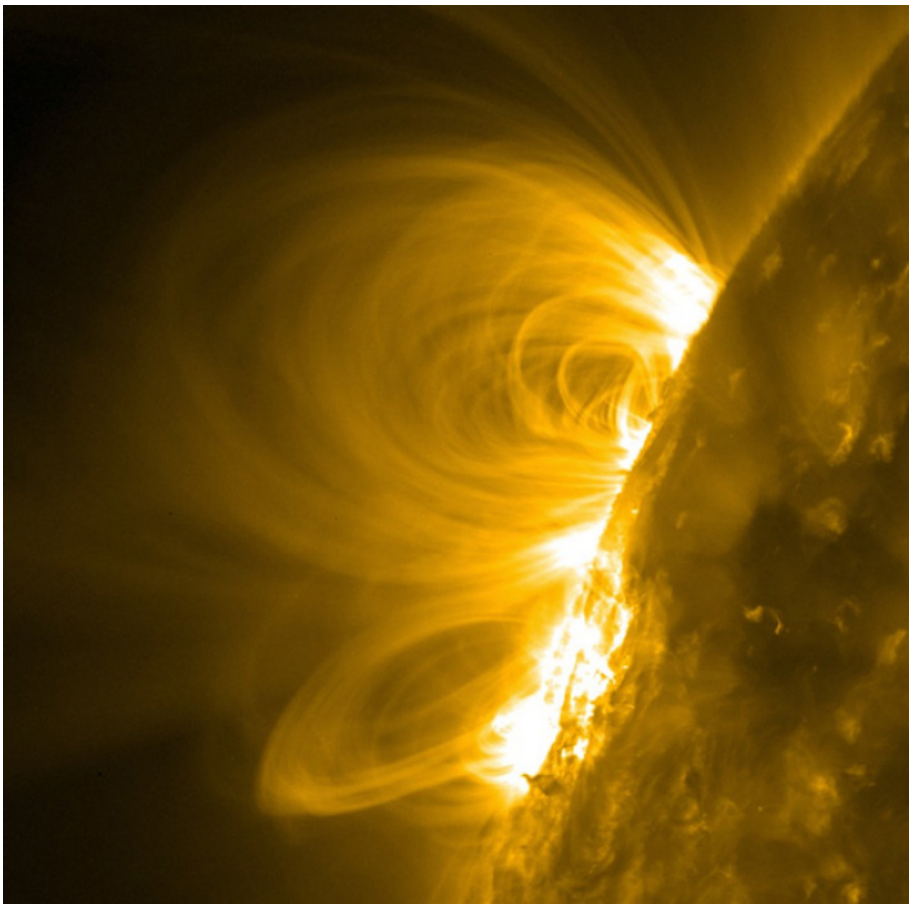

Figure 1.3: An image of active region coronal loops from AIA on SDO at 171Å (6.3×10^5K, quiet corona and the upper transition region) taken on 24th February 2011 (NASA). Figure based on Figure 3 from Reale (2014).

thesis focusses on modelling the evaporative response of the plasma confined in coronal loops when subjected to heating.

1.2 Coronal Heating Problem

It has been known since the 1940s that the Sun's atmosphere is more than two orders of magnitude hotter than the solar surface but there still is no detailed understanding of the heating mechanisms involved. It is generally accepted that the magnetic field, moved by surface (photosphere) motions generated by sub-surface convective motions, is ultimately responsible for the heating and observations have shown that these movements generate sufficient energy (Poynting flux) to account for the required atmospheric energy budget. However, the details of how this energy is transported into the atmosphere and converted into heat are still poorly understood (Klimchuk, 2006; Parnell and De Moortel, 2012;

Reale, 2014).

Based on the speed of the photospheric footpoint motions that act on the magnetic field, there are two main groups into which heating mechanisms are classified: slow and fast, relative to the local Alfvén speed ($v_{\rm A}$). Slow photospheric motions lead to the build up and storage of energy in the coronal magnetic field until, eventually, magnetic reconnection releases this available energy. This process, known as DC heating, has been shown to produce heating events but the heating associated with such events is very intermittent, with a long time for energy build-up and short periods of energy release. Fast photospheric motions, on the other hand, generate waves that immediately transport energy into the corona. However, these waves dissipate their energy only if the plasma is sufficiently structured, with plasma density and magnetic field variations on sufficiently short length scales. This is known as AC heating. For wave heating mechanisms, this structure must be pre-existing or else they are inefficient (see e.g. Cargill et al., 2016).

It remains to be explained which mechanism can dissipate the energy, either stored in the magnetic field or transported into the atmosphere in the form of waves, at the required timescales and values to explain the observations. Furthermore, it is clear that the heating of the solar corona cannot be treated in isolation but needs to be considered as part of the complex coupled solar atmosphere with the TR and chromosphere included.

1.3 Chromospheric Evaporation

The interaction between the solar corona and chromosphere is central to understanding the observed properties of magnetically closed coronal loops. It is well known that if the corona is heated impulsively (by for example, a flare, microflare or nanoflare), both the temperature and density increase and then decline, with the time of peak temperature preceding that of the peak density (e.g. Reale, 2007; Klimchuk et al., 2008; Cargill et al., 2012a). The changes in density can only be accounted for by mass exchange between the corona and chromosphere, mediated by the transition region (TR).

Recognising the role of the TR is essential for developing reliable models of impulsive heating. For a static equilibrium loop with steady heating, the TR is defined as the region extending from the top of the chromosphere to the location where thermal conduction changes from an energy loss to a gain (e.g. Vesecky et al., 1979). For a typical coronal loop, the full TR occupies roughly 10% of the total loop length, the radiation from it is roughly twice that from the corona, and the temperature at its top is of order 60% the temperature at the loop apex (Cargill et al., 2012a). The energy balance in the TR is approximately between downward thermal conduction and optically thin radiation (for a loop in thermal equilibrium).

The change in coronal density in response to impulsive heating arises because the

increased coronal temperature implied by the heating gives rise to an excess downward heat flux that the TR is unable to radiate (Klimchuk et al., 2008; Cargill et al., 2012a). The outcome is an enthalpy flux from the chromosphere, through the TR, to the corona, often called (chromospheric) 'evaporation' (e.g. Antiochos and Sturrock, 1978). The location of the TR moves downward in the atmosphere, and during the evaporation process chromospheric material is heated to coronal temperatures. The process is reversed after the density peaks when the TR requires a larger heat flux than the corona can provide, and so instead an enthalpy flux from the corona is set up, which both drains the corona and powers the TR radiative losses (Bradshaw and Cargill, 2010a,b). The TR now moves upwards as the corona cools and the plasma returns to its pre-heated state.

1.4 Magnetohydrodynamics

In Chapter 6, chromospheric evaporation in coronal loops will be modelled using magnetohydrodynamics (MHD). The MHD approximation couples the laws of fluid dynamics with Maxwells laws of electromagnetism to model the plasma as a single, macroscopic, electrically conducting fluid and its large scale interaction with the magnetic field. There are many important assumptions that are made when deriving the MHD equations, which include:

- the plasma speeds are much smaller than the speed of light (i.e. non-relativistic),
- the plasma is assumed to be quasi-neutral, which means that the plasma acts as if the overall charge is zero (i.e. $n_i - n_e << n$, where n_i and n_e are the number densities of positive ions and negative electrons and n is the total number density),
- the plasma is treated as a single fluid,
- the plasma length scales are much greater than the microscopic length scales of the electron and ion dynamics (i.e. larger than the gyro-radius and mean free path length),
- the plasma time scales are much longer than the time scales of the electron and ion dynamics,
- the plasma is assumed to be in thermodynamic equilibrium.

1.4.1 Summary of the Magnetohydrodynamic Equations

$$\frac{\partial \rho}{\partial t} = -\nabla \cdot (\rho \mathbf{v}), \qquad \text{(mass continuity equation)} \quad (1.1)$$

$$\rho\frac{D\mathbf{v}}{Dt} = -\nabla P - \rho\mathbf{g} + \mathbf{j}\times\mathbf{B} + \mathbf{F}, \qquad \text{(equation of motion)} \qquad (1.2)$$

$$\rho\frac{D\epsilon}{Dt} = -P\nabla\cdot\mathbf{v} - \nabla\cdot\mathbf{q} + Q - n^2\Lambda(T) + \frac{j^2}{\sigma}, \qquad \text{(energy equation)} \qquad (1.3)$$

$$\frac{\partial\mathbf{B}}{\partial t} = \nabla\times(\mathbf{v}\times\mathbf{B}) + \eta\nabla^2\mathbf{B}, \qquad \text{(induction equation)} \qquad (1.4)$$

$$P = \frac{k_B}{\mu_m}nT, \qquad \text{(ideal gas law)} \qquad (1.5)$$

where the variables $\mathbf{j}$ and $\mathbf{E}$ are given by:

$$\nabla\times\mathbf{B} = \mu_0\mathbf{j}, \qquad \text{(Ampère's law)} \qquad (1.6)$$

$$\mathbf{j} = \sigma(\mathbf{E} + \mathbf{v}\times\mathbf{B}), \qquad \text{(Ohm's law)} \qquad (1.7)$$

with the initial condition for the magnetic field:

$$\nabla\cdot\mathbf{B} = 0. \qquad \text{(solenoidal constraint)} \qquad (1.8)$$

Here, ρ is the mass density, t is time, $\mathbf{v}$ is the velocity, P is the gas pressure, $\mathbf{g}$ is the gravitational acceleration, $\mathbf{j}$ is the electric current density, $\mathbf{B}$ is the magnetic field, $\mathbf{F}$ represents any additional forces such as viscosity, $\epsilon = P/(\gamma-1)\rho$ is the specific internal energy density (where γ is the ratio of specific heats), $\mathbf{q} = -\kappa(\mathbf{B}\cdot\nabla T)\mathbf{B}/B^2$ is the parallel heat flux vector, Q is the volumetric heating rate, n is the number density ($n = \rho/1.2m_p$, where $m_p = 1.6726\times10^{-27}$kg is the proton mass), $\Lambda(T)$ is the optically thin radiative loss function, σ is the electrical conductivity, η is the resistivity, $k_B = 1.3807\times10^{23}\mathrm{JK}^{-1}$ is the Boltzmann constant, μ_m is the reduced mass (i.e. the average mass of all particles in the plasma and for a fully ionised plasma is taken to be $0.5m_p$), T is the temperature and $\mu_0 = 4\pi\times10^{-7}\mathrm{Hm}^{-1}$ is the magnetic permeability of a vacuum.

1.4.2 Total Energy Equation

The total energy density of the plasma is the sum of internal, kinetic, gravitational potential and magnetic energy,

$$E = \frac{P}{\gamma-1} + \frac{1}{2}\rho v^2 + \rho\Phi + \frac{B^2}{2\mu_0}. \qquad (1.9)$$

From the MHD equations (1.1)–(1.5), one can derive the total energy equation.

Rate of change of internal energy

Starting with the energy equation (1.3), expanding out the derivatives we obtain,

$$\frac{1}{\gamma-1}\left\{\frac{\partial P}{\partial t}+(\mathbf{v}\cdot\nabla)P\right\}-\frac{P}{(\gamma-1)\rho}\left\{\frac{\partial \rho}{\partial t}+(\mathbf{v}\cdot\nabla)\rho\right\}=-P\nabla\cdot\mathbf{v}-\mathcal{L}, \tag{1.10}$$

where,

$$-\mathcal{L}=-\nabla\cdot\mathbf{q}+Q-n^2\Lambda(T)+\frac{j^2}{\sigma}. \tag{1.11}$$

Applying mass conservation it follows that,

$$\frac{1}{\gamma-1}\left\{\frac{\partial P}{\partial t}+(\mathbf{v}\cdot\nabla)P\right\}=-\frac{\gamma}{\gamma-1}P\nabla\cdot\mathbf{v}-\mathcal{L}. \tag{1.12}$$

Finally, using the vector identity $\nabla\cdot(a\mathbf{b})=\nabla a\cdot\mathbf{b}+a\nabla\cdot\mathbf{b}$, we obtain that the rate of change of internal energy is given by,

$$\frac{\partial}{\partial t}\left(\frac{P}{\gamma-1}\right)+\nabla\cdot\left(\frac{\gamma}{\gamma-1}P\mathbf{v}+\mathbf{q}\right)=(\mathbf{v}\cdot\nabla)P+Q-n^2\Lambda(T)+\frac{j^2}{\sigma}. \tag{1.13}$$

Rate of change of kinetic energy

The rate of change of kinetic energy is obtained from the equations of mass and momentum conservation. Multiplying the continuity equation (1.1) by $v^2/2$ and taking the scalar product of the equation of motion (1.2) with $\mathbf{v}$, we obtain,

$$\frac{v^2}{2}\frac{\partial\rho}{\partial t}+\frac{v^2}{2}\nabla\cdot(\rho\mathbf{v})=0 \tag{1.14}$$

$$\rho\frac{\partial}{\partial t}\left(\frac{v^2}{2}\right)+\rho(\mathbf{v}\cdot\nabla)\left(\frac{v^2}{2}\right)=-\mathbf{v}\cdot\nabla P-\rho\mathbf{v}\cdot\mathbf{g}+\mathbf{v}\cdot(\mathbf{j}\times\mathbf{B}). \tag{1.15}$$

Expanding out the derivatives on the LHS of Eq. (1.15) and using Eq. (1.14) we obtain that,

$$\frac{\partial}{\partial t}\left(\frac{1}{2}\rho v^2\right)+\nabla\cdot\left(\frac{1}{2}\rho v^2\mathbf{v}\right)=-\mathbf{v}\cdot\nabla P-\rho\mathbf{v}\cdot\mathbf{g}+\mathbf{v}\cdot(\mathbf{j}\times\mathbf{B}). \tag{1.16}$$

Rate of change of gravitational potential energy

Let Φ be a potential function for the gravitational field,

$$\mathbf{g} = \nabla\Phi. \tag{1.17}$$

Multiplying the continuity equation (1.1) by Φ and rearranging, we obtain that the rate of change of gravitational potential energy is given by,

$$\frac{\partial}{\partial t}(\rho\Phi) + \nabla\cdot(\rho\Phi\mathbf{v}) = \rho\mathbf{v}\cdot\mathbf{g}. \tag{1.18}$$

Rate of change of magnetic energy

To obtain the rate of change of magnetic energy, we write the induction equation (1.4) as,

$$\frac{\partial\mathbf{B}}{\partial t} = \nabla\times(\mathbf{v}\times\mathbf{B}) - \nabla\times(\eta\nabla\times\mathbf{B}) = -\nabla\times\mathbf{E}. \tag{1.19}$$

Then taking the scalar product with $\mathbf{B}/\mu_0$, it follows that,

$$\frac{\partial}{\partial t}\left(\frac{B^2}{2\mu_0}\right) = \frac{\mathbf{B}}{\mu_0}\cdot\left\{\nabla\times(\mathbf{v}\times\mathbf{B} - \eta\nabla\times\mathbf{B})\right\}. \tag{1.20}$$

Finally, applying the vector identity $\nabla\cdot(\mathbf{A}\times\mathbf{B}) = \mathbf{B}\cdot(\nabla\times\mathbf{A}) - \mathbf{A}\cdot(\nabla\times\mathbf{B})$, together with Ampère's law (1.6) and Ohm's law (1.6), we obtain that,

$$\frac{\partial}{\partial t}\left(\frac{B^2}{2\mu_0}\right) + \nabla\cdot\left(\frac{\mathbf{E}\times\mathbf{B}}{\mu_0}\right) = -\frac{j^2}{\sigma} - \mathbf{v}\cdot(\mathbf{j}\times\mathbf{B}). \tag{1.21}$$

Rate of change of total energy

The rate of change of total energy equation is then obtained by summing the component equations,

$$\frac{\partial}{\partial t}\left(\frac{P}{\gamma-1} + \frac{1}{2}\rho v^2 + \rho\Phi + \frac{B^2}{2\mu_0}\right) + \nabla\cdot\left(\frac{\gamma}{\gamma-1}P\mathbf{v} + \mathbf{q} + \frac{1}{2}\rho v^2\mathbf{v} + \rho\Phi\mathbf{v} + \frac{\mathbf{E}\times\mathbf{B}}{\mu_0}\right)$$

$$= Q - n^2\Lambda(T). \tag{1.22}$$

1.4.3 Derived Quantities

Magnetic Tension and Magnetic Pressure

The $\mathbf{j} \times \mathbf{B}$ term in the equation of motion (1.2) is known as the Lorentz force. Using Ampère's law (1.6) and vector identities this can be written as,

$$\mathbf{j} \times \mathbf{B} = \frac{1}{\mu_0}(\nabla \times \mathbf{B}) \times \mathbf{B} = \frac{1}{\mu_0}(\mathbf{B} \cdot \nabla)\mathbf{B} - \nabla\left(\frac{B^2}{2\mu_0}\right) \tag{1.23}$$

Therefore, the Lorentz force can be separated into two different parts: the magnetic tension force ($(\mathbf{B} \cdot \nabla)\mathbf{B}/\mu_0$) and the magnetic pressure force ($-\nabla(B^2/2\mu_0)$).

Plasma Beta

The ratio of the gas pressure (P) and the magnetic pressure ($B^2/2\mu_0$) is a dimensionless parameter, which is called the plasma beta (β),

$$\beta = \frac{P}{B^2/2\mu_0}. \tag{1.24}$$

Typically $\beta > 1$ in the photosphere and the plasma is considered to mostly dominate the magnetic field. The plasma beta then reduces rapidly with height above the photosphere so that in the corona $\beta << 1$ and the magnetic field dominates the plasma.

1.4.4 MHD Waves

By linearising the MHD equations, it can be shown that in a uniform plasma, there are three different types of MHD waves (Priest, 2014):

- Alfvén waves – incompressible waves whose energy is carried along the field lines with a characteristic speed given by $c_{\mathrm{A}}^2 = B^2/(\mu_0\rho)$,
- Fast magnetoacoustic waves – compressible waves that can propagate perpendicular to the magnetic field and have a characteristic speed of $c_{\mathrm{f}}^2 = c_{\mathrm{A}}^2 + c_{\mathrm{s}}^2$ (where $c_{\mathrm{s}}^2 = \gamma p/\rho$ is the sound speed),
- Slow magnetoacoustic waves – compressible waves that propagate largely parallel to the magnetic field with a slow characteristic speed given by $c_{\mathrm{ms}}^2 = c_{\mathrm{s}}^2 c_{\mathrm{A}}^2/(c_{\mathrm{s}}^2 + c_{\mathrm{A}}^2)$.

1.5 Hydrodynamics

In Chapters 3–5, the plasma confined in magnetically closed coronal loops is modelled using a single coordinate along the loop (z, see Figure 1.4). The plasma evolution can be described using the one-dimensional (1D) hydrodynamic equations for a compressible fluid together with an energy equation that aims to capture all of the important loop plasma physics (see e.g. Reale, 2014, for a review). There are many important assumptions that are made when recovering the hydrodynamic equations from the MHD equations, which include:

- the magnetic pressure is much greater than the gas pressure and so the plasma beta is assumed to be low ($\beta << 1$),
- the gradients and flows perpendicular to the magnetic field are much smaller than those parallel to the field i.e. the plasma is treated as being confined to the field with mass and energy transported only in the direction of the field (2D variations will be investigated in Chapter 6),
- the loop cross-sectional area is assumed to be constant,
- the effects of curvature and twisting of the magnetic field are neglected as are currents and transverse waves.

1.5.1 Summary of the Hydrodynamic Equations

$$\frac{\partial \rho}{\partial t} + v\frac{\partial \rho}{\partial z} = -\rho\frac{\partial v}{\partial z}, \qquad \text{(mass continuity equation)} \quad (1.25)$$

$$\rho\frac{\partial v}{\partial t} + \rho v\frac{\partial v}{\partial z} = -\frac{\partial P}{\partial z} - \rho g_{\parallel}(z) + \rho\nu\frac{\partial^2 v}{\partial z^2}, \qquad \text{(equation of motion)} \quad (1.26)$$

$$\rho\frac{\partial \epsilon}{\partial t} + \rho v\frac{\partial \epsilon}{\partial z} = -P\frac{\partial v}{\partial z} - \frac{\partial F_c}{\partial z} + Q - n^2\Lambda(T) + \rho\nu\left(\frac{\partial v}{\partial z}\right)^2, \qquad \text{(energy equation)} \quad (1.27)$$

$$P = \frac{k_B}{\mu_m}nT. \qquad \text{(ideal gas law)} \quad (1.28)$$

Here, z is the spatial coordinate along the magnetic field, v is the velocity parallel to the magnetic field, $g_{\parallel}$ is the field-aligned gravitational acceleration, ν is the viscosity and $F_c = -\kappa_0 T^{5/2}\partial T/\partial z$ is the heat flux in the direction along the magnetic field.

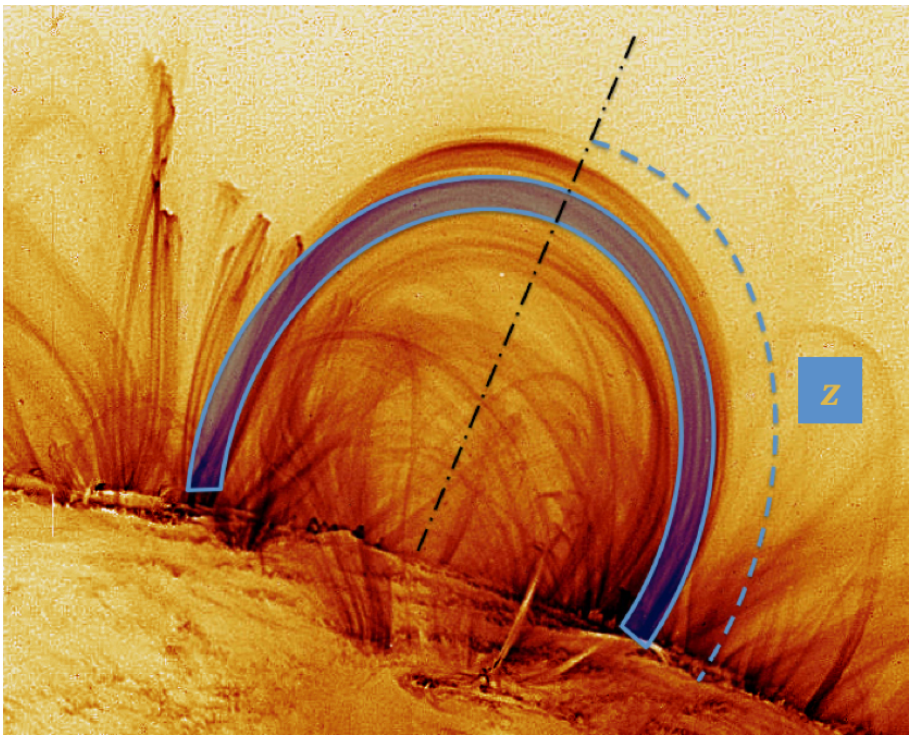

Figure 1.4: A schematic representation of the the plasma confined in a coronal loop and the spatial coordinate along the magnetic field (z), imposed on top of an image of coronal loops from the Transition Region And Coronal Explorer (TRACE) taken on 6th November 1999 (NASA). Figure based on Figure 12 from Reale (2014).

1.5.2 Modelling Coronal Loops

While straightforward in principle, the heating and upflow followed by cooling and downflow cycle which is characteristic of the evaporative response to heating in coronal loops, poses major challenges for computational modelling, with conductive cooling being the most severe. For a loop in static equilibrium, in the TR one has an approximate energy equation that equates conduction and radiation as,

$$\kappa_0 T^{7/2}/L_T^2 \sim (P/2k_B)^2 \Lambda(T)/T^2, \tag{1.29}$$

where L_T is the temperature length scale ($L_T = T/|dT/dz|$, where T is the temperature and z the spatial coordinate along the magnetic field) and the radiative loss function $\Lambda(T)$ decreases as a function of temperature above 10^5K. Thus, one finds $L_T^2 \sim T^{11/2}/\Lambda(T)$, assuming the pressure is constant. Since T decreases in the TR, L_T must also decrease rapidly. For a loop in thermal equilibrium, L_T can be less than 1km at 10^5K. When impulsive heating occurs, L_T is even smaller, because of the steep temperature dependence of thermal conduction and the location of the peak of the radiative losses between 10^5 &

10^6 K. This leads to one of the main difficulties encountered with computational models of loop evolution: how to implement a grid that fully resolves the steep TR, which is also very dynamic, moving in response to the coronal heating and cooling. Good resolution is essential in order to obtain the correct coronal density in response to coronal heating (Bradshaw and Cargill, 2013, hereafter BC13). Otherwise, the downward heat flux from the corona 'jumps' over an under-resolved TR to the chromosphere, where the incoming energy is then strongly radiated away, rather than going into driving the evaporation. The outcome is a diminished upward enthalpy flux. BC13 showed that major errors in the coronal density were likely with lack of spatial resolution. In particular, in their study, an under-resolved loop typically had a peak density of at least a factor of two lower than the resolved loop value (which had grid cell widths of 98m in the most highly resolved regions) when subjected to the same heating. The discrepancies in the density evolution were even larger during the draining phase.

Furthermore, since the conductive timescale across a grid point has real physical meaning for the problems at hand, an explicit numerical method is to be preferred (implicit solvers require matrix inversion with no guarantee of convergence). One option is to use brute force on a fixed grid with a large number of grid points. This is slow, since numerical stability of an explicit algorithm requires $\Delta t \leq \min(k_B n(\Delta z)^2/(2\kappa_0 T^{5/2}))$ (where Δz is the cell width and the timestep is the minimum over the whole grid), so that a lot of time is wasted computing in the corona where L_T is large and high spatial resolution is not required. A non-uniform fixed grid, with points localised at the TR is an option, but since the TR moves (see above), there is no guarantee that high resolution will be where it is required. Instead, modern schemes use an adaptive mesh which allocates points where they are needed (Betta et al., 1997; Bradshaw and Mason, 2003, BC13). This also means that effort is no longer wasted computing highly resolved coronal solutions. However, in order to achieve numerical stability, the time step restriction is the same as for a uniform grid, scaling as the minimum of L_T^2 over the whole grid and therefore implying long computation times for fully resolved simulations.

Thus far we have not distinguished between 1D hydrodynamic (field-aligned) modelling and multi-dimensional MHD simulations. It is straightforward for a 1D code with an adaptive mesh and a large computer to model a single heating event, and, with patience, to model a nanoflare train lasting several tens of thousands of seconds (Cargill et al., 2015). However, ensembles of thousands of loop strands heated by nanoflares pose more severe computational challenges. This has led to the development of zero-dimensional field-aligned hydrodynamical models (e.g. Klimchuk et al., 2008; Cargill et al., 2012a,b, 2015) that provide a quick and accurate answer to the coronal response of a loop to heating.

The implementation of field-aligned loop plasma evolution into multi-dimensional MHD models poses much more serious challenges due to the number of grid points that

can be used, so that 3D MHD simulations run in a realistic time. This is of the order of 500^3 at the present time. If one desires to resolve the TR with a fixed grid, one needs several thousand points in one direction, so that there will be a loss of resolution elsewhere as well as a potentially crippling reduction of the time step.

The second difficulty is that while an adaptive mesh can still be used in the TR, with commensurate computational benefits, there can be other parts of such simulations that have equally pressing requirements for high resolution, such as current sheets or phase mixing, and, once again, an adaptive mesh does not eliminate the time step problem. Therefore, there is a need for a simple and computationally efficient method, that can be employed in both 1D hydrodynamic and multi-dimensional MHD models, to help obtain the correct coronal response to impulsive heating events.

1.6 Outline

Obtaining artificially low coronal densities is the main consequence of under-resolving the TR (BC13). This has significant implications for modelling coronal loops. The aim of this thesis is to develop a physically motivated approach to deal with this problem. In particular, to sidestep the need for high spatial resolution in the TR, we propose using an integrated form of the energy equation that essentially treats the unresolved region of the lower TR as a discontinuity. The response of the TR to changing coronal conditions can then be determined through the imposition of a jump condition, which compensates for the energy lost when the heat flux jumps over an unresolved region by imposing a local velocity correction.

In Chapter 2, we begin by outlining the numerical methods which will be used throughout this thesis to model coronal loops. We introduce super time stepping methods to treat thermal conduction and derive the Runge-Kutta Legendre method with second-order temporal accuracy. This scheme is tested for appropriateness of use in coronal plasma conditions.

We then go on to develop the jump condition approach for modelling chromospheric evaporation in response to coronal heating in Chapter 3. To benchmark this method against a fully resolved 1D model, we consider a wide range of impulsive, spatially uniform heating events. The results are also compared with a 1D code run without using the jump condition but with the same grid. Examples of non-uniform heating and a more detailed analysis of the method are presented in Chapter 4.

Subsequently, we use the jump condition approach to investigate steady footpoint heating and thermal non-equilibrium (TNE) in coronal loop models in Chapter 5. The effects of numerical resolution, background heating and adjusting the heating parameters are studied to determine their influence on TNE limit cycles.

In Chapter 6, we demonstrate that the jump condition method can be generalised to multi-dimensional MHD models. We present a first, basic extension of the method to 2D where the magnetic field remains locally uniform in the unresolved part of the lower TR.

Finally, in Chapter 7 we summarise our findings and discuss possible future work.

Chapter 2

Model Set Up & Numerical Methods

The main purpose of this chapter is to introduce the mathematical model set-up and the numerical methods used in the chapters that follow. This involves deriving the appropriate normalisation factors for the implementation of thermal conduction, optically thin radiation and heating, stating the finite different schemes employed for these effects and detailing the coupling of such solvers. The Runge-Kutta Legendre method with second-order temporal accuracy is also derived. Used to treat thermal conduction, this scheme is tested for consistency and stability in coronal plasma conditions.

2.1 Equations and Numerical Method

In order to model chromospheric evaporation in response to enhanced impulsive coronal heating, we consider the 1D field-aligned MHD equations for a single magnetic strand, with uniform cross-section,

$$\frac{\partial \rho}{\partial t} + v\frac{\partial \rho}{\partial z} = -\rho\frac{\partial v}{\partial z}, \tag{2.1}$$

$$\rho\frac{\partial v}{\partial t} + \rho v\frac{\partial v}{\partial z} = -\frac{\partial P}{\partial z} - \rho g_{\parallel} + \rho\nu\frac{\partial^2 v}{\partial z^2}, \tag{2.2}$$

$$\rho\frac{\partial \epsilon}{\partial t} + \rho v\frac{\partial \epsilon}{\partial z} = -P\frac{\partial v}{\partial z} - \frac{\partial F_c}{\partial z} + Q - n^2\Lambda(T) + \rho\nu\left(\frac{\partial v}{\partial z}\right)^2, \tag{2.3}$$

$$P = 2\,k_B n T. \tag{2.4}$$

Here, z is the spatial coordinate along the magnetic field, ρ is the mass density, P is the gas pressure, T is the temperature, k_B is the Boltzmann constant, $\epsilon = P/(\gamma-1)\rho$ is the specific internal energy density, n is the number density ($n = \rho/1.2m_p$, m_p is the proton mass), v is the velocity parallel to the magnetic field, $g_\parallel$ is the field-aligned gravitational acceleration (for which we use a profile that corresponds to a semi-circular strand), ν is the viscosity (shock viscosity is also included as discussed in Arber et al. (2001)), $F_c = -\kappa_0 T^{5/2}\partial T/\partial z$ is the heat flux, Q is the volumetric heating rate and $\Lambda(T)$ is the optically thin radiative loss function that is approximated by the piecewise continuous form defined in Klimchuk et al. (2008).

2.2 Lare1D with Thermal Conduction and Radiation

The 1D field-aligned MHD equations (2.1) – (2.4) are solved using a Lagrangian remap (Lare) approach, as described for 3D MHD in Arber et al. (2001), adapted for 1D field-aligned hydrodynamics. Time-splitting methods are used to split the field-aligned equations into an ideal hyperbolic component and non-ideal components. This allows thermal conduction and optically thin radiation to be updated separately from the advection terms since these effects formulate the non-ideal components.

During a single time step, we first assume that there are no changes to the velocity and density, so that only the temperature (specific-internal energy density) can change. The temperature is updated based on the effects of thermal conduction, optically thin radiation and heating. Then we use a one-dimensional Lagrangian remap method (Lare1D) to solve the field-aligned ideal MHD equations, updating the pressure, density, velocity and temperature (specific-internal energy density). Note that adiabatic changes to the temperature are dealt with when the ideal MHD equations are solved.

The Lagrangian remap code (Lare) splits each time step into a Lagrangian step followed by a remap step. The Lagrangian step solves the ideal MHD equations in a frame of reference that moves with the fluid. By using time-splitting methods, thermal conduction, optically thin radiation and heating have been included in the Lagrangian step. The remap step then maps the variables back onto the original grid.

2.2.1 Field-aligned Ideal MHD Equations

The Lare1d code solves the normalised field-aligned ideal MHD equations on a staggered grid (velocities are defined at the cell boundaries and all scalars are defined at the cell centres). Normalisation is obtained through the choice of normalising magnetic field ($\mathbf{B} = B_0\hat{\mathbf{B}}$), density ($\rho = \rho_0\hat{\rho}$) and length ($z = L_0\hat{z}$). These three chosen normalisation constants

are then used to define the normalisation of the remaining variables,

$$v_0 = \frac{B_0}{\sqrt{\mu_0 \rho_0}}, \tag{2.5}$$

$$P_0 = \frac{B_0^2}{\mu_0}, \tag{2.6}$$

$$t_0 = \frac{L_0}{v_0}, \tag{2.7}$$

$$\epsilon_0 = v_0^2, \tag{2.8}$$

$$T_0 = \frac{\epsilon_0 \bar{m}}{k_B}, \tag{2.9}$$

$$\mu_{m_0} = \bar{m}, \tag{2.10}$$

where $\bar{m} = 1.2 m_p$ is the average mass of ions in the plasma. Removing all the hats from the normalised variables, the normalised one-dimensional ideal MHD equations are then given by,

$$\frac{\partial \rho}{\partial t} + v \frac{\partial \rho}{\partial z} = -\rho \frac{\partial v}{\partial z}, \tag{2.11}$$

$$\rho \frac{\partial v}{\partial t} + \rho v \frac{\partial v}{\partial z} = -\frac{\partial P}{\partial z} - \rho g_{\parallel} + \rho \nu \frac{\partial^2 v}{\partial z^2}, \tag{2.12}$$

$$\rho \frac{\partial \epsilon}{\partial t} + \rho v \frac{\partial \epsilon}{\partial z} = -P \frac{\partial v}{\partial z} + \rho \nu \left(\frac{\partial v}{\partial z} \right)^2, \tag{2.13}$$

$$P = 2 \rho T, \tag{2.14}$$

where $\epsilon = 2T/(\gamma - 1)$ is now the normalised specific internal energy density. The Lare code solves these equations, in the Lagrangian step, using a predictor corrector scheme that is second-order accurate in both space and time. This method stably integrates the solution, on an advective time step that is governed by the Courant-Friedrichs-Lewy (CFL) condition,

$$\Delta t_{\text{adv}} \leq \min \left(\frac{\Delta z}{\sqrt{c_s^2 + v^2}} \right), \tag{2.15}$$

where Δz is the cell width and c_s is the local sound speed.

2.2.2 Thermal Conduction

The thermal conduction model is based on the classical Spitzer-Harm heat flux formulation (Spitzer, 1962). In the time-splitting update, the thermal conduction step is of the form,

$$\rho\frac{\partial\epsilon}{\partial t} = -\frac{\partial}{\partial z}\left(-\kappa_0 T^{5/2}\frac{\partial T}{\partial z}\right). \tag{2.16}$$

Applying the Lare normalisation we obtain,

$$\hat{\rho}\frac{\partial\hat{\epsilon}}{\partial\hat{t}} = -\frac{T_0^{7/2}}{\rho_0 L_0 \epsilon_0^{3/2}}\ \frac{\partial}{\partial\hat{z}}\left(-\kappa_0\hat{T}^{5/2}\frac{\partial\hat{T}}{\partial\hat{z}}\right). \tag{2.17}$$

Consequently, the thermal conductivity normalisation is given by,

$$\hat{\kappa_0} = \frac{\kappa_0 T_0^{7/2}}{\rho_0 L_0 \epsilon_0^{3/2}}. \tag{2.18}$$

Removing all the hats from the normalised variables, the normalised thermal conduction step is then of the form (2.16).

We treat thermal conduction using the second-order accurate Runge-Kutta Legendre (RKL2) super time stepping (STS) method, as described in Meyer et al. (2012, 2014) and discussed in Section 2.4. For the RKL2, method we approximate the parabolic conduction operator using central differencing of the heat flux,

$$\mathbf{L}^{\mathrm{C}}(T) = -\frac{1}{\rho}\frac{\partial}{\partial z}\left(-\kappa_0 T^{5/2}\frac{\partial T}{\partial z}\right) \approx -\frac{1}{\rho}\frac{F_{sp,\,i+\frac{1}{2}} - F_{sp,\,i-\frac{1}{2}}}{dzb_i}, \tag{2.19}$$

where,

$$F_{sp,\,i+\frac{1}{2}} = -\kappa_0\left(\frac{T_{i+1}+T_i}{2}\right)^{5/2}\left(\frac{T_{i+1}-T_i}{dzc_i}\right), \tag{2.20}$$

and dzb_i (dzc_i) is the distance between cell boundaries (centres). For a discussion on alternative finite difference schemes for the heat flux see Bradshaw and Cargill (2013)[hereafter BC13].

While the full derivation of the RKL2 super time stepping method is presented in Section 2.4 together with additional details for the implementation, here we introduce the componentwise formulation that is used to integrate the conduction step,

$$\mathbf{Y}_i^0 = \boldsymbol{\epsilon}_i^n,$$

$$\mathbf{Y}_i^1 = \mathbf{Y}_i^0 + \tilde{\mu}_1\Delta t_{\mathrm{STS}}\mathbf{L}^{\mathrm{C}}((\gamma-1)\mathbf{Y}_i^0/2),$$

$$\mathbf{Y}_i^j = \mu_j \mathbf{Y}_i^{j-1} + \nu_j \mathbf{Y}_i^{j-2} + (1-\mu_j-\nu_j)\mathbf{Y}_i^0$$
$$+ \tilde{\mu}_j \Delta t_{\rm STS} \mathbf{L}^{\rm C}((\gamma-1)\mathbf{Y}_i^{j-1}/2) + \tilde{\gamma}_j \Delta t_{\rm STS} \mathbf{L}^{\rm C}((\gamma-1)\mathbf{Y}_i^0/2), \qquad 2 \le j \le s,$$

$$\boldsymbol{\epsilon}_i^{n+1} = \mathbf{Y}_i^s, \tag{2.21}$$

with the parameters,

$$\mu_j = \frac{(2j-1)(j+2)(j-1)^2}{j(j-2)(j+1)^2},$$

$$\nu_j = -\frac{(j-1)^3(j^2-4)}{j^3(j+1)(j-3)},$$

$$\tilde{\mu}_j = \frac{(2j-1)(j+2)(j-1)^2}{j(j-2)(j+1)^2}\frac{4}{s^2+s-2}, \qquad \tilde{\mu}_1 = \frac{4}{3(s^2+s-2)},$$

$$\tilde{\gamma}_j = -\frac{(j-1)(j+2)(2j-1)(j^2-j+2)}{2j^2(j-2)(j+1)^2}, \tag{2.22}$$

where s is the number of explicit Runge-Kutta stages and $\Delta t_{\rm STS}$ is the overall time step we intend to take with the RKL2 method, defined by the time-splitting update. This will usually be the advective time step, Δt_{adv}, enforced by the Lare predictor-corrector scheme that is used to solve the ideal MHD equations. Therefore, we "super-step" conduction to the advection time step, while standard explicit methods can only stably integrate the solution, in time, on the conductive timescale,

$$\Delta t_{\rm cond} \le \min\left(\frac{1}{2}\frac{\rho(\Delta z)^2}{\kappa_0 T^{5/2}}\right), \tag{2.23}$$

where the time step is the minimum over the whole grid.

The conductive flux-saturation limit describes the maximum heat flux that the plasma is capable of supporting (Bradshaw and Cargill, 2006). This limit is reached when all of the particles travel in the same direction at the electron thermal speed, $v_{th} = (k_B T/m_e)^{1/2}$, and is given by,

$$F_{sa} = \frac{3}{2m_p\sqrt{m_e}}\rho(k_B T)^{3/2}, \tag{2.24}$$

where m_p and m_e are the proton and electron masses, respectively. In our numerical simulations, heat flux limiting is important because there is a sufficient amount of heating, in many of the events considered, so that the Spitzer-Harm heat flux,

$$F_{sp} = -\kappa_0 T^{5/2}\frac{\partial T}{\partial z}, \tag{2.25}$$

can exceed the conductive flux-saturation limit. Therefore, under such circumstances the Spitzer heat flux needs to be limited. To impose a heat flux limiter both the normalised Spitzer heat flux and the corresponding normalised flux-saturation limit need to be calculated. The normalised Spitzer heat flux is calculated during the internal stages of the RKL2 method and the normalised flux saturation limit is given by,

$$F_{sa} = \frac{3}{2}\sqrt{\frac{m_p}{m_e}}\rho T^{3/2}. \tag{2.26}$$

We replace the Spitzer heat flux terms, in the RKL2 method, with the following heat flux limiter that was described in BC13,

$$F_c = \frac{F_{sp} \times F_{sa}}{\sqrt{F_{sp}^2 + F_{sa}^2}}, \tag{2.27}$$

to limit the Spitzer-Harm heat flux. This heat flux limiter limits the heat flux contributions obtained from high temperatures ($T^{5/2}$) and steep gradients ($\partial T/\partial z$), in the Spitzer formulation, in order to ensure that we do not exceed the flux-saturation limit. It also preserves the sign of the conductive flux. Clearly, when $F_{sa} >> F_{sp}$, we recover the Spitzer heat flux and when $F_{sp} >> F_{sa}$, we recover the flux-saturation limit.

2.2.3 Optically Thin Radiation (OTR)

For the optically thin radiative loss function ($\Lambda(T)$) we use a piecewise continuous power law,

$$L_r = n^2 \chi T^{\alpha}, \tag{2.28}$$

where the temperature dependent constants χ and α are defined following Klimchuk et al. (2008). These radiation constants are presented in Table 2.1 and $\Lambda(T)$ is shown in Figure 2.1.

In the time-splitting update, the radiation step is of the form,

$$\rho \frac{\partial \epsilon}{\partial t} = -n^2 \chi T^{\alpha}. \tag{2.29}$$

However, since the Lare code is formulated in terms of the mass density (ρ), we also normalise the radiative losses in terms of the mass density,

$$L_r = n^2 \chi T^{\alpha} = \frac{\rho^2}{m_f^2 m_p^2} \chi T^{\alpha} = \chi_0 \frac{\rho_0^2}{\bar{m}^2} \hat{\rho}^2 \frac{\chi}{\chi_0} T_0^{\alpha} \hat{T}^{\alpha} = L_r^* \hat{\rho}^2 \chi^* \hat{T}^{\alpha}, \tag{2.30}$$

Table 2.1: OTR constants.

T (MK)	$\Lambda(T) = \chi T^{\alpha}$ (J m^{3}s^{-1})
$0.0100 < T \leq 0.0933$	$1.09 \times 10^{-44}\, T^{2}$
$0.0933 < T \leq 0.4677$	$8.87 \times 10^{-30}\, T^{-1}$
$0.4677 < T \leq 1.5136$	1.90×10^{-35}
$1.5136 < T \leq 3.5481$	$3.53 \times 10^{-26}\, T^{-3/2}$
$3.5481 < T \leq 7.9433$	$3.46 \times 10^{-38}\, T^{1/3}$
$7.9433 < T \leq 42.658$	$5.49 \times 10^{-29}\, T^{-1}$
$42.658 < T \leq 100.00$	$1.96 \times 10^{-40}\, T^{1/2}$

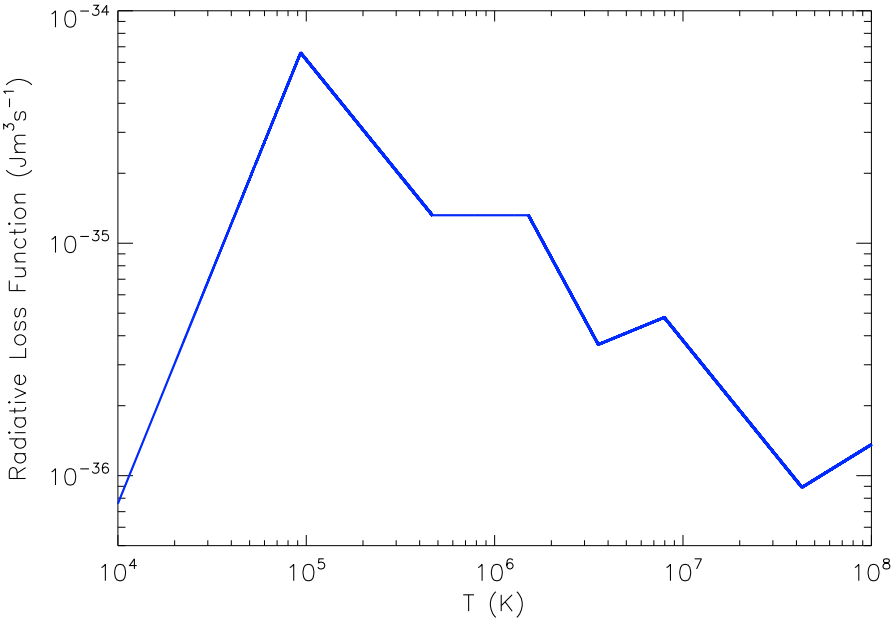

Figure 2.1: Klimchuk et al. (2008) optically thin radiative loss function ($\Lambda(T)$).

where $L_r^* = \chi_0 \frac{\rho_0^2}{\bar{m}^2}$, $\chi^* = \frac{\chi}{\chi_0} T_0^{\alpha}$, $\chi_0 = \chi(T_0)$ and $m_f = 1.2$. T_0 is the normalising temperature that is defined through the choice of normalisation constants ρ_0, B_0 and L_0.

Now applying the Lare normalisation, to the radiation step, we obtain,

$$\hat{\rho}\frac{\partial \hat{\epsilon}}{\partial \hat{t}} = -\, h^* L_r^* \, \frac{T_0^{\alpha}}{\chi_0} \, \hat{\rho}^2 \chi \hat{T}^{\alpha}, \tag{2.31}$$

where $h^* = \frac{L_0}{\rho_0 v_0^3}$. Therefore, it then follows that the radiation normalisation is given by,

$$\hat{\chi} = h^* L_r^* \frac{T_0^\alpha}{\chi_0}\chi. \tag{2.32}$$

Removing all the hats from the normalised variables, the normalised radiation step, given in terms of the mass density, is then of the form,

$$\rho\frac{\partial \epsilon}{\partial t} = -\rho^2 \chi T^\alpha. \tag{2.33}$$

To integrate the radiation step (2.33), we use a second-order time-centred finite difference method (FDM). This method is derived by letting $\Delta\epsilon = \epsilon^{n+1} - \epsilon^n$ be the change in specific internal energy density during a time step, then,

$$\frac{\Delta\epsilon}{\Delta t} = -\frac{1}{\rho^n}\left(\frac{L_r(\rho^{n+1}, T^{n+1}) + L_r(\rho^n, T^n)}{2}\right). \tag{2.34}$$

Since we assume that we have no flows during the radiation update it follows that $\rho^{n+1} = \rho^n$. Linearising the radiative loss function at temperature T^{n+1}, we obtain,

$$\epsilon^{n+1} - \epsilon^n = -\Delta t\ \rho^n \chi^n \left((T^n)^\alpha + \frac{\alpha}{2}\frac{(T^n)^\alpha}{(T^n)}(T^{n+1} - T^n)\right). \tag{2.35}$$

Defining $L_r^n = (\rho^n)^2\,\chi^n (T^n)^\alpha$, the radiation update is then given by,

$$\epsilon^{n+1} = \epsilon^n\ -\ \frac{L_r^n}{\rho^n/\Delta t + \alpha L_r^n/(2\epsilon^n)}. \tag{2.36}$$

To prevent the plasma from over cooling under the effects of OTR in a single time step without thermal conduction and heating being able to respond, we impose a radiation time step restriction (Δt_{rad}), on the integration, that prevents the temperature (specific internal energy density) from decreasing by more than 1%. This radiation time step is obtained by solving the radiation update (2.36) for Δt,

$$\Delta t_{\rm rad} \leq 2\frac{\rho^n \epsilon^n}{L_r^n}\frac{(\frac{\epsilon^n - \epsilon^{n+1}}{\epsilon^n})}{(2 - \alpha(\frac{\epsilon^n - \epsilon^{n+1}}{\epsilon^n}))}. \tag{2.37}$$

The 1% temperature restriction is ensured by selecting $(\frac{\epsilon^n - \epsilon^{n+1}}{\epsilon^n}) = 0.01$. This radiation time step (2.37) is not as severe at the advection time step (2.15) and conductive time step (2.23) but can become important when the radiative losses peak. Note that an analytic solution can be used to solve the radiation step (e.g. Townsend, 2009) but the time step still needs to be restricted.

We use a simple model for the chromosphere (the density increases exponentially with

depth for an isothermal temperature) that provides a mass reservoir to allow plasma to flow upwards through the transition region and into the corona, in response to heating. To maintain our isothermal chromosphere, at a temperature of 10,000K, radiation is smoothly turned off over a 100K interval, above the chromospheric temperature (e.g. Klimchuk et al., 1987, BC13). This is done by using the following Gaussian function,

$$L^n_{r_{\rm switch}}(\rho^n, T^n) = L^n_r(\rho^n, T^*) \exp\left[-\frac{(T^n - T^*)^2}{2(\Delta T_{\rm int}/3)^2}\right], \quad \forall\ T^n \leq T^*, \tag{2.38}$$

to reduce the radiative losses for $T^n \in (T_{\rm ch}, T^*]$, where we have defined $T^* = T_{ch} + \Delta T_{int}$, as the sum of the temperature switch-off interval ($\Delta T_{\rm int}$) and chromospheric temperature ($T_{\rm ch}$). The control width ($\Delta T_{\rm int}/3$) is carefully selected in order to ensure that the gradient of the radiative switch function is steeper than the gradient of the radiative loss function.

2.2.4 Heating

The Lare code deals with the effects of viscous heating during the advection step. However, we also include a separate heating step of the form,

$$\rho \frac{\partial \epsilon}{\partial t} = Q, \tag{2.39}$$

where our heating function, which is the dominant source of heating in our numerical simulations, is defined as the sum of contributions from both the background heating (Q_{bg}) and additional heating (Q_H),

$$Q = Q_{bg} + Q_H. \tag{2.40}$$

Applying the Lare normalisation we obtain,

$$\hat{\rho} \frac{\partial \hat{\epsilon}}{\partial \hat{t}} = h^* Q. \tag{2.41}$$

Consequently, the heating normalisation is given by,

$$\hat{Q} = h^* Q, \tag{2.42}$$

and $Q_0 = 1/h^*$. Removing all the hats from the normalised variables, the normalised heating step is then of the form (2.39). We integrate the heating step (2.39), using the following simple finite difference,

$$\epsilon^{n+1} = \epsilon^n + \frac{\Delta t}{\rho^n} Q^n, \tag{2.43}$$

which can be incorporated into the radiation step (2.33) or integrated separately.

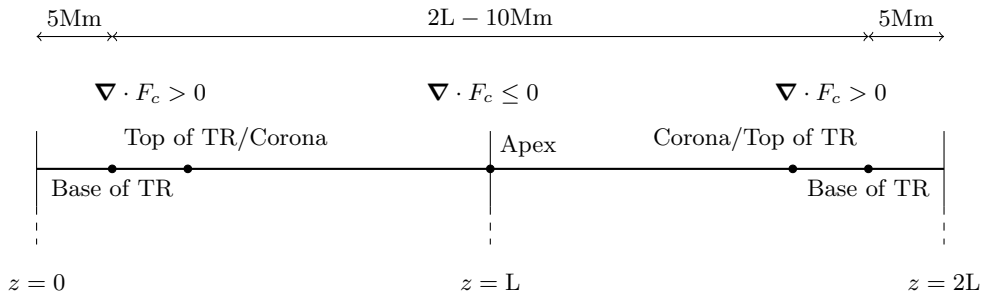

Figure 2.2: Spatial coordinate locations for a coronal loop of total length 2L.

2.2.5 Gravity

We impose a gravitational model that corresponds to a semi-circular loop. This geometry requires that gravity acts directly downwards at the base of the chromosphere ($z = 0$) and is zero at the loop apex ($z = \mathrm{L}$). We model coronal loops of total length 2L that include a 5Mm chromospheric layer at the base of each TR ($z = 5\mathrm{Mm}$) as outlined in Figure 2.2. Based on this configuration it then follows that the required gravitational model is given by,

$$g_{\parallel}(z) = g_{\odot} \cos\left(\frac{\pi z}{2L}\right), \tag{2.44}$$

where $g_{\odot} = 274 ms^{-2}$. The gravitational profile for a 90Mm loop is shown in Figure 2.3. Note that Eq. (2.44) can be adjusted to accommodate alternative spatial coordinate locations e.g. $z \in [-\mathrm{L}, \mathrm{L}]$ so that the loop apex is at $z = 0$.

Applying the Lare normalisation, we obtain that the normalised gravitational function is given by,

$$\hat{g}_{\parallel} = \frac{L_0}{v_0^2}\, g_{\parallel}(z), \tag{2.45}$$

where $\hat{g}_{\parallel}$ (the field-aligned gravitational acceleration) is defined on the cell boundary in the same location as the velocity.

2.2.6 Time-splitting Update

Let $\mathbf{U} = [P, \rho, v, \epsilon, T]$, be a vector of the model variables. The one-dimensional field-aligned MHD equations can then be written in terms of an ideal MHD component and non-ideal components,

$$\frac{\partial \mathbf{U}}{\partial t} = \mathbf{L}^{\mathrm{C}}(\mathbf{U}) + \mathbf{L}^{\mathrm{R}}(\mathbf{U}) + \mathbf{L}^{\mathrm{MHD}}(\mathbf{U}), \tag{2.46}$$

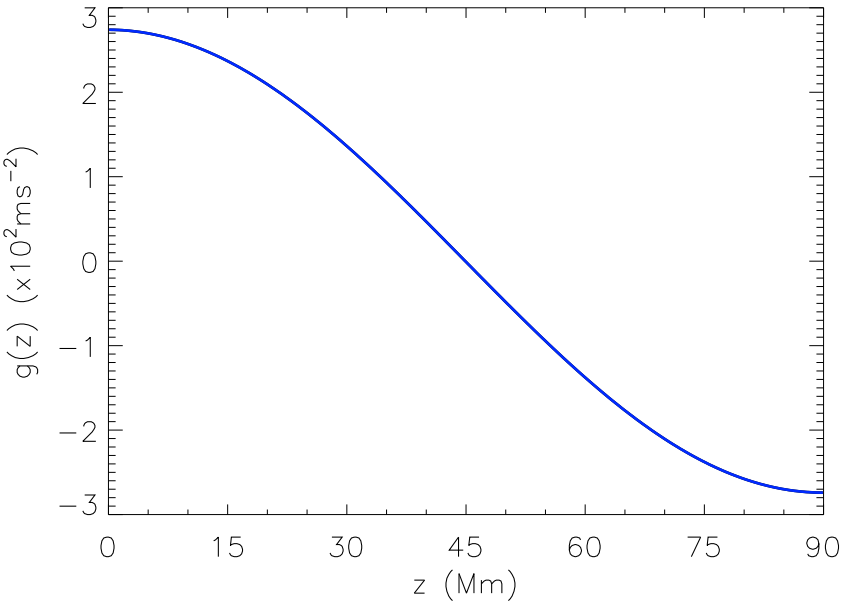

Figure 2.3: Gravitational profile as a function of position along the loop for a 90Mm loop.

where $\mathbf{L}^{\mathrm{C}}$, $\mathbf{L}^{\mathrm{R}}$ and $\mathbf{L}^{\mathrm{MHD}}$ are the thermal conduction, radiation and heating, and ideal MHD operators respectively. During a single time step, we use the Lie-splitting (sequential splitting) method to integrate these operators separately.

The temperature (specific internal energy density) is updated first, due to thermal conduction, then OTR and heating, before the ideal field-aligned MHD equations are solved. Following this strategy, the Lie-splitting update for one complete time step is given by,

$$\begin{aligned} \mathbf{U}^{*} &= \mathbf{C}(\mathbf{U}^{n}, \Delta t), \\ \mathbf{U}^{**} &= \mathbf{R}(\mathbf{U}^{*}, \Delta t), \\ \mathbf{U}^{\mathbf{n+1}} &= \mathbf{MHD}(\mathbf{U}^{**}, \Delta t), \end{aligned} \tag{2.47}$$

where $\mathbf{U}^{n+1} = \mathbf{C}(\mathbf{U}^{n}, \Delta t)$, $\mathbf{U}^{n+1} = \mathbf{R}(\mathbf{U}^{n}, \Delta t)$ and $\mathbf{U}^{n+1} = \mathbf{MHD}(\mathbf{U}^{n}, \Delta t)$ represent the updates of thermal conduction, radiation and heating (updated one after the other), and ideal MHD, for the time step Δt. This sequential update strategy is shown in Figure 2.4. It is first-order accurate in time.

Since we treat thermal conduction using STS methods, we super-step the conductive timescale restriction (accelerate the explicit time step sub-cycling). Therefore, the time-splitting strategy (2.47) stably integrates the field-aligned MHD equations, on a time step

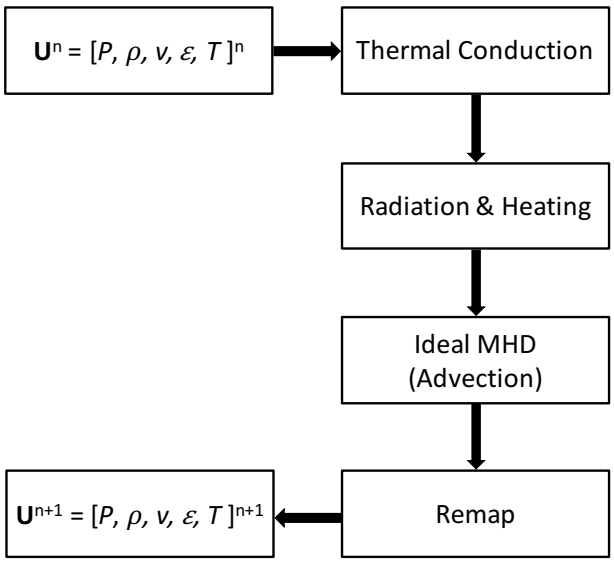

Figure 2.4: Lare1D with Thermal Conduction and Radiation time-splitting update strategy.

that is given by,

$$\Delta t = \min\left(\Delta t_{\rm adv},\, \Delta t_{\rm rad}\right). \tag{2.48}$$

We note that it may be possible to integrate Eq. (2.46) with higher temporal accuracy using the Strang-splitting method. However, Strang-splitting is computationally more expensive and second-order accuracy cannot be guaranteed due to the strong non-linear nature of the equations. Therefore, we have implemented the Lie splitting in order to simplify the update strategy and minimise the computational cost.

2.3 Hydrostatic Equilibrium

The model is a magnetic strand (loop) that is in initial hydrostatic and thermodynamic equilibrium. This is obtained by starting with an extremely high resolution uniform grid with 5×10^5 grid points along the length of the loop, which is later interpolated onto grids with much coarser spatial resolutions. The first step is to prescribe T and n at the base of the TR. The initial equilibrium temperature and density profiles are then derived using the same approach as described in Bradshaw and Mason (2003).

We set the conductive flux at the base of the TR to zero and obtain the equilibrium

by integrating the normalised hydrostatic equations,

$$\frac{dP}{dz} = -\rho g_{\parallel}(z), \tag{2.49}$$

$$\frac{dF_c}{dz} = Q_{bg} - \rho^2 \chi T^{\alpha} \tag{2.50}$$

$$P = 2\rho T, \tag{2.51}$$

between the base of the TR (at the left-hand leg of the loop) and loop apex. To achieve thermal balance we note that a small background heating term is necessary (Q_{bg}). The spatial profile of the background heating is uniform along the loop. Q_{bg} is adjusted using a bisection method until we minimise the heat flux at the loop apex. Hence, when solving the hydrostatic equations, we obtain the equilibrium temperature and density profiles, and the background heating value.

A two stage Runge-Kutta method (RK2) is used to solve the hydrostatic equations (2.49) – (2.51). Second-order accuracy in space is achieved by first predicting the values of the pressure, heat flux, temperature and density at the half spatial-step, on the cell boundary (zb_i) between the initial cell centre (zc_i) and its neighbouring right-hand cell centre (zc_{i+1}). These predicted values are then used to calculate the corrected values at the neighbouring right-hand cell centre (zc_{i+1}). Therefore, it is necessary to define the heat flux at the cell centre when solving the hydrostatic equations.

The predictor step is given by,

$$P_p = P_i - \frac{dzc_i}{2}\rho_i \left(\frac{g_{\parallel,i} + g_{\parallel,i-1}}{2} \right), \tag{2.52}$$

$$F_{c,p} = F_{c,i} + \frac{dzc_i}{2} \left(Q_{bg} - \rho^2 \chi T^{\alpha} \right), \tag{2.53}$$

$$T_p = T_i - \frac{dzc_i}{2} \frac{F_{c,i}}{\kappa_0 T_i^{5/2}} \tag{2.54}$$

$$\rho_p = \frac{P_p}{2T_p}, \tag{2.55}$$

where the index i indicates a quantity that is defined at the cell centre (zc_i) (gravity being the only exception since it is defined on the cell boundary) and the index p indicates a predicted variable that is defined on the cell boundary (zb_i). Using the predicted values, the hydrostatic corrector step is then given by,

$$P_{i+1} = P_i - dzc_i \, \rho_p \, g_{\parallel,i} \,, \tag{2.56}$$

$$F_{c,i+1} = F_{c,i} + dzc_i \left(Q_{bg} - \rho_p^2 \chi T_p^{\alpha} \right), \tag{2.57}$$

$$T_{i+1} = T_i - dzc_i \frac{F_{c,p}}{\kappa_0 T_p^{5/2}}, \tag{2.58}$$

$$\rho_{i+1} = \frac{P_{i+1}}{2T_{i+1}}, \tag{2.59}$$

where the index $i+1$ indicates a quantity that is defined at the cell centre (zc_{i+1}).

Applying this method we obtain the equilibrium temperature and density profiles over half of the loop (between the base of the TR and the loop apex). An isothermal chromosphere is then added to the loop between $z = 0$ and the base of the TR ($z = 5$Mm) by solving the hydrostatic equations for constant T. Since radiation is turned off at the chromospheric temperature ($T_{\rm ch}$) and the isothermal condition suppresses thermal conduction, we note that no background heating is initially included in the chromosphere to ensure that the thermal balance equation (2.50) is trivially satisfied. Hence, to obtain the chromospheric profiles only the force balance equation (2.50) needs to be solved. Using Eq. (2.51), one can write the force balance equation in terms of the pressure and temperature,

$$\frac{dP}{dz} = -\frac{P}{2T} g_{\parallel}(z). \tag{2.60}$$

With the pressure gradient and gravitational forces defined on the cell boundary, Eq. (2.60) is integrated spatially from the base of the TR to the base of the chromosphere (from right to left) using the following simple finite difference method (FDM),

$$P_i = P_{i+1} \frac{\left(1 + \frac{g_i\, dzc_i}{4T_{\rm ch}}\right)}{\left(1 - \frac{g_i\, dzc_i}{4T_{\rm ch}}\right)}. \tag{2.61}$$

$T_{\rm ch}$ is the isothermal temperature and the chromospheric density profile is extracted from the pressure profile using the normalised ideal gas law ($\rho_i = P_i/(2T_{\rm ch})$). To ensure force balance the density must increase exponentially in space towards the base of the chromosphere ($z = 0$).

The equilibrium profiles are then obtained for the whole loop (between $z = 0$ and $z = 2$L) by enforcing symmetry about the loop apex. Thus, the conductive flux is also zero at the loop apex. In the final step, the fully resolved equilibrium solutions are then interpolated onto the much coarser grids used for the time-dependent evolution.

Row 1 of Figure 2.5 shows the hydrostatic equilibrium obtained for a loop of total length 2L=90Mm, with $T = 10,000$K and n=10^{17}m^{-3} prescribed at the base of the TR. As we move upwards from the chromosphere, through the steep TR, to the corona, the equilibrium temperature increases by two orders of magnitude, from 10^4 to 10^6K. The density profile is approximately constant in the corona but increases by two orders of magnitude across the TR (to preserve constant pressure) before increasing exponentially

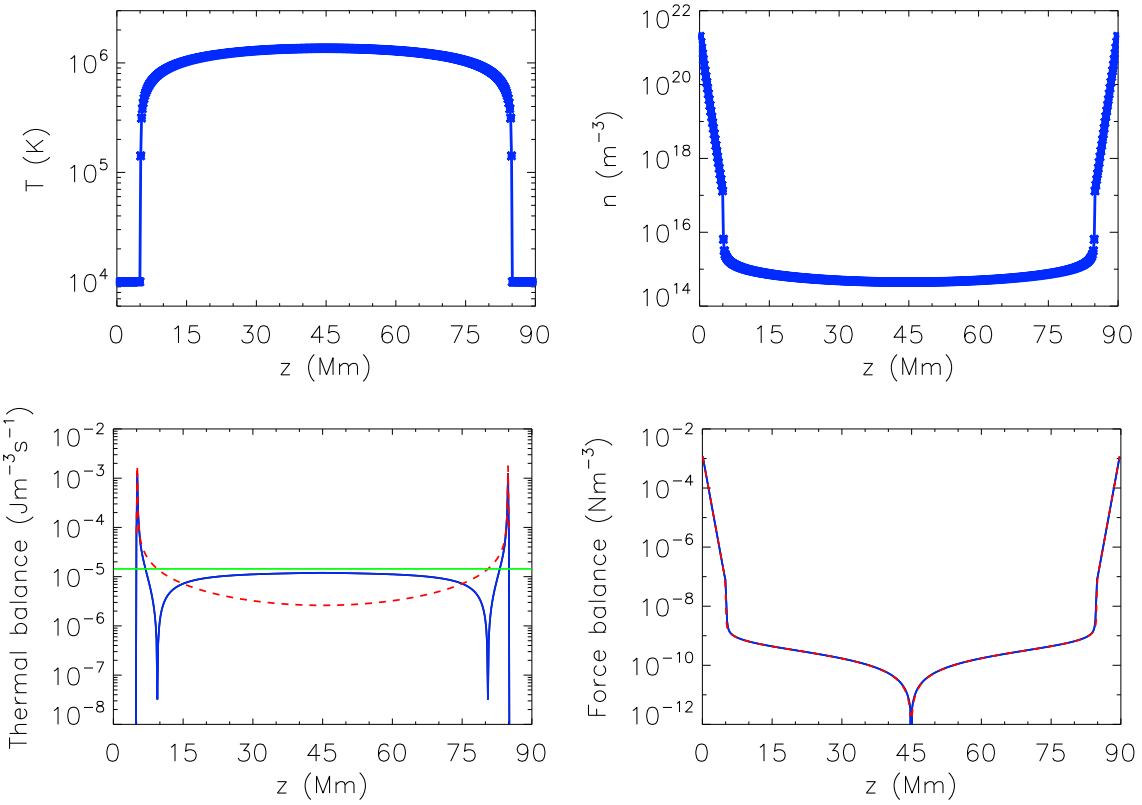

Figure 2.5: Hydrostatic equilibrium for a 90Mm loop with $Q_{bg} = 1.4367 \times 10^{-5}\mathrm{Jm}^{-3}\mathrm{s}^{-1}$. Row 1 shows the temperature and density profiles with 500 grid points along the length of the loop. Each asterisk represents a single grid point. Row 2 shows the terms in the hydrostatic equations that control the thermal and force balance as functions of position along the loop. Namely, the conduction term (solid blue line, the absolute value is shown), radiation term (dashed red line) and background heating term (solid green line) for thermal balance, and the pressure gradient (solid blue line) and gravitational (dashed red line) forces for force balance.

from the base of the TR towards the base of the chromosphere.

The terms that appear in the thermal (force) balance equation are shown in the left-hand (right-hand) column of Row 2 in Figure 2.5. The blue line is the absolute value of the conduction term ($|dF_c/dz|$), the dashed red line is the radiation term and the green line corresponds to the background heating term. (Based on the loop length and prescribed base quantities $Q_{bg} = 1.4367 \times 10^{-5} Jm^{-3}s^{-1}$ is the required background heating rate.) The top of the TR is the location where conduction changes sign from an energy loss to an energy gain. Thus, thermal conduction is a cooling term in the corona but becomes a heating term at the top of the TR. (The change in sign of conduction is seen in the figure as the rapid drop off then subsequent increase in $|dF_c/dz|$). Figure 2.5 shows that the energy balance is (1) predominantly between the background heating and thermal conduc-

tion in the corona and (2) between thermal conduction and OTR in the TR. The figure also shows that the pressure gradient (solid blue line) and gravitational forces (dashed red line) are in balance throughout the loop. Furthermore, the hydrostatic solutions quickly settle to maintain these equilibrium conditions when used as the initial conditions in the hydrodynamic solver (Lare1d with thermal conduction and radiation), with only minor adjustments to the energy balance in the TR required (when moving from a fine to coarse grid).

2.4 Super Time Stepping Methods to treat Thermal Conduction

The conduction term in the thermal energy equation is a parabolic operator while the ideal MHD equations form a hyperbolic system of partial differential equations (PDEs). We split this mixed parabolic-hyperbolic system into its ideal hyperbolic component and non-ideal components by using time-splitting methods, as discussed in Section 2.2. This allows the parabolic conduction term to be updated separately from the hyperbolic ideal MHD equations.

To treat thermal conduction either an explicit or implicit parabolic solver can be used. Explicit methods are simple to implement but for stability they suffer from an extremely restrictive time step that is proportional to the square of the spatial resolution ($\Delta t_{\rm cond} \sim (\Delta z)^2$). Therefore, for high (small) enough spatial resolutions (mesh sizes) $\Delta t_{\rm cond} << \Delta t_{\rm adv} \sim \Delta z$. This imbalance in time steps becomes even more severe when the plasma is at sufficiently high temperatures because $\Delta t_{\rm cond}$ also scales strongly with the inverse of temperature. Thus, in the time-splitting update either the parabolic time step has to be imposed on the advective solver or we have to sub-cycle the conduction term, in order to integrate to the advective time step.

Implicit methods can be unconditionally stable, allowing larger time steps than explicit methods. Consequently, with an implicit method, we can take a time step for conduction that is equivalent to the advection time step. However, implicit methods require far more computational effort, in each solution step, than explicit methods and the iterative schemes used to solve the matrix inversions can suffer from slow convergence. Furthermore, implicit methods only guarantee convergence to the equilibrium solutions but since we are interested in understanding the details of the dynamics, time accuracy is very important. On the other hand, the accuracy condition for an implicit method is equivalent to the stability condition for an explicit method (Bradshaw and Cargill, 2006). Therefore, the principal physical timescale which is the conductive time step across a grid point still needs to be resolved with an implicit method and so an explicit numerical method is

preferable.

In the interests of computational efficiency, to relax the conductive timescale stability restriction of an explicit method ($\Delta t_{\rm cond} \leq \rho(\Delta z)^2/(2\kappa_0 T^{5/2})$), we treat thermal conduction by using super time stepping (STS) methods, as described in Meyer et al. (2012, 2014). These methods are essentially an acceleration of explicit time step sub-cycling and have been used effectively to speed up the integration of parabolic operators. STS methods are explicit methods that are formulated to relax the restriction on the parabolic time step, $\Delta t_{\rm cond}$, while remaining simple to implement. These methods use "s" strategically designed, explicit Runge-Kutta stages that are choosen so that the overall time step, $\Delta t_{\rm STS}$, is stable up to $\sim s^2 \Delta t_{\rm cond}$ (Meyer et al. (2012)). Thus, with STS methods the number of stages is selected so that $s^2 \Delta t_{\rm cond} \sim \Delta t_{\rm adv}$. This allows the conduction term to be integrated to the advective time step using only s stages. Therefore, with STS methods, we obtain an s-fold gain in computational efficiency over explicit time step sub-cycling (Meyer et al. (2014)). Furthermore, when comparing STS methods with an explicit method which imposes the parabolic time step on the advective solver, the computational gains obtained are even more considerable.

2.4.1 Second-order Accurate Runge-Kutta Legendre Method (RKL2)

STS methods are designed to integrate the ordinary differential equation (ODE) system,

$$\frac{du}{dt} = \mathbf{L}_{\rm P} u(t), \tag{2.62}$$

that results from the spatial discretisation of a parabolic PDE. Here, $\mathbf{L}_{\rm P}$ is a symmetric, constant coefficient matrix which represents the discretisation of a parabolic operator and so has non-positive, real eigenvalues. The analytical solution for the update of Eq. (2.62) from time t^n to $t^{n+1} = t^n + \Delta t$ is given by,

$$\begin{aligned} u(t^n + \Delta t) &= \mathrm{e}^{\Delta t \mathbf{L}_{\rm P}} u(t^n), \\ &\approx \left\{ \mathbf{I} + \Delta t \mathbf{L}_{\rm P} + \frac{(\Delta t \mathbf{L}_{\rm P})^2}{2!} + \frac{(\Delta t \mathbf{L}_{\rm P})^3}{3!} + \ldots \right\} u(t^n). \end{aligned} \tag{2.63}$$

Now let λ be the eigenvalue of the operator $\mathbf{L}_{\rm P}$ so that we can write $\mathbf{L}_{\rm P} u(t) = \lambda u(t)$ for any eigenvector $u(t)$ of the operator. Defining $z = \lambda \Delta t$ the exact solution (2.63) can then be expressed in terms of z,

$$u(t^n + \Delta t) \approx \left\{ 1 + z + \frac{z^2}{2!} + \frac{z^3}{3!} + \ldots \right\} u(t^n). \tag{2.64}$$

To solve the ODE system (2.62) numerically the update of an s stage scheme can be written in terms of the method's stability polynomial,

$$\begin{aligned} u(t^n + \Delta t) &= R_s(\Delta t \mathbf{L}_{\mathrm{P}}) u(t^n), \\ &= R_s(\lambda \Delta t) u(t^n) = R_s(z) u(t^n), \end{aligned} \tag{2.65}$$

and stability is ensured if,

$$|R_s(\lambda \Delta t)| \leq 1 \quad \forall\, \lambda \in [-\lambda_{\max}, 0], \tag{2.66}$$

where $\lambda_{\max}$ is the spectral radius of the matrix $\mathbf{L}_{\mathrm{P}}$. The Runge-Kutta Legendre (RKL) methods are based on using shifted Legendre polynomials as the method's stability polynomial (Meyer et al. (2012, 2014)). This is because these polynomials are bounded in magnitude by unity and so give a stable scheme,

$$|P_n(x)| \leq 1 \quad \forall\, x \in [-1, 1], \tag{2.67}$$

where $P_n(x)$ is the nth Legendre polynomial. The Legendre polynomials are solutions to Legendre's differential equation. $P_n(x)$ is an nth-degree polynomial which can be defined as,

$$P_n(x) = \frac{1}{2^n} \sum_{k=0}^{n} \binom{n}{k}^2 (x-1)^{n-k} (x+1)^k. \tag{2.68}$$

The first eight Legendre polynomials (up to $n = 7$) are shown in Table 2.2 and Figure 2.6. Differentiating $P_n(x)$ with respect to x we obtain,

$$P_n'(x) = \frac{1}{2^n} \sum_{k=0}^{n} \binom{n}{k}^2 \Big\{ (n-k)(x-1)^{n-k-1}(x+1)^k + k(x-1)^{n-k}(x+1)^{k-1} \Big\}, \tag{2.69}$$

$$\begin{aligned} P_n''(x) = \frac{1}{2^n} \sum_{k=0}^{n} \binom{n}{k}^2 \Big\{ &(n-k)(n-k-1)(x-1)^{n-k-2}(x+1)^k \\ &+ 2k(n-k)(x-1)^{n-k-1}(x+1)^{k-1} + k(k-1)(x-1)^{n-k}(x+1)^{k-2} \Big\}, \end{aligned} \tag{2.70}$$

relations which we will use to derive the second-order accurate RKL method.

For the general s stage RKL method the stability polynomial is given by,

$$R_s(z) = a_s + b_s P_s(1 + w_1 z). \tag{2.71}$$

Table 2.2: Legendre polynomials up to $n = 7$.

n	$P_n(x)$
0	1
1	x
2	$\frac{1}{2}(3x^2 - 1)$
3	$\frac{1}{2}(5x^3 - 3x)$
4	$\frac{1}{8}(35x^4 - 30x^2 + 3)$
5	$\frac{1}{8}(63x^5 - 70x^3 + 15x)$
6	$\frac{1}{16}(231x^6 - 315x^4 + 105x^2 - 5)$
7	$\frac{1}{16}(429x^7 - 693x^5 + 315x^3 - 35x)$

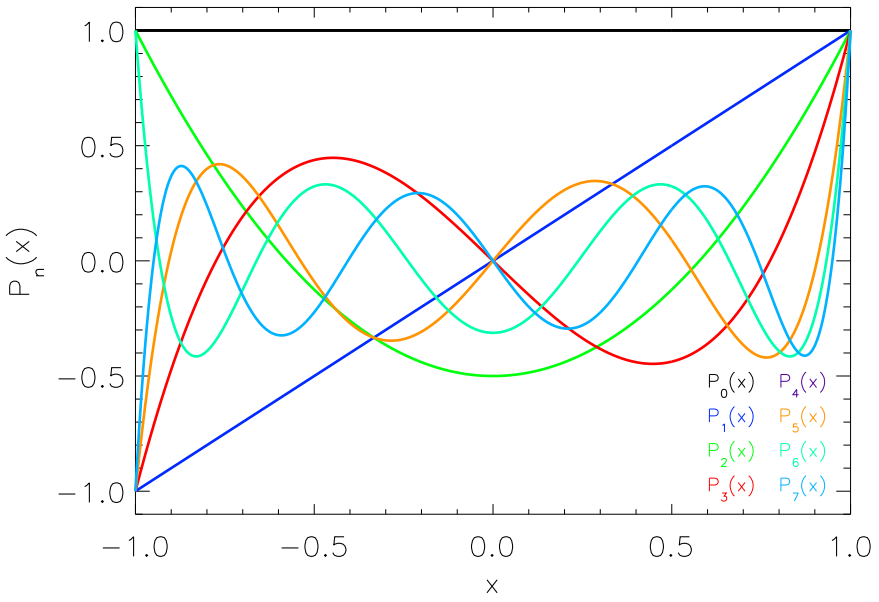

Figure 2.6: The Legendre polynomials, $P_n(x)$, up to $n = 7$.

Applying a Taylor series expansion of $R_s(z)$ about $z = 0$, the numerical update of Eq. (2.62) can be written in the form,

$$u(t^n + \Delta t) \approx \left\{ R_s(0) + R'_s(0)z + \frac{R''_s(0)z^2}{2!} + \frac{R'''_s(0)z^3}{3!} + \ldots \right\} u(t^n). \quad (2.72)$$

By comparing this expansion of the stability polynomial with the analytical solution (2.64), the parameters a_s, b_s and w_1 in the stability polynomial (R_s) are selected to ensure con-

sistency with the desired order of temporal accuracy for a particular scheme.

We treat thermal conduction by using the RKL2 STS method which has second-order temporal accuracy. This requires that $R_s(0) = 1$, $R'_s(0) = 1$ and $R''_s(0) = 1$ where,

$$R'_s(z) = b_s w_1 P'_s(1 + w_1 z); \quad R''_s(z) = b_s w_1^2 P''_s(1 + w_1 z). \tag{2.73}$$

Substituting $z = 0$ into the stability polynomial terms we obtain that,

$$\begin{aligned} a_s + b_s P_s(1) &= 1, \\ b_s w_1 P'_s(1) &= 1, \\ b_s w_1^2 P''_s(1) &= 1. \end{aligned} \tag{2.74}$$

Hence, for second-order accuracy the parameters in the stability polynomial must satisfy,

$$\begin{aligned} a_s &= 1 - b_s P_s(1), \\ b_s &= \frac{P''_s(1)}{(P'_s(1))^2}, \\ w_1 &= \frac{P'_s(1)}{P''_s(1)}. \end{aligned} \tag{2.75}$$

Rewriting equations (2.68) – (2.70) to group terms with and without $(x - 1)$ as a factor,

$$\begin{aligned} P_n(x) &= \frac{1}{2^n}\left\{ \binom{n}{n}^2 (x+1)^n \right\} + (x-1) \text{ factor terms}, \\ &= \frac{(x+1)^n}{2^n} + (x-1) \text{ factor terms}, \end{aligned} \tag{2.76}$$

$$\begin{aligned} P'_n(x) &= \frac{1}{2^n}\left\{ \binom{n}{n-1}^2 (x+1)^{n-1} + \binom{n}{n}^2 n(x+1)^{n-1} \right\} + (x-1) \text{ factor terms}, \\ &= n(n+1)\frac{(x+1)^{n-1}}{2^n} + (x-1) \text{ factor terms}, \end{aligned} \tag{2.77}$$

$$\begin{aligned} P''_n(x) = \frac{1}{2^n}\Bigg\{ &\binom{n}{n-2}^2 2(x+1)^{n-2} + \binom{n}{n-1}^2 2(n-1)(x+1)^{n-2} \\ &+ \binom{n}{n}^2 n(n-1)(x+1)^{n-2} \Bigg\} + (x-1) \text{ factor terms}, \end{aligned}$$

$$= n(n-1)(n+1)(n+2)\frac{(x+1)^{n-2}}{2^{n+1}} + (x-1) \text{ factor terms}, \tag{2.78}$$

it is clear that,

$$\begin{aligned} P_n(1) &= 1, \\ P_n'(1) &= \frac{n(n+1)}{2}, \\ P_n''(1) &= \frac{n(n-1)(n+1)(n+2)}{8}. \end{aligned} \tag{2.79}$$

Therefore, for the s stage RKL2 method we take,

$$\begin{aligned} a_s &= 1 - b_s, \\ b_s &= \frac{s^2+s-2}{2s(s+1)}, \\ w_1 &= \frac{4}{s^2+s-2}. \end{aligned} \tag{2.80}$$

The RKL methods also require that each internal stage has a stability polynomial that corresponds to a Legendre polynomial. Thus, for the j-th stage of an s stage RKL2 scheme we take,

$$R_j(z) = a_j + b_j P_j(1 + w_1 z). \tag{2.81}$$

The Legendre polynomials satisfy a three point recursion relation,

$$(n)P_n(x) = (2n-1)xP_{n-1}(x) - (n-1)P_{n-2}(x). \tag{2.82}$$

Thus, the stability polynomials of the internal stages can be generated recursively using this relationship and for $s < 2$ we have the freedom to prescribe $b_0 = b_1 = b_2 = 1/3$. Substituting $R_j(z)$ into Eq. (2.82) and rearranging we obtain,

$$\begin{aligned} a_j + b_j P_j(1+w_1 z) &= \frac{(2j-1)}{j} b_j (1+w_1 z) P_{j-1}(1+w_1 z) - \frac{(j-1)}{j} b_j P_{j-2}(1+w_1 z) + 1 - b_j, \\ &= \frac{(2j-1)}{j}\frac{b_j}{b_{j-1}}(b_{j-1}P_{j-1}(1+w_1 z)) + \frac{(1-j)}{j}\frac{b_j}{b_{j-2}}(b_{j-2}P_{j-2}(1+w_1 z)) \\ &+ \frac{(2j-1)}{j}\frac{b_j}{b_{j-1}} w_1 z (b_{j-1}P_{j-1}(1+w_1 z)) \end{aligned}$$

$$
\begin{aligned}
&+\left(1-\frac{(2j-1)}{j}\frac{b_j(1-a_{j-1})}{b_{j-1}}-\frac{(1-j)}{j}\frac{b_j(1-a_{j-2})}{b_{j-2}}\right),\\
&=\frac{(2j-1)}{j}\frac{b_j}{b_{j-1}}(a_{j-1}+b_{j-1}P_{j-1}(1+w_1z))\\
&+\frac{(1-j)}{j}\frac{b_j}{b_{j-2}}(a_{j-2}+b_{j-2}P_{j-2}(1+w_1z))\\
&+\left(1-\frac{(2j-1)}{j}\frac{b_j}{b_{j-1}}-\frac{(1-j)}{j}\frac{b_j}{b_{j-2}}\right)\\
&+\frac{(2j-1)}{j}\frac{b_j}{b_{j-1}}w_1z(a_{j-1}+b_{j-1}P_{j-1}(1+w_1z))\\
&-a_{j-1}\frac{(2j-1)}{j}\frac{b_j}{b_{j-1}}w_1z. \qquad (2.83)
\end{aligned}
$$

so that the stability polynomial of the j-th stage is given by,

$$
\begin{aligned}
R_j(z)=&\frac{(2j-1)}{j}\frac{b_j}{b_{j-1}}R_{j-1}(z)+\frac{(1-j)}{j}\frac{b_j}{b_{j-2}}R_{j-2}(z)+\left(1-\frac{(2j-1)}{j}\frac{b_j}{b_{j-1}}-\frac{(1-j)}{j}\frac{b_j}{b_{j-2}}\right)\\
&+\frac{(2j-1)}{j}\frac{b_j}{b_{j-1}}w_1zR_{j-1}(z)-a_{j-1}\frac{(2j-1)}{j}\frac{b_j}{b_{j-1}}w_1z. \qquad (2.84)
\end{aligned}
$$

Therefore, written out as a numerical scheme, the s stage RKL2 method to integrate Eq. (2.62) from time t^n to $t^{n+1}=t^n+\Delta t$ is given by,

$$
\begin{aligned}
&\mathbf{Y}_0=\mathbf{u}^n,\\
&\mathbf{Y}_1=\mathbf{Y}_0+\tilde{\mu}_1\Delta t\mathbf{L}_{\mathrm{P}}\mathbf{Y}_0,\\
&\mathbf{Y}_j=\mu_j\mathbf{Y}_{j-1}+\nu_j\mathbf{Y}_{j-2}+(1-\mu_j-\nu_j)\mathbf{Y}_0\tilde{\mu}_j\Delta t\mathbf{L}_{\mathrm{P}}\mathbf{Y}_{j-1}+\tilde{\gamma}_j\Delta t\mathbf{L}_{\mathrm{P}}\mathbf{Y}_0,\quad 2\le j\le s,\\
&\mathbf{u}^{n+1}=\mathbf{Y}_s. \qquad (2.85)
\end{aligned}
$$

with the parameters,

$$
\begin{aligned}
\mu_j&=\frac{(2j-1)}{j}\frac{b_j}{b_{j-1}}=\frac{(2j-1)(j+2)(j-1)^2}{j(j-2)(j+1)^2},\\
\nu_j&=-\frac{(j-1)}{j}\frac{b_j}{b_{j-2}}=-\frac{(j-1)^3(j^2-4)}{j^3(j+1)(j-3)},\\
\tilde{\mu}_j&=\frac{(2j-1)}{j}\frac{b_j}{b_{j-1}}w_1=\mu_jw_1=\frac{(2j-1)(j+2)(j-1)^2}{j(j-2)(j+1)^2}\frac{4}{s^2+s-2},
\end{aligned}
$$

$$\tilde{\mu}_1 = \frac{4}{3(s^2+s-2)},$$

$$\tilde{\gamma_j} = -a_{j-1}\frac{(2j-1)}{j}\frac{b_j}{b_{j-1}} - = -a_{j-1}\tilde{\mu}_j = \frac{(j-1)(j+2)(2j-1)(j^2-j+2)}{2j^2(j-2)(j+1)^2}. \quad (2.86)$$

The stability condition for the time step, Δt, is derived from the criteria given in Eq. (2.66). $|R_s(\lambda\Delta t)| \leq 1$ is satisfied for $P_s(1+w_1 z) \leq 1$. Since, the Legendre polynomials $P_n(x)$ are bounded in magnitude by unity $\forall\, x \in [-1,1]$, this requires that,

$$-1 \leq 1 + w_1\lambda\Delta t \leq 1. \quad (2.87)$$

The right-hand inequality is trivially satisfied for non-positive, real eigenvalues and so the left-hand inequality controls the stability, requiring that,

$$\Delta t \leq \frac{2}{w_1|\lambda_{\max}|}, \quad (2.88)$$

For an explicit forward Euler update of equation (2.62) the parabolic time step restriction, $\Delta t_{\rm parab}$, is related to the spectral radius of the matrix $\mathbf{L}_{\rm P}$ by $\Delta t_{\rm parab} = 2/\lambda_{\max}$. Therefore, the RKL2 method is stable if,

$$\Delta t_{\rm STS} \leq \frac{s^2+s-2}{4}\Delta t_{\rm parab}, \quad (2.89)$$

where $\Delta t_{\rm STS}$ is the overall time step we intend to take through the s stage scheme. The j-th stage of the RKL2 method can thus be interpreted as a second-order accurate approximation of the solution at time $t = t^n + \Delta t_{\rm STS}(j^2+j-2)/(s^2+s-2)$ and additional stages can be used to increase the maximum stable time step (Meyer et al., 2014). When Eq. (2.62) represents the thermal conduction step (2.16), $\Delta t_{\rm parab}$ is given by the conductive timescale, $\Delta t_{\rm cond}$, defined in Eq. (2.23). However, note that the formulation presented here also holds for any general parabolic operator e.g. viscosity.

Based on this stability condition, the number of explicit Runge-Kutta stages required for the RKL2 scheme is determined by selecting the smallest odd integer value of s satisfying,

$$s \geq \frac{1}{2}\left(\sqrt{9+16\frac{\Delta t_{\rm STS}}{\Delta t_{parab}}} - 1\right). \quad (2.90)$$

When necessary the number of stages is rounded upwards to ensure that the stability criteria (2.89) is satisfied.

The integration of the RKL2 method to treat thermal conduction in conjunction with

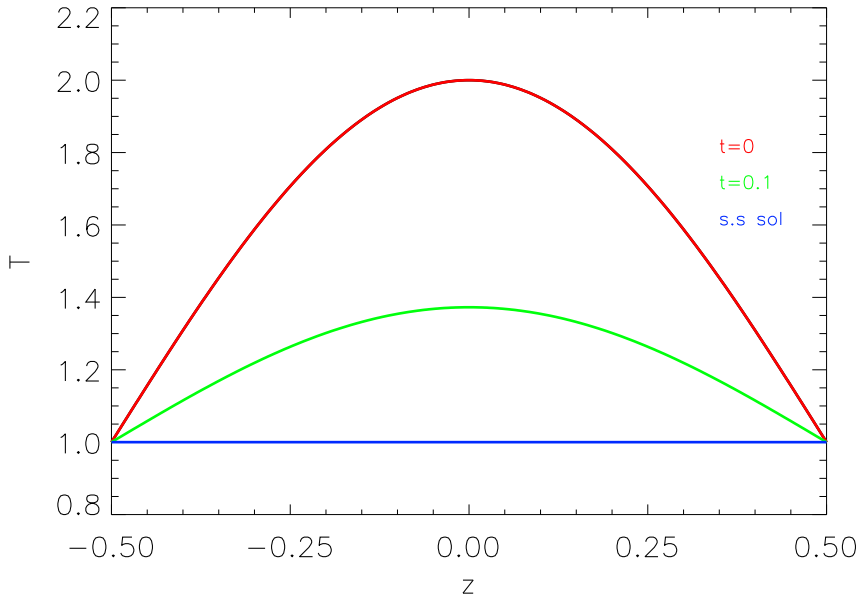

Figure 2.7: Exact solution $T(z,t)$ for the linear conduction BVP. The solid red line is the initial condition ($t = 0$), the solid green line is the solution at the final time $t = 0.1$ and the solid blue line corresponds to the steady state solution.

the Lare ideal MHD solver is discussed in Section 2.2. Note that since the Legendre polynomials are also bounded by unity in the complex plane, the restriction that the parabolic operator $\mathbf{L}_{\rm P}$ is a symmetric, constant coefficient matrix can be relaxed (Meyer et al., 2012, 2014), thereby making it possible to use the RKL2 method outlined in Eq. (2.85) to integrate the thermal conduction operator in the MHD equations whose diffusion coefficient is both strongly non-linear and temperature dependent.

Extending the test problems considered in Meyer et al. (2012, 2014), we test the RKL2 method for appropriateness of use in coronal plasma conditions, in order to ensure that the increased conductive time step does not influence the correct temporal evolution.

2.4.2 Linear Conduction

However, first we demonstrate the accuracy and order of the RKL2 method by solving the following linear conduction boundary value problem (BVP),

$$\frac{\partial T}{\partial t} = -\frac{\partial}{\partial z}\left(-\frac{\partial T}{\partial z}\right), \qquad -1/2 \le z \le 1/2,$$
$$T(-1/2,t) = T(1/2,t) = 1, \tag{2.91}$$

Table 2.3: Numerical errors and experimental orders of convergence for the RKL2 and forward Euler methods in solving the linear conduction BVP at the final time $t = 0.1$.

s	N_z	N_t	ℓ_1 error	ℓ_1 convergence	ℓ_∞ error	ℓ_∞ convergence
RKL2						
3	10	8	2.078E-3	-	3.619E-3	-
5	20	16	5.200E-4	2.00	8.593E-4	2.07
7	40	32	1.314E-4	1.98	2.117E-4	2.02
9	80	64	3.308E-5	1.99	5.261E-5	2.01
13	160	128	8.283E-6	2.00	1.309E-5	2.01
19	320	256	2.072E-6	2.00	3.265E-6	2.00
Euler						
	10	20	3.538E-3	-	6.164E-3	-
	20	80	9.195E-4	0.97	1.520E-3	1.01
	40	320	2.350E-4	0.98	3.786E-4	1.00
	80	1280	5.946E-5	0.99	9.457E-5	1.00
	160	5120	1.495E-5	1.00	2.364E-5	1.00
	320	20480	3.750E-6	1.00	5.909E-6	1.00

Notes. From left to right the columns show the number of stages in the RKL2 scheme, the number of grid points (uniform grid used), the number of time steps required to reach the final time, the ℓ_1 norm error and order of convergence, and the ℓ_∞ norm error and order of convergence.

with the initial condition,

$$T(z, 0) = \cos(\pi z) + 1, \quad -1/2 \leq z \leq 1/2.$$

The exact solution of this model equation is given by $T(z, t) = e^{-\pi^2 t} \cos(\pi z) + 1$. We use the explicit forward Euler method as a benchmark solution and compare the performance of both numerical methods in approximating this exact solution at the final time $t = 0.1$, which is selected in order to ensure that the solution is significantly different from the unity steady state solution.

The linear conduction operator is approximated using spatial central differences,

$$\mathbf{L}^{\mathrm{C}}(T) = \frac{\partial^2 T}{\partial z^2} \approx \frac{T_{i-1} - 2T_i + T_{i+1}}{(\Delta z)^2}, \tag{2.92}$$

and for the forward Euler method we take the maximum stable parabolic time-step ($\Delta t_{\mathrm{parab}} \leq (\Delta z)^2/2$). With the RKL2 method we start by selecting an $s = 3$ stage scheme and take $N_z = 10$ as the initial number of grid points. The maximum stable super

time step, $\Delta t_{\rm STS}$, is then calculated together with the number of super time steps, $N_{t_{\rm STS}}$, required to reach the final time. For subsequent resolutions, both the number of super time steps and the number of spatial grid points, N_z, are doubled before selecting the smallest odd value of s satisfying the stability criteria given in Eq. (2.89). The results are presented in Table 2.3, where the ℓ_1 and ℓ_∞ norm errors are shown together with their orders of accuracy.

It is clear that the RKL2 method achieves its second-order in time design accuracy whilst permitting the use of a relaxed time step ($\Delta t_{\rm STS} \leq (s^2 + s - 2)\Delta t_{\rm parab}/4$). Comparing the results for the $N_z = 80$ resolution, the RKL2 method requires only 64 super time steps, each consisting of 9 internal stages. Therefore, to integrate Eq. (2.91) to the final time, the RKL2 method requires only 576 update operations while the first-order accurate forward Euler method requires 1,280 explicit updates. Hence, in addition to improved temporal accuracy, the RKL2 method also obtains an $\sim \frac{s}{4}$-fold gain in computational efficiency over the explicit forward Euler method. Furthermore, as we increase the resolution, the number of stages in the RKL2 scheme increases and so the gains obtained become increasingly more significant.

2.4.3 Non-Linear Conduction

Reflective of the non-linear, temperature dependent conduction term in the thermal energy equation, we now demonstrate how the RKL2 method performs in solving the Zel'dovich problem of a propagating conduction front (Zel'dovich and Raizer, 1967),

$$\begin{aligned} &\frac{\partial T}{\partial t} = -\frac{\partial}{\partial z}\left(-T^{5/2}\frac{\partial T}{\partial z}\right), \qquad 0 \leq z \leq 2, \\ &T'(0,t) = 0 \end{aligned} \tag{2.93}$$

with the initial condition,

$$T(z,0) = \begin{cases} \left(1 - \frac{5}{4}z^2\right)^{2/5}, & 0 \leq z \leq 2/\sqrt{5}. \\ 0, & 2/\sqrt{5} < z \leq 2 \end{cases}$$

Following Zel'dovich and Raizer (1967) the self-similar solution for this model BVP is given by,

$$T(z,t) = \begin{cases} \frac{1}{\left(1+\frac{9}{2}t\right)^{2/9}}\left(1 - \dfrac{z^2}{\frac{4}{5}\left(1+\frac{9}{2}t\right)^{4/9}}\right)^{2/5}, & 0 \leq z \leq \frac{2}{\sqrt{5}}\left(1+\frac{9}{2}t\right)^{2/9}, \\ 0, & \left(\frac{2}{\sqrt{5}}1 + \frac{9}{2}t\right)^{2/9} < z \leq 2. \end{cases} \tag{2.94}$$

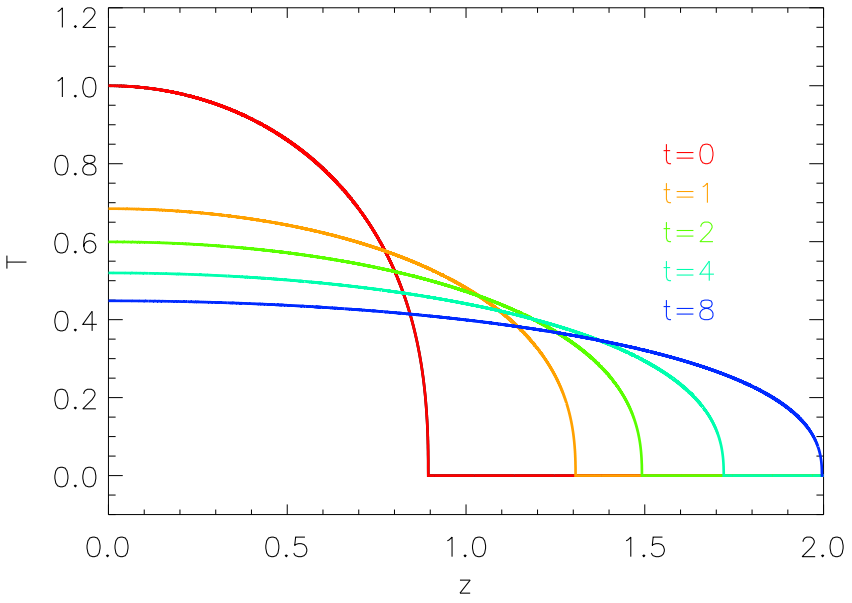

Figure 2.8: Exact solution $T(z,t)$ for the non-linear conduction BVP. The solid red line is the initial condition ($t = 0$), the solid orange, green and cyan lines correspond to the solutions at time $t = 1$, $t = 2$ and $t = 4$ respectively, and the solid blue line is the solution at the final time $t = 8$.

Table 2.4: Numerical errors and experimental order of convergence for the RKL2 method in solving the non-linear conduction BVP at the final time $t = 8$.

s_0	N_z	$N_{t_{\text{STS}}}$	ℓ_1 error	ℓ_1 convergence
RKL2				
11	20	50	7.814E-3	-
17	40	100	2.440E-3	1.68
23	80	200	5.165E-4	2.24
33	160	400	4.178E-4	0.31
45	320	800	2.502E-4	0.74
65	640	1600	9.930E-5	1.33
91	1280	3200	3.226E-5	1.62

Notes. From left to right the columns show the initial number of stages in the RKL2 scheme, the number of grid points (uniform grid used), the number of super time steps required to reach the final time and the ℓ_1 norm error and order of convergence.

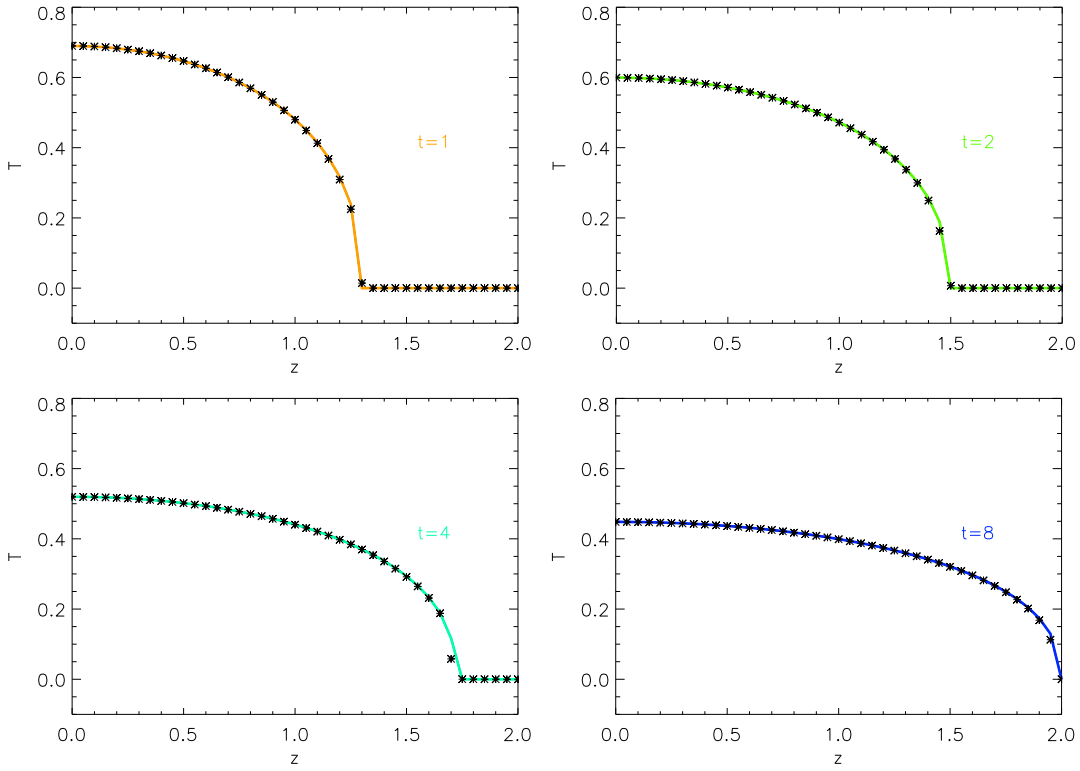

Figure 2.9: Results for the non-linear conduction BVP. The panels show the solutions at time $t = 1$, $t = 2$, $t = 4$ and $t = 8$ as functions of position. The solid lines represent the exact solution $T(z,t)$ and the black asterisks correspond to the numerical solution T_i^n obtained by using the RKL2 method with the resolution $N_z = 40$ and $N_t = 100$.

Thus, the solutions propagate along the z-axis with the travelling wavefront location,

$$z_f(t) = \frac{2}{\sqrt{5}}\left(1 + \frac{9}{2}t\right)^{2/9}, \tag{2.95}$$

and as the solutions propagate, the maximum temperature decreases.

For the RKL2 method, consistent with the Lare implementation, we approximate the non-linear conduction operator using central differencing of the heat flux (see Eq. (2.19)). Solutions are computed using the RKL2 scheme together with the initial and boundary conditions defined in (2.93) and an additional boundary condition taken as $T(2,t) = 0$. This additional boundary condition is imposed based on observations from the exact solution.

We begin by selecting an RKL2 scheme that starts initially with $s_0 = 11$ stages for a spatial resolution of $N_z = 20$ grid points. The maximum stable time step is enforced for the parabolic time step ($\Delta t_{\text{parab}} = (\Delta x)^2/2\max(T^{5/2})$). This time step increases in time as the solutions propagate since the maximum temperature decreases. On the other hand,

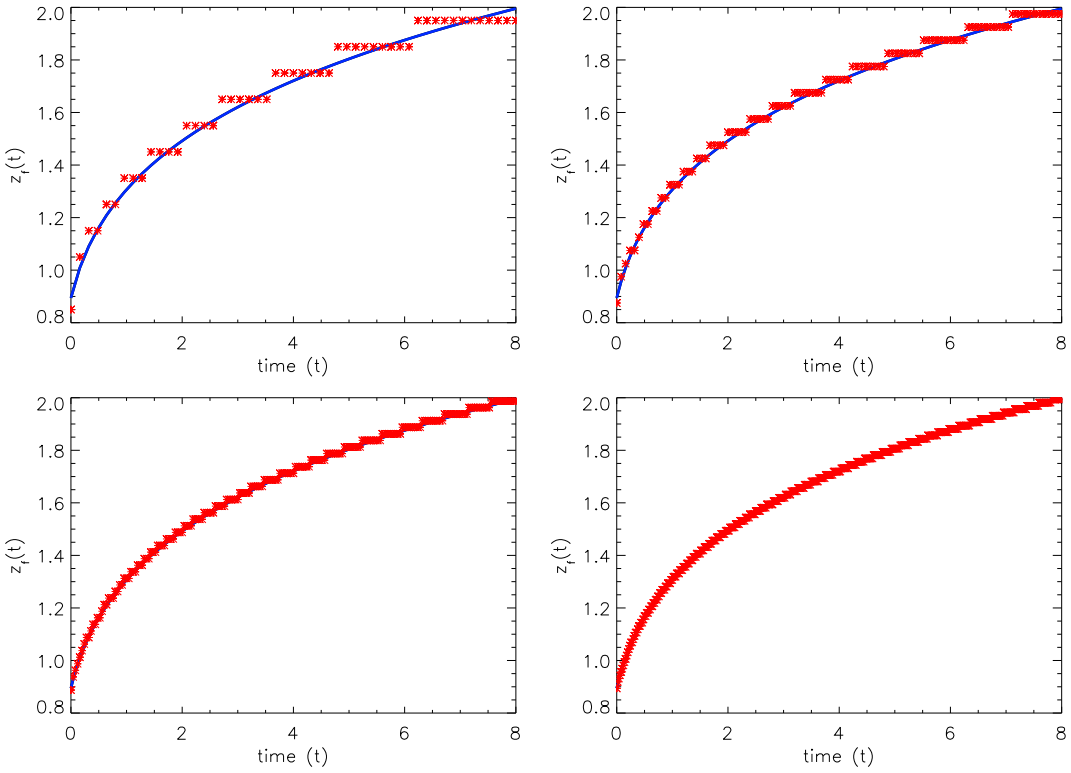

Figure 2.10: Results for the non-linear conduction BVP. The panels show the travelling wavefront locations as a function of time for different spatial and temporal resolutions employed with the RKL2 method. The solid blue curve represents the exact solution $z_f(t)$ and the red asterisks correspond to the numerical solutions z_f^n obtained by using the RKL2 method. The spatial resolutions shown are $N_z = 20$, $N_z = 40$, $N_z = 80$ and $N_z = 160$, respectively (from top left to bottom right) and the grid resolution is $\Delta z = 0.1$, 0.05, 0.025 and 0.0125. The corresponding temporal resolutions are given in Table 2.4.

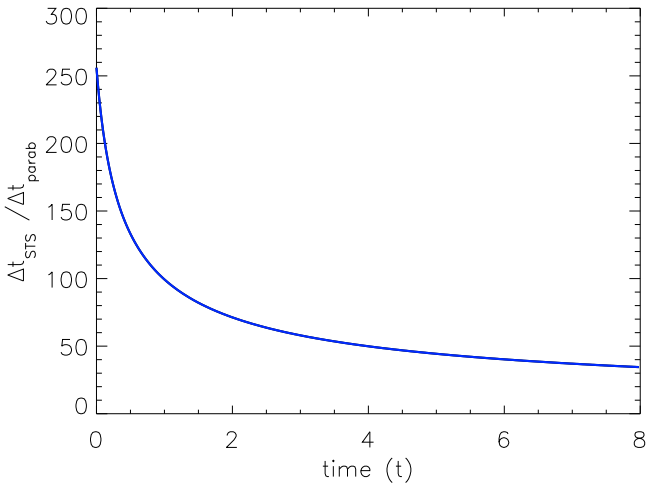

Figure 2.11: Results for the non-linear conduction BVP. The panel shows the time step ratio, $\Delta t_{\rm STS}/\Delta t_{\rm parab}$, obtained by using the RKL2 method with the resolution $N_z = 160$ and $N_t = 400$.

we take a uniform super time step, Δt_{STS}, that is calculated based on the initial temperature profile and corresponds to the maximum stable super time step at time $t = 0$. This means that the number of super time steps ($N_{t_{\text{STS}}}$) required to reach the final time $t = 8$ can be easily calculated but note that the number of internal stages in the RKL2 scheme must decrease in time as the parabolic time step increases. For subsequent resolutions, both the number of super time steps and the number of spatial grid points, N_z, are doubled before selecting the smallest odd value of s satisfying the stability criteria given in Eq. (2.89). The results are presented in Table 2.4 and the time evolution of the RKL2 numerical solution with $N_z = 40$ is displayed as asterisks on top of the exact solution in Figure 2.9. The temporal evolution of the analytical and RKL2 travelling wavefront locations are also shown in Figure 2.10. For non-linear conduction, the ℓ_1 convergence rate achieved is reduced in comparison to the linear case. However, the RKL2 solutions still remain sufficiently accurate to correctly capture the time evolution of the conduction wavefront. Figure 2.10 demonstrates that as the spatial resolution is increased, the RKL2 wavefront locations converge to the corresponding exact locations. At the resolution where convergence is first observed, the super time step, Δt_{STS}, is on average 60 times larger than the parabolic time step, Δt_{parab}, as shown in Figure 2.11. Therefore, the temporal evolution of the conduction front is correctly resolved when using STS methods and substantial computational gains are obtained because of the permitted increased conductive time step.

2.4.4 Non-Linear Conduction with Radiation and Heating

In this section, we investigate whether or not STS methods can correctly obtain the growth rate when leaving a thermally unstable isothermal equilibrium and the subsequent decay rate when approaching a thermally stable non-isothermal equilibrium. Using a model equation, under the assumption of constant density, we solve the boundary value problem,

$$\begin{aligned} &\frac{\partial T}{\partial t} = -\frac{\partial}{\partial z}\left(-T^{5/2}\frac{\partial T}{\partial z}\right) - \chi T^{\alpha} + H, \ -1/2 \leq z \leq 1/2, \\ &T(-1/2, t) = T(1/2, t) = T_0, \end{aligned} \tag{2.96}$$

with the initial condition,

$$T(z, 0) = T_0 + \bar{T_1}\cos(\pi z), \quad -1/2 \leq z \leq 1/2.$$

T_0 is the isothermal unstable temperature and $\bar{T_1}\cos(\pi z)$ is a small perturbation. Lin-

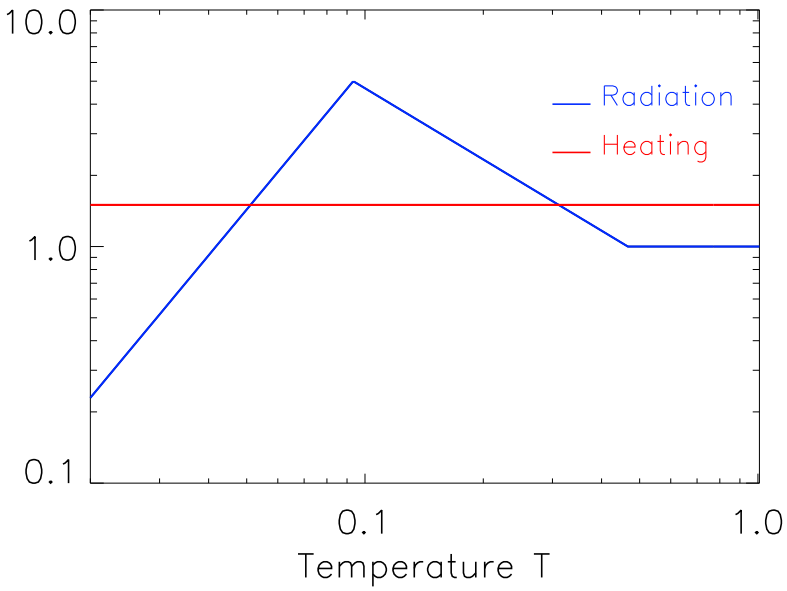

Figure 2.12: The optically thin radiative loss function ($\Lambda(T) = \chi T^{\alpha}$) and heating term $H = 1.5$ that are used in the non-linear conduction with radiation and heating BVP. The temperature dependent constants χ and α defined as in Table 2.1. The isothermal unstable equilibrium is the larger temperature value where the heating intersects the radiative loss function i.e. $T_0 = (H/\chi^*)^{(1/\alpha^*)}$ with $\alpha^* = -1$ and $\chi^* = 0.4668$. The units on both axes are arbitary.

earising equation (2.96), the temperature grows as,

$$T(0,t) = T_0 + \bar{T_1}(0)e^{\sigma t}, \tag{2.97}$$

with $\sigma = -\pi^2 T_0^{5/2} - \alpha\chi T_0^{\alpha-1}$.

Time-splitting methods are used to split Eq. (2.96) into its non-linear conduction, radiation and heating parts. Numerical solutions are computed using the RKL2 scheme to treat thermal conduction together with integration methods that are consistent with those outlined in Section 2.2 to update the radiation and heating steps. We take a final time $t = 4$ with a spatial resolution of $N_z = 80$. Note that since the RKL2 method is now coupled with a radiation and heating solver, in order to solve Eq. (2.96), the number of stages in the STS scheme is defined by super stepping conduction to the radiation time step.

Figure 2.13 shows the temporal evolution of $T(0,t)$ using the RKL2 method, as a solid red curve labelled T_a^n. The linear solution (2.97) is shown as asterisks and the exact growth rate matches the rate calculated from the computational solution. A similar analysis confirms that the exact decay rate, as the temperature evolves towards the non-

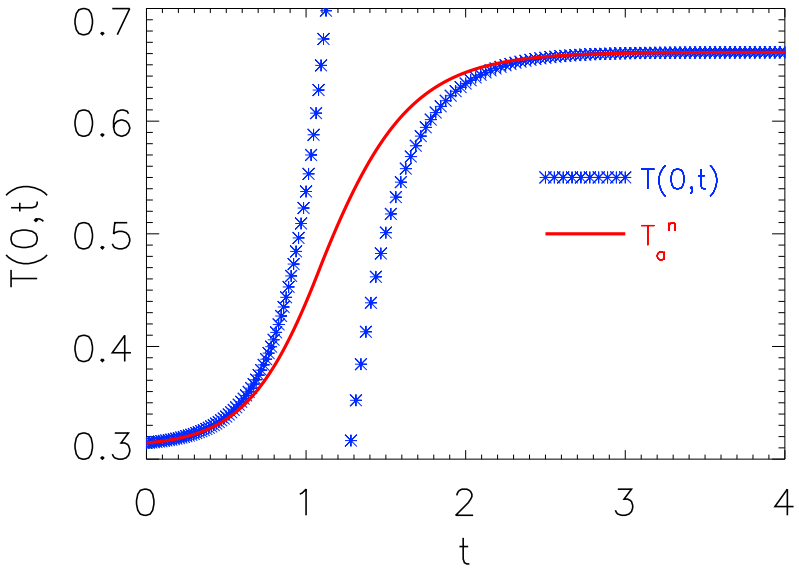

Figure 2.13: The panel shows the temporal evolution of $T(0,t)$. The solution leaves a thermally unstable isothermal equilibrium and approaches a new stable, non-isothermal equilibrium. The solid red curve is the numerical solution obtained by using the RKL2 STS method (T_a^n) and the blue asterisks represent the corresponding linear solutions ($T(0,t)$). The units on both axes are arbitrary.

isothermal stable equilibrium, is also correctly predicted by the STS method. Therefore, we believe that STS methods are appropriate for use in solving more complex coronal plasma based problems, where the effect of thermal conduction plays an important role.

2.4.5 Field-aligned Ideal MHD Simulations

Although STS methods have already been implemented in some 3D MHD codes (e.g. Reale et al., 2016), it remains instructive here to present a quantification of the computational gains involved for a subset of the chromospheric evaporation simulations that are considered in detail in the chapter that follows. Thermal conduction is treated using three different methods; the RKL2 STS method, explicit time step sub-cycling and explicit time step evolution. Note that the evaporative response is consistent between each of the methods used in these simulations. However, based on the computation time ratios in Table 2.5, the benefit of using STS methods is immediately clear, especially as the coronal temperature, which scales strongly with the heating event (case number) increases and the conductive timescale decreases.

Table 2.5: Numerical simulation computation times (run on a single processor) for three different methods to treat thermal conduction.

Case	N_z	$\tau_{\rm sts}$ (mins)	$\tau_{\rm cyc}$ (mins)	$\tau_{\rm exp}$ (mins)	$\tau_{\rm cyc}/\tau_{\rm sts}$	$\tau_{\rm exp}/\tau_{\rm sts}$
1	500	2.45	1.98	2.25	0.81	0.92
	1,000	6.73	6.47	15.72	0.96	2.34
	2,000	12.23	29.07	128	2.38	10.5
	4,000	42.6	199	592	4.67	13.9
	8,000	205	1,537	4,699	7.50	22.9
2	500	6.32	8.12	25.7	1.28	4.07
	1,000	18.5	45.02	122	2.43	6.59
	2,000	48.8	308	970	6.31	19.9
	4,000	135	2,385	7,772	17.7	57.6
	8,000	607	18,778	47,123*	30.9	77.6
3	500	12.15	33.13	168	2.73	13.8
	1,000	49.67	257	790	5.17	15.9
	2,000	138	2,023	6,238	14.7	45.2
	4,000	579	15,958	48,405*	27.6	83.6
	8,000	2,440	108,898*	238,620*	44.6	97.8

Notes. From left to right the columns show the case number, the number of grid points (uniform grid used), the computation times by treating thermal conduction using super time stepping methods (sts), explicit time step sub-cycling (cyc) and explicit time step evolution (exp), and the computation time ratios between these methods. The simulations (Cases 1-3 of Table 3.1) are run to a final time of 60s, which coincides with the end of the heating period. The asterisks indicate runs where the computation time to the final time has been estimated based on results over a shorter period.

2.5 Chapter Summary

The numerical method that will be employed throughout this thesis to solve the MHD equations has been discussed. In particular, super time stepping (STS) methods have been introduced to treat thermal conduction. Advantages over other explicit and implicit methods have been discussed, serving to motivate the implementation of these stabilised Runge-Kutta methods. The derivation of the second-order accurate Runge-Kutta Legendre (RKL2) method has been presented and we have demonstrated that this method achieves (i) its temporal design accuracy, (ii) the correct temporal evolution with an increased conductive time step and (iii) substantial computational gains. The following chapter will discuss how we use the numerical methods outlined here together with a jump condition to model chromospheric evaporation in response to enhanced coronal heating.

Chapter 3

A New Approach for Modelling Chromospheric Evaporation in Response to Enhanced Coronal Heating

This chapter introduces a new computational approach that addresses the difficulty of obtaining the correct interaction between the solar corona and the transition region (TR) in response to rapid heating events, and is based on work published in the paper Johnston et al. (2017a). In the coupled corona, TR and chromosphere system, the heating increases the coronal temperature and then an enhanced downward conductive flux creates an upflow (chromospheric evaporation). However, obtaining the correct upflow generally requires high spatial resolution in order to resolve the TR. With an unresolved TR, artificially low coronal densities are obtained because the downward heat flux 'jumps' across the unresolved region to the chromosphere where the incoming energy is then strongly radiated (Bradshaw and Cargill, 2013, hereafter BC13). This leaves little excess energy to drive an upward enthalpy flux and so the upflows are underestimated. Here, we treat the unresolved region of the lower TR, which we refer to as the unresolved transition region (UTR), as a discontinuity that responds to changing coronal conditions through the imposition of a jump condition. The jump condition used is derived from an integrated form of energy conservation.

To illustrate and benchmark this approach against a fully resolved one-dimensional (1D) model, we present field-aligned simulations of coronal loops in response to a range of impulsive (spatially uniform) heating events. We show that our approach leads to a significant improvement in the coronal density evolution when compared to equivalent

simulations run without the jump condition but using the same coarse grid (insufficient to resolve the lower TR). Our approach compensates for the jumping of the heat flux by imposing a velocity correction that ensures that the energy from the heat flux goes into driving the TR dynamics, rather than being lost through radiation. Hence, making it possible to obtain improved coronal densities.

The chapter has the following structure: we describe the numerical method and definitions used to locate the UTR in Section 3.1. The UTR jump condition is derived and the implementation described in Section 3.2. In Section 3.3, we present example simulations and compare our approach with a fully resolved 1D model. We conclude with a discussion of our new approach and the advantages of employing it, in both 1D hydrodynamic and 3D magnetohydrodynamic (MHD) simulations, in Section 3.4.

3.1 Numerical Method & Definitions

The full details of the numerical method are discussed in Chapter 2 and so are just restated briefly here. We model chromospheric evaporation in response to enhanced impulsive coronal heating by solving the 1D field-aligned MHD (hydrodynamic) equations (2.1)–(2.4) using two different methods, a Lagrangian remap (Lare) approach, as described for 3D MHD in Arber et al. (2001), adapted for 1D field-aligned hydrodynamics (Lare1D) and the adaptive mesh code HYDRAD (Bradshaw and Mason, 2003). Time-splitting methods are used in Lare to update thermal conduction and optically thin radiation separately from the advection terms, as discussed in Section 2.2. Furthermore, to treat thermal conduction we use super time stepping (STS) methods, as described in Meyer et al. (2012, 2014) and discussed in Section 2.4.

The initial condition of the model is a magnetic strand (loop) in static equilibrium. This is obtained by using the method described in Section 2.3 with $T = 10,000$K and n=10^{17}m^{-3} prescribed at the base of the TR. We consider both a short (60Mm) and long (180Mm) loop, where the total length of each loop ($2L$) includes a 5Mm model chromosphere (included as a mass reservoir) at the base of each TR ($z = 5$Mm). Figure 3.1 shows the initial conditions, with 500 grid points along the length of the loop, for both the short and long loop. We note that neither solution is numerically resolved below approximately 2×10^5K until the chromospheric temperature is reached.

Instead of trying to implement a grid that fully resolves the TR, we use coarse spatial resolutions and address the influence of poor numerical resolution by modelling the unresolved region of the atmosphere (UTR) as a discontinuity and use an appropriate jump condition. To facilitate the formulation of this approach, we first introduce some

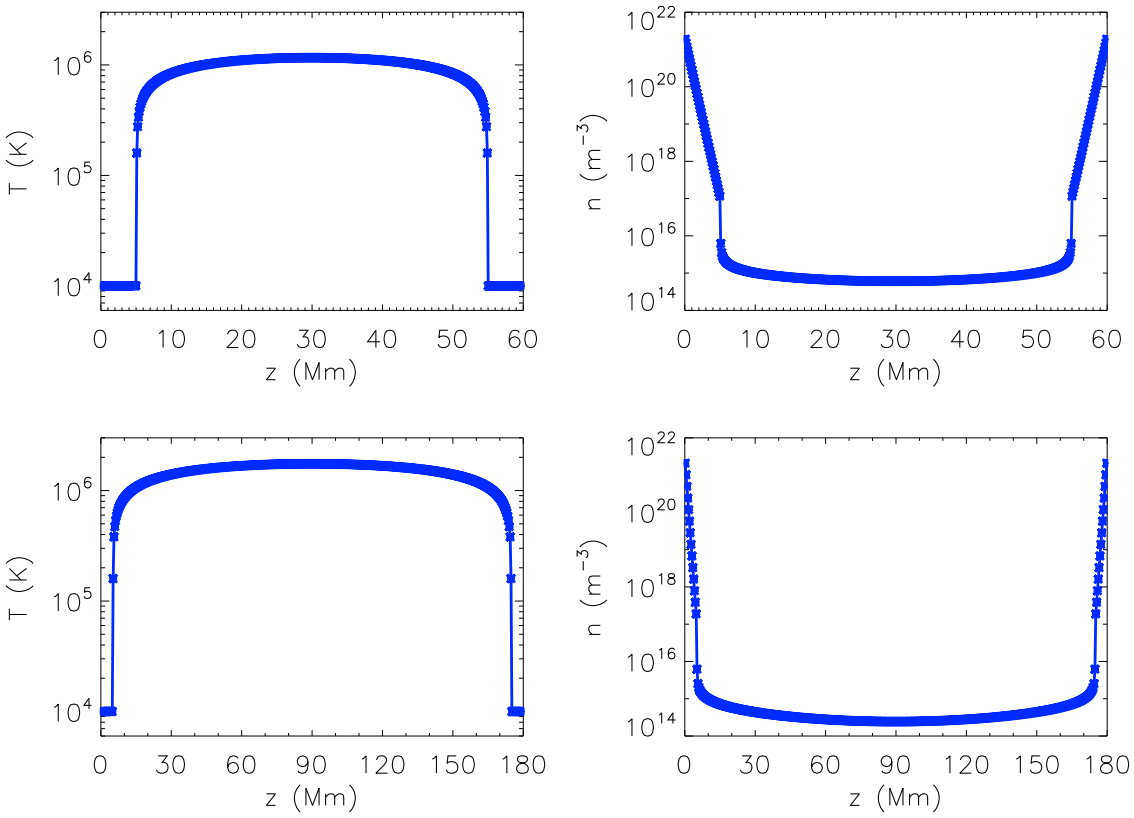

Figure 3.1: Temperature and density initial conditions with 500 grid points along the length of the loop. Upper panels: 60Mm loop with $Q_{bg} = 2.2167 \times 10^{-5}\mathrm{Jm^{-3}s^{-1}}$. Lower panels: 180Mm loop with $Q_{bg} = 6.8682 \times 10^{-6}\mathrm{Jm^{-3}s^{-1}}$. Each asterisk represents a single grid point.

definitions. We define the temperature length scale as,

$$L_T = \frac{T}{|dT/dz|} = \frac{\kappa_0 T^{7/2}}{|F_c|}. \tag{3.1}$$

With a uniform grid, the resolution in the simulation is given by,

$$L_R = \frac{2L}{N_z - 1}, \tag{3.2}$$

where N_z is the number of grid points along the length of the loop ($2L$). (A non-uniform grid will have the same problems, amenable with a similar solution.) Using these definitions, we define the top of the UTR (z_0) to be the final location, when moving downwards from the loop apex (z_a), at which the criteria,

$$\frac{L_R}{L_T} \leq \delta < 1, \tag{3.3}$$

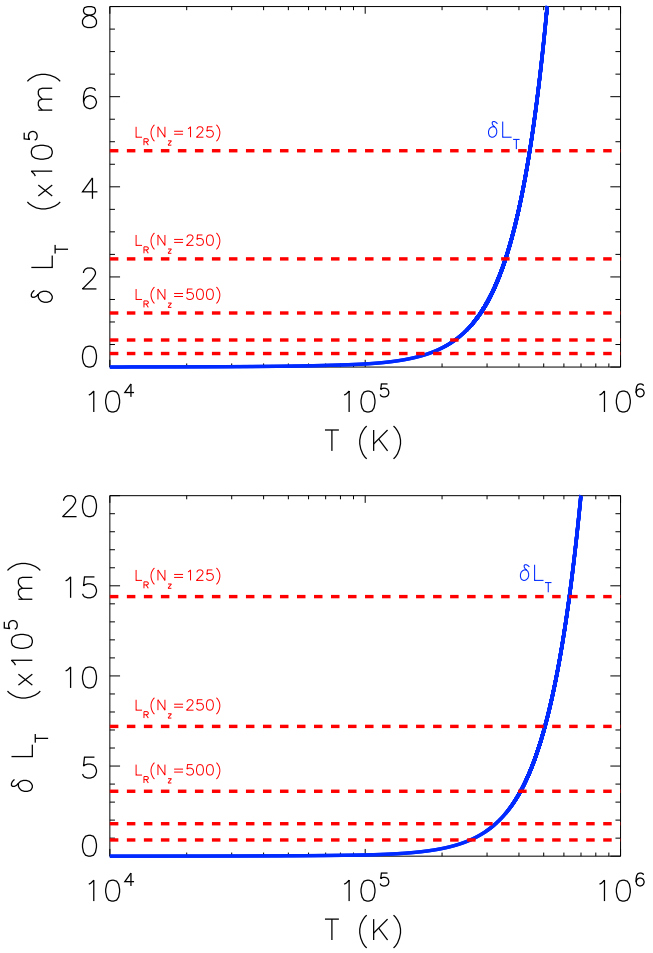

Figure 3.2: The product of δ and the temperature length scale (L_T) as a function of temperature (solid blue line) based on fully resolved equilibrium solutions that are computed with 5×10^5 grid points along the length of the loop and are consistent with the short and long loop initial conditions shown in Figure 3.1. Upper panel: 60Mm loop. Lower panel: 180Mm loop. The dashed red lines are the simulation resolutions (L_R) obtained by using different numbers of grid points. In both plots, starting from the top the first dashed red line corresponds to 125 grid points, the second to 250 grid points, the third to 500 grid points, the fourth to 1,000 grid points and the fifth to 2,000 grid points.

is satisfied. To ensure that we have sufficient resolution at the top of this region, that is multiple grid points across the temperature length scale, we take $\delta = 1/4$ throughout this work.

Figure 3.2 demonstrates the consequences of Eq. (3.3) for short (long) loops in the upper (lower) panel. The product of δ and L_T is shown as a function of temperature (solid blue line) with the dashed red lines showing different values of L_R. Any temperature that falls below the dashed lines will be part of an UTR, for the particular simulation

resolution (L_R). For example, this arises below a few 10^5K with $N_z = 500$, highlighting the resolution issue. An indication of the temperature at the top of the UTR is given by the temperature at which the dashed lines (L_R) intersect the δL_T curve. Therefore, Figure 3.2 also shows that when coarse resolution is used, the temperature at the top of the UTR (T_0) is only weakly dependent on the spatial resolution. For example, as can be seen in the upper panel of Figure 3.2, when using between 250 and 1,000 grid points (i.e. $250 \leq N_z \leq 1,000$) for the short loop ($2L = 60$Mm), the T_0 range varies by less than a factor of 2 ($2.1 \times 10^5\text{K} \leq T_0 \leq 3.5 \times 10^5\text{K}$).

Lastly, we define the base of the TR (z_b) to be the location at which the temperature first reaches or falls below the prescribed chromospheric temperature (10,000K). Employing these definitions, it is straightforward to locate both the top of the UTR and the base of the TR at all time steps during a simulation. This is crucial because the UTR is dynamic. It moves in response to coronal heating and cooling. Thus, we note here that z_b and z_0 are not fixed locations, their definitions allow for temporal variations.

3.2 Unresolved Transition Region Jump Condition

On use of equations (2.1)–(2.4), one can write an equation for the total energy in conservative form,

$$\frac{\partial E}{\partial t} = -\frac{\partial}{\partial z}(Ev + Pv + F_c) + Q - n^2\Lambda(T), \tag{3.4}$$

where the total energy is the sum of internal, kinetic and gravitational potential energy,

$$E = \frac{P}{\gamma - 1} + \frac{1}{2}\rho v^2 + \rho\Phi. \tag{3.5}$$

Here, P is the gas pressure, ρ is the density, v is the velocity, Φ is the gravitational potential ($g_\parallel = d\Phi/dz$), $F_c = -\kappa_0 T^{5/2}\partial T/\partial z$ is the heat flux, Q is the volumetric heating rate, n is the number density and $\Lambda(T)$ is the radiative loss function in an optically thin plasma.

We integrate Eq. (3.4) over the UTR (of length ℓ), from the base of the TR (z_b) upwards to the top of the UTR (z_0), to obtain,

$$\begin{aligned}\ell\frac{d\bar{E}}{dt} =& - E_0 v_0 - P_0 v_0 - F_{c,0} \\ &+ E_b v_b + P_b v_b + F_{c,b} + \ell\bar{Q} - \mathcal{R}_{utr},\end{aligned} \tag{3.6}$$

where the subscripts 0 and b indicate quantities evaluated at the top and base of the UTR, respectively. The overbars indicate spatial averages over the UTR, defined as,

$$\frac{d\bar{E}}{dt} = \frac{1}{\ell}\int_{z_b}^{z_0} \frac{\partial E}{\partial t}\, dz; \tag{3.7}$$

$$\bar{Q} = \frac{1}{\ell}\int_{z_b}^{z_0} Q\, dz. \tag{3.8}$$

For spatially uniform heating we note that $\bar{Q}$ reduces to Q. Lastly, $\mathcal{R}_{utr}$ is the integrated radiative losses (IRL) in the UTR,

$$\mathcal{R}_{utr} = \int_{z_b}^{z_0} n^2 \Lambda(T)\, dz. \tag{3.9}$$

Using the fully resolved HYDRAD results, we have confirmed that $F_{c,b}$ is always small ($F_{c,b} << F_{c,0}$) and that after the initial downward motion of the TR (during the heating phase), the terms containing v_b are also significantly smaller than the remaining terms on the right-hand side (RHS) of Eq. (3.6). It is these remaining terms that control the coronal response. Hence, since the heat flux and flow are small at the base of the TR, we follow Cargill et al. (2012a) and neglect these base terms ($E_b v_b, P_b v_b \,\&\, F_{c,b}$) from now on. We return to this point in Chapter 4, where we present a full analysis of the terms appearing in Eq. (3.6), both retained and neglected.

We have also confirmed, from the fully resolved results, that there are only short intervals (at the start of the heating period) when $\ell d\bar{E}/dt$ can be significant. However, the problem with including this term is that, with the resolution of current 3D MHD models, it is very difficult to calculate $\ell d\bar{E}/dt$ accurately because the calculation requires dE/dt to be integrated across the UTR. If the TR is not fully resolved then the heat flux jumps across the UTR, resulting in the estimates of dE/dt being in error. Indeed, if we could calculate $\ell d\bar{E}/dt$ accurately, with coarse spatial resolutions, then it would not be necessary to implement a method to obtain the correct upflow and evaporation. Therefore, the final assumption in the derivation of our jump condition is to adopt the approach of Klimchuk et al. (2008) and neglect the left-hand side (LHS) of Eq. (3.6).

Under these assumptions, by combining equations (3.5) & (3.6), we obtain the jump condition at the top of the UTR,

$$\frac{\gamma}{\gamma-1} P_0 v_0 + \frac{1}{2}\rho_0 v_0^3 + \rho_0 \Phi_0 v_0 = -F_{c,0} + \ell\bar{Q} - \mathcal{R}_{utr}, \tag{3.10}$$

where the terms on the LHS are the enthalpy flux, kinetic energy flux and gravitational potential energy flux, respectively. The terms on the RHS are the heat flux, the average

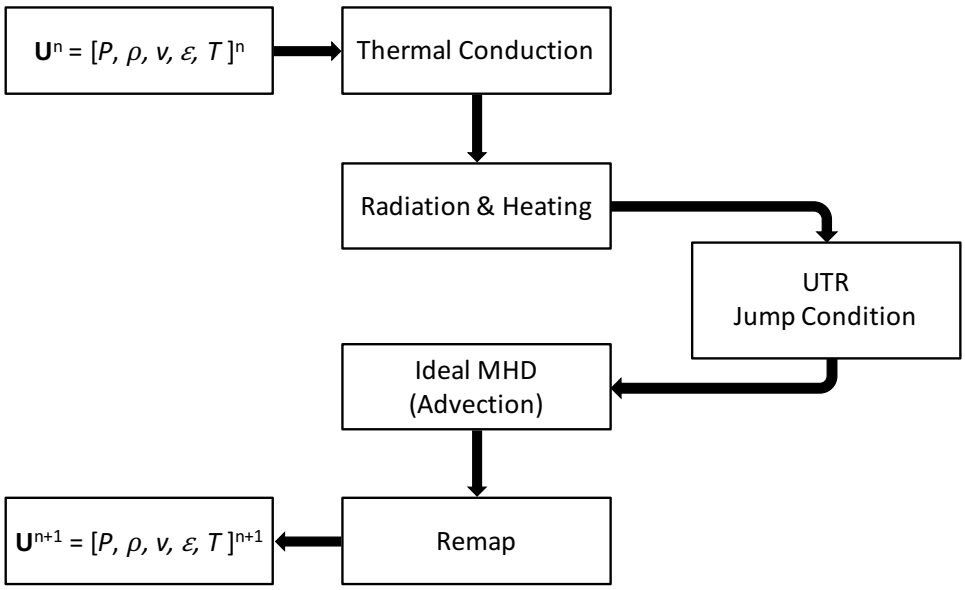

Figure 3.3: Modification to Lare1D with Thermal Conduction and Radiation time-splitting update strategy to include the UTR jump condition. This step is ignored when the Lare1D code is employed without the jump condition e.g. see Figure 2.4.

volumetric heating rate per unit cross-sectional area and the IRL in the UTR respectively. We refer to Eq. (3.10) as the UTR jump condition and model the UTR as a discontinuity using Eq. (3.10) to impose a corrected velocity (v_0) at the top of the UTR, during each time step.

This corrected velocity is imposed following the conduction and radiation and heating steps, prior to the advection step, as illustrated in Figure 3.3, while the flow at the base of the TR (v_b) is subsequently accounted for during the advection step. Consequently, at the time of calculation of v_0, it is possible to calculate the heat flux ($F_{c,0}$) and the average volumetric heating rate per unit cross-sectional area in the UTR ($\ell\bar{Q}$). Of the terms on the LHS of the UTR jump condition (3.10), the pressure (P_0), density (ρ_0), and gravitational potential (Φ_0) are also all known. The main challenge is the calculation of the IRL in the UTR ($\mathcal{R}_{utr}$).

3.2.1 Integrated Radiative Losses in the Unresolved Transition Region

Direct integration of the radiative losses in the UTR is not possible due to the lack of spatial resolution and we do not yet resort to using interpolation methods to help overcome this problem (see Chapter 6). Instead, at this stage a simpler method for approximating the IRL is used. Motivated by equilibrium results, we estimate $\mathcal{R}_{utr}$ using the IRL from

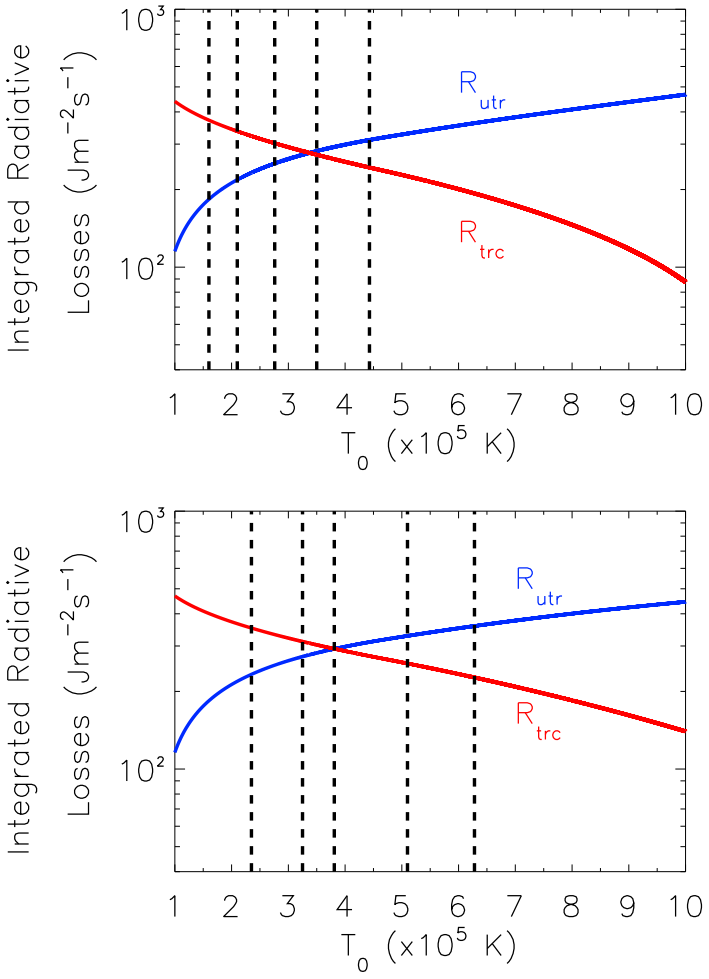

Figure 3.4: IRL in the UTR (solid blue line) and resolved upper TR and corona (solid red line) based on fully resolved equilibrium solutions that are computed with 5×10^5 grid points along the length of the loop and are consistent with the short and long loop initial conditions shown in Figure 3.1. Upper panel: 60Mm loop. Lower panel: 180Mm loop. The dashed black lines are the temperatures at the top of the UTR (T_0) that are obtained by using different simulation resolutions (L_R). In both plots, starting from the right the first dashed black line corresponds to 125 grid points, the second to 250 grid points, the third to 500 grid points, the fourth to 1,000 grid points and the fifth to 2,000 grid points.

the resolved upper TR and corona ($\mathcal{R}_{trc}$),

$$\mathcal{R}_{utr} \approx \mathcal{R}_{trc} = \int_{z_0}^{z_a} n^2 \Lambda(T)\, dz. \tag{3.11}$$

To demonstrate the justification of (3.11), in Figure 3.4 we plot the IRL in the UTR ($\mathcal{R}_{utr}$) and resolved upper TR and corona ($\mathcal{R}_{trc}$) as functions of the temperature at the

top of the UTR (T_0), for both our short and long loop initial conditions. These curves are obtained by integrating the radiative losses from fully resolved solutions (using 5×10^5 uniformly spaced grid points) while adjusting the integration limits so that the spatial location of the top of the UTR changes with the temperature at this location (i.e. $z_0(T_0)$). Previously, we have seen that when coarse resolution is used the temperature at the top of the UTR is only weakly dependent on the spatial resolution (see Figure 3.2). This means that there is only a small range of resolvable TR temperatures (which we highlight with the dashed black lines that represent the values of T_0 that are obtained when using different values of L_R) before the unresolved region of the atmosphere is reached. Figure 3.4 shows that within these small temperature ranges (i.e. the values of T_0 bounded by the dashed black lines) the agreement between the values of $\mathcal{R}_{trc}$ and $\mathcal{R}_{utr}$ is reasonably good. For example, as can be seen in the lower panel of Figure 3.4, when using 1,000 grid points with $2L = 180$Mm, $T_0 = 3.25 \times 10^5$K and $\mathcal{R}_{utr}\,(272\,\mathrm{J\,m^{-2}s^{-1}}) \approx \mathcal{R}_{trc}\,(312\,\mathrm{J\,m^{-2}s^{-1}})$. We note that the agreement is even better when using 500 grid points.

However, when coarse resolution is used, a single grid point lower down in the atmosphere can have a considerable effect on the IRL in the resolved upper TR and corona ($\mathcal{R}_{trc}$). Therefore, we note that it is safer to define the top of the UTR to be a few grid cells higher up than previously defined in Section 3.1. This acts as a numerical safety buffer to ensure that $\mathcal{R}_{trc}$ (which is used to approximate $\mathcal{R}_{utr}$) remains smooth in time, when transient unresolved points that move upwards in the UTR become resolved.

3.2.2 Implementation of the Jump Condition

Once the IRL in the UTR ($\mathcal{R}_{utr}$) have been estimated, the corrected velocity (v_0) is then calculated, by firstly solving the UTR jump condition (3.10), which is a cubic in v_0, using a simple Newton-Raphson solver with the starting condition,

$$v_i = \frac{-F_{c,0} + \ell\bar{Q} - \mathcal{R}_{utr}}{(\gamma - 1)/\gamma P_0}. \tag{3.12}$$

This is obtained by neglecting the kinetic energy and gravitational potential energy fluxes in Eq. (3.10). Convergence to a solution of the complete equation is rapid.

In some cases (1) approximation (3.11) underestimates the IRL in the UTR and (2) $\ell d\bar{E}/dt$ can be significant at the start of the heating period, acting to delay the onset of the upward enthalpy flux in the fully resolved model. This behaviour may lead to spurious supersonic upflows for the class of problems considered in this chapter. Therefore, the solution to Eq. (3.10), $\tilde{v}_0$, is adjusted by using the following sound speed limiter,

$$v_0 = \frac{\tilde{v}_0 \times c_s}{\sqrt{\tilde{v}_0^2 + c_s^2}}, \tag{3.13}$$

where c_s is the local sound speed at the top of the UTR. It is this adjusted velocity (v_0) that we impose at the top of the UTR. This is consistent with the corresponding fully resolved loop simulations (that use an adaptive mesh), since no supersonic flows are present at the location where the jump condition is implemented, in all of the 12 cases considered. Hence, this approximation is satisfactory for the problems presented here and it does not inhibit the existence of supersonic flows higher up in the atmosphere.

3.3 Results

The effectiveness of the UTR jump condition to obtain a physically realistic evolution, through the complete coronal heating and cooling cycle, when employed with coarse resolution is investigated for a series of impulsive coronal heating events. The heating events considered are based on the cases (1-12) that were previously studied in BC13. These events are described in Table 3.1 and cover several orders of magnitude and duration of heating for both a short and long loop, ranging from that required to maintain quiet-Sun conditions to reasonably powerful flares. The energy release is also the same as that used in BC13. The temporal profile is triangular with a peak value of Q_{H_0} and total duration of τ_H:

$$Q_H(t) = Q_{H_0}\left(1 + \frac{(t - \tau_H/2)}{\tau_H/2}\right), \quad 0 < t < \tau_H/2; \tag{3.14}$$

$$Q_H(t) = Q_{H_0}\left(1 - \frac{(t - \tau_H/2)}{\tau_H/2}\right), \quad \tau_H/2 < t < \tau_H, \tag{3.15}$$

while the spatial profile is uniform along the loop.

For each case, the main assessment of the performance of the UTR jump condition model is a comparison of Lare1D using 500 grid points employed with the jump condition (referred to as LareJ), with both Lare1D without the jump condition but using up to 8,000 grid points and the adaptive mesh code HYDRAD. The choice of 500 grid points is motivated by what is routinely used in current multi-dimensional MHD models (e.g. Bourdin et al., 2013; Hansteen et al., 2015; Hood et al., 2016; Dahlburg et al., 2016). The spatial resolution of these solutions is 120km and 360km for the short and long loop, respectively.

For the Lare1D solutions we employ a uniform grid and repeat each run with $N_z = [500;\ 1,000;\ 2,000;\ 4,000;\ 8,000]$ grid points along the length of the loop. We note that because we are using a uniform grid each time we double the number of grid points, even although we improve the TR resolution, we also further reduce the thermal conduction ti-

Table 3.1: A summary of the parameter space used and results from the numerical simulations.

Case	$2L$ (Mm)	Q_{H_0} ($\mathrm{J\,m^{-3}\,s^{-1}}$)	τ_H (s)	$T_{\max}$(HYDRAD) (MK)	$T_{\max}$(LareJ) (MK)	$T_{\max}$(Lare1D(500)) (MK)	$n_{\max}$(HYDRAD) ($10^{15}\mathrm{m^{-3}}$)	$n_{\max}$(LareJ) ($10^{15}\mathrm{m^{-3}}$)	$n_{\max}$(Lare1D(500)) ($10^{15}\mathrm{m^{-3}}$)
1	60	8×10^{-4}	60	1.9	2.1	2.1	0.86	0.92	0.74
2	60	8×10^{-3}	60	5.7	6.1	6.1	2.2	2.6	1.5
3	60	8×10^{-2}	60	12.5	12.9	13.1	9.0	11.6	4.9
4	60	8×10^{-4}	600	3.4	3.5	3.5	2.2	2.6	1.0
5	60	8×10^{-3}	600	6.9	7.1	6.9	9.1	11.4	2.9
6	60	8×10^{-2}	600	13.7	14.1	13.8	40.3	49.7	10.4
7	180	5×10^{-5}	60	1.8	1.8	1.8	0.28	0.29	0.27
8	180	5×10^{-4}	60	2.9	3.1	3.1	0.37	0.40	0.33
9	180	5×10^{-3}	60	9.3	10.2	10.2	1.0	1.13	0.42
10	180	5×10^{-5}	600	2.5	2.7	2.7	0.36	0.40	0.33
11	180	5×10^{-4}	600	5.7	6.0	6.0	0.98	1.18	0.39
12	180	5×10^{-3}	600	12.3	12.7	12.3	4.2	5.4	1.2

Notes. From left to right the columns show the case number, the total length of the loop, the peak heating rate, the duration of the heating pulse and the maximum averaged temperature and density attained by HYDRAD (in single fluid mode) with the largest grid cell of width 400km and 12 levels of refinement employed, and Lare1D using 500 grid points along the length of the loop (coarse resolution) employed with (LareJ) and without (Lare1D(500)) the jump condition, respectively.

me step in the corona and so the computational time increases. Therefore, we have limited the most refined resolution used here because of the increased computation time required.

Consistent with our model equations (2.1)–(2.4), we run the HYDRAD code in single fluid mode. The HYDRAD code has an adaptive grid that is capable of increasing the numerical resolution wherever it is needed based on selected refinement conditions. This enables the code to fully resolve the small length scales in the TR while retaining a coarser grid elsewhere. Following BC13, we select the largest grid cell to be of width 400km and employ 12 levels of refinement, so that in the most highly resolved regions the grid cells are of width 98m. In this chapter, we assume that the HYDRAD solution is 'correct'.

3.3.1 Case 9

BC13 found their Case 9 (a strong nanoflare in a long loop) to be one of the more challenging examples for obtaining correct coronal densities. Figure 3.5 shows the temporal evolution of the coronal averaged temperature (T), density (n), pressure (P) and the corresponding temperature versus density phase space plot. The coronal averages are computed by spatially averaging over the uppermost 50% of the loop. For example, the coronal averaged temperature is defined as,

$$\bar{T} = \frac{1}{L} \int_{z_a - L/2}^{z_a + L/2} T \, dz, \tag{3.16}$$

where L is the loop half-length and z_a is the loop apex. (The trends are the same if either the averages are computed over the full portion of the loop above z_0 or the values are compared at the top of the UTR.) In the plots each solid line corresponds to a Lare1D solution that was calculated by employing a different number of grid points along the length of the loop. The solid blue line has 500 grid points ($L_R = 360$km), the green line has 1,000 grid points ($L_R = 180$km), the red line has 2,000 grid points ($L_R = 90$km), the purple line has 4,000 grid points ($L_R = 45$km) and the black line has 8,000 grid points ($L_R = 22.5$km). The dashed blue line is the LareJ solution that is computed with 500 grid points along the length of the loop and the dot-dashed orange line corresponds to the HYDRAD solution.

Starting with the Lare1D solutions it is clear that we recover the result presented by BC13, namely that the main effect of insufficient resolution is on the coronal density while the temperature is far less resolution dependent. We also note that in this case, as is predicted by BC13 the most refined resolution that we employed with the Lare1D code is still not capable of reproducing the fully resolved HYDRAD solution.

However, if we focus on the UTR jump condition model (LareJ), there is good agreement between the LareJ and HYDRAD solutions. At the initial density peak, the LareJ

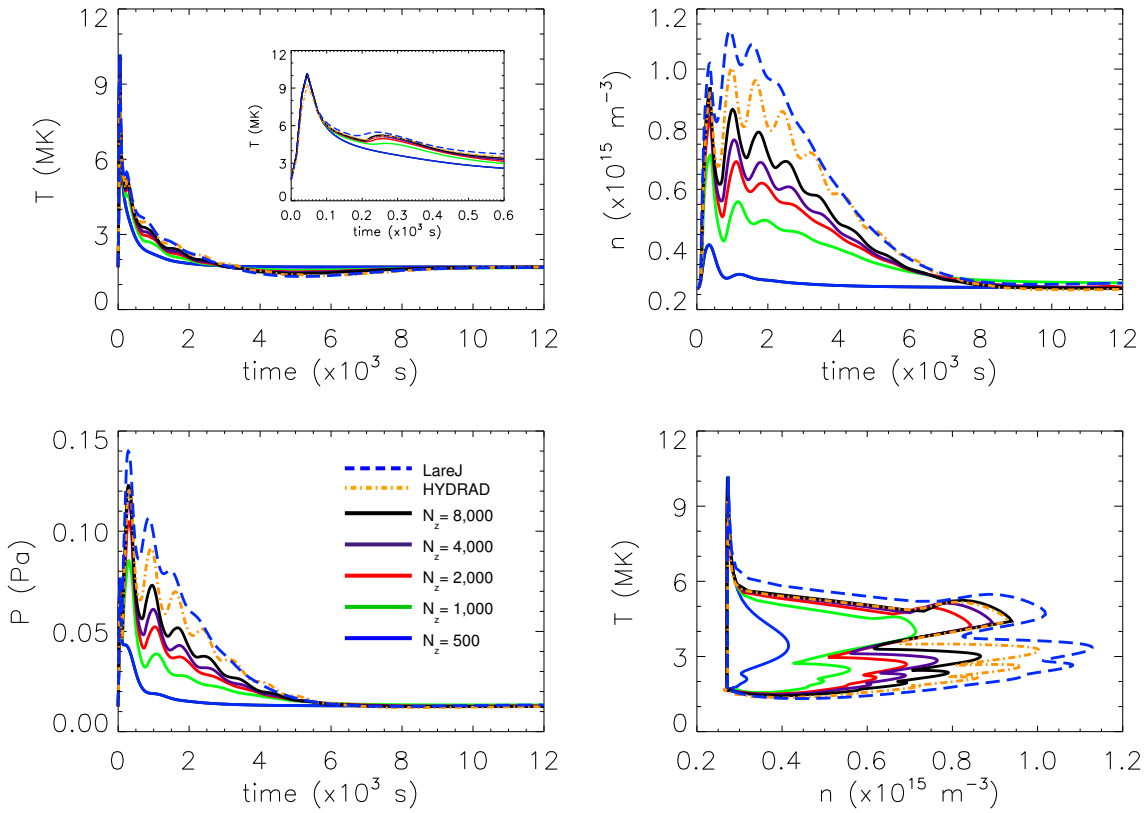

Figure 3.5: Results for Case 9. The panels show the coronal averaged temperature, density and pressure as functions of time, and the temperature versus density phase space plot. The solid lines represent the Lare1D solutions obtained by using different numbers of grid points along the length of the loop, the dashed blue line is the LareJ solution (that is computed with the same spatial resolution as the solid blue curve) and the dot-dashed orange line corresponds to the fully resolved HYDRAD solution.

solution evaporates about 10% too much material upwards into the corona, in comparison to the HYDRAD solution, while the density of the corresponding coarse Lare1D solution (run with the same spatial resolution, solid blue line) is more than a factor of two lower than the resolved loop value. As a consequence of this difference in densities, because the conductive cooling timescale scales as $n/T^{5/2}$, the LareJ solution cools at the correct rate while there is evidence that the corresponding coarse Lare1D solution cools more rapidly.

The density then oscillates as the plasma sloshes to and fro within the loop. These oscillations are captured to a large extent by the LareJ solution but are not prominent in the corresponding coarse Lare1D solution. During these oscillations, even although the LareJ density remains slightly too high, the accuracy of the LareJ solution is still an improvement on even the most refined Lare1D solution. The LareJ solution then goes on to attain the correct draining rate during the density decay phase before recovering the

Table 3.2: Numerical simulation computation times.

Case	τ(LareJ) (mins)	τ(HYDRAD) (mins)	τ(Lare1D(8,000)) (mins)	τ(HYDRAD)/ τ(LareJ)	τ(Lare1D(8,000))/ τ(LareJ)
1	17	316	7,426	18.6	436.8
2	19	340	7,766	17.9	408.7
3	51	1,943	13,886	38.1	272.3
4	22	370	6,341	16.8	288.2
5	82	2,617	8,594*	31.9	106.0
6	154	5,177	12,732*	33.6	82.7
7	26	1,559	18,893	60.0	726.7
8	28	1,566	18,059	56.0	645.0
9	35	1,605	16,833	45.9	480.9
10	26	1,805	11,138	69.4	428.4
11	32	1,914	11,997	59.8	374.9
12	86	2,269	12,973*	26.4	150.8

Notes. From left to right the columns show the case number, the computation times (run on a single processor) using the Lare1D code with 500 grid points (coarse resolution) employed with the jump condition (LareJ), the HYDRAD code (in single fluid mode) with the largest grid cell of width 400km and 12 levels of refinement employed, the Lare1D code using 8,000 grid points along the length of the loop (Lare1D(8,000)), and the computational time ratios between these methods. The short loop simulations (Cases 1-6) are run to a final time of 4,000s and the long loop simulations (Cases 7-12) are run to a final time of 12,000s. The asterisks indicate cases where the Lare1D code using 8,000 grid points was unable to resolve the density to within 75% of the HYDRAD solution.

equilibrium.

Bringing all these factors together, in the phase space plot it is evident that the LareJ solution captures the evolution of the density as a function of temperature more accurately than the entire set of Lare1D solutions. This includes the most refined Lare1D solution that has a factor of 16 more grid points along the length of the loop.

Table 3.2 summarises the central processing unit (CPU) requirements for all the cases considered. The table demonstrates the large gain in CPU time of the UTR jump condition method over both the HYDRAD and most refined Lare1D runs. Therefore, in this particular case, LareJ obtains (1) a coronal density comparable to HYDRAD (fully resolved 1D model) but with a significantly faster computation time and (2) also provides a significant improvement in the accuracy of the coronal density evolution when compared to the equivalent simulation run without the jump condition.

We now turn our attention to understanding why the LareJ solution performs well for this particular heating event (Case 9). Figure 3.6 shows the temporal evolution of the heat and enthalpy fluxes at the top of the UTR ($F_{c,0}$ & $F_{e,0}$) and the IRL in the UTR ($\mathcal{R}_{utr}$). These quantities are the dominant terms in the UTR jump condition (3.10) although the loop's evolution can be influenced by the additional terms in Eq. (3.10) that are not shown here. The dashed blue lines represent the appropriate LareJ quantities and the dot-dashed

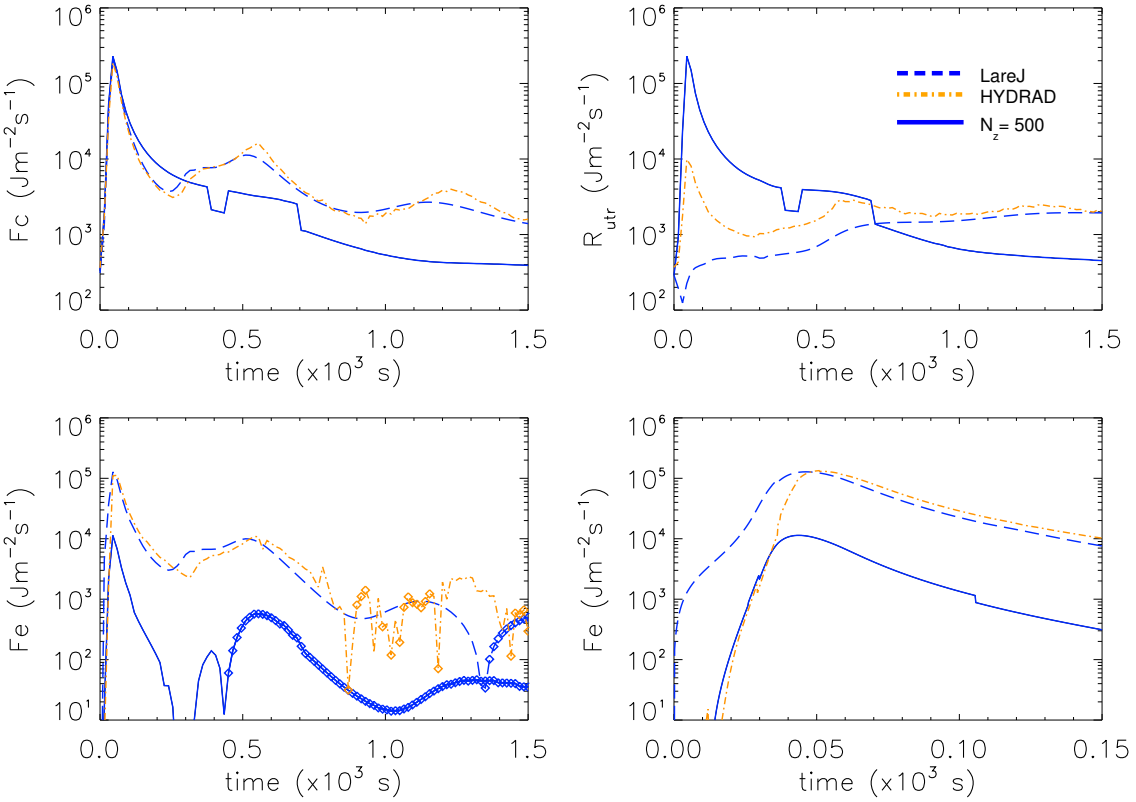

Figure 3.6: Results for Case 9. The panels show the heat flux at the top of UTR ($F_{c,0}$), IRL in the UTR ($\mathcal{R}_{utr}$) and enthalpy flux at the top of the UTR ($F_{e,0}$, lines connected by diamond symbols indicate where the enthalpy flux is downflowing and lines without diamonds indicate where the enthalpy flux is upflowing) over two different time intervals as functions of time. The dashed blue line is the LareJ solution (that is computed with 500 grid points along the length of the loop), the solid blue line is the Lare1D solution that is computed with 500 grid points along the length of the loop and the dot-dashed orange line corresponds to the fully resolved HYDRAD solution.

orange (solid blue) lines represent the appropriate quantities that are obtained throughout the evolution of the HYDRAD solution (Lare1D solution computed with 500 grid points along the length of the loop). To calculate these quantities the definition of the UTR is determined based on the time evolution of the temperature from the LareJ solution.

During the initial evaporation phase (first 400s) the excess heat flux drives an upward enthalpy flux. Throughout this phase there is good agreement between the enthalpy fluxes of the LareJ and HYDRAD solutions. This agreement is achieved because the downward heat flux dominates $\mathcal{R}_{utr}$ and so the UTR jump condition principally returns $F_{c,0}$ as an upward enthalpy flux ($F_{e,0}$).

However, close inspection reveals that, throughout the first 40s (see lower right panel in Figure 3.6), the enthalpy flux of the LareJ solution exceeds that of the HYDRAD so-

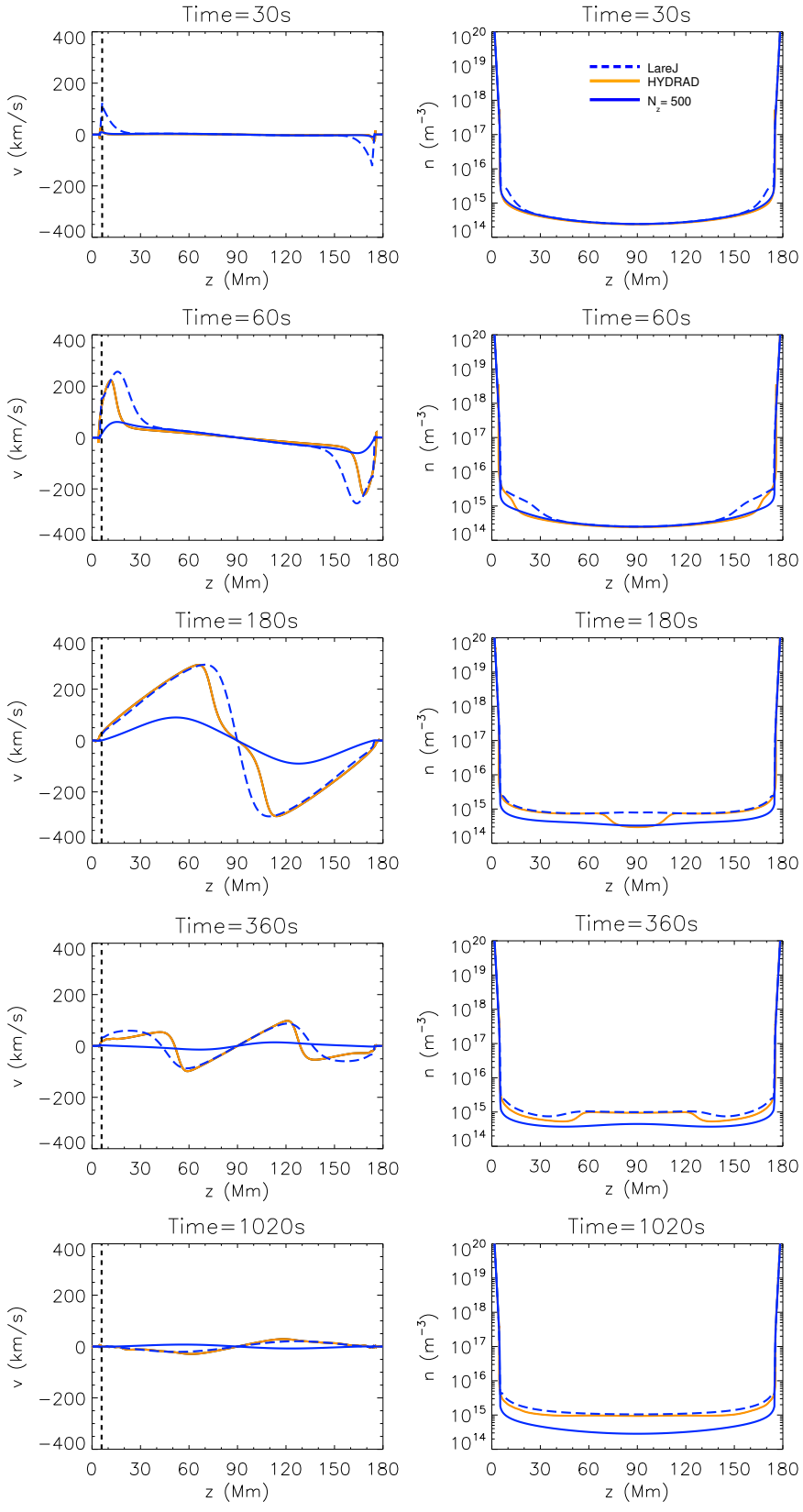

Figure 3.7: Results for Case 9. The panels show the velocity and density as functions of position for times during the evaporation phase up until the second density peak. The dashed blue line is the LareJ solution (that is computed with 500 grid points along the length of the loop), the solid blue line is the Lare1D solution that is computed with 500 grid points along the length of the loop and the solid orange line corresponds to the fully resolved HYDRAD solution. The dashed black line indicates the position of the top of the UTR (z_0).

lution. During this period (1) the LareJ radiation approximation (3.11) is least accurate and leads to an underestimation of the IRL in the UTR and (2) terms neglected from the jump condition play a significant role in the evolution of the fully resolved model (as discussed in Section 3.2). It is the combination of these factors that is responsible for the enhanced LareJ enthalpy flux.

Figure 3.7 shows the velocity and density as functions of position, from the LareJ, coarse Lare1D and HYDRAD simulations, for times during the evaporation phase up until the second density peak. The enhanced enthalpy flux, throughout the first 40s, indicates that the correcting velocity (v_0), imposed at the top of the UTR, is overestimated during this period. This is confirmed in the top left panel in Figure 3.7. Furthermore, the figure also demonstrates that the overestimation in the initial upflow, locally at the top of the UTR, then generates an enhanced global velocity that facilitates the over evaporation of the LareJ solution.

Despite this overestimation in the initial upflow, by imposing the correcting velocity (v_0) locally at the top of UTR, the jump condition method is still able to capture the global velocity much more accurately, in time, than the corresponding simulation run without the jump condition (see Figure 3.7). Since the global velocity is more accurate with the jump condition this ensures that LareJ solution follows the evolution of the fully resolved model much more accurately than the coarse Lare1D solution. Therefore, the underestimation of the IRL in the UTR is not a major problem because radiation should not significantly influence the loop's evolution, during the initial evaporation phase.

However, this is exactly what can be observed in the case of the coarse Lare1D solution. The radiation peak during the initial evaporation phase is characteristic of the heat flux jumping across the TR. This allows the incoming energy from the heat flux to be strongly radiated (BC13), leaving little excess energy to drive an upflow. As a consequence, the upward enthalpy flux is diminished and so an insufficient amount of material gets evaporated upwards into the corona.

It is evident that once the heat flux jumps across the TR, the coarse Lare1D solution follows a completely different evolution to the LareJ and HYDRAD solutions. The velocity correction implied by the jump condition effectively ensures that the energy from the heat flux goes into driving the TR dynamics, rather than being lost from the loop through radiation. It is this difference in where the energy from the heat flux is deposited that provides the explanation for the contrasting solution behaviour: LareJ evaporates close to the correct amount of material at the initial density peak while the corresponding coarse Lare1D solution suffers from obvious discrepancies.

Radiation becomes increasingly important as the density increases. Then, at the time when $\mathcal{R}_{utr}$ finally exceeds $F_{c,0}$, the loop enters the density decay phase because a downward enthalpy flux (condensation) is required to power the TR radiation. During this decay phase, the LareJ solution drains material from the corona at the correct rate due to

the improvement in the accuracy of the LareJ radiation estimation (3.11), following the first density peak.

Using HYDRAD, BC13 demonstrated that for reasonably accurate solutions in the case of 180Mm loops and peak temperatures exceeding 6MK, cell widths of no more than 5km are required. What we have shown in Figures 3.5 - 3.7 is that it is possible to obtain realistic densities, temperatures and velocities with cell widths of 360km by using the UTR jump condition employed in LareJ.

3.3.2 Case 3

BC13 found their Case 3 (a small flare in a short loop) demanded the most severe requirements on the spatial resolution. Grid cells of width 390m were needed, in the most refined regions, in order for the coronal density to exceed 90% of the fully resolved value. The results for the numerical simulations included in this case are shown in Figures 3.8 & 3.9. To show the comparison exclusively between the key solutions, we now drop the intermediate Lare1D solutions from the coronal averaged plots.

In this particular case, the LareJ solution suffers from its most significant over evaporation at the initial density peak (about 30%) and the density remains too high throughout the first 1,000s. However, its performance remains reasonably encouraging from the viewpoint that the LareJ solution follows the same fundamental evolution as the HYDRAD solution up to the peak density and their agreement is good throughout the density decay phase.

During the same period the corresponding Lare1D solution (run with the same coarse spatial resolution) under evaporates the initial density peak by about 40% and then follows an entirely different evolution to the HYDRAD solution. This is most noticeable during the density decay (condensation) phase where the discrepancies in the evolution are largest. But we highlight that from a modelling perspective it is critical to get this decay phase correct because the plasma is indeed cooling and draining in many observations of coronal loops. Therefore, the benefit of implementing the UTR jump condition is reiterated, in this case, by the fact that the LareJ solution captures the density decay phase much more accurately than the corresponding Lare1D solution.

We note that in this heating event the peak temperature comfortably exceeds 6MK in a 60Mm loop. In this regime BC13 have shown that for fully converged solutions cell widths of less than 1km are required. Therefore, the ability of the LareJ solution to sufficiently reproduce the main features of the HYDRAD solution is striking because we use cell widths of 120km. This result further demonstrates that it is possible to obtain reasonably accurate solutions with coarse resolutions when they are employed with the UTR jump condition.

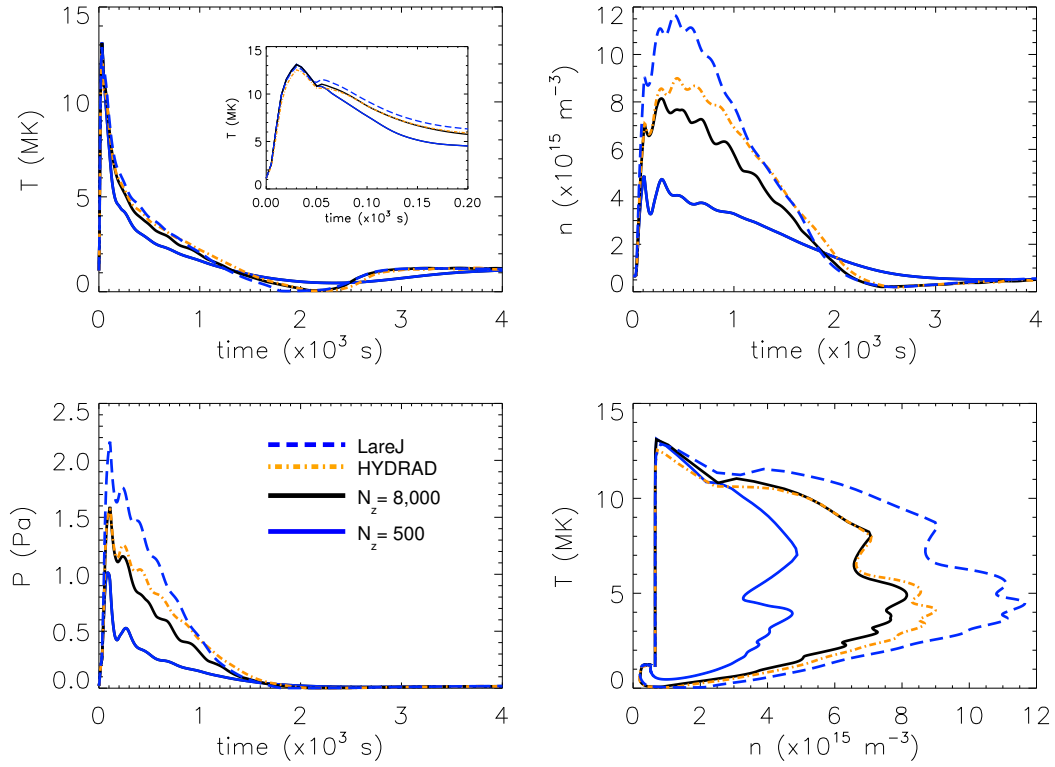

Figure 3.8: Results for Case 3. Notation is the same as Figure 3.5 but note the different time axis.

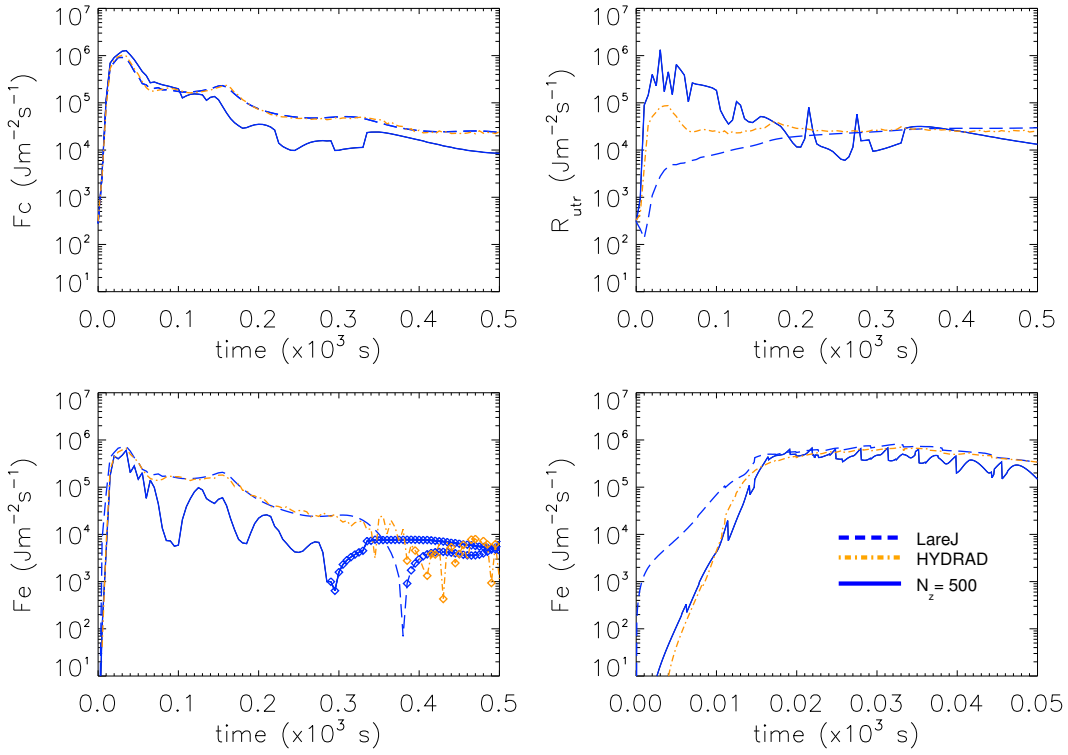

Figure 3.9: Results for Case 3. Notation is the same as Figure 3.6 but note the different time axis.

However, throughout the first 12s, the enthalpy flux of the LareJ solution does again exceed that of the fully resolved model. The factors responsible for driving this behaviour are the same as those discussed previously in Case 9. Additional energy from the heat flux is allowed to go into driving the upward enthalpy flux. The outcome is that the corrected upflow (v_0) in LareJ is enhanced over the upflow at the same point in the HYDRAD solution. This drives the over evaporation of the LareJ solution.

On the other hand, with the coarse Lare1D solution there is clear evidence (just before 100s) of the heat flux jumping across the TR. Specifically, the overestimation of $\mathcal{R}_{utr}$ allows a considerable portion of the energy from the heat flux to leave the loop, instead of driving an upflow. Consequently, the enthalpy flux is significantly reduced, explaining the 40% discrepancy in the density at the initial peak. This again underlines the importance of ensuring that the energy from the heat flux is returned as an upward enthalpy flux and not lost from the loop through radiation.

3.3.3 Remaining Cases

We present the numerical comparison for the remaining cases in Table 3.1, where the maximum averaged coronal temperature and density attained by the HYDRAD, LareJ and corresponding coarse Lare1D solutions are shown. In all 12 cases, the table shows that the accuracy of the maximum coronal density is considerably improved by the LareJ solution when compared with the equivalent coarse resolution simulation run without using the jump condition.

The results for Cases 2, 6, 8 & 12 are shown in Figure 3.10. Previously, we have seen that the temporal evolution of the coronal averaged temperature is only weakly dependent on both the spatial resolution and computational method used. This is because the temperature is essentially driven throughout the impulsive heating event. Therefore, it is sufficient now to show only the temporal evolution of the coronal averaged density and the corresponding temperature versus density phase space plots.

In these cases, the UTR jump condition method consistently captures a physically realistic evolution, through the complete coronal heating and cooling cycle, comparable to that of the HYDRAD solutions. The estimation of the IRL in the UTR and the role of terms neglected from the jump condition are again identified as the main sources of error that drive the observed over evaporation. Despite this, it remains clear that the LareJ solutions are reasonably good, providing a significant improvement on the corresponding coarse simulations run without the jump condition.

However, we note from the phase space plot of Case 8 that for this particular heating event, the most refined Lare1D solution (the black line, computed with 8,000 grid points) has a much better agreement with HYDRAD than the LareJ solution. Furthermore, the

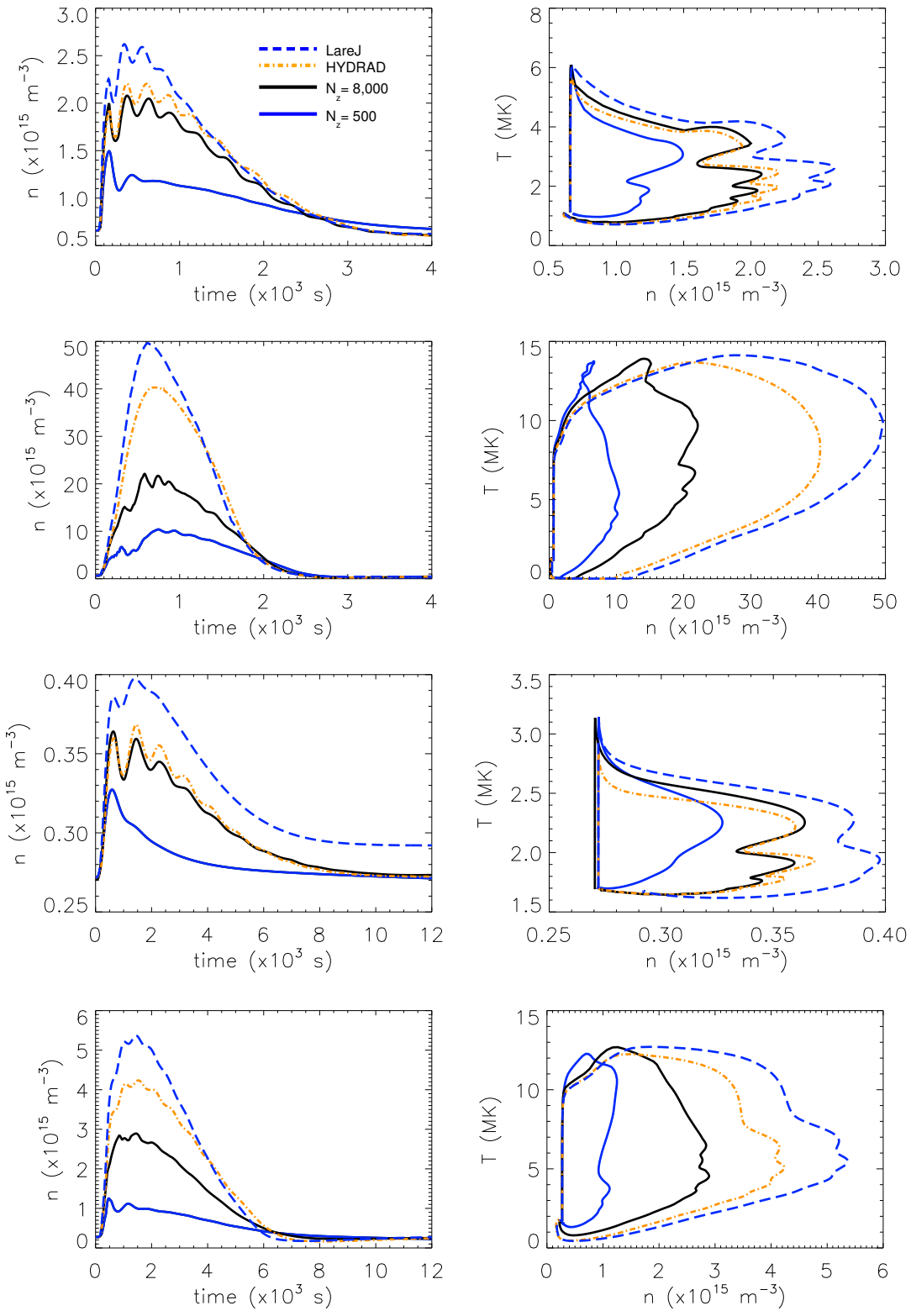

Figure 3.10: Results for Cases 2, 6, 8 & 12 shown in rows 1, 2, 3 & 4, respectively. The panels show the coronal averaged density as a function of time and the temperature versus density phase space plot.

LareJ solution does not recover the 'exact' long loop initial equilibrium but instead returns to another nearby equilibrium with an increased density of around 7% (similar behaviour was also seen in BC13). This is true in all of the long loop cases considered but is only noticeable in those where the density increase, in response to the heating event, is small (e.g. Cases 7 & 8).

3.4 Chapter Discussion and Conclusions

The difficulty of obtaining adequate spatial resolution in numerical simulations of the corona, TR and chromosphere system has been a long-standing problem. As pointed out by BC13, the main consequence of not resolving the TR is that the resulting coronal density is artificially low. This chapter has presented an approach to deal with this problem by using an integrated form of energy conservation that essentially treats the lower TR as a discontinuity. Hence, the response of the TR to changing coronal conditions is determined through the imposition of a jump condition. When compared to fully resolved 1D models (e.g. BC13), our new approach generated improved coronal densities with significantly faster computation times than the corresponding high-resolution and fully resolved models. Specifically, our approach required between one and two orders of magnitude less computational time than fully resolved models. The computational gains are even larger when compared with using a fixed grid with a large number of grid points.

The 12 cases presented in this chapter were selected to correspond to the benchmark cases presented by BC13. In all 12 cases, the evolution of the coronal density is considerably improved when compared with the same resolution run without the jump condition implemented.

The advantages of this new approach are multiple. For 1D hydrodynamic simulations of the coronal response to heating (see e.g. Reale, 2014, for a review), the short computation time means that (a) simulations of coronal heating events can be run quickly, permitting an extensive survey of the (large) parameter space and (b) simulations of multiple loop strands (thousands or more) that either comprise a single observed loop (e.g. a core loop), or an entire active region, can be performed with relative ease. In 3D MHD codes, the method can be included without the need for higher spatial resolution and a corresponding extended computation time. Indeed, our results suggest that good accuracy can be obtained with the order of 500 grid points, typical of what is routinely used in current 3D MHD simulations. The extension to multi-dimensions will be addressed in Chapter 6.

The work presented here has adopted a simple model for the radiation in the lower, unresolved transition region (UTR), and leads to improved coronal densities. The estimate used was motivated by the calculation of the radiation integrals for the equilibrium

conditions (as shown in Figure 3.4), at which the error is at most around a factor of 2 when using a uniform grid with between 125 and 2,000 grid points. On the other hand, the densities are systematically higher than those in fully resolved 1D models, which can be tracked down to the simple model underestimating the true value of the integrated radiative losses in the UTR (R_{utr}) and the influence of terms neglected from the jump condition, at the very start of the heating phase. The role of these neglected terms will be quantified further in Chapter 4. However, for the present, the density draining phase is captured correctly which is important as this is the phase that is seen in many observations of coronal loops. We note that in Case 8, during this phase and throughout the entire evolution, the most refined uniform grid solution (Lare1D with 8,000 grid points) achieved a better agreement with the fully resolved model than the jump condition solution (LareJ with 500 grid points) but at significantly greater computational cost.

Our emphasis here has been on obtaining an improved coronal density. This is important for interpreting observations of, for example, active region loop cores, 'warm' loops, as well as microflare and flare coronal emission. On the other hand, by treating the lower (unresolved) TR as a discontinuity, information will be lost on detailed TR emission lines such as CIV. If the jump condition is applied close to 1 MK (i.e. between 5×10^5 K and 1 MK) the details of the (bright) TR will be lost, although integrated TR quantities can of course still be deduced. This loss of detail would particularly affect studies of, for example, the bright TR 'moss' - bright emission at the footpoints of very hot loops (see e.g. Fletcher and De Pontieu, 1999). Full numerical resolution is still required to deduce these, with the corresponding risk of serious errors in the plasma density. Model setups with smaller coronal domains (coronal heights) and or lower temperatures (say below 1-2 MK) are likely to have adequate resolution (e.g. Zacharias et al., 2011; Hansteen et al., 2015).

We have considered only spatially uniform impulsive heating events. Simulations with the heating concentrated at the loop base and the loop apex will be presented in the subsequent chapter.

In summary, this chapter has presented an approach to deal with the difficulty of obtaining the correct interaction between a downward conductive flux from the corona and the resulting upflow from the TR. A wide range of impulsive (spatially uniform) heating events was considered for both short and long loops. Our new method was used in simulations with coarse resolutions that do not resolve the lower transition region. The main result is that the method leads to (i) coronal densities comparable to fully resolved 1D models but with significantly faster computation times, and (ii) significant improvements in the accuracy of both the coronal density and temperature temporal evolution when compared to the equivalent simulations run without this approach.

Chapter 4

Non-Uniform Heating

In the previous chapter we demonstrated that the use of an approximate 'jump condition' at the solar transition region permits fast and accurate numerical solutions of the one dimensional hydrodynamic equations when the corona undergoes impulsive heating. In particular, it eliminates the need for the very short time steps imposed by a highly resolved numerical grid. This chapter presents further examples of the applicability of the method for cases of non-uniform heating, in particular, nanoflare trains (uniform in space but non-uniform in time) and spatially localised impulsive heating, including at the loop apex and base of the transition region, and is based on work published in the paper Johnston et al. (2017b). In all cases the overall behaviour of the coronal density and temperature shows good agreement with a fully resolved one dimensional model and is significantly better than the equivalent results from a 1D code run without using the jump condition but with the same coarse grid. A detailed assessment of the errors introduced by the jump condition is presented showing that the causes of discrepancy with the fully resolved code are (i) the neglect of the terms corresponding to the rate of change of total energy in the unresolved atmsophere, (ii) mass motions at the base of the transition region and (iii) for some cases with footpoint heating, an over-estimation of the radiative losses in the transition region (TR).

The method uses an integrated form of the energy equation that essentially treats the unresolved region of the lower TR as a discontinuity. The response of the TR to changing coronal conditions is then determined through the imposition of a jump condition, which compensates for the energy lost when the heat flux jumps over an unresolved TR by imposing a local velocity correction. In Chapter 3 we showed that this new approach obtains coronal densities comparable to fully resolved 1D models (e.g. BC13) but with computation times that are between one and two orders of magnitude faster, since the computational timestep is not limited by thermal conduction in the TR.

However, in Chapter 3 we considered only the case of spatially uniform heating. The

purpose of this chapter is two-fold. Firstly, it is important to consider how the jump condition performs for different (spatially non-uniform) heating functions and initial plasma conditions in order for future users to have confidence in the model. The latter is addressed through consideration of a nanoflare train. The former involves studies of highly localised heating pulses, including a challenging case where the heating is located at the base of the TR. Secondly, it has become clear that the coronal plasma parameters, in particular the density, show systematic deviations from those in fully resolved simulations. A full analysis of the terms in the jump condition (both retained and neglected) has been undertaken to understand the cause of this. This chapter is not intended as a physical comparison between the different heating models but is intended to demonstrate the wide applicability of the jump condition used.

The chapter has the following layout: we briefly review the jump condition and implementation of the method in Section 4.1. In Section 4.2 & 4.3, we demonstrate the application of our approach through a series of examples. A detailed discussion of the quantities associated with the jump condition is presented in Section 4.4. We present our conclusions for the chapter in Section 4.5.

4.1 Numerical method and experiments

4.1.1 Numerical method

Consistent with Chapter 3, we solve the 1D field-aligned MHD equations using two different methods. A Lagrangian remap (Lare) approach adapted for 1D field-aligned hydrodynamics as described in Section 2.2 and the adaptive mesh refinement code HYDRAD (Bradshaw and Mason, 2003; Bradshaw and Cargill, 2006, BC13). For the initial condition we use a magnetic strand (loop) in static equilibrium of total length $2L$ that includes a 5Mm model chromosphere (acting mainly as a mass reservoir) at the base of each TR.

4.1.2 Overview of the unresolved transition region jump condition

A complete description of the jump condition approach is provided in Section 3.2 and so we just summarise the details here. The 1D energy conservation equation is given by,

$$\frac{\partial E}{\partial t} = -\frac{\partial}{\partial z}(Ev + Pv + F_c) + Q(z,t) - n^2\Lambda(T), \tag{4.1}$$

where $E = P/(\gamma - 1) + 1/2\rho v^2$ (gravity is neglected for this discussion but is included in the 1D field-aligned MHD equations that we solve), v is the velocity, P is the gas pressure,

ρ is the density, n is the number density, $F_c = -\kappa_0 T^{5/2}\partial T/\partial z$ is the heat flux and $Q(z,t)$ is a heating function that includes background uniform heating and a time dependent component that can be dependent on position. $\Lambda(T)$ is the radiative loss function in an optically thin plasma, which we approximate using the piecewise continuous function defined in Klimchuk et al. (2008).

We define the unresolved transition region (UTR) as the region of thickness ℓ that extends from the final location in the TR at which the temperature length scale (L_T) is resolved (z_0, i.e. where the criteria $L_R/L_T \leq \delta < 1$ is satisfied, with L_R denoting the simulation resolution and $\delta = 1/4$ is used throughout this chapter) downwards to the base of the TR (z_b, which is the location where the temperature first reaches or falls below the chromospheric temperature of 10^4K), as outlined in Section 3.1. Integrating Eq. (4.1) over the UTR, from the base of the TR (z_b) upwards to the top of the UTR (z_0), we obtain,

$$N = -\left(E_0 v_0 + P_0 v_0 + F_{c,0}\right) + \ell\bar{Q} - \mathcal{R}_{utr}, \tag{4.2}$$

where N is defined as $N \equiv \ell d\bar{E}/dt - (E_b v_b + P_b v_b + F_{c,b})$ and the subscripts 0 and b indicate quantities evaluated at the top and base of the UTR respectively. The overbars indicate spatial averages over the UTR, $\mathcal{R}_{utr}$ is the integrated radiative losses and $\ell\bar{Q}$ is the volumetric heating rate in the UTR.

We assume that the left-hand side (LHS) of Eq. (4.2) can be neglected based on the arguments presented in Chapter 3 (see also, e.g. Klimchuk et al., 2008; Cargill et al., 2012a,b), so that N represents the neglected terms. Hence, we obtain the UTR jump condition,

$$\frac{\gamma}{\gamma-1}P_0 v_0 + \frac{1}{2}\rho_0 v_0^3 = -F_{c,0} + \ell\bar{Q} - \mathcal{R}_{utr}, \tag{4.3}$$

where the terms on the LHS are the enthalpy ($F_{e,0}$) and kinetic energy ($F_{ke,0}$) fluxes, respectively. The terms on the RHS are the heat flux, the integrated volumetric heating rate and the radiative losses ($\mathcal{R}_{utr} = \int_{z_b}^{z_0} n^2\Lambda(T)\,dz$) in the UTR respectively.

The lower TR is modelled as a discontinuity that responds to changing coronal conditions through the imposition of the jump condition (4.3) which in turn implies a local velocity correction (v_0), as discussed in Chapter 3. We reiterate here that to calculate this velocity correction based on the equilibrium results, the integrated radiative losses (IRL) in the UTR ($\mathcal{R}_{utr}$) are approximated using the radiative loss integral from the resolved part of the upper atmosphere ($\mathcal{R}_{trc} = \int_{z_0}^{z_a} n^2\Lambda(T)\,dz$ where z_a represents the loop apex), that is $\mathcal{R}_{utr} = \mathcal{R}_{trc}$. This approximation of $\mathcal{R}_{utr}$ is used only in the calculation of v_0. It remains necessary to solve the full set of equations in the UTR (see Figure 3.3, Chapter 3) in order to retain the structure of the TR. Moreover, to accommodate the case of spatially

non-uniform heating, the integrated volumetric heating rate ($\ell\bar{Q}$) is now calculated as,

$$\ell\bar{Q}(t) = \int_{z_b}^{z_0} Q(z,t)\, dz, \tag{4.4}$$

which reduces to ℓQ for uniform heating (as used in Chapter 3). This new formalism (4.4) can also be used to incorporate other energy deposition methods such as that from electron or ion beams (e.g. Reep et al., 2013b).

Using HYDRAD results, a detailed comparison of the magnitude of all the terms that appear in Eq. (4.2) shows that in the neglected term N, $\ell d\bar{E}/dt$ and the mass motions at the base of the TR ($F_{e,b} + F_{ke,b}$) can have a measurable impact on the coronal plasma response. For uniform heating this led to larger coronal densities than HYDRAD. One objective of this chapter is to quantify the role of these neglected terms further, and this is carried out in Section 4.4. We note here that the difficulty of including the $\ell d\bar{E}/dt$ term remains as discussed in Chapter 3. In particular, if we could calculate $\ell d\bar{E}/dt$ and the base motion terms accurately, with coarse spatial resolutions, then it would not be necessary to implement the jump condition.

4.1.3 Experiments

To appreciate the usefulness of the UTR jump condition method, we assess its performance for a much wider range of examples than those presented in Chapter 3. Specifically, the experiments considered in this chapter explore nanoflare trains and spatially non-uniform heating events. The examples studied cover spatially symmetric and asymmetric heating for both short and long loops.

For each experiment, we assess the performance of the UTR jump condition method (referred to as LareJ) by comparing the results with Lare1D (1D code run without using the jump condition but with the same grid) and HYDRAD (fully resolved 1D model). LareJ and Lare1D use 500 uniformly spaced grid points. This choice of the number of grid points is motivated by what is routinely used in current multi-dimensional MHD models (Bourdin et al., 2013; Hansteen et al., 2015; Hood et al., 2016; Dahlburg et al., 2016; O'Hara and De Moortel, 2016), so that the simulations run in a realistic time.

The HYDRAD code is run in single fluid mode with a largest grid cell width of 400km and 12 levels of refinement employed, so that in the most highly resolved regions the grid cells are of width 98m (BC13). In this chapter we use HYDRAD as a benchmark solution.

4.2 Uniform heating: nanoflare trains

We consider first the case of a nanoflare train (a sequence of heating events e.g. Reep et al., 2013a; Cargill et al., 2015; Bradshaw and Viall, 2016; Barnes et al., 2016). The aim is to investigate how the jump condition copes with heating events in loops that start with a range of densities and temperatures because they have not undergone a full evaporation and draining cycle. We model a coronal loop of total length 90Mm and use the same nanoflare train as in Cargill et al. (2015), consisting of 23 square wave heating pulses over an 8 hour period, as shown in the upper panel of Figure 4.1. This set up is representative of the modelling challenge faced when trying to understand the heating of the core loops found in active regions (e.g. Warren et al., 2011, 2012). Each nanoflare lasts 200s and they cover a range of magnitudes of heating, each with an energy dependent waiting time between events. The spatial profile of the heating is uniform along the loop while we use a piecewise expression for the temporal profile:

$$Q_H(t) = Q_{H_0}\left(1 + \frac{(t - t_Q)}{t_i}\right), \quad t_Q - t_i < t < t_Q; \tag{4.5}$$

$$Q_H(t) = Q_{H_0}, \quad t_Q \leq t \leq t_Q + t_d; \tag{4.6}$$

$$Q_H(t) = Q_{H_0}\left(1 - \frac{(t - (t_Q + t_d))}{t_f}\right), \quad t_Q + t_d < t < t_Q + t_d + t_f. \tag{4.7}$$

Q_{H_0} and t_Q are the peak heating rate and starting time of the energy release, respectively. Both these parameters are prescribed independently for each nanoflare whereas the remaining parameters in the heating function (t_i, t_f & t_d) are fixed. The heating ramps up linearly during the increase time ($t_i = 0.1$s), remains constant for the duration time ($t_d = 200$s) and then ramps down to zero over the fall time ($t_f = 0.1$s) but note that a small background heating term is always present ($Q(t) = Q_{bg} + Q_H(t)$).

Figure 4.1 shows the coronal response of the loop to the nanoflare train together with the volumetric heating rate as a function of time (upper panel). The central and lower panels show the temporal evolution of the coronal averaged temperature (T) and density (n), respectively. The coronal averages are calculated by spatially averaging over the uppermost 50% of the loop, as defined in Eq. (3.16). As an example of the plasma evolution, consider the HYDRAD solution for the nanoflare at approximately 3 hours. The temperature peaks first during the heating period, then falls quite rapidly. The density increases over a few hundred seconds and then both temperature and density fall. As described by Cargill et al. (2015), there are three phases: (i) heating is balanced by conductive losses in the corona up to 200s, (ii) conductive losses drive an upflow from the TR between 200

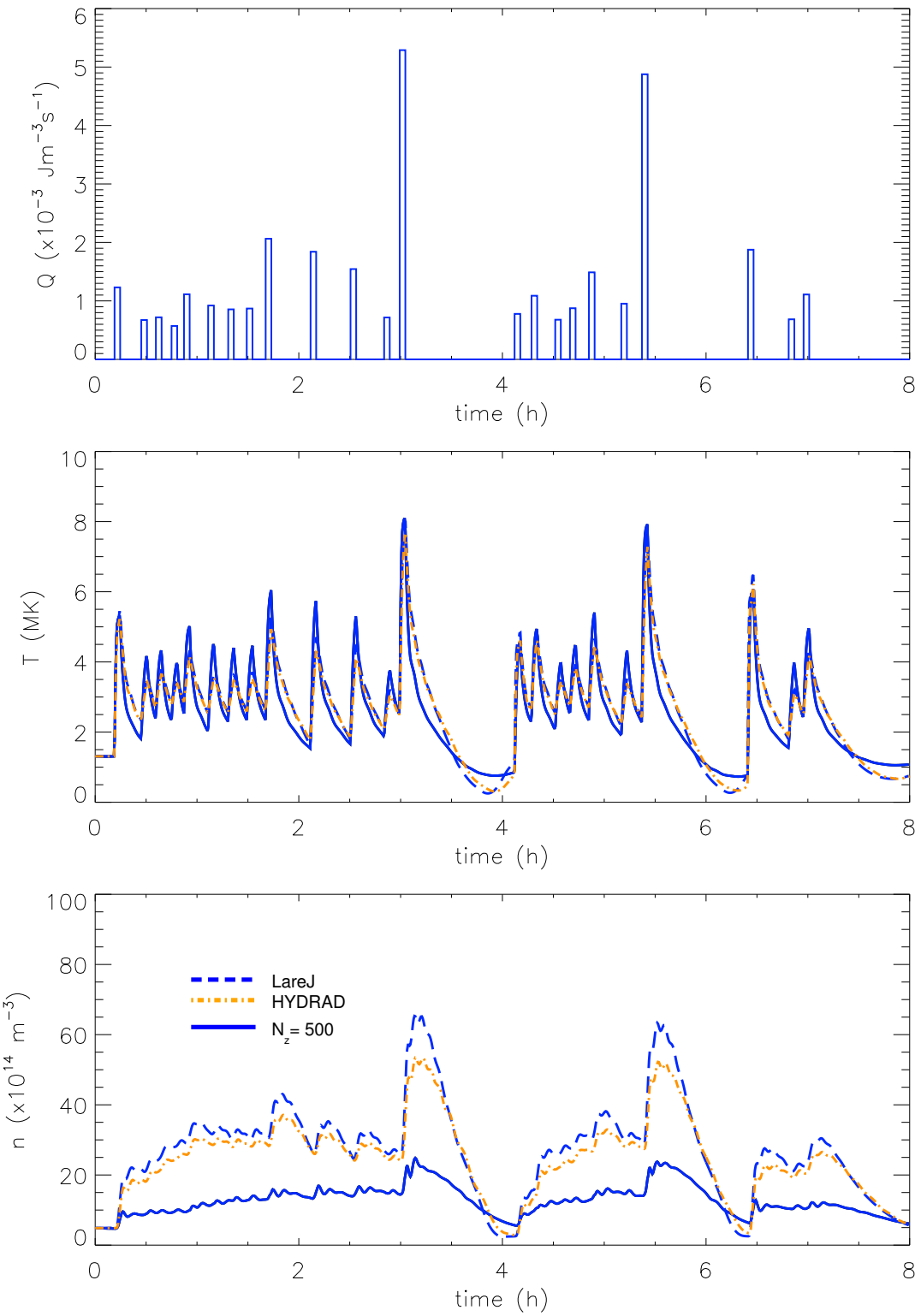

Figure 4.1: Coronal response of the plasma to a nanoflare train in a loop of total length 90Mm over an 8h period. The duration of each nanoflare is 200s. The panels show the volumetric heating rate and the coronal averaged temperature and density as functions of time. The dashed blue line is the LareJ solution (computed with 500 grid points along the length of the loop with the jump condition employed), the solid blue line is the Lare1D solution (computed with the same spatial resolution as the LareJ solution but without the jump condition employed) and the dot-dashed orange line corresponds to the fully resolved HYDRAD solution.

and approximately 800s at which stage the peak coronal density is reached, and (iii) after 800s, the loop cools by radiation and drains by a downward enthalpy flux to the TR. The temperature cools below the equilibrium temperature at around 2000s but is then recovered by the background heating. Therefore, the characteristic cooling time of the plasma involves conductive and radiative phases because the loop evolves through a cycle where first conductive cooling dominates, then radiative cooling.

However, when the waiting time between nanoflares is significantly shorter than the cooling time the temperature and density only partially complete this cycle and so remain above their equilibrium values. This behaviour can be seen in the plasma evolution for the first 3 hours, up until the large nanoflare (discussed above) which is then followed by a longer waiting time. Thus, the plasma response during the nanoflare train is governed by the nanoflare frequency, which is defined with respect to the cooling time. Low (high) frequency nanoflares are those where the waiting time between events is longer (significantly shorter) than the characteristic cooling time.

We now focus on the comparison between the LareJ, Lare1D and HYDRAD solutions. Comparing first LareJ and HYDRAD, we see that their densities follow the same basic evolution, with the LareJ density larger only by about 15–20%, due to the neglect of $\ell d\bar{E}/dt$ and the base motion terms as discussed above. The temperature evolution also shows good agreement. On the other hand, the Lare1D density is systematically lower than HYDRAD throughout the nanoflare train, on average by around a factor of 2 during small heating events or periods of no heating and a factor of 3 during larger events. Often there is a premature density peak and no substantial draining phase. Moreover, the density being lower has two important consequences for the Lare1D temperature evolution: (1) the peak temperature is higher during each heating event and (2) the subsequent cooling is more rapid. The first of these happens because, when releasing the same total amount of energy, a lower coronal density is heated to a higher temperature. The second arises because thermal conduction is more effective at lower density and with the temperature being higher, the conductive cooling timescale which scales as $n/T^{5/2}$ is shorter. This is a generic feature of the Lare1D solution.

Figure 4.1 thus shows that the application of the jump condition approach is not limited to a single heating and cooling cycle. The approach deals equally well with periods of both low and high nanoflare frequency. This is because the underlying physics that drives the evaporation (e.g. Klimchuk et al., 2008) is the same in each regime, for loops that have cooled and drained to sub-million degree temperatures and low densities between heating events (low frequency) and those that have not (high frequency).

We have also tested nanoflare trains in loops of total length 60Mm (short) and 180Mm (long). These simulations show the same fundamental properties as those discussed for the 90Mm loop.

4.3 Non-uniform heating

Having considered the case of uniform heating in Chapter 3 and Section 4.2, we now turn our attention to studying spatially non-uniform heating (e.g. Lionello et al., 2009; Mikić et al., 2013; Reale, 2016; Reale et al., 2016). In this section we explore both symmetric and asymmetric heating events within short (60Mm) and long (180Mm) loops. The results are summarised in Table 4.1 and the individual events are described below.

For each case we present key metrics in the table that enable a comparison between the density and temperature attained by the different methods (LareJ, Lare1D and HYDRAD). The latter uses the maximum averaged temperature while the former, in contrast to Chapter 3, uses the coronal averaged density at the time of the HYDRAD peak value. This is a better metric for the density than using the maximum averaged value (as was done in Chapter 3) because in many cases the Lare1D density maximum occurs prematurely in the initial response, after which time the accuracy of the solution fails.

Using the metrics it can be seen that the discrepancies between the LareJ and HYDRAD results vary from being small to significant while there is always significant discrepancy between both these methods (LareJ and HYDRAD) and the Lare1D density. Our discussion focusses primarily on the most difficult cases where typically the discrepancies are largest but it should not be ignored that the jump condition method in fact works very well (the errors are smaller) in the majority of the other cases.

The events considered are based on a subset of the cases that were previously studied in Chapter 3 (Cases 3, 5, 9 & 11 there) now referred to as Cases 1–4 respectively. However, the energy deposition is now localised to one of three distinct spatial locations. These are concentrated at the loop apex and the footpoints, as illustrated for both the short and long loop in Figure 4.2. For footpoint heating, we consider profiles that release the energy at the base of the corona (above the top of the TR) and at the base of the TR (i.e. $z = z_b$ in the initial equilibrium), which we refer to as fp1 and fp2 heating, respectively.

We have also tested profiles that release the energy entirely in the chromosphere. However, if you heat the chromosphere then all of the energy released is lost from the loop through radiation and no evaporation is observed. This is because the chromosphere is so dense that it requires a large amount of energy in order to overcome the radiative losses and drive an upflow.

The temporal profile of the energy release is triangular, over a total duration of τ_H as defined in equations (3.14)–(3.15), and the spatial profile is given by,

$$Q_H(z) = Q_{H_0} \exp\left(\frac{-(z - z_0)^2}{2z_H^2}\right), \tag{4.8}$$

Table 4.1: A summary of the parameter space used and results from the non-uniform heating simulations.

Case (Heating location)	2L (Mm)	Q_{H_0} ($\mathrm{J\,m^{-3}s^{-1}}$)	τ_H (s)	$T_{\max}$(HYDRAD) (MK)	$T_{\max}$(LareJ) (MK)	$T_{\max}$(Lare1D) (MK)	$n_{\max}$(HYDRAD) ($10^{15}\mathrm{m^{-3}}$)	n(LareJ) ($10^{15}\mathrm{m^{-3}}$)	n(Lare1D) ($10^{15}\mathrm{m^{-3}}$)
1 (apex)	60	2.1	60	14.6	15.7	15.9	8.8	11.2	3.6
1 (fp1)	60	2.1	60	10.2	10.9	10.6	8.8	11.3	3.6
1 (afp1)	60	2.1	60	8.0	8.2	8.4	5.4	7.2	2.4
1 (fp2)	60	2.1	60	8.4	8.2	7.6	8.3	10.0	3.3
1 (afp2)	60	2.1	60	4.6	4.7	4.6	4.7	6.5	2.1
2 (apex)	60	2.1×10^{-1}	600	7.6	7.7	7.7	8.6	10.9	2.7
2 (fp1)	60	2.1×10^{-1}	600	6.1	6.2	5.8	8.9	11.3	2.9
2 (afp1)	60	2.1×10^{-1}	600	5.4	5.5	5.0	5.6	7.1	2.1
2 (fp2)	60	2.1×10^{-1}	600	4.6	3.1	3.8	9.9	11.4	3.2
2 (afp2)	60	2.1×10^{-1}	600	4.1	2.2	3.3	5.7	5.0	2.4
3 (apex)	180	2.3×10^{-1}	60	11.1	12.0	12.0	0.98	1.01	0.31
3 (fp1)	180	2.3×10^{-1}	60	5.1	6.5	6.4	1.01	1.04	0.32
3 (afp1)	180	2.3×10^{-1}	60	3.6	4.4	4.2	0.63	0.69	0.30
3 (fp2)	180	2.3×10^{-1}	60	3.7	3.3	2.2	0.91	0.81	0.40
3 (afp2)	180	2.3×10^{-1}	60	2.6	2.5	2.0	0.59	0.53	0.34
4 (apex)	180	2.3×10^{-2}	600	6.6	6.9	6.9	0.95	1.16	0.43
4 (fp1)	180	2.3×10^{-2}	600	4.4	5.0	4.5	1.04	1.18	0.32
4 (afp1)	180	2.3×10^{-2}	600	3.1	3.6	3.4	0.67	0.78	0.29
4 (fp2)	180	2.3×10^{-2}	600	2.5	2.3	2.1	1.31	1.09	0.46
4 (afp2)	180	2.3×10^{-2}	600	2.0	1.96	1.86	0.73	0.67	0.36

Notes. From left to right the columns show the case number and heating location, the total length of the loop, the maximum heating rate, the duration of the heating pulse, the maximum averaged temperature attained by HYDRAD (in single fluid mode) with the largest grid cell of width 400km and 12 levels of refinement employed, LareJ (computed with 500 grid points along the length of the loop with the jump condition employed) and Lare1D (computed with the same spatial resolution as the LareJ solution but without the jump condition employed) and their respective coronal averaged densities at the time of the HYDRAD peak density. Cases 1, 2, 3 & 4 are the equivalent of Cases 3, 5, 9 & 11, respectively (in terms of the total energy released) that were studied previously in Chapter 3. fp1 and fp2 heating refers to symmetric footpoint heating concentrated at the base of the corona and base of the TR respectively, while afp1 and afp2 heating are the asymmetric footpoint heating counterparts where the energy is released only at one loop leg.

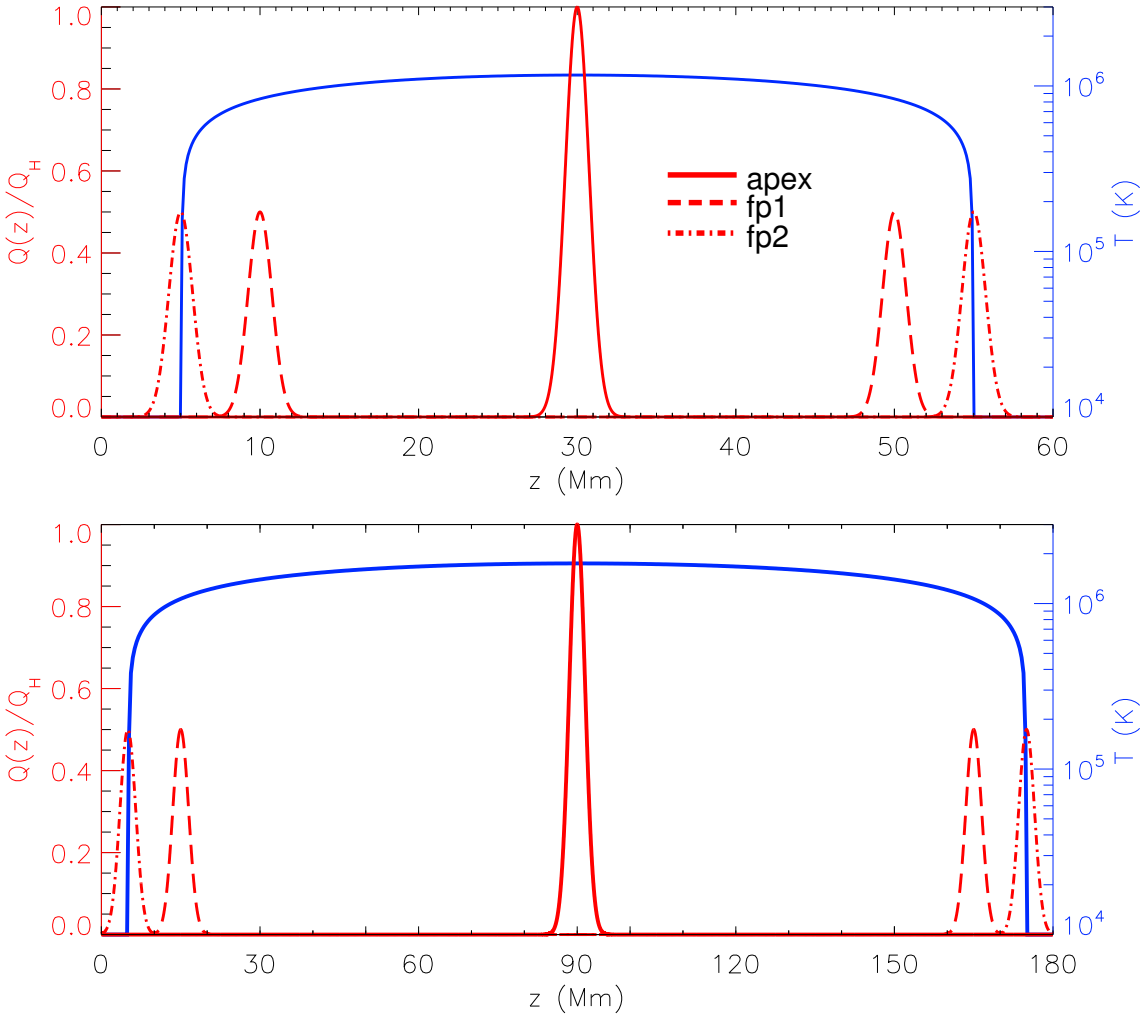

Figure 4.2: Symmetric non-uniform heating profiles $Q_H(z)/Q_{H_0}$ (left-hand axis), for apex (solid red line), fp1 (base of corona, dashed red line) and fp2 (base of TR, dot-dashed red line) heating (see Section 4.3), imposed on top of the temperature initial condition (solid blue line, right-hand axis). The upper (lower) panel corresponds to a 60Mm (180Mm) loop for which we take $z_H = 0.75$Mm ($z_H = 1.5$Mm) as the length scale of heat deposition.

where z_0 is the location of maximum heating, z_H is the length scale of heat deposition and Q_{H_0} is the maximum heating rate. We relate the results to Chapter 3 by releasing the same total amount of energy in the symmetric non-uniform heating events as was released in the corresponding uniform heating (Q_U) cases,

$$\int_0^{2L_C} Q_U \, dz = \int_0^{2L_C} Q_{H_0} \exp\left(\frac{-(z-z_0)^2}{2z_H^2}\right) dz,$$

$$Q_U 2L_C \approx \int_{-\infty}^{\infty} Q_{H_0} \exp\left(\frac{-(z-z_0)^2}{2z_H^2}\right) dz,$$
$$= Q_{H_0} z_H \sqrt{2\pi}.$$

Hence, the maximum heating rate is calculated as,

$$Q_{H_0} = Q_U 2L_C / z_H \sqrt{2\pi}, \tag{4.9}$$

where $2L_C$ is the total coronal length between the TR bases.

Asymmetric heating is studied by adjusting the symmetric footpoint heating profiles to release energy only at the left-hand leg of the loop. Thus, the total energy deposited in the asymmetric heating events (referred to as afp1 and afp2 heating) is only 50% that of the symmetric heating counterparts, but the heating at the left footpoint is the same.

4.3.1 Case 1

Case 1 is representative of a small flare in a short loop. For uniform heating (Chapter 3), this case proved to be the most challenging one for obtaining agreement between LareJ and HYDRAD. Figure 4.3 shows the temporal evolution of the coronal averaged temperature (T), density (n) and the corresponding temperature versus density phase space plot, in response to apex, fp1, fp2, afp1 and afp2 heating (columns 1–5).

Figure 4.3 demonstrates the level of agreement between the LareJ and HYDRAD solutions. Starting with the plasma response to apex heating, column 1 of Figure 4.3 shows that the LareJ density has the same generic evolution with respect to the evaporation required by the heating, the time of peak density and the subsequent decay phase. The discrepancy between the LareJ density and the HYDRAD density is about 30% at the density peak, the source of which will be discussed in detail in Section 4.4 but we note that this is of the same order as found in Chapter 3. Furthermore, any differences in the temperature are smaller than those in the density, because of its weaker dependency on the spatial resolution for this class of problem (BC13). It can also be seen that LareJ represents a considerable improvement on the Lare1D solution, whose temperature and density suffer from rapid cooling and a premature density peak. Here, the latter arises because the heat flux jumps across an under-resolved TR (BC13), resulting in a diminished upward enthalpy flux that changes sign too soon. The former is once again due to the influence of the subsequent lower coronal density on the conductive cooling timescale (e.g. see Chapter 3 and Section 4.2).

Due to the fact that thermal conduction is very efficient at coronal temperatures, the density response to fp1 heating is similar to apex heating (and both are similar to uniform

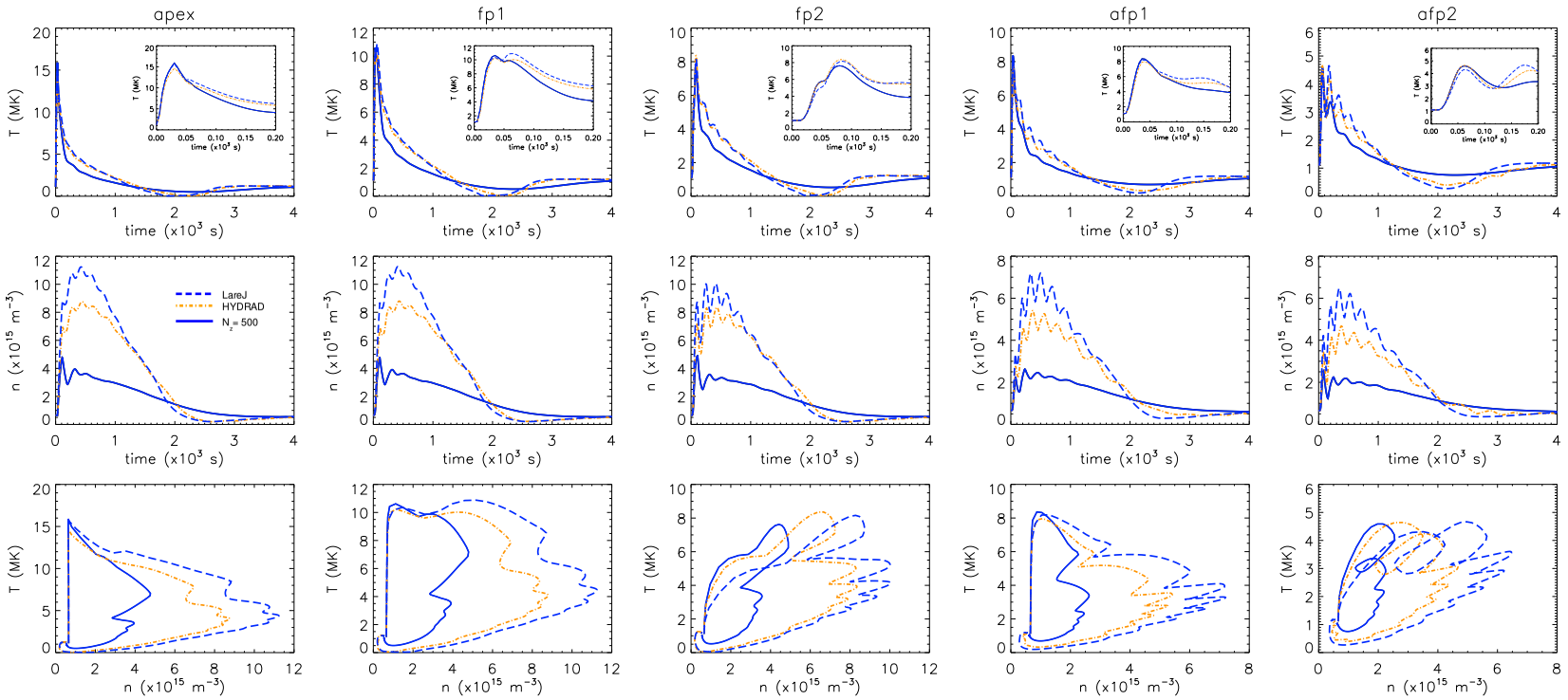

Figure 4.3: Results for Case 1. The panels show the coronal averaged temperature and density as functions of time, and the temperature versus density phase space plot. The sub-panels show the time evolution of the coronal averaged temperature over a shorter time interval (the first 200s). Columns 1, 2, 3, 4 & 5 correspond to apex, fp1 (base of corona), fp2 (base of TR) afp1 and afp2 (asymmetric) heating, respectively. The dashed blue line is the LareJ solution (computed with 500 grid points along the length of the loop with the jump condition employed), the solid blue line is the Lare1D solution (computed with the same spatial resolution as the LareJ solution but without the jump condition employed) and the dot-dashed orange line corresponds to the fully resolved HYDRAD solution. The total energy deposited in the asymmetric heating events (afp1 & afp2) is only 50% that of the symmetric heating events (apex, fp1 & fp2) because only the left-hand leg of the loop is heated.

heating). Following the energy release in fp1 heating there is an upward propagating conduction front that heats the coronal plasma (so the peak temperature is lower than for apex heating) and a downward propagating front that drives the evaporation from the TR. Figure 4.3 and Table 4.1 shows that the agreement obtained between the LareJ and HYDRAD solutions (for the fp1 heating event) is similar to apex heating. The Lare1D solution has the same problems as before.

For fp2 heating, the energy deposition is centred on the base of the TR and so is deposited in the chromosphere and UTR. Hence, the coronal plasma is heated by an upward propagating conduction front while simultaneously the evaporation (density front) from the TR is driven by a combination of the local energy release and conductive heating. Therefore, fp2 heating poses different challenges from apex and fp1 heating. In particular a difficulty with fp2 heating is that part of the energy released may be lost to artificially large radiation within the UTR (see Section 4.4.2).

However, column 3 in Figure 4.3 shows that for the fp2 heating event considered in Case 1, the agreement between the temporal evolution of the LareJ temperature and density and the corresponding HYDRAD quantities is respectable and still significantly better than Lare1D. The fact that the HYDRAD peak temperature now marginally exceeds that of the LareJ solution demonstrates that energy was lost lower down in the UTR (usually the reverse is true, see Table 4.1), although it was only a small amount for this particular heating event.

The response of the TR to afp1 and afp2 asymmetric footpoint heating is different for each loop leg. On one hand the initial response at the left-hand leg of the loop is equivalent to the symmetric footpoint heating events, while on the other hand the response at the right-hand leg is consistent with a weakened apex heating event because it only undergoes heating following the arrival of the conduction front that is launched from the left-hand leg. In accordance with these differences in the TR response, Figure 4.3 shows that for the afp1 and afp2 heating events, the coronal temperature and density peaks are lower than the equivalent symmetric heating quantities. However, the level of agreement between the LareJ and HYDRAD solutions is similar to that discussed above for the symmetric heating events. Thus, the jump condition model can be employed to capture the coronal response to both symmetric and asymmetric non-uniform heating events.

In summary, for Case 1, the jump condition solutions (LareJ) obtain a coronal density comparable to HYDRAD (fully resolved 1D model) but with a significantly faster computation time (the gains are consistent with those presented in Chapter 3, the speed-up is between one and two orders of magnitude) and the approach significantly improves the accuracy of both the coronal density and temperature evolution when compared to the equivalent simulations run without the jump condition (Lare1D, the solid blue lines). So despite the complexity of the type of heating considered, the jump condition still produces acceptable results when using coarse resolution.

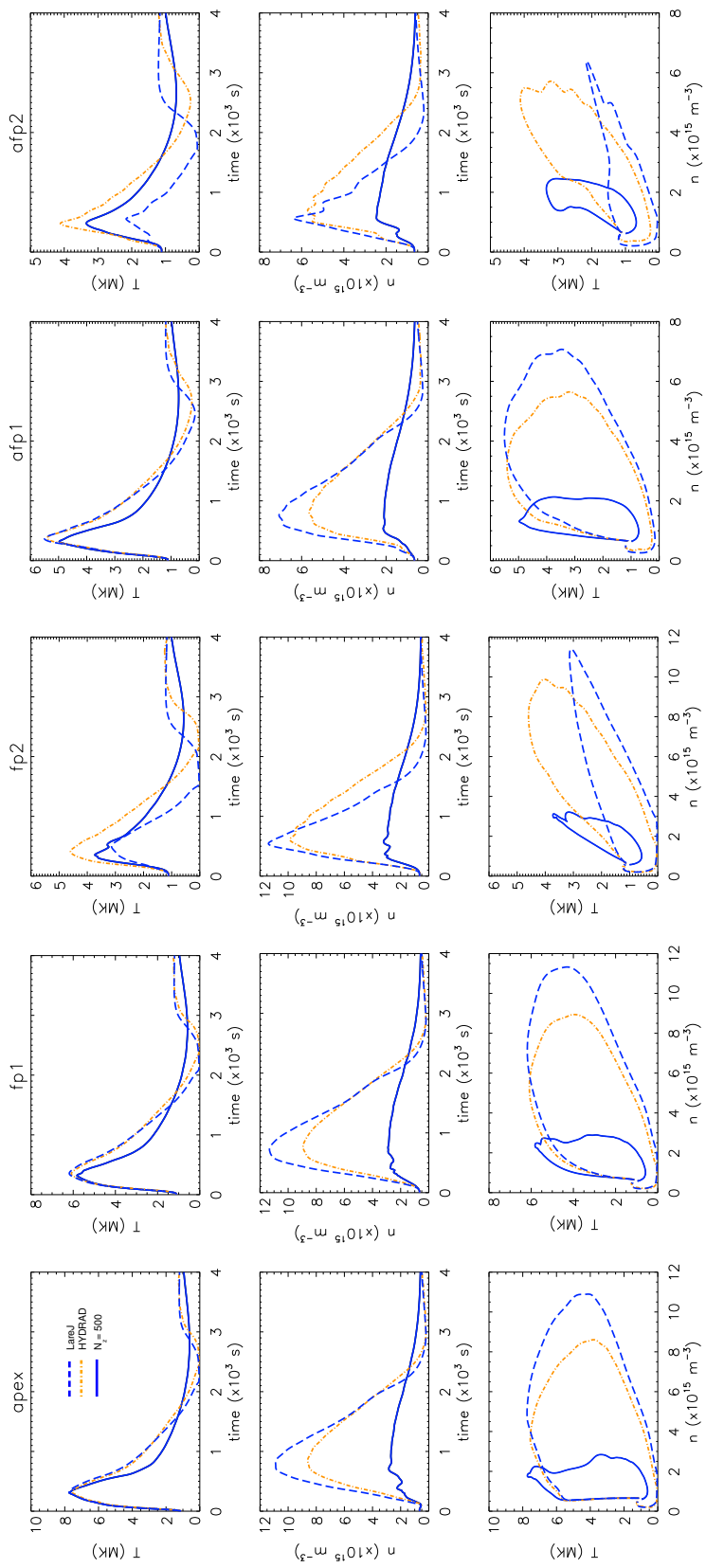

Figure 4.4: Results for Case 2. Notation is the same as Figure 4.3.

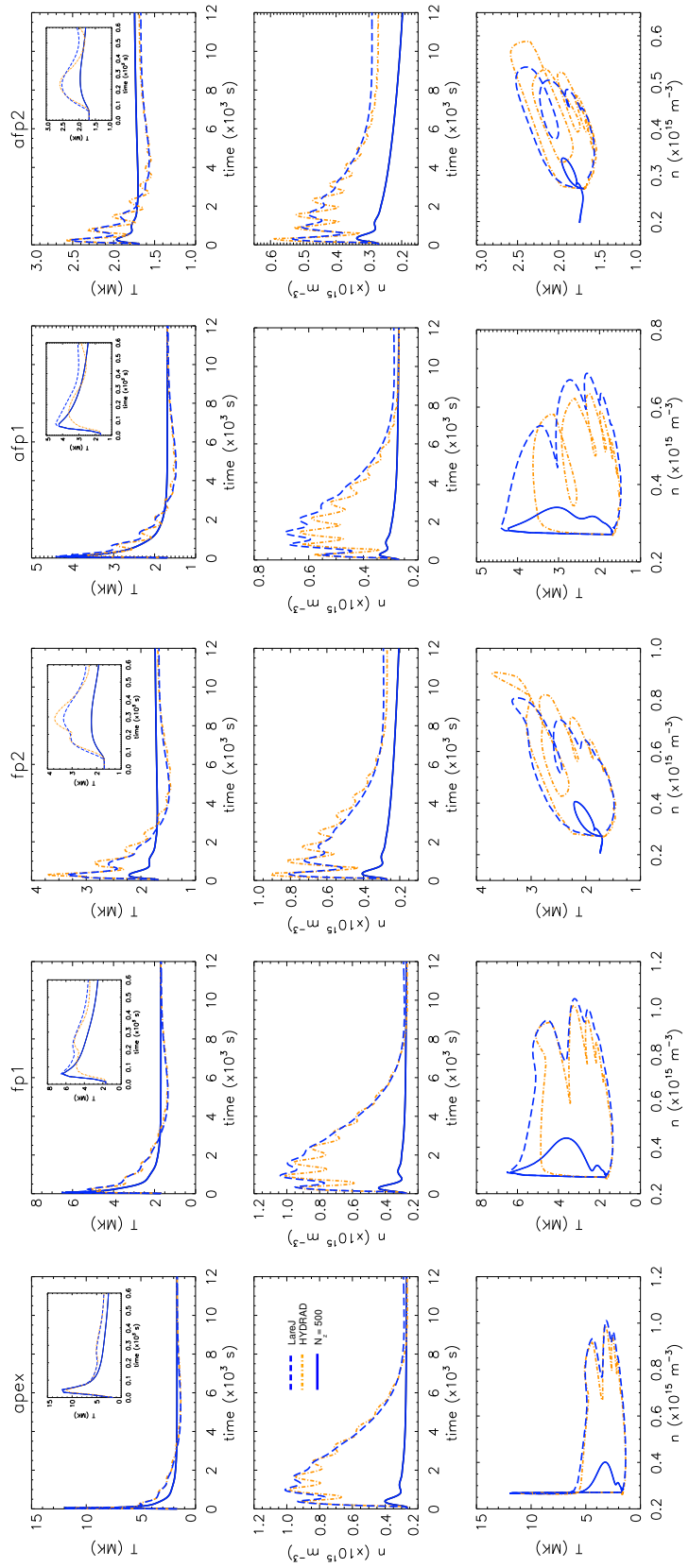

Figure 4.5: Results for Case 3. Notation is the same as Figure 4.3 but note the different time axis.

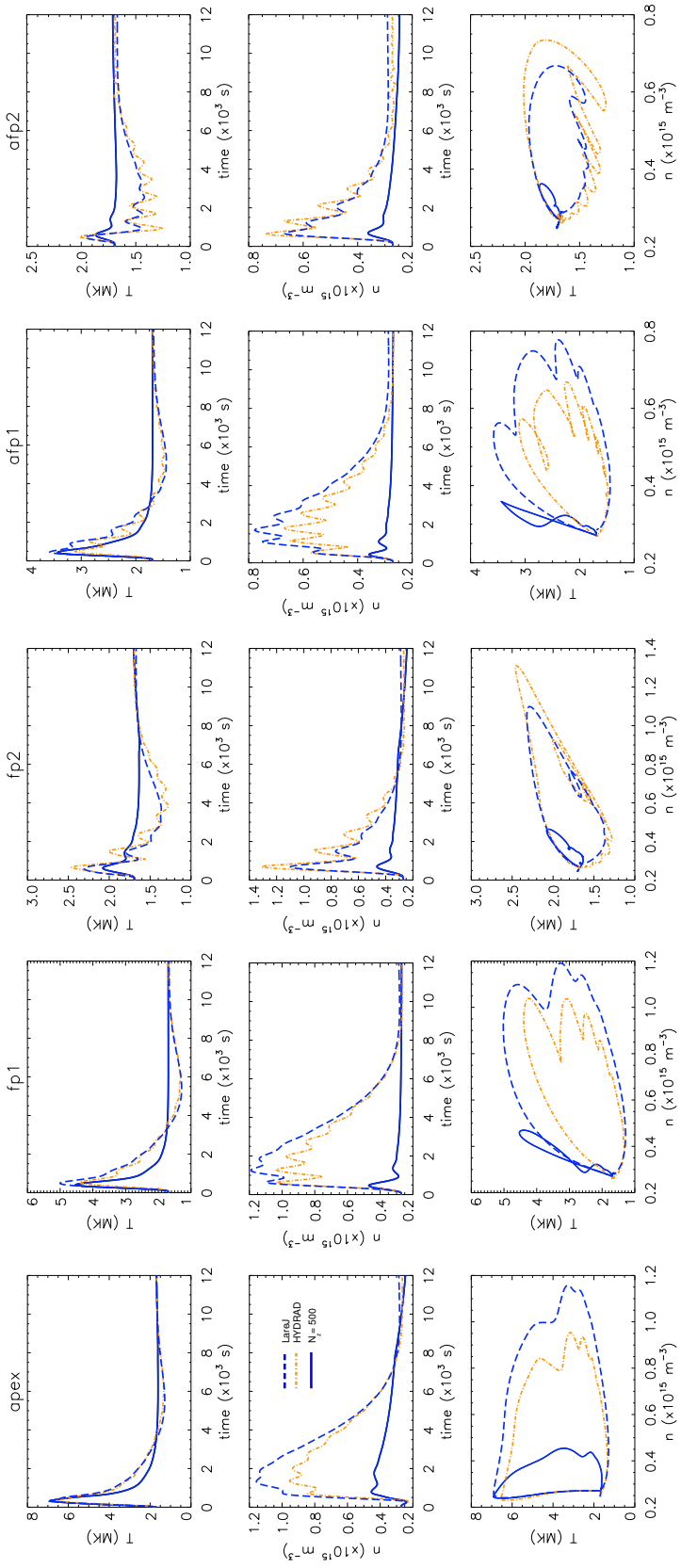

Figure 4.6: Results for Case 4. Notation is the same as Figure 4.3 but note the different time axis.

4.3.2 Case 2

Figure 4.4 shows the results for Case 2. Here, the total amount of energy released is the same as Case 1 but the heating is slower, taking place over a longer timescale (600s). When compared with HYDRAD, the performance of the LareJ solution once again shows good agreement, for the apex, fp1 and afp1 heating events. This is expected because the terms that control the evaporation are essentially the same as those in Case 1, but acting over longer timescales.

On the other hand, for the fp2 heating event the LareJ solution has its largest discrepancies (in response to symmetric energy deposition) when compared over the complete heating and cooling cycle with the fully resolved 1D model (HYDRAD). Column 3 in Figure 4.4 shows that the temperature is lower and while the density gives a good description up until the time of the maximum, the draining phase begins slightly early. These discrepancies are related to energy losses in the UTR with LareJ. This will be discussed in detail in Section 4.4.2. Similar problems are also observed in the afp2 heating event but the energy losses are more significant for asymmetric footpoint heating (afp2) because there is only one upward propagating conduction front.

However, when we compare the LareJ solution with the equivalent simulation run without the jump condition (Lare1D), it remains clear that we still significantly improve the accuracy of the coronal density. Hence, we capture a more realistic evolution in response to the heating by employing the jump condition (LareJ), despite the energy losses in the UTR.

4.3.3 Cases 3 & 4

We present the results for the long (180Mm) loop simulations in Figure 4.5 & 4.6. In all of the ten heating events considered in Cases 3 & 4, the figures show that the LareJ solutions significantly improve the Lare1D results to accurately capture the coronal response of the fully resolved 1D model (HYDRAD). The details are analogous to the short loop simulations previously discussed with only one exception. Namely, in the fp2 and afp2 heating events, the LareJ density peak somewhat underestimates the HYDRAD value whereas in general the reverse is true (see Table 4.1). The explanation for these two different types of behaviour, over and under-evaporating, will be discussed next in Section 4.4.

4.4 Discussion of the quantities associated with the UTR jump condition

We now turn to a more detailed discussion of the results obtained with the different methods used in each experiment. The principal issue to be addressed is the discrepancy

between the density evolution in LareJ and HYDRAD. In most cases the LareJ peak density exceeds that obtained by HYDRAD (referred to as over-evaporation), although for some footpoint heating cases, the opposite is true (under-evaporation). (The causes for the differences between the under-resolved Lare1D and the other simulations have been discussed earlier and in Chapter 3 and will not be considered further.) This comparison of the models is undertaken through an analysis of the terms associated with the UTR jump condition (4.3), in particular the various terms in the definition of the terms neglected in LareJ (N: Eq. (4.2)). The cases where the LareJ density exceeds (falls below) the HYDRAD value are discussed in Section 4.4.1 (4.4.2).

In general, there are two important terms in N. One is the rate of change of total energy in the UTR ($\ell d\bar{E}/dt$) and when this is positive (negative), the corrected upflow (v_0) in LareJ is enhanced (decreased) over the upflow at the same point in the HYDRAD solution. The second important term in N involves the mass motions at the base of the TR ($F_{e,b} + F_{ke,b}$). When the TR moves downwards (upwards) the neglect of this motion in LareJ leads to enhanced (decreased) values of v_0. The heat flux at the base of the TR ($F_{c,b}$) is negligible for all cases.

An analysis of the resolved HYDRAD results enables us to quantify the importance of the terms neglected in LareJ, and Figure 4.7 shows the quantities obtained by HYDRAD that are present in the UTR equations. The left column shows the various terms from Eq. (4.2) and the right breaks down N into its important components. Figure 4.8 shows quantities in Eq. (4.3) obtained from the HYDRAD and LareJ simulations. The definition of the 'UTR' is based on the time evolution of the temperature from the LareJ solution, though of course it is fully resolved in HYDRAD. Apex heating for Cases 1 & 3 are shown in the upper two rows, only for the first 50s in Case 1 and the first 200s in Case 3. The lower two rows show the fp2 heating events for Cases 3 & 4 where the LareJ density peak falls below that given by HYDRAD. The first 200s are shown for Case 3 in row 3 and the first 800s for Case 4 in row 4. We only consider the time evolution until the first density peak because this time interval is the main source of error in the subsequent peak density.

4.4.1 Sources of error: over-evaporation (apex & fp1 heating)

For the Case 1 apex heating event, the HYDRAD solution (first row of Figure 4.7) shows that following an initial phase where the TR retains its pre-heating properties, the arrival of the coronal conduction front leads to a short interval (12–15s) when the downward heat flux ($F_{c,0}$) is balanced by the terms neglected in LareJ (N). This interval is also associated with a small downward enthalpy flux ($F_{c,0} \approx 50\,|F_{e,0}|$) that leads to enhanced radiative losses in the UTR. The components of N (right panel) show that in the early phase, the base terms remain unimportant, and the $\ell\bar{E}/dt$ term (change of UTR total

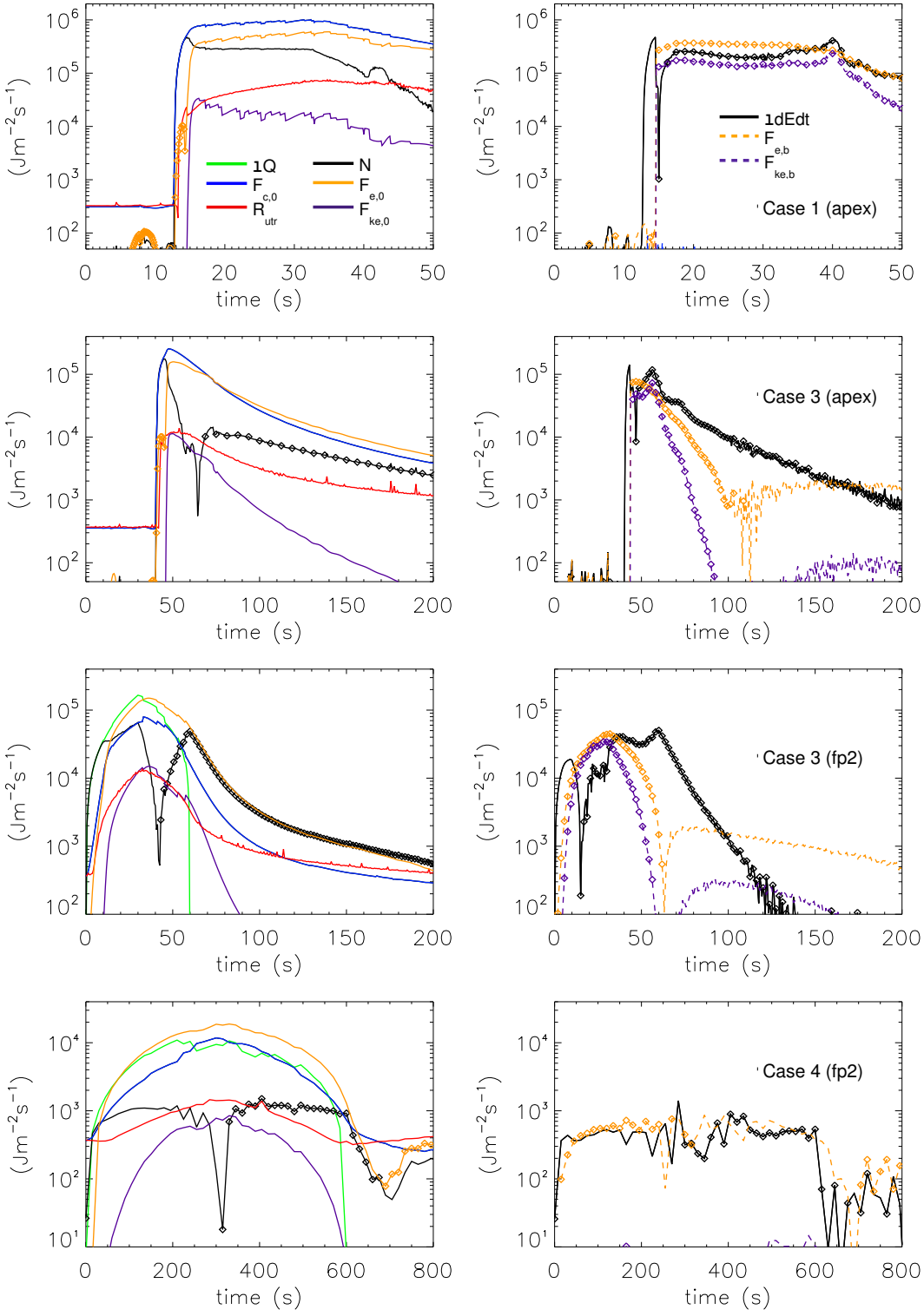

Figure 4.7: Analysis of quantities associated with the UTR jump condition based on fully resolved HYDRAD simulations. Rows 1, 2, 3 & 4 correspond to Case 1 apex, Case 3 apex, Case 3 fp2 and Case 4 fp2 heating, respectively. The left-hand panels show the terms in Eq. (4.2) that control the plasma response, namely the volumetric heating rate in the UTR ($\ell\bar{Q}$, green line), heat flux at the top of the UTR ($F_{c,0}$, blue line), IRL in the UTR (R_{utr}, red line), neglected terms (N, black line, the LHS of Eq. (4.2)), enthalpy flux at the top of the UTR ($F_{e,0}$, orange line) and the kinetic energy flux at the top of the UTR ($F_{ke,0}$, purple line). In the upper two left-hand panels (Cases 1 & 3 apex heating) there is no green line ($\ell\bar{Q}$) because there is no heating in the UTR except that from the background. The right-hand panels show the breakdown of the neglected terms (N), consisting of $\ell d\bar{E}/dt$ (black line), the enthalpy flux at the base of the TR ($F_{e,b}$, dashed orange line) and the kinetic energy flux at the base of the TR ($F_{ke,b}$, dashed purple line). The heat flux at the base of the TR ($F_{c,b}$) is not shown in the breakdown of the neglected terms (N) because it is always negligible. Lines connected by diamond symbols indicate negative quantities and lines without diamonds indicate positive quantities.

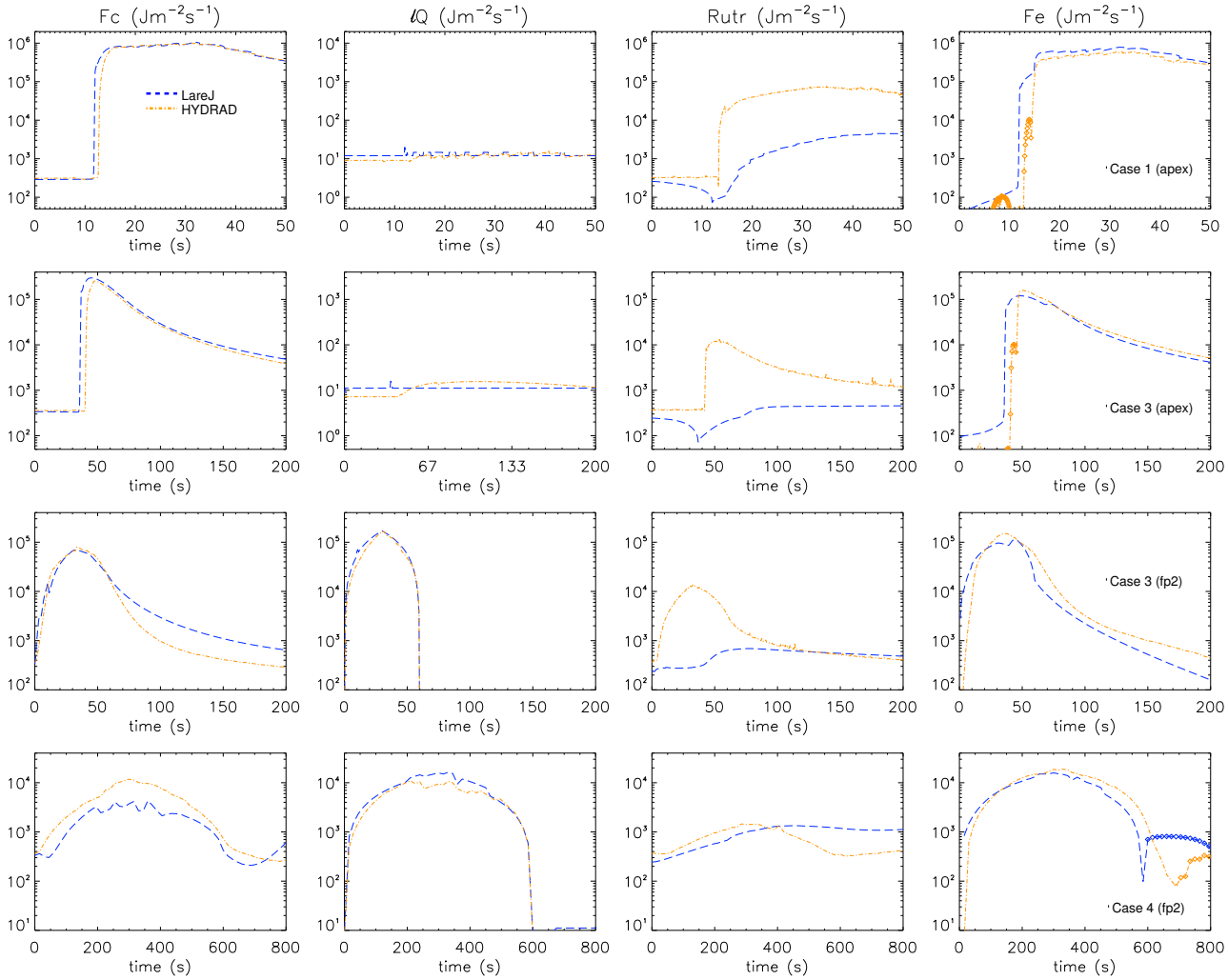

Figure 4.8: Comparison of the dominant quantities in the UTR jump condition obtained from the HYDRAD and LareJ solutions. Rows 1, 2, 3 & 4 correspond to Case 1 apex, Case 3 apex, Case 3 fp2 and Case 4 fp2 heating, respectively. From left to right the columns show the heat flux at the top of UTR ($F_{c,0}$), volumetric heating rate in the UTR ($\ell\bar{Q}$), IRL in the UTR ($\mathcal{R}_{utr}$) and enthalpy flux at the top of the UTR ($F_{e,0}$, lines connected by diamond symbols indicate where the enthalpy flux is downflowing and lines without diamonds indicate where the enthalpy flux is upflowing). The upper two rows (Cases 1 & 3 apex heating) in the second column ($\ell\bar{Q}$) show only the background heating and have a different vertical axis. The dashed blue line is the LareJ solution (computed with 500 grid points along the length of the loop with the jump condition employed) and the dot-dashed orange line corresponds to the fully resolved HYDRAD solution.

thermal energy) dominates. Looking at Figure 4.8, we see that with LareJ the initial 12s is similar to HYDRAD, though the radiative losses decrease in the corona and hence our estimate of $\mathcal{R}_{utr}$ decreases, leading to a small upward enthalpy flux. Then, between 12–15s, LareJ shows a premature upflow with the enthalpy flux being driven immediately by

the conductive losses, a direct consequence of the neglect of $\ell \bar{E}/dt$ in the jump condition.

With HYDRAD, from 15s until the time of the first density peak (100s), both N and radiative losses decline and become negligible after 50s, with the downward heat flux driving an upward enthalpy flux. However, it should be noted that up to 40s, N is still under an order of magnitude smaller than $F_{e,0}$ so the retention of these terms in HYDRAD leads to a smaller upflow than in LareJ, as shown in Figure 4.8. At later times the HYDRAD values of N are negligible.

The apex and fp1 examples all show broadly similar behaviour: for fp1 heating the UTR is still driven by a downward heat flux. We have provided a summary of this general scenario in Table 4.2, which breaks down the atmospheric response to impulsive heating into 4 distinct phases that are listed by their time of importance: (i) the initial atmosphere is undisturbed, (ii) a short phase when the UTR internal energy changes are important, (iii) an evaporative phase with the components of N being of diminishing importance leading to (iv) the first and subsequent density peaks. We also note that for stronger (weaker) heating events the terms neglected in LareJ are more (less) important so the errors at the peak density are larger (smaller): see Table 3.1 in Chapter 3.

However, within this framework, there are some subtle differences between short and long loops for apex and fp1 heating. One is that in the long loop examples, the heat flux that hits the UTR is systematically smaller because the total energy released is chosen to be lower. Therefore, there is less reaction at the base to the incoming heat flux which in turn means that the neglect of N in LareJ is less important and smaller errors in the peak density arise (Table 4.1). This suggests that an important parameter is the 'thermal energy impulse' on the UTR, defined as $\int F_{c,0}\, dt$.

The second minor (and related) exception arises for the Case 3 apex example (short heating pulse in a long loop). In this case, the conductive travel time along the loop (40s) is longer than the half width duration of the heating pulse (30s). From the second row of Figures 4.7 & 4.8, as well as Table 4.3, we see that the LareJ upflow is no longer enhanced over that obtained by HYDRAD because the energy input into the UTR is not sustained. What is seen in Figure 4.7 is not in fact a decrease in the importance in N, but instead a deficit in the dominant terms from the jump condition. A similar argument also applies to the fp1 heating event for Case 3 but for the return time of the upward propagating conduction front.

4.4.2 Sources of error: under-evaporation (fp2 heating)

As already noted, footpoint heating at the base of the TR (fp2) is the most challenging case but a broad outline of the results is as follows. There is over-evaporation in a number

Table 4.2: A summary of the terms from Eq. (4.2) that control the plasma response to the apex and fp1 heating events, considered in Section 4.3, from the HYDRAD results.

Case (Heating location)	$F_{c,0}$ balances $\mathcal{R}_{utr}$	$\ell d\bar{E}/dt$ balances $F_{c,0}$	$F_{c,0}$ drives upward $F_{e,0}$ ($F_{e,0}$ reduced due to terms associated with N)	First density peak (peak density)
1 (apex)	0–12s	12–15s	15–100s (15–40s)	100s (500s)
1 (fp1)	0–5s	5–8s	8–100s (8–35s)	100s (500s)
2 (apex)	0–65s	65–80s	80–500s (80–150s)	800s
2 (fp1)	0–20s	20–40s	40–500s (40–100s)	800s
3 (apex)	0–40s	40–45s	45–270s (45–50s)	300s (1000s)
3 (fp1)	0–13s	13–25s	25–230s (25–30s)	300s (1000s)
4 (apex)	0–190s	190–230s	230–1000s (230–300s)	700s (1500s)
4 (fp1)	0–50s	50–90s	90–900s (90–120s)	500s (1500s)

Notes. The columns show the time interval during which conductive heating ($F_{c,0}$) balances the radiative losses ($\mathcal{R}_{utr}$), the rate of change of total energy in the UTR ($\ell d\bar{E}/dt$) balances the conductive heating, conductive losses drive an upward enthalpy flux (with the upflow, $F_{e,0}$, reduced due to terms associated with N) and the time of the first density peak (and subsequent peak density).

Table 4.3: A summary of the terms from Eq. (4.2) that control the plasma response to the fp2 heating events, considered in Section 4.3, from the HYDRAD results.

Case (Heating location)	Total local heating balances total losses	Imbalance drives upward $F_{e,0}$	Local heating drives upward $F_{e,0}$ ($F_{e,0}$ reduced due to terms associated with N)	Upflow associated with inclusion of terms in N	First density peak (peak density)
1 (fp2)	0–5s	5–20s	20–60s (5–30s)	60–80s	100s (500s)
2 (fp2)	0–10s	10–50s	50–450s (10–100s)	–	600s
3 (fp2)	0–10s	10–35s	35–60s (10–35s)	60-200s	300s
4 (fp2)	0–20s	20–50s	50–600s (20–100s)	–	700s

Notes. The columns show the time interval during which the total local heating ($F_{c,0} + \ell\bar{Q}$) balances the total losses ($\ell d\bar{E}/dt + \mathcal{R}_{utr}$), the imbalance between these terms ($F_{c,0} + \ell\bar{Q} - N - \mathcal{R}_{utr}$) drives an upward enthalpy flux ($F_{e,0}$), local heating drives an upward enthalpy flux (with the upflow reduced due to terms associated with N), the upflow is associated with the inclusion of terms in N, and the time of the first density peak (and subsequent peak density).

of cases but we also now find cases with LareJ with (1) under-evaporation and (2) an underestimation of the coronal temperature.

An important aspect of this is the update calculation of radiation within the UTR in LareJ. As outlined in Chapter 3 and Section 4.1, we use time splitting methods to advance the energy equation. During the conduction and radiation steps we solve the full set of equations in the UTR. This is necessary in order to retain the structure of the TR but can lead to artificially high radiative losses in the UTR that are consistent with the coarse spatial resolution used (e.g. BC13, Chapter 3). The HYDRAD solutions enable us to quantify this error which is limited to only the fp2 heating examples.

So the difficulty with fp2 heating is that part of the energy released during the heating event ($\ell\bar{Q}$) may be lost due to (artificially high) radiation in the UTR rather than transported to the corona by heat conduction, and the LareJ solutions indeed have a spurious reduction of the heat flux into the corona ($F_{c,0}$). This also provides the explanation for the underestimation of the coronal temperature. Furthermore, it is clear from Eq. (4.3) that any reductions in $F_{c,0}$ may then also affect the upflow.

For Case 3 fp2 heating event, the HYDRAD solution shows that for a short interval (0–10s) at the start of the heating period, the local energy released ($\ell\bar{Q}$) is balanced by N (with $\ell d\bar{E}/dt$ the dominant term as above). In contrast, Figure 4.8 shows that the LareJ solution starts with a premature upflow (0–10s) that is powered by $\ell\bar{Q}$ precisely because the $\ell d\bar{E}/dt$ term is neglected. At 10s an upflow begins in HYDRAD which remains present until 230s. In this evaporation phase, the upward enthalpy flux is first driven for a short time (10–60s) by the total local heating ($F_{c,0} + \ell\bar{Q}$) and then for a much longer period (60–200s) by the terms associated with N. During this longer period, $\ell d\bar{E}/dt$ first peaks as a negative term at 60s due to the rapid drop off in the energy release ($\ell\bar{Q}$). $\ell d\bar{E}/dt$ then balances $F_{e,0}$ from 60–100s. After 100s the enthalpy flux at the base becomes important as the TR moves back upwards (following the end of the heating) and the base motions take over the driving of the upward enthalpy flux. On the other hand, the jump condition does not model this part of the upflow. Hence, the LareJ solution underestimates $F_{e,0}$ for the duration of this period (60–200s), as can be seen in Figure 4.8.

For the Case 4 fp2 heating, the HYDRAD solution shows generally a similar response, however, in this slower heating event, the main evaporation phase takes place between 50–600s, with the upward enthalpy flux driven by the total local heating ($F_{c,0} + \ell\bar{Q}$). In contrast, these local heating mechanisms do not have equal weighting in driving the LareJ evaporation. Figure 4.8 shows that from 50–600s, a somewhat overestimated $\ell\bar{Q}$ dominates a significantly underestimated $F_{c,0}$. This behaviour arises as a direct consequence of the artificial energy losses in the UTR. The outcome is that LareJ underestimates the upward enthalpy flux between 200–600s.

The quantities that control the evaporation in response to fp2 heating are predominantly the same for short and long loops. They are summarised together in Table 4.3

which shows additional subtleties. For example, LareJ overestimates the initial upward enthalpy flux in Cases 1 & 2 for the reasons discussed in Section 4.4.1 but underestimates $F_{e,0}$ at later times due to the behaviour described above in this section for slow and fast heating. The net effect is for a reduced over-evaporation in comparison to the corresponding apex and fp1 heating events.

4.5 Chapter Conclusions

We introduced the jump condition approach for 1D hydrodynamic modelling in Chapter 3. This is a simple method that can be employed with an under-resolved TR to deal with the difficulty of obtaining the correct interaction between a downward conductive flux and the resulting upflow. Thus, the evaporative response to a coronal heating event can be modelled *without fully resolving the TR* (BC13). In this further analysis of the method, the experiments presented were selected to be some of the most challenging cases.

In all of the experiments considered, the jump condition approach leads to coronal densities that are comparable to fully resolved 1D models (HYDRAD) but with computation times that are between one and two orders of magnitude faster. Therefore, the applicability of the jump condition is not affected by introducing complexities, both spatially and temporally, in the energy release (heating).

On the other hand, the densities are predominantly higher than those from a fully resolved 1D code (HYDRAD in this case) which is explained by the presence of an overestimated upward enthalpy flux. This can be attributed to the neglect of terms corresponding to the rate of change of total energy in the unresolved atmosphere and mass motions at the base of the TR. It would certainly be advantageous to include these terms in the jump condition in order to remove the over-evaporation. However, if we could calculate these neglected terms accurately then it would not be necessary to implement such an approach. Furthermore, the interaction between these terms is such that either both must be included or neither. Of course at some point diminishing returns will be reached and the simplicity of the method weakened.

Most importantly, despite the (relatively small) remaining error when comparing with a fully resolved 1D code (HYDRAD), the implementation of the jump condition leads to a significant improvement compared with the equivalent (coarse resolution) simulations run without the jump condition. Both the coronal density and temperature evolution are comparable with those obtained from fully resolved simulations, especially at the time of peak density and throughout the draining phase for both uniform (Chapter 3) and non-uniform heating (this chapter).

Chapter 5

Footpoint Heating in Coronal Loops & Thermal Non-equilibrium

Having rigorously validated the use of the UTR jump condition method to approximate the response of the TR to changing coronal conditions in the previous two chapters, we now focus on the application of our approach to coronal loop models with footpoint heating and thermal non-equilibrium (TNE). In particular, the experiments considered in this chapter investigate the effects of numerical resolution, background heating and adjusting the heating parameters on the occurrence of TNE.

TNE is a phenomenon that can occur in coronal loops when the heating is concentrated towards the footpoints (e.g. Müller et al., 2003, 2004, 2005; Mok et al., 2008; Antolin et al., 2010; Susino et al., 2010; Lionello et al., 2013; Mikić et al., 2013; Susino et al., 2013; Mok et al., 2016). This localised energy deposition drives evaporative upflows that fill the loop with hot dense plasma, increasing the coronal density and radiative losses. Eventually, when the coronal radiative losses overcome the heating source(s) at the top of the loop, the thermal instability is triggered locally in the corona (e.g. Parker, 1953; Field, 1965; Hildner, 1974). The subsequent runaway cooling leads to the formation of coronal condensations in the region around the loop apex (Mok et al., 1990; Antiochos and Klimchuk, 1991; Antiochos et al., 1999). These condensations then fall back down to the chromosphere if they are gravitationally unstable, with the loop draining along the magnetic field.

Furthermore, if the heating frequency is high in comparison to the characteristic cooling time of the loop then this evolution of evaporation followed by condensation can become cyclic. The response of a loop to such quasi-steady heating is to oscillate in time, whilst undergoing evaporation and condensation cycles with a period on the timescale of

hours. This highly nonlinear and unstable behaviour has been termed TNE (Müller et al., 2003, 2004; Peter et al., 2012; Mikić et al., 2013) and we refer to these evaporation and condensation cycles as TNE limit cycles (Kuin and Martens, 1982). These limit cycles are thought to provide the explanation for the long period extreme ultraviolet pulsations that are observed in coronal loops, with periods between 2 and 16 hours (Auchère et al., 2014; Froment et al., 2015, 2017, 2018). Mikić et al. (2013) suggested that two different types of TNE limit cycles could exist in coronal loops, each with significantly different observations signatures. They classified cycles as experiencing complete and incomplete condensations based on the response of the coronal temperature and density. Complete condensation cycles describe the scenario where condensations catastrophically cool to chromospheric temperatures at the loop apex, forming dense cool blobs that are believed to manifest as coronal rain in observations (e.g. Antolin et al., 2015). In contrast, in the case of incomplete condensations, the coronal temperature only cools to around 1MK and the density remains relatively low.

The chapter has the following structure: the effect of numerical resolution on TNE limit cycles is investigated in Section 5.1, through a series of simulations with steady and impulsive footpoint heating. In Section 5.2, we present example cases that use different background heating models in order to explore the influence of the background heating on the onset of TNE in coronal loop models. The uniqueness of TNE limits cycles is then analysed in Section 5.3, by comparing the responses obtained in simulations run with different heating parameters. We present our conclusions for the chapter in Section 5.4.

5.1 The Effect of Numerical Resolution on Thermal Non-Equilibrium Limit Cycles

We start by exploring the effect of numerical resolution on the existence of TNE limit cycles in coronal loop models. To facilitate this investigation, we make use of the UTR jump condition method (LareJ) and compare the results with Lare1D without the jump condition but with the same coarse spatial resolution. We model a coronal loop of total length 180Mm and use a numerical resolution of 500 uniformly spaced grid points. LareJ is used as a benchmark solution and contrasted with Lare1D which is considered to be representative of a typical simulation where the numerical resolution under-resolves the TR.

5.1.1 Model 1: Steady Symmetric Footpoint Heating

We start by considering the case of steady symmetric footpoint heating, which we refer to as Model 1. For this model the spatial profile of the heating is given by the sum of two

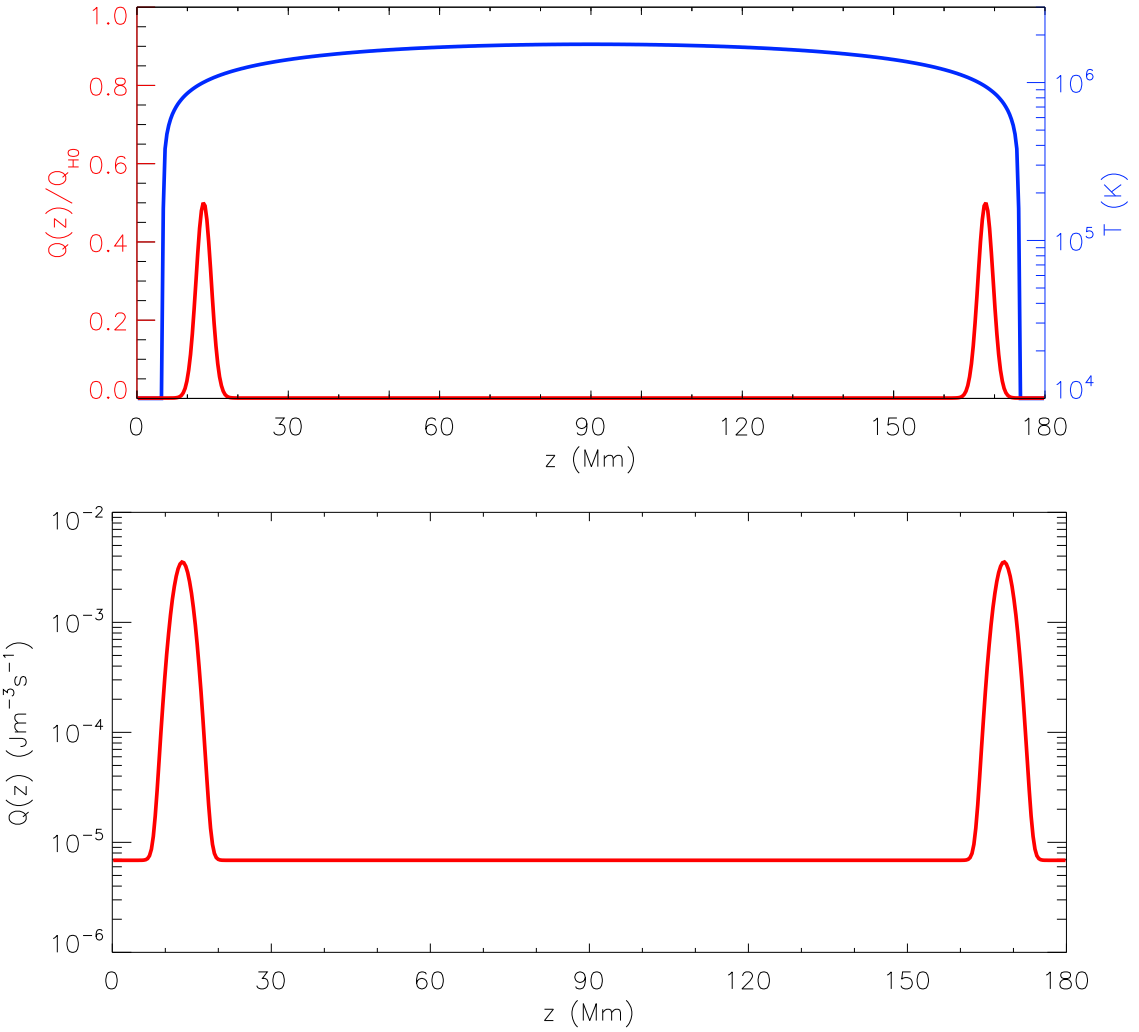

Figure 5.1: Model 1 steady symmetric footpoint heating profile. The panels show $Q(z)/Q_{H_0}$ (red line, left hand axis) imposed on top of the temperature initial condition (blue line, right-hand axis) and the heating function $Q(z) = Q_{bg} + Q_H(z)$. We take $Q_{H_0} = 3.5273 \times 10^{-3}\mathrm{Jm}^{-3}\mathrm{s}^{-1}$ and $z_H = 1.5\mathrm{Mm}$ as the length scale of heat deposition. For the 180Mm loop initial condition $Q_{bg} = 6.8682 \times 10^{-6}\mathrm{Jm}^{-3}\mathrm{s}^{-1}$.

Gaussian peaks (one at each loop leg), with each peak defined as in Eq. (4.8). These peaks are localised between the base of the corona and base of the TR (i.e. footpoint heating lying between fp1 and fp2 heating with a maximal value at $z = 12.5\mathrm{Mm}$) as shown in the upper panel of Figure 5.1. However, note that a small spatially uniform background heating term is always present ($Q(z) = Q_{bg} + Q_H(z)$, e.g. see the lower panel of Figure 5.1). Following an initial linear ramp up phase (30s), the temporal profile of the heating is uniform with a peak value of $Q_{bg} + Q_{H_0}/2$. Here the background heating term (Q_{bg}) is

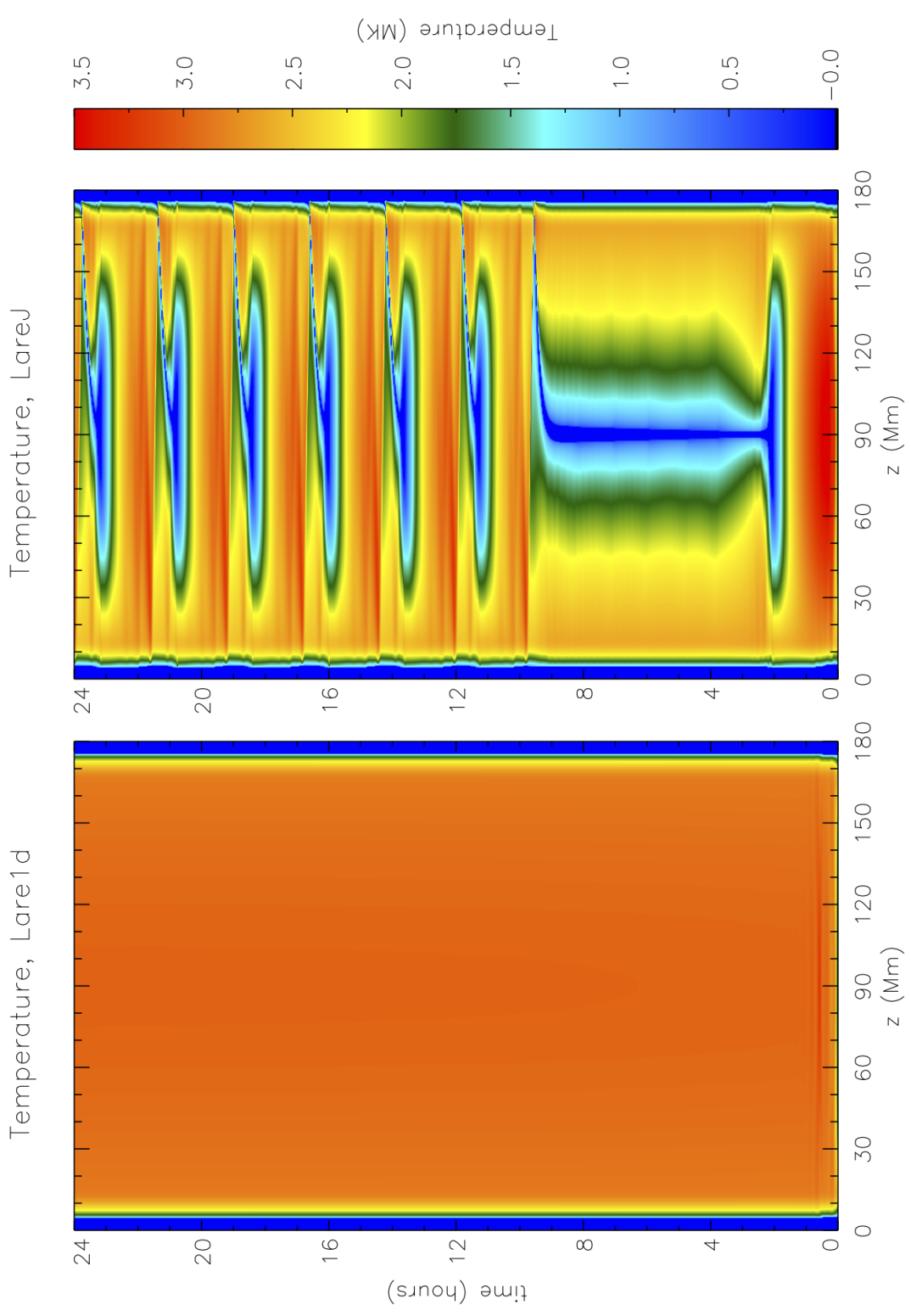

Figure 5.2: The effect of obtaining the correct evaporative response on TNE limit cycles. Results for Model 1 (steady symmetric footpoint heating). The panels show the time evolution of the temperature as a function of position along the loop obtained in two different simulations, each with the same spatial resolution of 500 grid points along the length of the loop (coarse resolution). Columns 1 & 2 correspond to the Lare1D and LareJ (Lare1D with the jump condition employed) solutions, respectively.

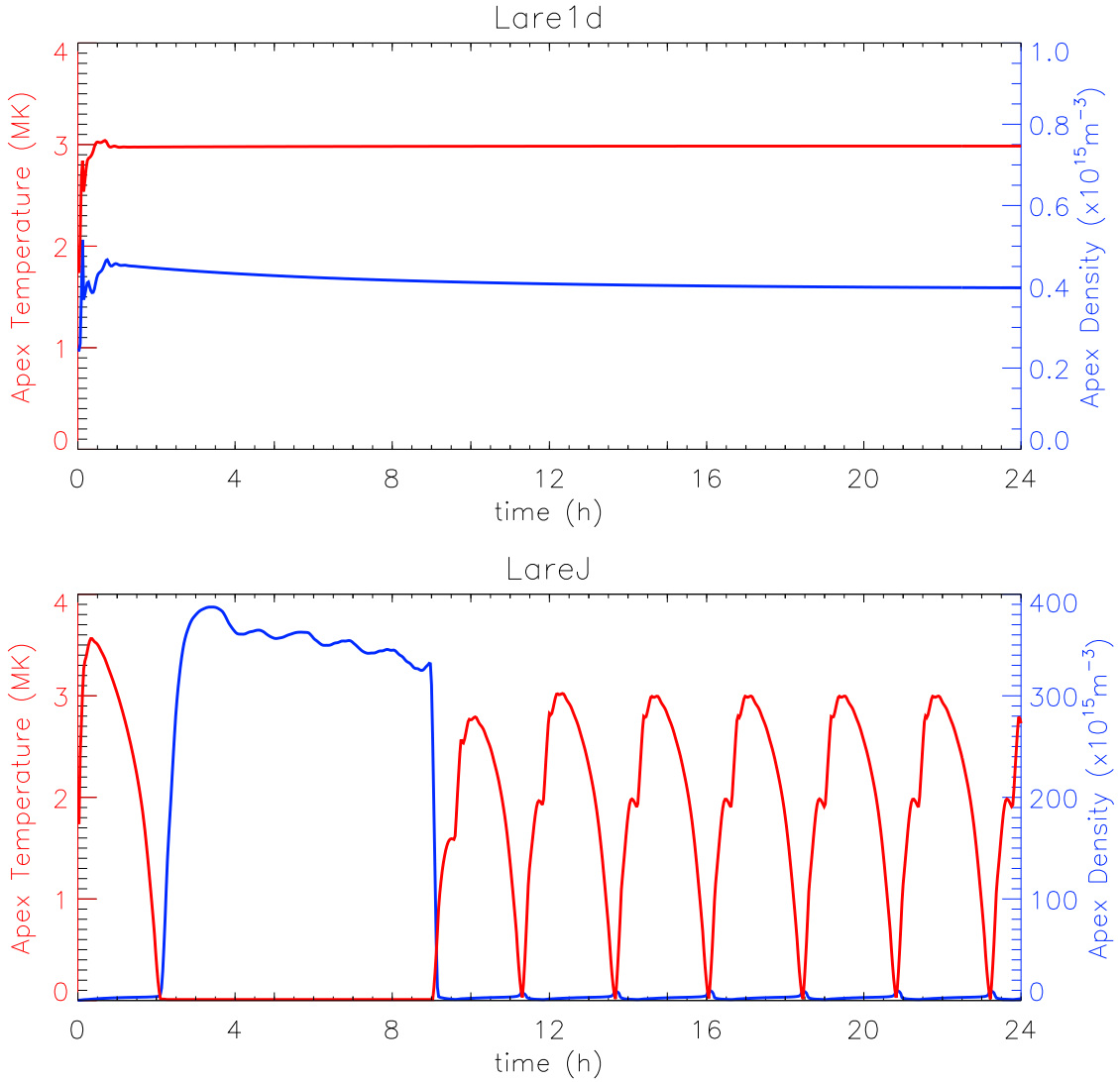

Figure 5.3: Results for Model 1 (steady symmetric footpoint heating). The panels show the time evolution of the apex temperature (red line, left hand axis) and density (blue line, right hand axis) obtained in two different simulations, each with the same spatial resolution of 500 grid points along the length of the loop (coarse resolution). The Lare1D solution is shown in the upper panel and the LareJ (Lare1D with the jump condition employed) solution is shown in the lower panel.

determined based on the equilibrium solution and Q_{H_0} is prescribed in order to give a maximum temperature of approximately 3.5MK. This set up is representative of the conditions necessary to induce TNE in coronal loop models (e.g. Müller et al., 2003; Antolin et al., 2010; Peter et al., 2012; Mikić et al., 2013; Froment et al., 2018).

Figure 5.2 shows the time evolution and spatial variation of the temperature response to the Model 1 heating profile, for loops computed with (LareJ, right) and without the

jump condition (Lare1D, left). The behaviour seen in the two simulations is completely different. The loop computed with the jump condition experiences TNE and develops complete condensations at the loop apex. Note here that the jump condition is applied only in the TR of each loop leg and not at the condensation. In contrast, the loop computed without the jump condition settles to a static equilibrium after an initial adjustment to the steady energy deposition and a weak draining phase.

The temporal evolution of the apex temperature (T_a) and density (n_a) from the Lare1D (top) and LareJ (bottom) loops are shown together in Figure 5.3. Starting with the Lare1D loop, it is clear that the apex temperature settles and remains at 3MK from around 2 hours onwards while the density slowly drains towards a value of $0.4 \times 10^{15}\mathrm{m}^{-3}$. On the other hand, the apex temperature of the LareJ loop is initially heated to 3.6MK before cooling to 10^4K at 2 hours, in response to an increased density that peaks just below $400 \times 10^{15}\mathrm{m}^{-3}$ after 3.5 hours. This massive condensation persists for a total time of 7 hours, during which the apex temperature remains at chromospheric levels (10^4K). Eventually after 9 hours the condensation falls down the right-hand leg of the loop under the effect of gravity due to the build up of a small numerical asymmetry. The evolution then repeats and the loop follows a regular TNE limit cycle. The period of the cycle is estimated from the peaks in apex temperature as about 2.25 hours (6 cycles in 14 hours) However, note that the massive initial condensation (seen between 2-9 hours) is unlikely to occur in practice because the large amount of mass accumulated by this condensation only arises as a consequence of the symmetric configuration of both the loop geometry and heating profile (e.g. Mikić et al., 2013). The subsequent condensations are more realistic, since the symmetry has already been broken by the first draining phase.

5.1.2 Model 2: Steady Perturbed Symmetric Heating

To remove the degenerate condensation, we now perturb the spatial symmetry of the heating profile by enhancing the Gaussian peak at the left-hand leg of the loop by 0.4%. We call this perturbed symmetric heating profile Model 2. The evolution of the loops computed with (LareJ) and without the jump condition (Lare1D), in response to the Model 2 heating profile with steady energy release, are contrasted in Figures 5.4 & 5.5. The major differences in the behaviour of the two simulations are striking. The loop computed without the jump condition shows no significant change from the Model 1 simulation, eventually settling to a static equilibrium. In comparison, the loop computed with the jump condition undergoes TNE with complete condensations as before but note that the weak asymmetry in the heating profile is now sufficient to reduce the lifetime of the previously degenerate condensation so that it falls much sooner, having accumulated less mass.

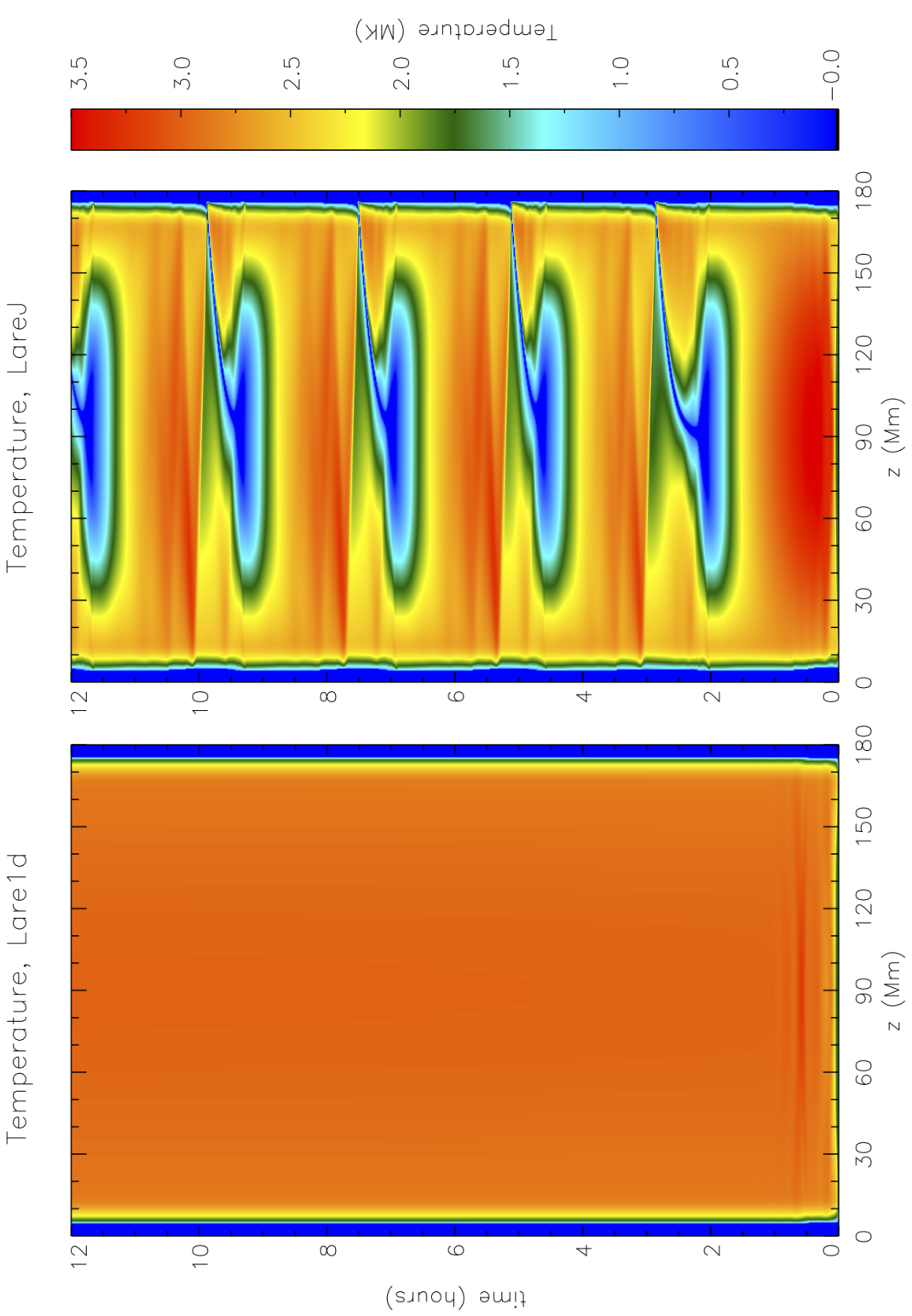

Figure 5.4: The effect of obtaining the correct evaporative response on TNE limit cycles. Results for Model 2 (steady perturbed symmetric footpoint heating). Notation is the same as Figure 5.4.

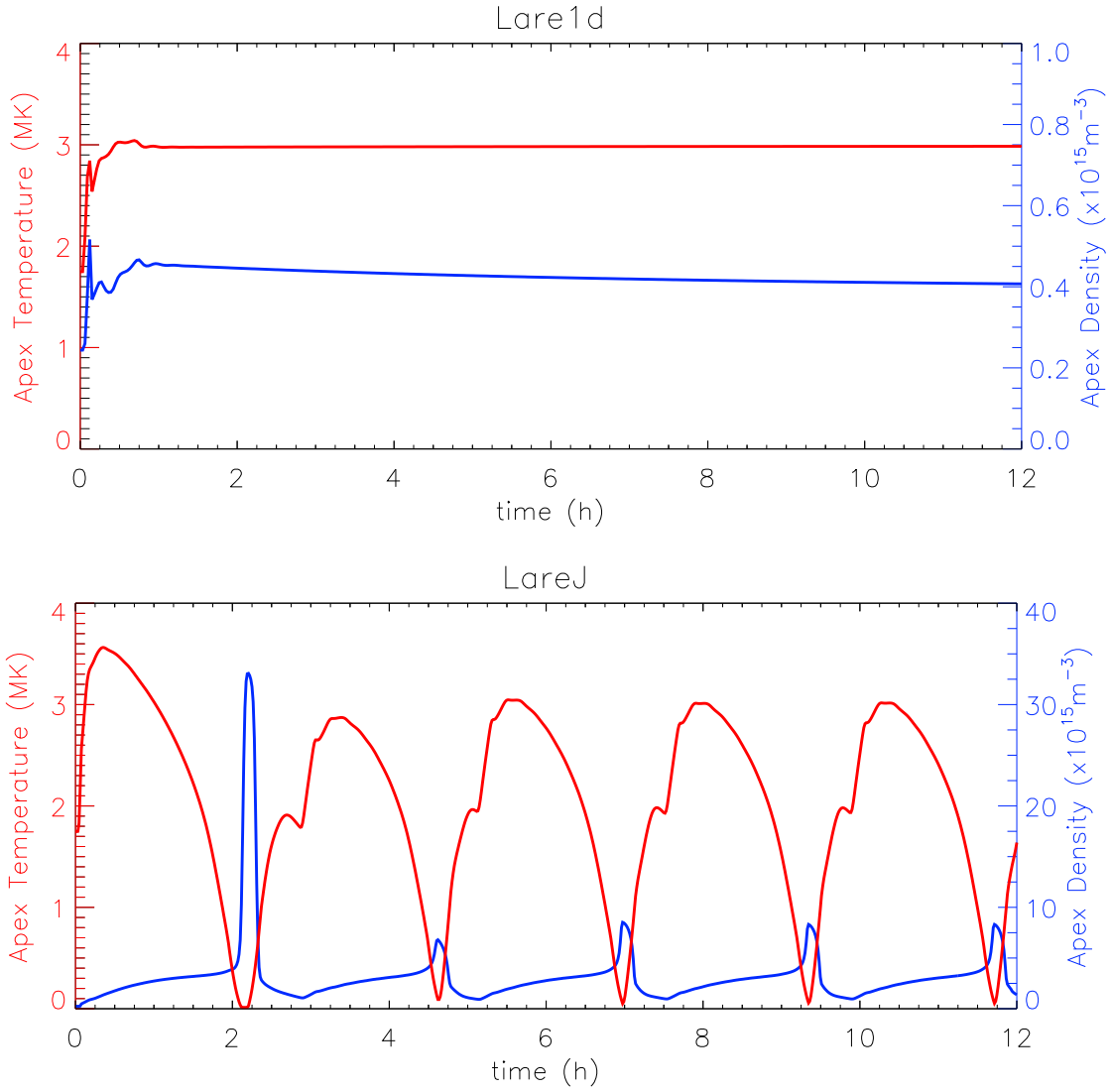

Figure 5.5: Results for Model 2 (steady perturbed symmetric footpoint heating). Notation is the same as Figure 5.3 but note the different density scales on the RHS.

We now turn our attention to understanding why the loops computed with and without the jump condition employed show such significant inconsistencies in their temporal evolution. As an example of the differences in the plasma evolution, we start by considering the first limit cycle of the LareJ loop. For the first 30 minutes, the temperature and density in the corona both increase. As the plasma is heated, the increased coronal temperature gives rise to an excess downward heat flux that the TR is unable to radiate (Klimchuk et al., 2008; Cargill et al., 2012a). This drives the evaporation of material upwards from the chromosphere into the corona, increasing the coronal density via an upward enthalpy flux. The temperature then falls quite rapidly from 3.6MK to 10^4K

between 30 and approximately 120 minutes, during which time the coronal density continues to increase but with reduced upflows. The rapid cooling is driven locally by the thermal instability and leads to the formation of the complete condensation at the loop apex. Crucial here in order to trigger the thermal instability, is the fact that the loop computed with the jump condition employed obtains the 'correct' evaporative response to the heat input (despite under-resolving the TR). The condensation has a peak density of around $32 \times 10^{15}\mathrm{m}^{-3}$ at 135 minutes but then quickly falls down the right-hand leg of the loop. After 135 minutes, the coronal density decreases due to the draining of the 'condensed' plasma downwards and back into the chromosphere. After this stage, the coronal plasma is reheated and coronal temperatures re-reached. Note that the coronal temperature oscillates, as it is reheated, due to shock waves that are generated when the mass associated with the condensation falls. The TNE limit cycle then repeats with a period of 2.25 hours with a more regular evolution that has a reduced peak apex density at the time of the temperature minimum.

Contrary to this, the behaviour of Lare1D loop shares more characteristics with the simulations seen previously in Chapters 3–4, that have an under-resolved TR and are run without the jump condition employed, rather than with the equivalent LareJ loop discussed above. Initially, the temperature in the corona increases but the evaporative response is significantly underestimated. Rather than passing through the TR continuously in a series of steps, the heat flux jumps across the TR. The incoming energy is then strongly radiated (BC13), leaving little excess energy to drive the upflow. Therefore, the lack of spatial resolution leads to a coronal density that is artificially low for the prescribed heating profile when the jump condition is not employed. This ensures that the loop remains thermally stable because the lower density is insufficient to trigger the runaway cooling and TNE. The outcome is that after a transient phase of around 2 hours and a longer weak draining phase, the loop settles to a static equilibrium with an apex temperature and density of 3MK and $0.4 \times 10^{15}\mathrm{m}^{-3}$ respectively.

In summary, the evolution of the loop computed with the jump condition is characterised by TNE limit cycles that have a period of 2.25 hours. Each cycle has three main phases: (i) coronal heating sets up chromospheric evaporation increasing the coronal density, (ii) the increased radiative losses induce a runaway thermal instability that results in the formation of a condensation, and (iii) asymmetries and the effect of gravity cause the condensation to drain from the loop apex. Without the jump condition employed the loop instead settles to a steady state solution.

Figures 5.4 & 5.5 thus show that the existence of TNE limit cycles in coronal loop models is strongly dependent on obtaining the 'correct' plasma response to the energy deposition at the footpoints of the loop. If the TR is under-resolved then the evaporative response can be underestimated (BC13), and this results in steady state solutions because the lower density is insufficient to trigger the thermal instability. This emphasises the

result presented by BC13, namely the importance of TR resolution and obtaining the correct evaporative response because the observational signatures of a loop experiencing TNE with complete condensation cycles are completely different to a loop in static equilibrium. The implication for 1D hydrodynamic and multi-dimensional MHD simulations, where the numerical resolution used under-resolves the TR, is that they can place constrains on the heating mechanism that are too severe for inducing TNE (i.e. inflate Q_H to get TNE comparable with observations). Indeed, TNE may actually be much more prevalent in these simulations that model the coronal response to heating than first thought. Furthermore, this combination of factors serves to highlight (i) the usefulness of the UTR jump condition approach and (ii) the importance of applying this method to model the coronal response when the number of grid points used in a simulation (so that it runs in a realistic time) is inadequate to fully resolve the TR.

5.1.3 Model 2 with Impulsive Heating

In order to study the case of evaporation and condensation cycles in response to impulsive footpoint heating, we consider one final adjustment to the heating function. Specifically, the temporal profile of the heating is now modified by assuming a time dependent heating cycle that is comprised of a heating period and waiting time with no additional heating. The heating period lasts for a duration time of t_d, throughout which the maximum footpoint heating rate (Q_{H_0}) is constant while during the waiting time (t_w), only the small background heating term remains. Hence, the period of the heating cycle is then given by the sum of the heating duration and waiting times.

The spatial profile used for the heating is consistent with Model 2 (weak asymmetric footpoint heating) and so we refer to this heating function as Model 2 with impulsive heating. However, to ensure that the total energy released, when averaged over the period of a heating cycle, is equivalent to the steady footpoint heating simulations, the peak heating rate (Q_{H_0}) imposed is increased by multiplying by an appropriate amplification factor. We note that this amplification factor is given by the ratio of the heating cycle period to the heating duration time. The impulsive temporal heating cases considered are described in Tables 5.1 & 5.2 for loops computed with (LareJ) and without the jump condition (Lare1D), respectively. These cases cover impulsive heating cycles with periods that range over several orders of magnitude. Waiting times shorter and longer than the characteristic cooling time of the loop are both considered together with amplification factors that correspond to equal weighting between the heating duration and waiting time, and waiting times that last significantly longer than the heating period.

Figures 5.6 – 5.9 show the coronal responses of loops computed with the jump condition (LareJ) to the impulsive temporal heating cases. A summary of the characteristic

behaviour seen in each of the simulations is also provided in Table 5.1, which classifies the observed responses into two main types of behaviour: (i) TNE with complete condensations, and (ii) global cooling and draining. The former is typical in cases where the waiting time is shorter than the loop cooling time while the latter tends to arise in cases where the waiting time is longer than the loop cooling time.

To illustrate the plasma evolution in the case of global cooling and draining, we now focus on a discussion of the results obtained in Case 6 of the impulsive temporal heating simulations. For this case the heating cycle consists of a 4000s heating period which is then followed by a 4000s waiting time. Figure 5.10 shows time ordered snapshots of the temperature, pressure, density and velocity at times throughout the fourth heating cycle, which starts at $t = 6.7$ hours. The temperature and density both increase approximately uniformly in the corona during the heating period and hence, the coronal pressure does too. After 1200s, the temperature peaks, at which time evaporative upflows continue to increase the coronal density and pressure ($t = 7$ hours). These upflows gradually decrease and turn to downflows following the peak density at $t = 7.8$ hours, coinciding with the end of the heating period. The loop then cools by radiation and drains by a downward enthalpy flux to the TR during the waiting period. Global downflows dominate the evolution because the waiting time is longer than the loop cooling time and so the temperature and density fall as the entire loop cools and drains. Note that the temperature drops below the equilibrium profile towards the end of the heating cycle but is then reheated at the start of the next cycle. This heating and upflow followed by cooling and downflow cycle has four defining properties: (i) the temperature and density remain largely in phase, (ii) the pressure principally evolves isobarically in space (iii) the velocity retains a globally uniform flow pattern during both the evaporation and draining phases, and (iv) the period of the cycle is controlled by the period of the heating cycle. Cases that exhibit these characteristic properties are identified as being of the global cooling and draining type, which is named after the behaviour observed in the downflow part of the cycle.

We compare these properties of the loop evolution with those observed in the case of TNE with complete condensations. To facilitate this comparison, Case 1 is considered to be representative of simulations whose characteristic behaviour experiences TNE. The heating cycle period for this particular case is 250s with equal weighting given between the heating period and waiting time, each lasting 125s. Figure 5.11 uses a series of snapshots to show the time evolution of the temperature, pressure, density and velocity profiles during the third TNE limit cycle that is seen in this impulsive temporal heating simulation (starting roughly at $t = 5.25$ hours). The coronal temperature and density increase, with both quantities showing spatial peaks towards the base of the corona, where the heating is localised. This gives rise to a variation in the pressure across the corona which at $t = 6$ hours is around a factor of 2. Evaporative upflows from the chromosphere that are driven by the heating continue to supply the corona with mass but flows driven by gradients in

Table 5.1: A summary of the parameter space used and results from the impulsive temporal heating cases computed with the jump condition employed (LareJ).

Case	t_d (s)	t_w (s)	Q_{H_0} factor	Behaviour	TNE Limit Cycle Period (hrs)	Heating Cycle Period (s)
1	125	125	2	TNE with CC	2.5	250
2	250	250	2	TNE with CC	2.75	500
3	500	500	2	TNE with CC	2.75	1000
4	1000	1000	2	TNE with CC	3.0	2000
5	2000	2000	2	TNE with CC, global cooling & draining	3.5	4000
6	4000	4000	2	Global cooling & draining	-	8000
7	8000	8000	2	Global cooling & draining with CC	-	16000
8	125	375	4	TNE with CC	3.25	500
9	250	750	4	TNE with CC	3.25	1000
10	500	1500	4	TNE with CC, global cooling & draining	3.5	2000
11	1000	3000	4	Global cooling & draining	-	4000
12	2000	6000	4	Global cooling & draining	-	8000
13	125	875	8	TNE with CC	3.75	1000
14	250	1750	8	Global cooling & draining	-	2000
15	500	3500	8	Global cooling & draining	-	4000

Notes. From left to right the columns show the case number, the heating duration and waiting times that comprise a single heating cycle, the amplification factor for the peak heating rate (Q_{H_0}) that is required to ensure the average total energy released is equivalent to the Model 2 steady heating simulation, the characteristic simulation behaviour (CC: complete condensations) and the periods of the TNE limit and heating cycles, respectively.

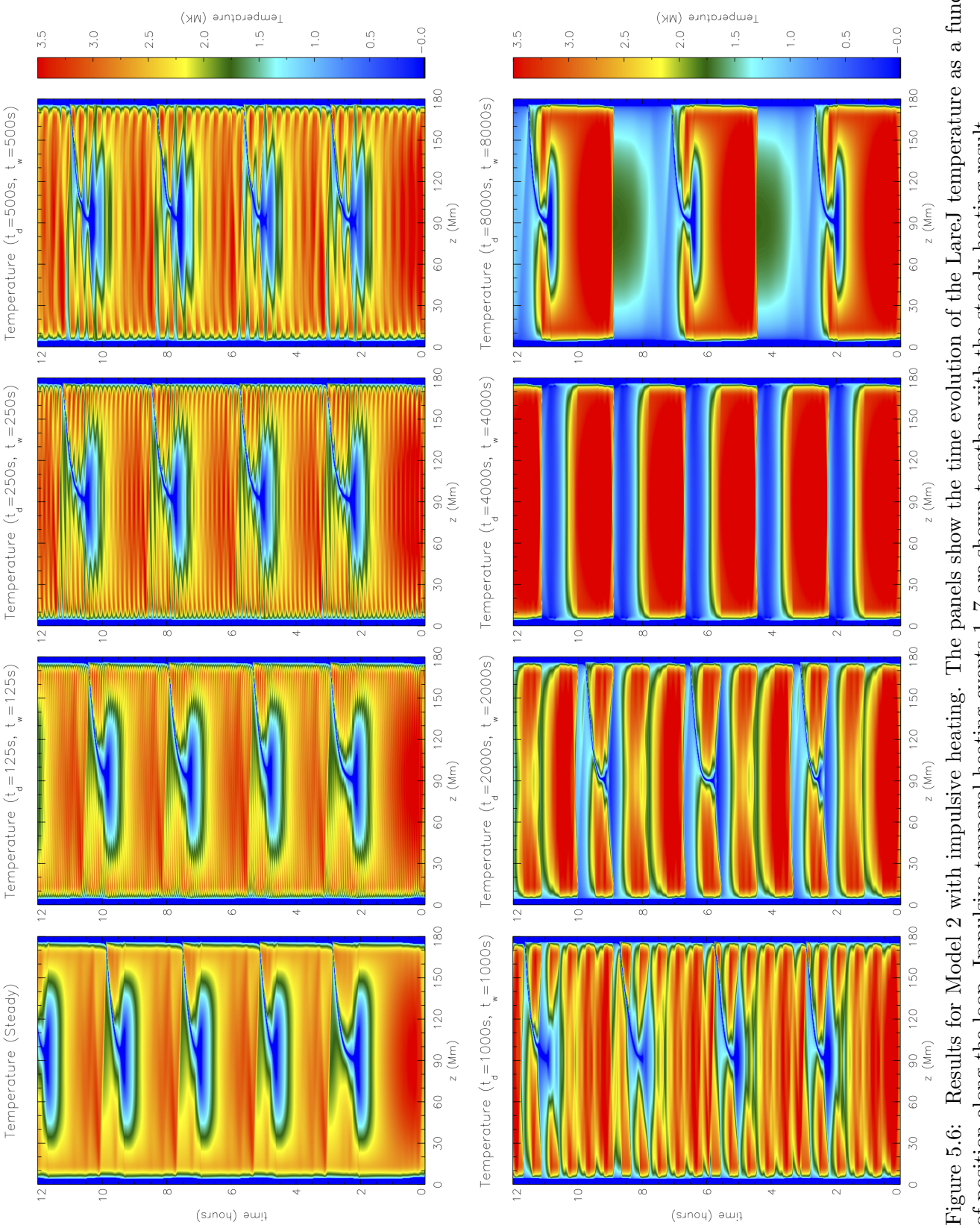

Figure 5.6: Results for Model 2 with impulsive heating. The panels show the time evolution of the LareJ temperature as a function of position along the loop. Impulsive temporal heating events 1–7 are shown together with the steady heating result.

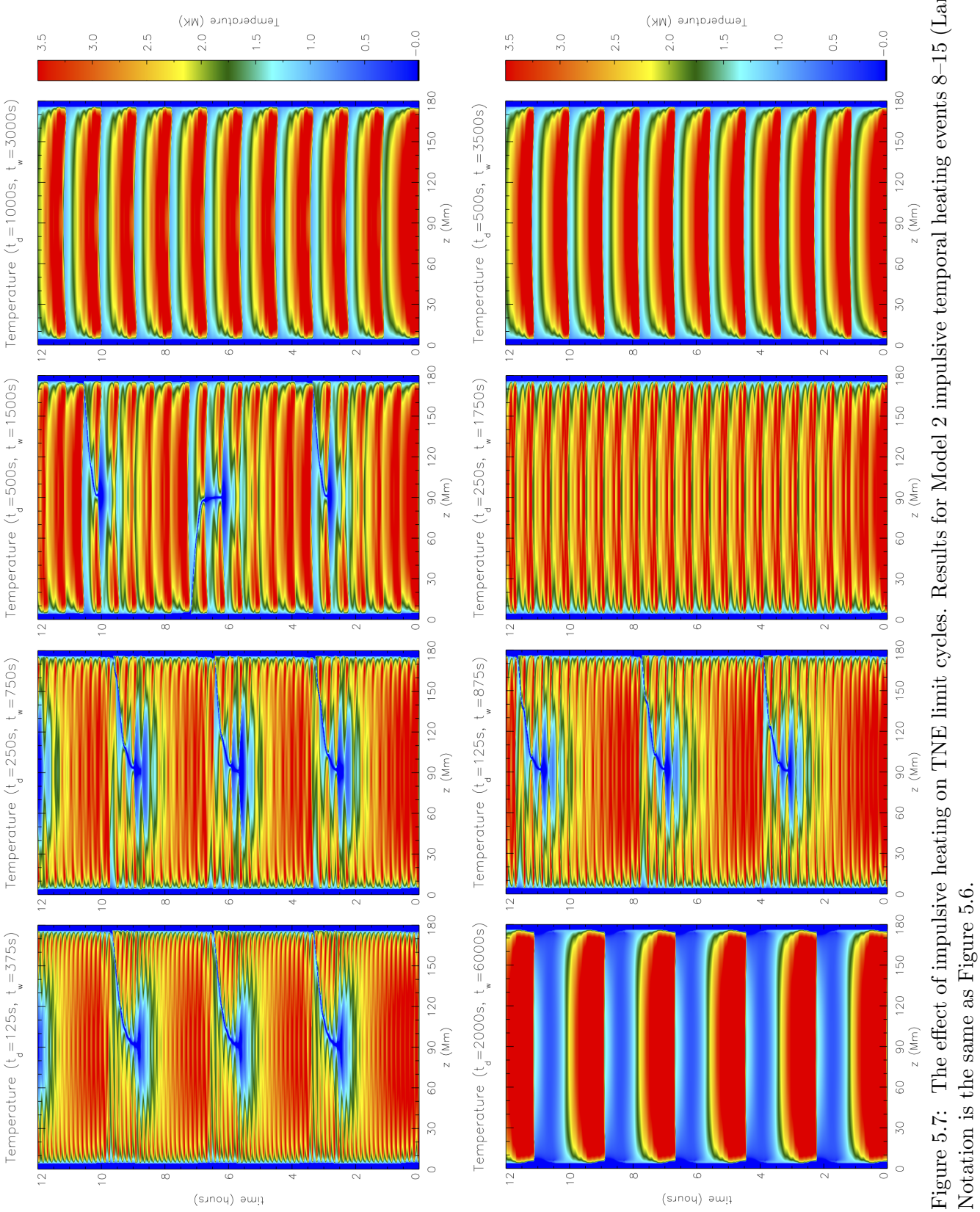

Figure 5.7: The effect of impulsive heating on TNE limit cycles. Results for Model 2 impulsive temporal heating events 8–15 (LareJ). Notation is the same as Figure 5.6.

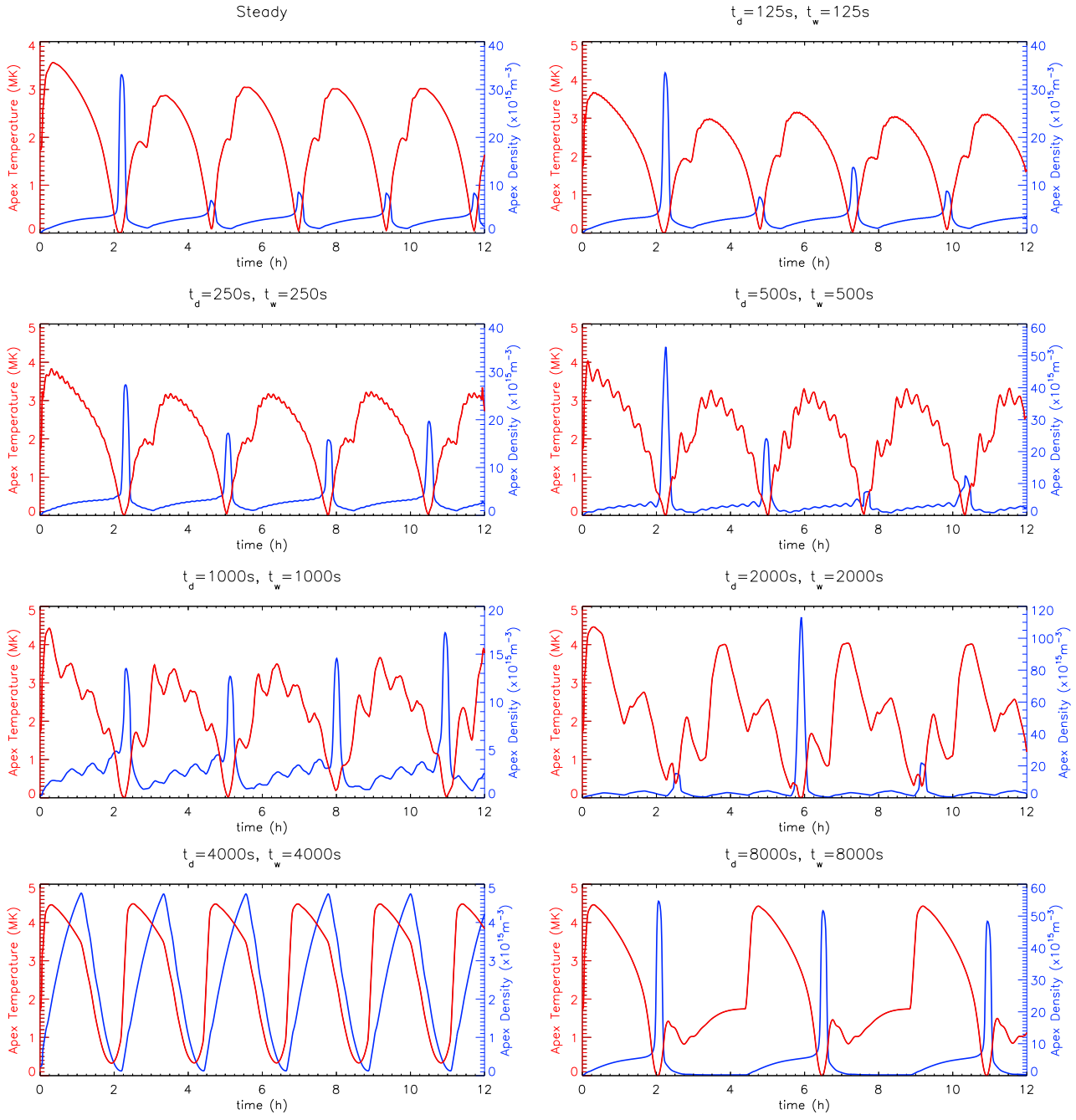

Figure 5.8: Results for Model 2 with impulsive heating. The panels show the time evolution of the LareJ apex temperature (red line, left hand axis) and density (blue line, right hand axis). Impulsive temporal heating Cases 1–7 are shown together with the steady heating result.

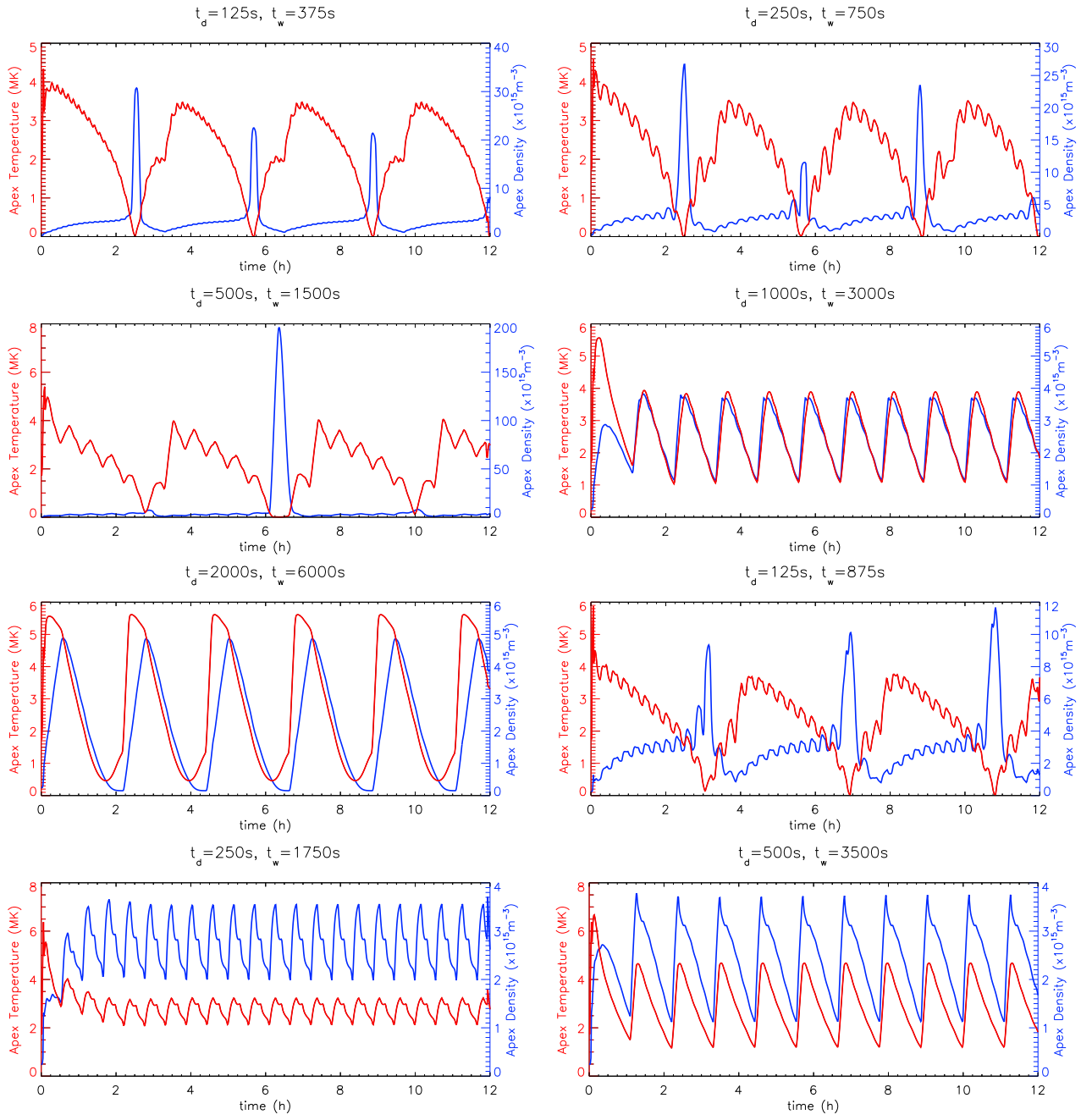

Figure 5.9: Results for Model 2 impulsive temporal heating Cases 8–15 (LareJ). Notation is the same as Figure 5.8.

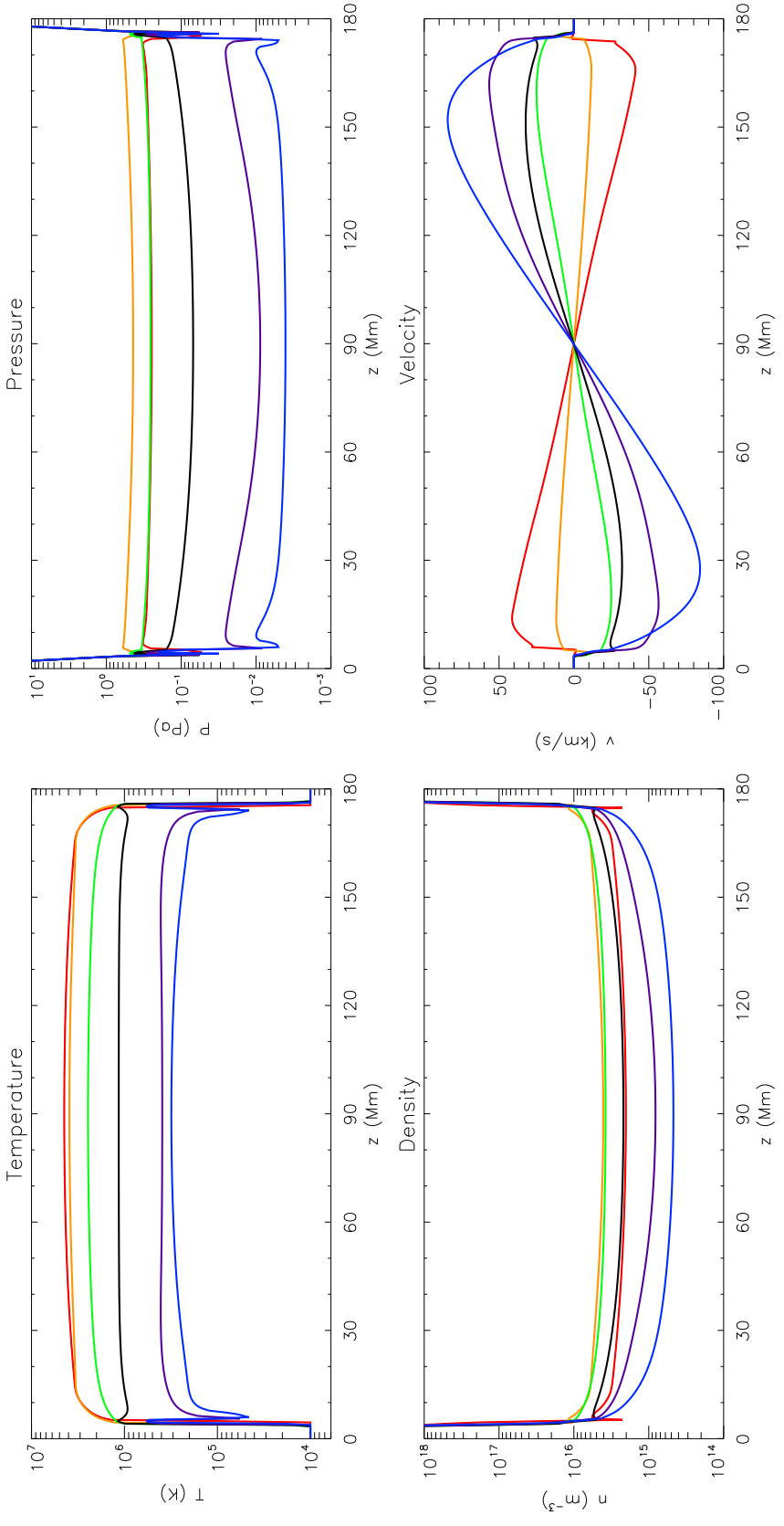

Figure 5.10: Results for impulsive temporal heating Case 6. The panels show the LareJ temperature, pressure, density and velocity as functions of position along the loop for times during the fourth heating cycle. The solid lines represent time ordered snapshots from red ($t = 7$ hrs) through to orange ($t = 7.5$ hrs), green ($t = 8$ hrs), black ($t = 8.25$ hrs), purple ($t = 8.5$ hrs), and blue ($t = 8.6$ hrs).

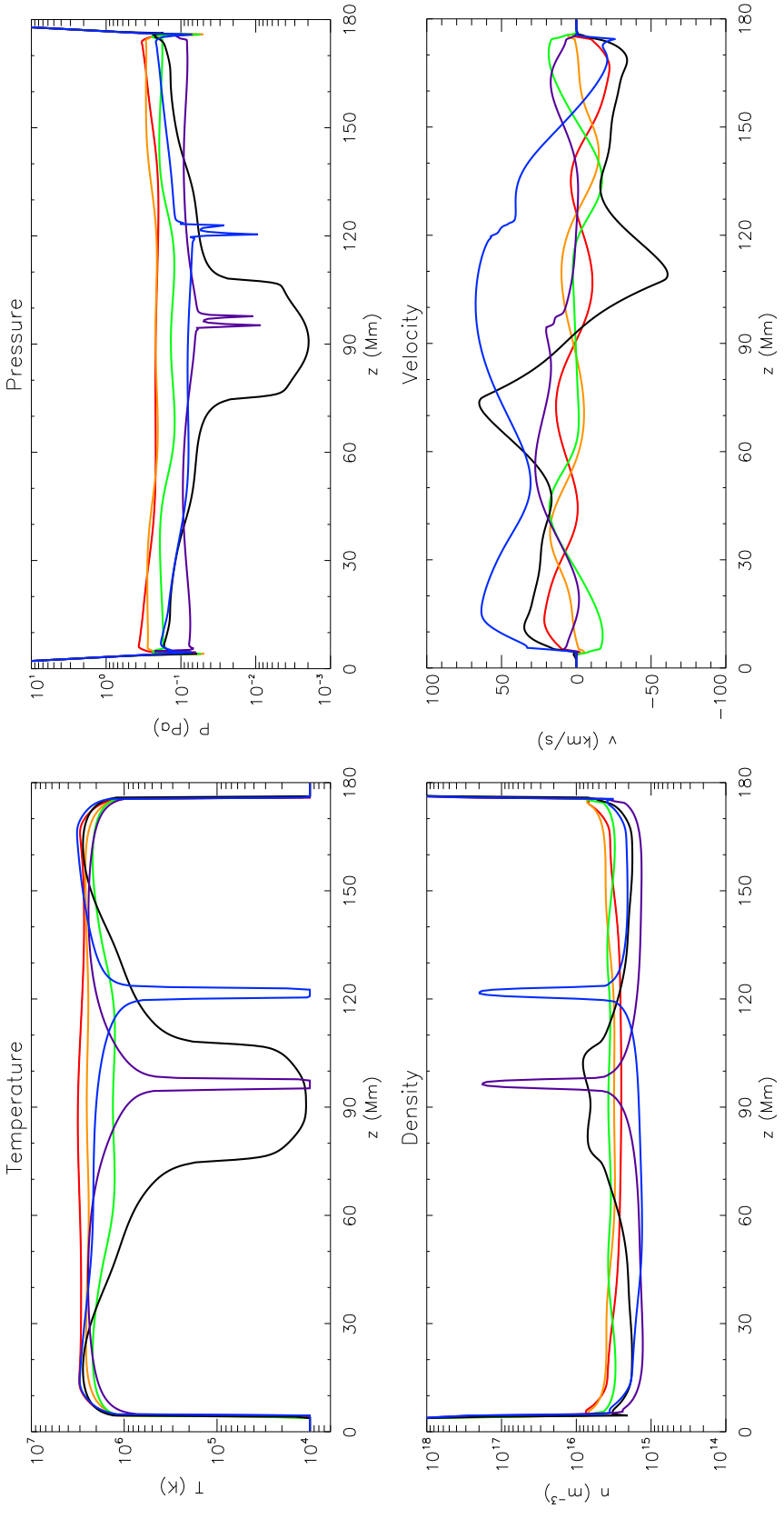

Figure 5.11: Results for impulsive temporal heating Case 1. The panels show the LareJ temperature, pressure, density and velocity as functions of position along the loop for times during the third TNE limit cycle. The solid lines represent time ordered snapshots from red ($t = 6$ hrs) through to orange ($t = 6.5$ hrs), green ($t = 7$ hrs), black ($t = 7.25$ hrs), purple ($t = 7.5$ hrs), and blue ($t = 7.75$ hrs).

the coronal pressure now also become important. These flows start to redistribute the coronal mass, concentrating it mainly around the loop apex. Eventually the mass accumulated by this redistribution becomes sufficient to trigger the thermal instability. The subsequent runaway cooling of the temperature profile to values below 10^5K is isochoric (at constant density) and so sets up pressure gradients in the corona that become stronger as the plasma cools. The flows generated by these gradients serve to supply the condensation with further mass from the corona (e.g. see snapshot at $t = 7.25$ hours) up until the time when the condensation starts to fall down the loop leg and the density drains. However, note that the cooling and draining observed, when the loop undergoes TNE, is localised only to the condensation because the waiting time between heating periods is shorter than the loop cooling time. Following the end of this localised draining, the cyclic evolution then repeats with a period of 2.5 hours. Therefore, in contrast to global cooling and draining, the cases described as TNE with complete condensations share the following fundamental properties: (i) the temperature and density become out of phase with the peak density occurring at the time of the temperature minimum, (ii) the evolution of the coronal pressure is strongly spatially dependent, (iii) the flow pattern of the velocity is highly non-uniform in response to coronal pressure gradients, and (iv) the oscillation associated with the period of the heating cycle is present but the period of the limit cycle is governed by the evaporation time required to trigger thermal runaway.

However, within this general classification, there are some subtleties when we switch between the two types of characteristic behaviour. This transition takes place when the waiting time between heating periods becomes comparable to the loop cooling time. For example, Cases 5 & 10 are characterised by properties that incorporate both types of behaviour. These cases have waiting times of 2000s and 1500s, respectively. On one hand, their responses have localised cooling and draining associated with a TNE limit cycle period, while on the other hand, the entire loop also cools and drains with a period matching that of the heating cycle. Thus, we have classified these transition cases as a combination of TNE with complete condensations and global cooling and draining.

Case 7 is particularly interesting even though it is not positioned next to the transition cases in the parameter space. The heating cycle in this case is comprised of a heating period and waiting time that each last 8000s. We note that the heating is sustained for a long enough period to facilitate the development of complete condensations at the loop apex. Hence, there is localised cooling and draining comparable to the TNE cases described above. However, the waiting time is significantly longer than the loop cooling time and so the loop also undergoes global cooling and draining. Furthermore, the period of the observed evaporation and condensation cycles coincide with the period of the heating cycle. Therefore, this case does not strictly satisfy our criteria for TNE and so instead is classified as global draining and cooling with complete condensations.

Table 5.2: A summary of the parameter space used and results from the impulsive temporal heating cases computed without the jump condition employed (Lare1D).

Case	t_d (s)	t_w (s)	Q_{H_0} factor	Behaviour	Heating Cycle Period (s)
1	125	125	2	Oscillates about static equilibrium	250
2	250	250	2	Oscillates about static equilibrium	500
3	500	500	2	Oscillates about static equilibrium	1000
4	1000	1000	2	Global cooling & draining	2000
5	2000	2000	2	Global cooling & draining	4000
6	4000	4000	2	Global cooling & draining	8000
7	8000	8000	2	Global cooling & draining	16000
8	125	375	4	Oscillates about static equilibrium	500
9	250	750	4	Oscillates about static equilibrium	1000
10	500	1500	4	Global cooling & draining	2000
11	1000	3000	4	Global cooling & draining	4000
12	2000	6000	4	Global cooling & draining	8000
13	125	875	8	Oscillates about static equilibrium	1000
14	250	1750	8	Global cooling & draining	2000
15	500	3500	8	Global cooling & draining	4000

Notes. From left to right the columns show the case number, the heating duration and waiting times that comprise a single heating cycle, the amplification factor for the peak heating rate (Q_{H_0}) that is required to ensure the average total energy released is equivalent to the Model 2 steady heating simulation, the characteristic simulation behaviour and the period of the heating cycle

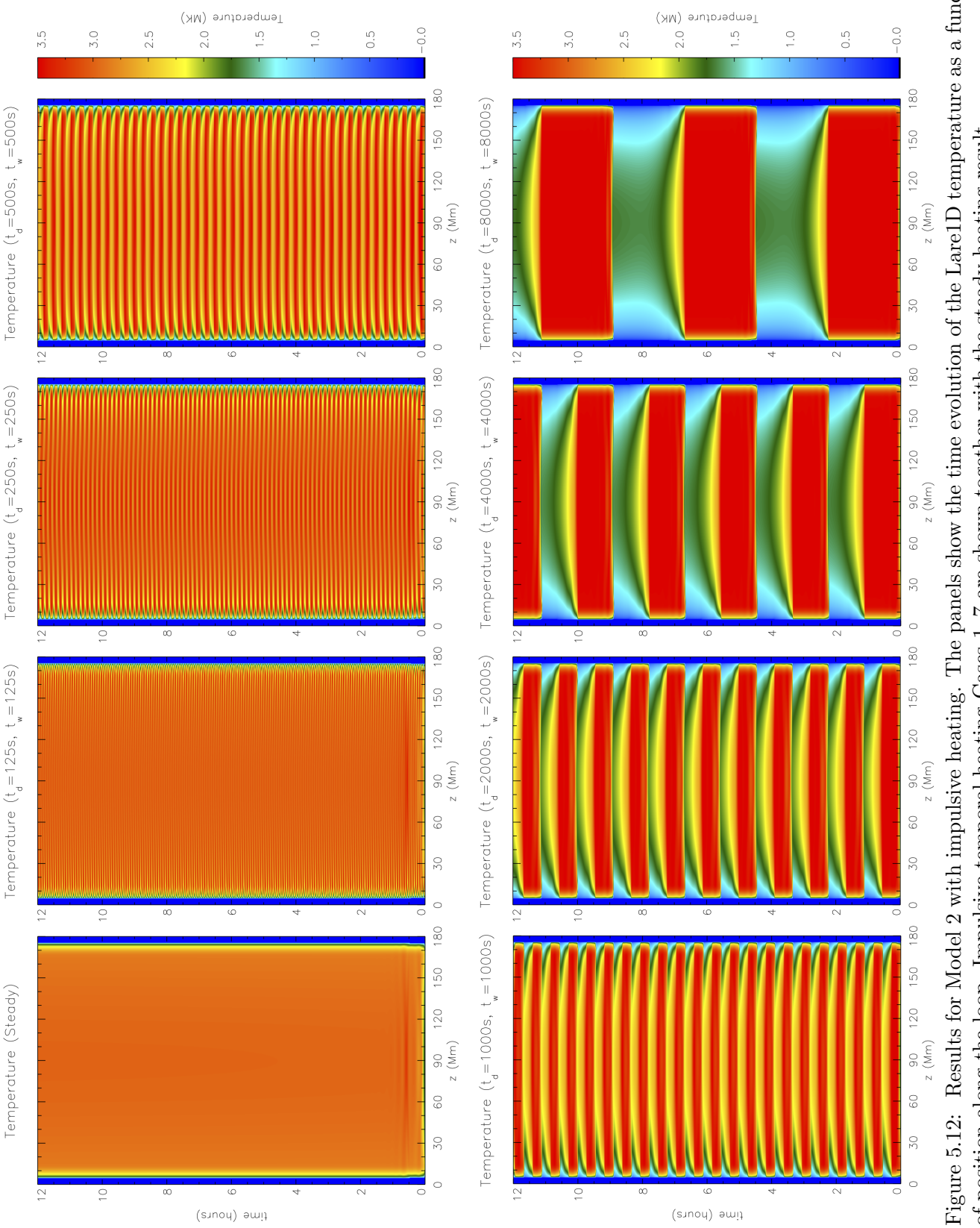

Figure 5.12: Results for Model 2 with impulsive heating. The panels show the time evolution of the Lare1D temperature as a function of position along the loop. Impulsive temporal heating Cases 1–7 are shown together with the steady heating result.

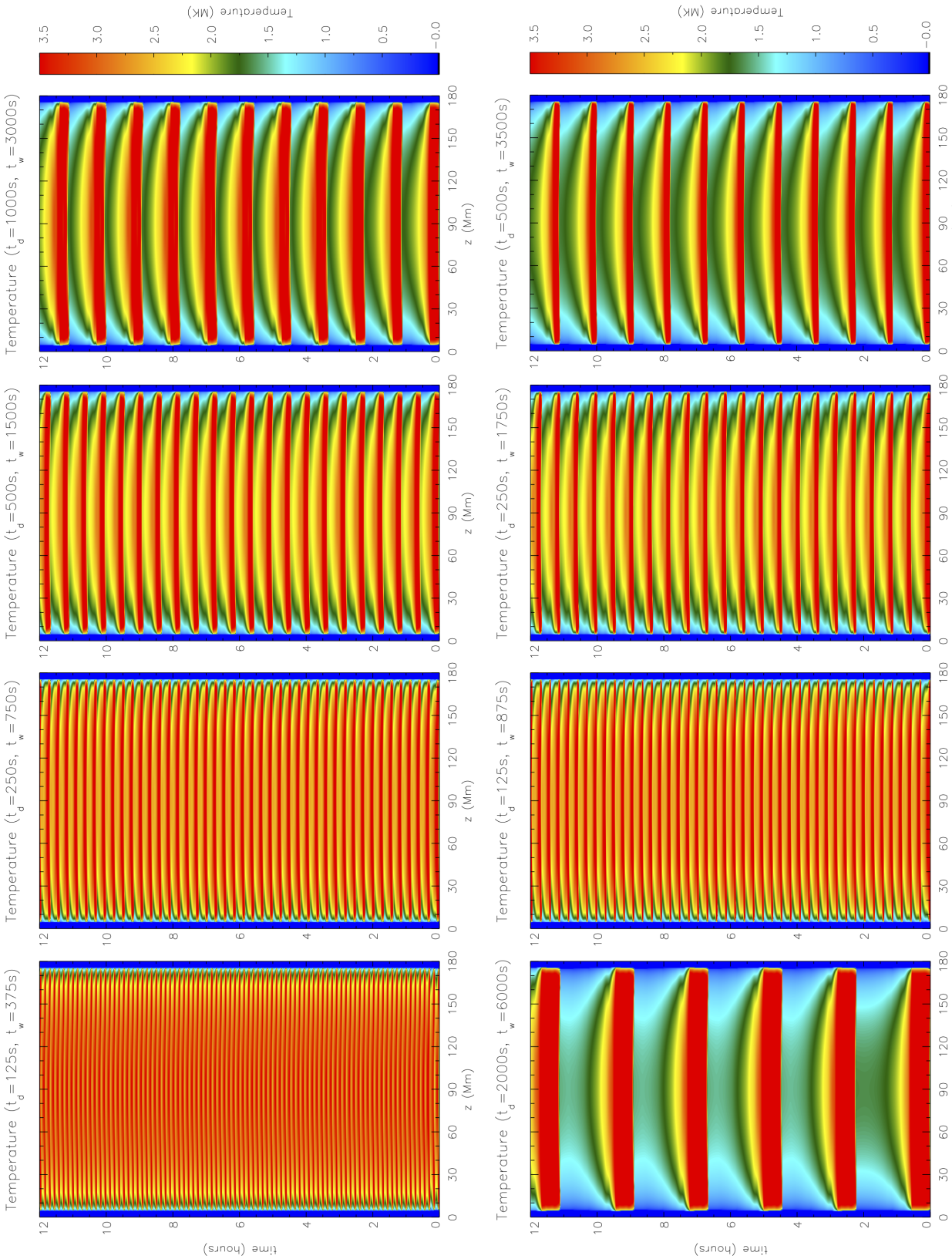

Figure 5.13: Results for Model 2 impulsive temporal heating Cases 8–15 (Lare1D). Notation is the same as Figure 5.12.

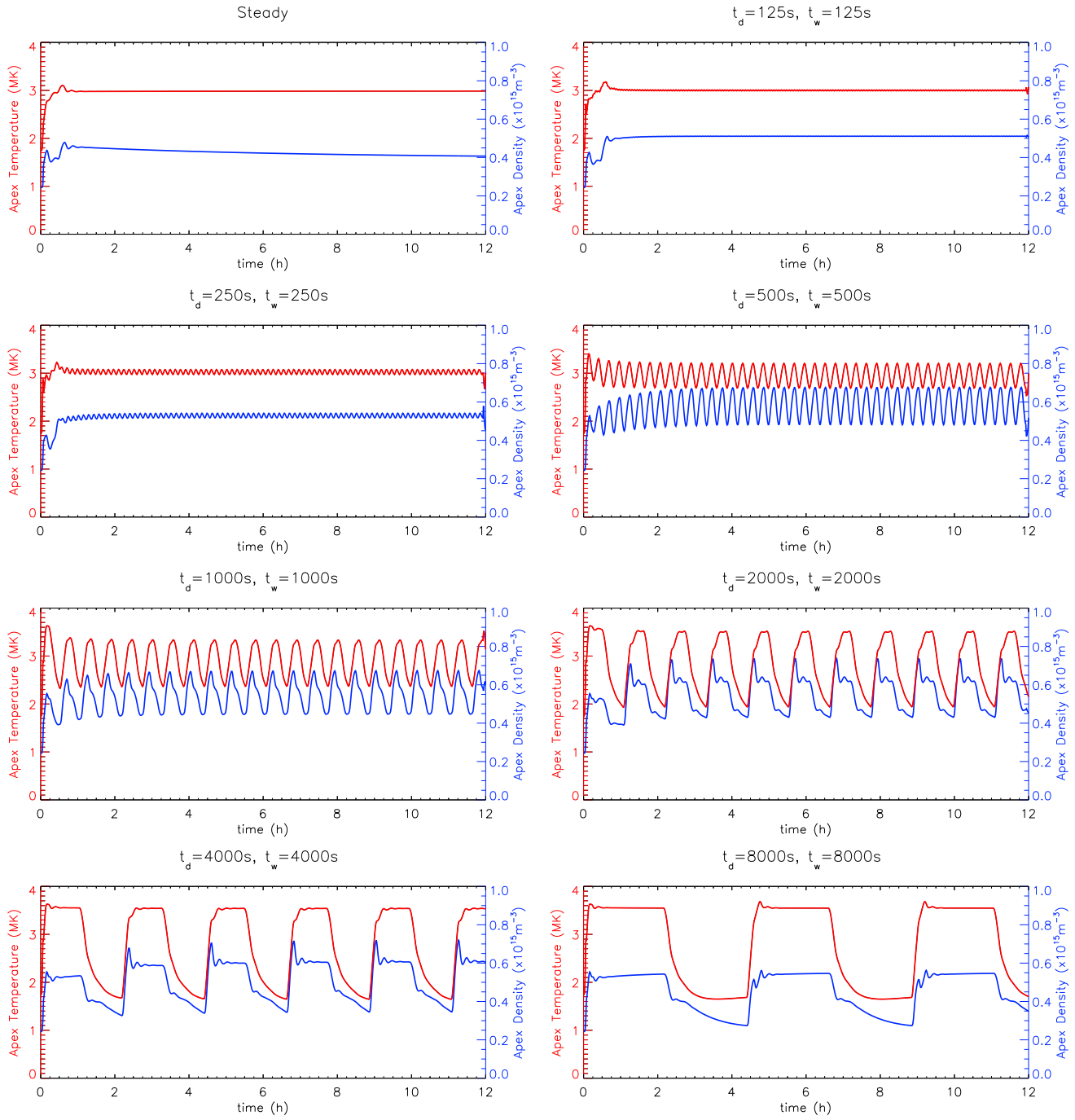

Figure 5.14: Results for Model 2 with impulsive heating. The panels show the time evolution of the Lare1D apex temperature (red line, left hand axis) and density (blue line, right hand axis). Impulsive temporal heating Cases 1–7 are shown together with the steady heating result.

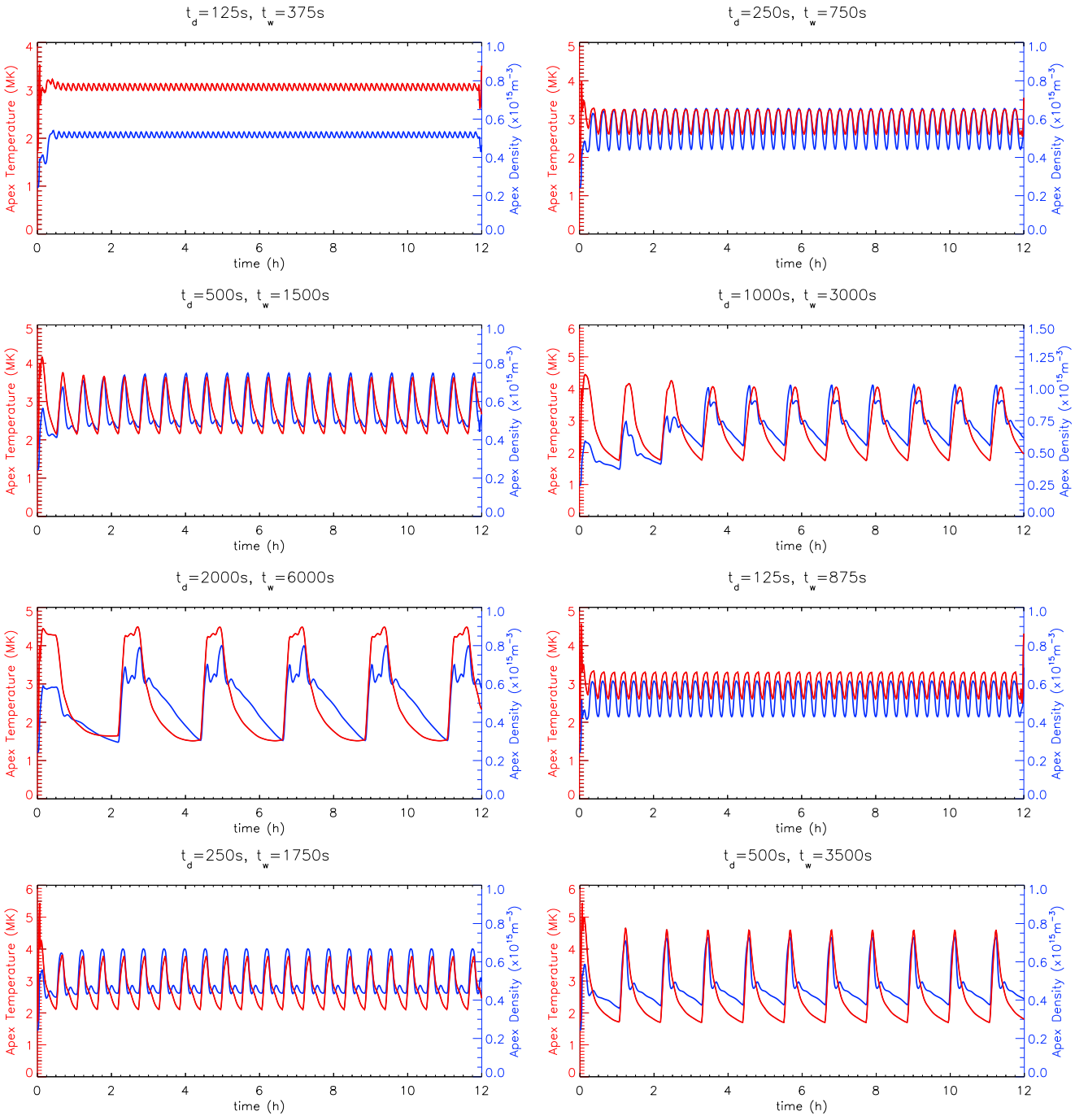

Figure 5.15: Results for Model 2 impulsive temporal heating Cases 8–15 (Lare1D). Notation is the same as Figure 5.14.

The evolution of the loops computed without the jump condition (Lare1D), in response to the impulsive temporal heating cases, are shown in Figures 5.12 – 5.15. There is one dominant trend: the temperature and density remain predominantly in phase. Therefore, there is no TNE seen in any of the cases considered. Instead, two different types of characteristic behaviour are observed in this series of simulations. The first type of behaviour is an oscillation about a static equilibrium with a period matching that of the heating cycle. This is typical in cases where the waiting time is shorter than the loop cooling time. The second type of behaviour is largely consistent with that described above as global cooling and draining. This tends to arise when the waiting time is longer than the loop cooling time. However, since this behaviour is also controlled by the period of the heating cycle we define any cases where the apex temperature drops below 2.5MK as global cooling and draining in order to distinguish between the two response types.

We have provided a summary of the simulation behaviour seen in each of the cases in Table 5.2. There are some weak correlations between (i) Lare1D cases that oscillate about a static equilibrium and LareJ cases that undergo TNE with complete condensations, and (ii) Lare1D and LareJ cases that experience global cooling and draining. The first of these relationships further demonstrates that the influence of under-resolving the TR is to suppress TNE (there is no physical stabilising mechanism but the coronal conditions in the simulations prevent TNE from developing) while the second implies that there are some cases where loops computed without the jump condition are able to correctly predict the characteristic behaviour of the simulation. However, even in these cases (e.g. Case 6), the range of the temperature and density response obtained is significantly limited because the evaporative upflows are underestimated when the TR is under-resolved.

5.2 The Effect of the Background Heating on Thermal Non-Equilibrium Limit Cycles

Next we investigate the effect of the background heating on TNE limit cycles in coronal loop models using the UTR jump condition method, through a series of footpoint heating simulations with different spatially uniform background heating models. The background heating (Q_{bg}) values cover several orders of magnitude, ranging from no background heating to an enhanced Q_{bg} that is significantly larger than the value determined when solving for the hydrostatic equilibrium. Consistent with Section 5.1, we model a coronal loop of total length 180Mm and use a numerical resolution of 500 uniformly spaced grid points. Impulsive and steady footpoint heating are both considered, each with a different spatial profile for the energy release.

Figure 5.16 shows the evolution of the temperature, as a function of time and position

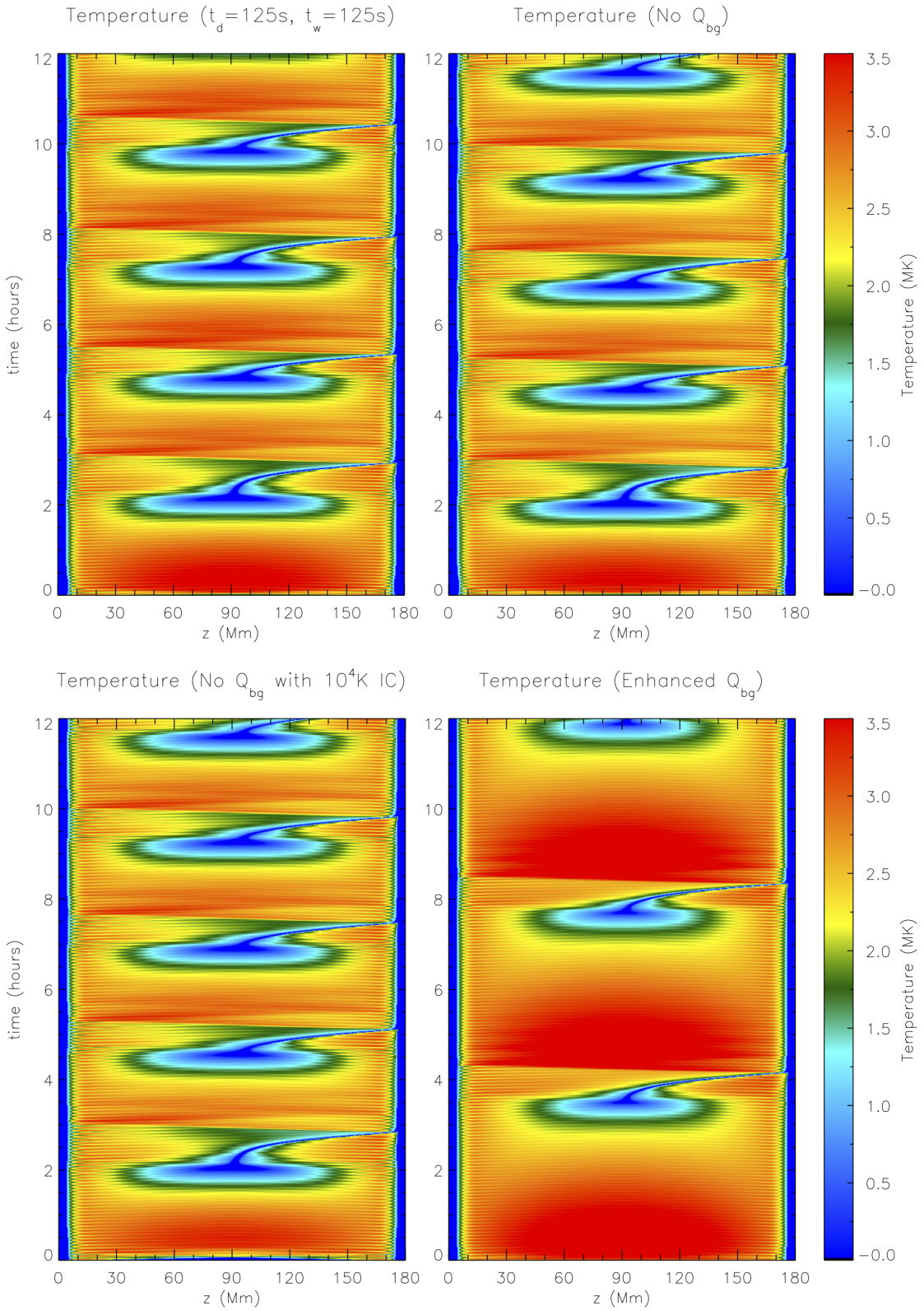

Figure 5.16: The effect of the background heating on TNE limit cycles. Results for Model 2 with impulsive heating. The panels show the time evolution of the LareJ temperature as a function of position along the loop obtained in simulations that are variations on the impulsive temporal heating Case 1 with different background heating models.

along the loop, in response to impulsive footpoint heating for loops computed with a range of background heating values. The heating models presented in the four panels are all variations on the impulsive temporal heating Case 1 that was described above in Section 5.1.3 and so their spatial profile is the sum of two Gaussian peaks with a weak asymmetry (Model 2). Simulations with no background heating, no background heating and an isothermal 10^4K temperature initial condition and an enhanced background heating are shown together with the impulsive temporal heating Case 1 result. For the enhanced background heating model we take $Q_{bg} = 6 \times 10^{-5}\text{Jm}^{-3}\text{s}^{-1}$. This was previously used as the background heating value in the Model 1 heating profile that was considered by Mikić et al. (2013). We also note that $Q_{bg} = 6.8682 \times 10^{-6}\text{Jm}^{-3}\text{s}^{-1}$ is the background heating term used in the impulsive temporal heating Case 1. This corresponds to the minimum value required to achieve thermal balance in the hydrostatic initial condition and will be referred to as the minimised background heating value.

All four simulations experience TNE with complete condensations but the periods of the limit cycle evolution are significantly different between those with different background heating models. On one hand, the impulsive temporal heating Case 1 has a limit cycle period of 2.5 hours, while on the other hand the 4.25 hour period observed in the enhanced background heating simulation is substantially longer. The temperature response of the simulations with no background heating and no background heating but starting with an isothermal 10^4K temperature initial condition are similar, and both have a limit cycle period of 2.25 hours. However, this period remains distinguishable from that seen when the minimised background heating value is employed. The influence of a small background heating value in preference to no background heating results in a limit cycle period that is 15 minutes longer for this particular simulation.

For the case of steady symmetric footpoint heating we consider a spatial profile that is based on the one used in Mikić et al. (2013), which we refer to as Model 3. For this model the heating profile is of the form,

$$Q(z) = Q_{bg} + Q_{H_0}\left(e^{-g(z)/\lambda} + e^{-g(2L-z)/\lambda}\right), \tag{5.1}$$

where $g(z) = \max(z - \Delta, 0)$. We select $\Delta = 7.5$Mm which makes the heating uniform in the chromosphere and lower TR of the loop. The heating profile then decreases exponentially towards the loop apex as shown in the upper panel of Figure 5.17. We take $Q_{H_0} = 45 \times 10^{-5}\text{Jm}^{-3}\text{s}^{-1}$ and $\lambda = 15$Mm and compare the results obtained with two different values of Q_{bg}. The background heating models considered are a subset of those employed for the impulsive heating study in Figure 5.16. Specifically, the simulations considered here use only the enhanced background heating value ($Q_{bg} = 6 \times 10^{-5}\text{Jm}^{-3}\text{s}^{-1}$) and the minimised background heating value ($Q_{bg} = 6.8682 \times 10^{-6}\text{Jm}^{-3}\text{s}^{-1}$) that is almost an order of magnitude smaller than the enhanced value. Both heating profiles are shown

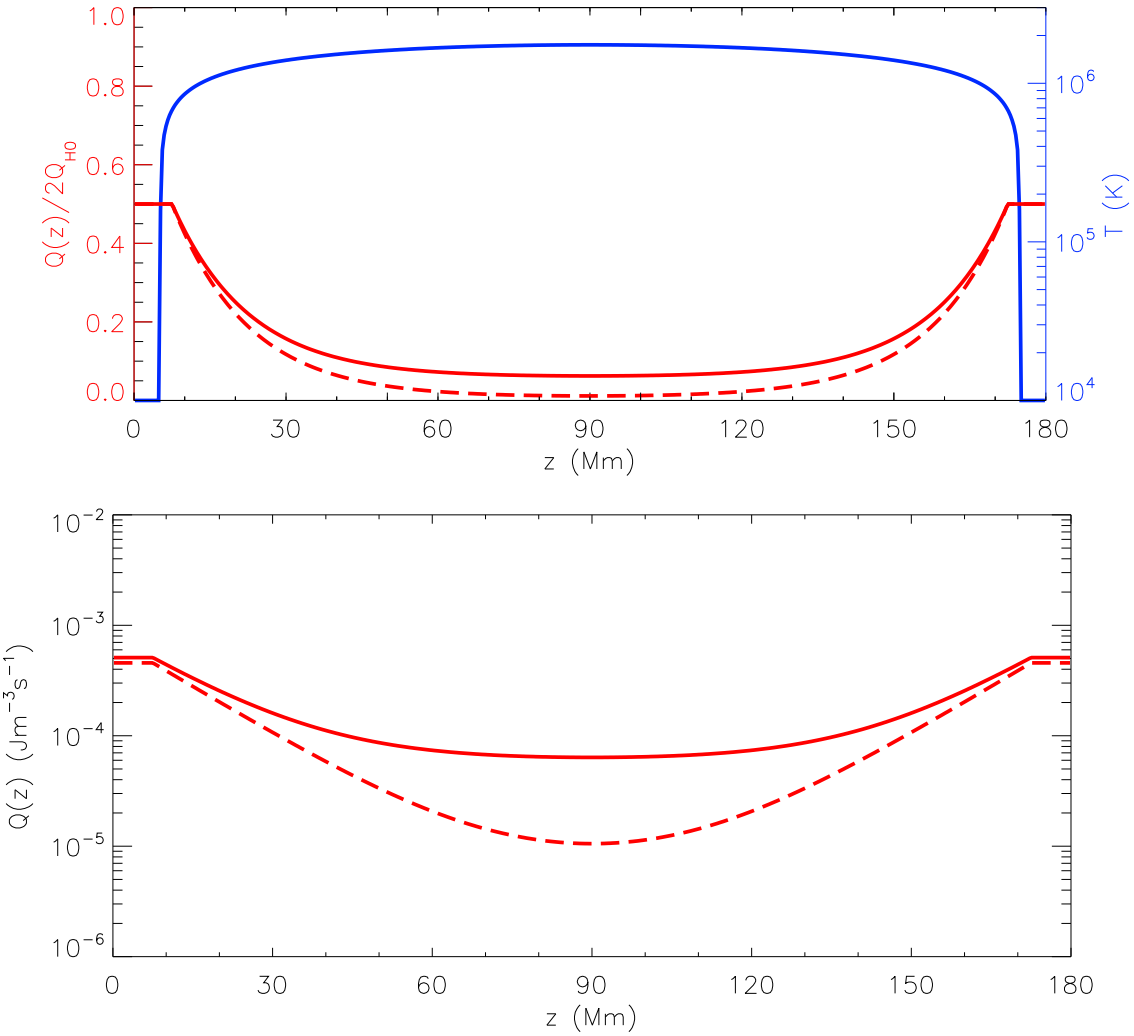

Figure 5.17: Model 3 footpoint heating profile. The panels show $Q(z)/Q_{H_0}$ (red line, left hand axis) imposed on top of the temperature initial condition (blue line, right-hand axis) and the heating function $Q(z) = Q_{bg} + Q_H(z)$. We take $Q_1 = 45 \times 10^{-5}\mathrm{Jm}^{-3}\mathrm{s}^{-1}$ and the solid red line represents the enhanced background heating profile ($Q_{bg} = 6 \times 10^{-5}\mathrm{Jm}^{-3}\mathrm{s}^{-1}$) while the dashed red lines correspond to the heating profile with $Q_{bg} = 6.8682 \times 10^{-6}\mathrm{Jm}^{-3}\mathrm{s}^{-1}$.

together in the lower panel of Figure 5.17.

We contrast the evolution of the loops computed with the enhanced and minimised background heating models in Figures 5.18 & 5.19. The configuration of these two simulations are identical, the only difference is the Q_{bg} value used. However, the adjustment of this parameter results in temporal responses that are fundamentally different. In the loop computed with the lower background heating value, the coronal response triggers the

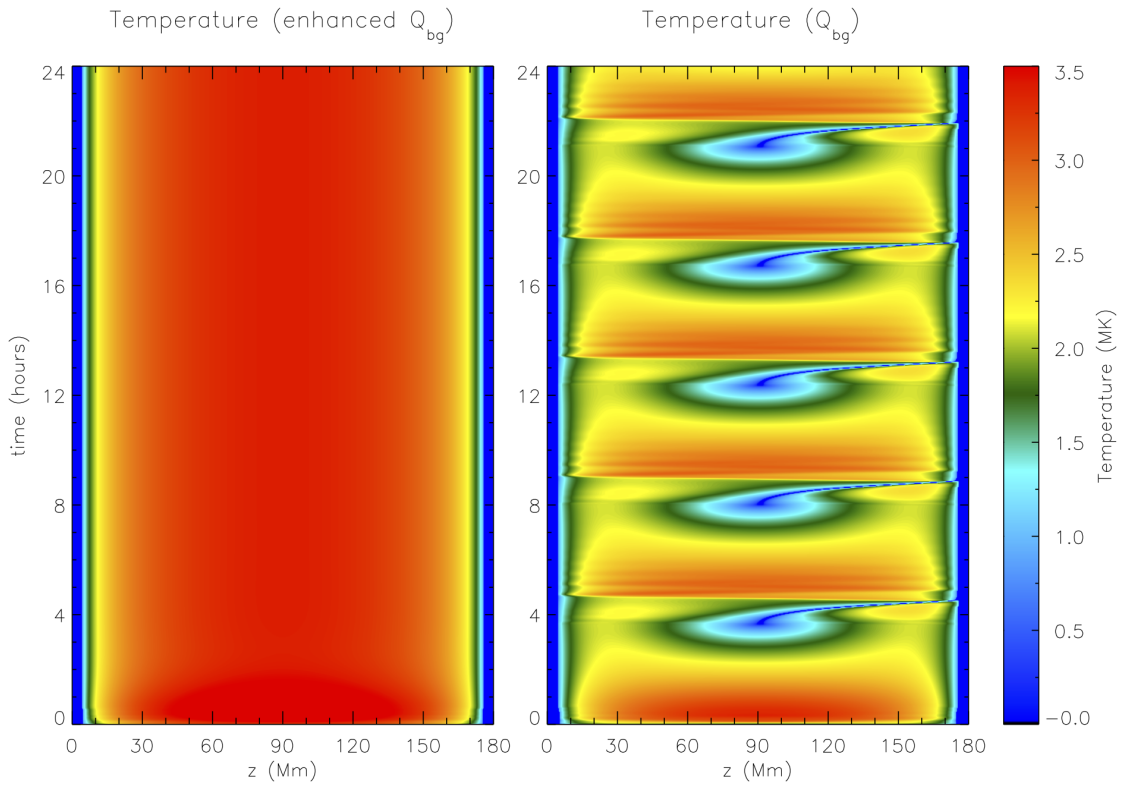

Figure 5.18: The effect on TNE cycles of adjusting the background heating value. Results for Model 3. The panels show the time evolution of the LareJ temperature as a function of position along the loop obtained by using different background heating models. The enhanced Q_{bg} simulation (LHS) is shown together with the minimised Q_{bg} result (RHS).

the thermal instability. This loop undergoes TNE with a limit cycle period of 4.5 hours. On the other hand, with the enhanced background heating value the loop is stable to the thermal instability and instead settles to a static equilibrium.

In summary, through the impulsive and steady footpoint heating cases, we have demonstrated that the use of a background heating term can either (i) significantly change the period of the TNE cycles observed in coronal loop models or (ii) act to suppress the thermal instability and the existence of such limit cycles. The justification for these effects is as follows. If the background heating value is increased, then in order for radiative cooling to dominate the heating and trigger the onset of TNE, the evaporative response must also be increased. However, an increased coronal density would largely be controlled by the footpoint heating rate. Therefore, triggering the thermal instability when an increased background heating value is used requires either (i) an extended time or (ii) an increase in the magnitude of the maximum footpoint heating rate (Q_{H_0}) in order to accumulate a sufficient amount of mass. The influence of the latter is observed as the suppression of TNE limit cycles when the footpoint heating rate is not increased relative to background

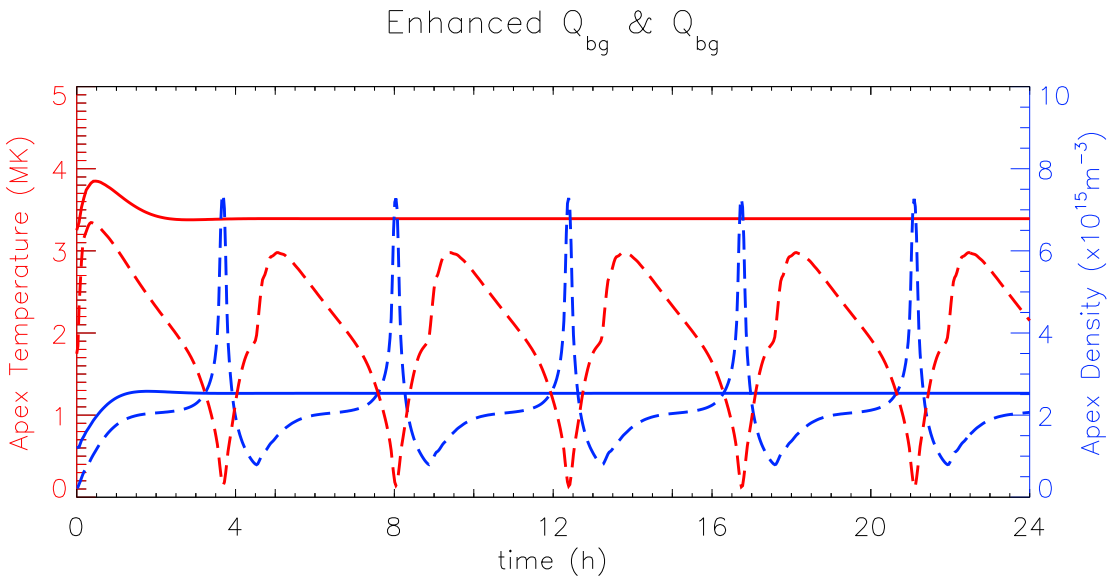

Figure 5.19: Results for Model 3. The panel shows the time evolution of the LareJ apex temperature (red line, left hand axis) and density (blue line, right hand axis) obtained by using different background heating values. The solid lines represent quantities from the enhanced Q_{bg} simulation and the dashed lines correspond to the minimised Q_{bg} result.

heating rate while the effect of the former is seen as an increase in the limit cycle period. We can thus conclude that the ratio of the the maximum footpoint heating rate to the background heating value (Q_{H_0}/Q_{bg}) plays a key role in the onset criteria for TNE.

5.3 The Effect of Adjusting the Heating Parameters on Thermal Non-Equilibrium Limit Cycles

In this section, we use the jump condition method to analyse the effect of adjusting the footpoint heating parameters on the periods of the TNE limit cycles that are obtained in coronal loop models. Two footpoint heating simulations, with different heating parameters, are studied. The first is the impulsive temporal heating Case 1 that was described above in Section 5.1.3. The heating model in this simulation is comprised of a heating pulse that lasts 125s, followed by a waiting time of 125s. This heating cycle then repeats and the average total energy released is equivalent to the Model 2 steady heating profile that was considered previously in Section 5.1.2. The second simulation studied is a variation on this Model 2 steady heating profile, where the maximum footpoint heating rate (Q_{H_0}) has been decreased so that the total energy released is reduced by a factor of one third.

The coronal response of these two simulations are compared in Figures 5.20 & 5.21.

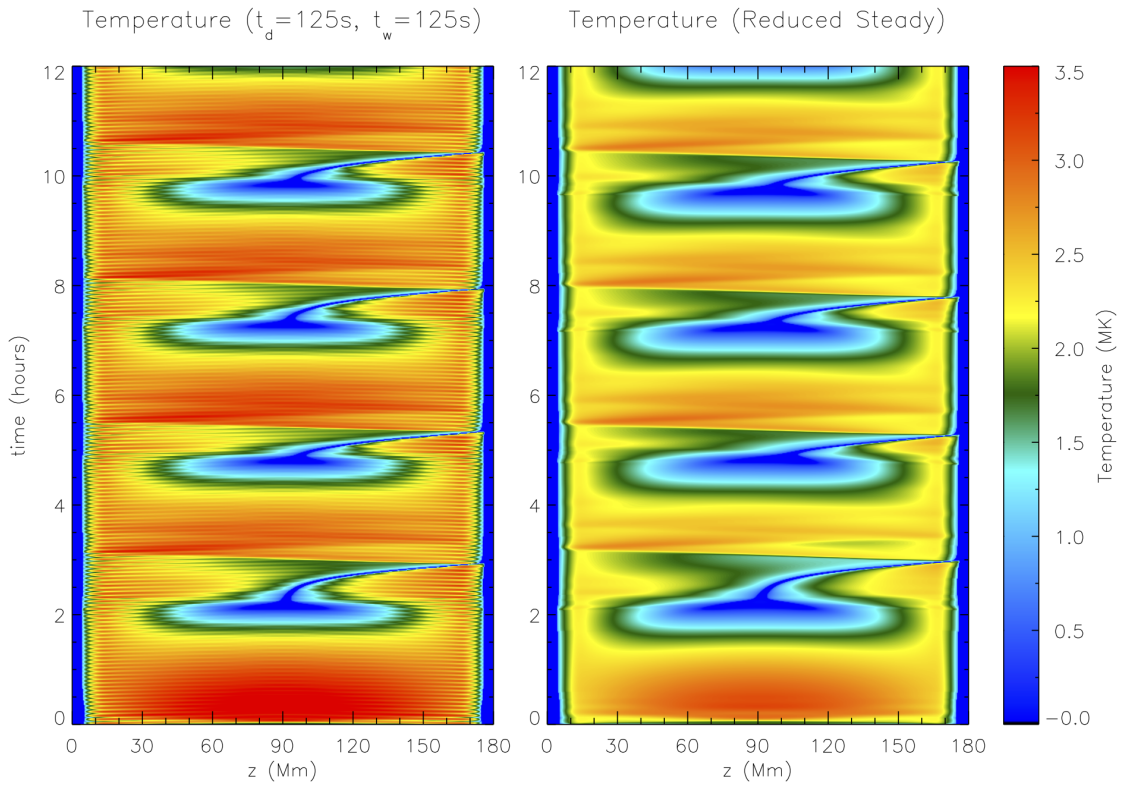

Figure 5.20: The effect on TNE cycles of adjusting the heating parameters. Results for Model 2. The panels show the time evolution of the LareJ temperature as a function of position along the loop. Impulsive temporal heating Case 1 (LHS) is shown together with the reduced steady heating result (RHS).

The latter allows a comparison between the apex temperatures and densities as a function of time while the former provides both spatial and temporal information to correlate. Starting with Figure 5.20, it is clear that the behaviour seen in the two simulations is quite similar. Both undergo TNE with complete condensations and their temperature ranges are comparable, though high frequency temperature oscillations are observed only in the impulsive temporal heating simulation. However, it is also interesting to note that the periods of the TNE limit cycles obtained in both simulations are remarkably similar. Indeed, Figure 5.21 confirms that (i) both simulations have a limit cycle period of 2.5 hours and (ii) the characteristics of their temperature and density responses are also comparable. This similarity in properties is particularly striking, given that the heating parameters used in both simulations are quite different. For example, the total energy released in the reduced steady heating simulation is on average one third less than that released in the impulsively heated simulation.

Figures 5.20 & 5.21 thus show that it is possible to obtain similar TNE limit cycles in response to heating functions that are considerably different. We have demonstrated

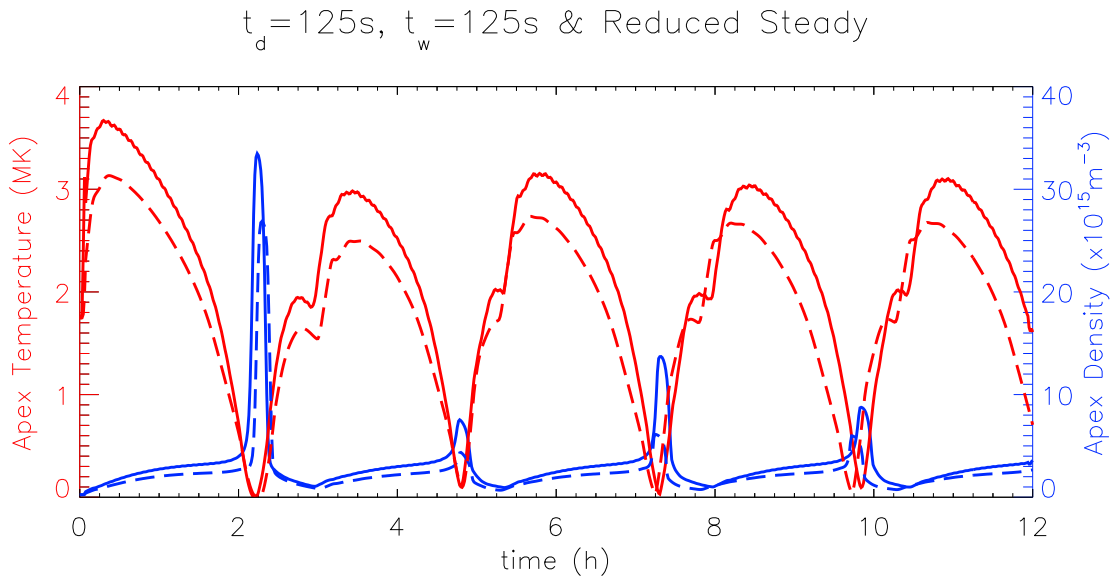

Figure 5.21: Results for Model 2. The panel shows the time evolution of the LareJ apex temperature (red line, left hand axis) and density (blue line, right hand axis) obtained by using different heating parameters. The solid lines represent quantities from the impulsive temporal heating Case 1 and the dashed lines correspond to the reduced steady heating result.

that by adjusting the heating parameters simulations with impulsive and steady footpoint heating can give rise to limit cycles with the same period.

5.4 Chapter Discussion & Conclusions

BC13 established that the main consequence of under-resolving the TR is that the resulting evaporative response is underestimated. They concluded that an under-resolved loop typically has a peak density of at least a factor of two lower than the resolved loop value when subjected to the same heating. However, their study, as in Chapter 3, considered only the case of spatially uniform impulsive heating, with singular heating pulses that lasted between 60–600s. Such impulsive heating events tend to give rise to responses where the entire loop cools and drains, following the time of the peak density. Therefore, there is no TNE seen in any of these cases that we considered in the previous chapters.

In contrast, the experiments presented in this chapter were selected to correspond to highly stratified, steady footpoint heating. What we have shown is that underestimating the evaporative response in numerical simulations with this form of steady and stratified energy deposition, results in steady state solutions because the artificially low coronal densities prevent TNE from developing. There is no physical stabilising mechanism but

this behaviour arises purely as a consequence of underestimating the evaporative upflows (when the heat flux jumps across the unresolved part of the TR) that transport mass from the chromosphere, upwards into the corona. Hence, preventing the onset of TNE is a secondary effect of inadequate spatial resolution in coronal loop models with steady footpoint heating.

We introduced the jump condition approach to deal with this difficulty of obtaining the correct plasma response (to coronal heating) when the TR is under-resolved in Chapters 3–4. In all of the cases considered here, when under-resolved loops were computed without the jump condition they either (i) settled to a static equilibrium or (ii) underwent global cooling and draining, with a diminished T and n response range. TNE was not observed in any of these cases. However, when comparing with the equivalent benchmark simulations (loops computed with the jump condition) there are striking differences seen in the behaviour obtained. The responses of the loops computed with the jump condition exhibited two main types of behaviour: (i) TNE with complete condensations and a cyclic evolution, and (ii) global cooling and draining but with a significantly broader T and n response range than those loops computed without the jump condition (e.g. the peak density is always more than a factor of two larger). Therefore, when subjected to steady footpoint heating, the observational signatures of (under-resolved) loops computed with and without the jump condition are entirely different and so the consequences of under-resolving the TR are more severe, when compared with singular impulsive heating events (e.g. BC13). Thus, the work presented here has further underlined the importance of using the jump condition approach to model the response of the TR to changing coronal conditions, when the numerical resolution used in a simulation is unable to fully resolve the TR.

Making use of the jump condition approach, we have demonstrated that the use of a background heating term can also significantly influence both the existence and period of TNE limit cycles observed in coronal loop models. We concluded that the onset criteria for TNE must depend on the ratio of the maximum footpoint heating rate to the background heating value (Q_{H_0}/Q_{bg}).

We have also shown that the mapping between the period of the obtained TNE limit cycles and the imposed heating function is not necessarily one-to-one. For example, we have demonstrated that, by adjusting the heating parameters, it is possible to obtain similar TNE limit cycles in response to heating functions that are considerably different. Furthermore, in this study, we have considered only loops with the simplest possible configuration that have the minimum number of free parameters (symmetric loops with symmetric heating profiles). Other factors such as the loop geometry, area expansion and stochastic heating (e.g. Mikić et al., 2013; Froment et al., 2018, Antolin et al., in preparation) also play an important role. However, the inclusion of these effects introduces additional free parameters which expands the scope for producing similar TNE cycles

with conflicting heating functions. Therefore, we conclude that there are likely to be complications when attempting to infer the heating properties of coronal loops based exclusively on evaporation and condensation cycles because the response can be non-unique, which makes this inversion problem ill-posed.

Chapter 6

Multi-dimensional Implementation

Thus far, we have presented a thorough analysis of using the jump condition method to model the TR in 1D hydrodynamic simulations (Johnston et al., 2017a,b) and so we now focus on demonstrating that the method can be generalised to multi-dimensional MHD models. In particular, the experiments considered in this chapter provide an initial proof of principle of a simple extension of the method to 2D.

The chapter has the following layout: we describe the initial set up and equilibrium used in our numerical simulations in Section 6.1. The simple two-dimensional implementation of the jump condition approach is then described in Section 6.2 and benchmarked against the 1D model in Section 6.3, for the case of uniform heating. In Section 6.4, we demonstrate the application of the method in 2D by presenting an example MHD simulation where the energy deposition is localised in the cross-field direction. The chapter is summarised in Section 6.5.

6.1 Initial Set Up & Equilibrium

To demonstrate the application of the jump condition approach in 2D, we consider the simple case where the initial set up consists of a uniform magnetic field that is directed along the x-coordinate axis, with a field strength of 10^{-2}T (100G). Thus, x is the field-aligned direction and y is the cross-field (y) direction. We model a coronal loop of total length 60Mm that starts in static equilibrium. This initial condition is obtained by stacking the 1D hydrostatic temperature and density profiles, that were shown previously in Figure 3.1 and used in Chapters 3–4, uniformly in the cross-field direction (y). To maintain this equilibrium, we note that a small spatially uniform background heating term is

necessary ($Q_{bg} = 2.2167 \times 10^{-5}\mathrm{Jm^{-3}s^{-1}}$) and that gravity acts only in the x direction. The two-dimensional temperature and density initial conditions (constructed from the 1D profiles) are shown in the top left-hand panels of Figures 6.1 & 6.2, with 512 grid points along the length of the loop (i.e. $N_x = 512$).

6.2 Multi-dimensional Jump Condition

The rate of change of total energy equation is given by,

$$\frac{\partial E}{\partial t} = -\nabla \cdot \left(\left(\frac{\gamma}{\gamma - 1} P + \frac{1}{2}\rho v^2 + \rho\Phi \right)\mathbf{v} + \mathbf{F}_c + \frac{\mathbf{E} \times \mathbf{B}}{\mu_0} \right) + Q - n^2\Lambda(T), \tag{6.1}$$

where the total energy is the sum of internal, kinetic, gravitational potential and magnetic energy,

$$E = \frac{P}{\gamma - 1} + \frac{1}{2}\rho v^2 + \rho\Phi + \frac{B^2}{2\mu_0}. \tag{6.2}$$

Here, P is the gas pressure, ρ is the density, $\mathbf{v}$ is the velocity, Φ is the gravitational potential, $\mathbf{F}_c$ is the heat flux vector, $\mathbf{E}$ is the electric field, $\mathbf{B}$ is the magnetic field, Q is the volumetric heating rate, n is the number density and $\Lambda(T)$ is the optically thin radiative loss function.

Integrating Eq. (6.1) over the volume of an UTR (V of length ℓ, width dy and height dz), and using Gauss's divergence theorem we obtain,

$$\begin{aligned} \iiint_V \frac{\partial E}{\partial t}\, dV = &- \oiint_S \left(\left(\frac{\gamma}{\gamma - 1} P + \frac{1}{2}\rho v^2 + \rho\Phi \right)\mathbf{v} + \mathbf{F}_c + \frac{\mathbf{E} \times \mathbf{B}}{\mu_0} \right) \cdot \hat{\mathbf{n}}\, dS \\ &+ \iiint_V Q - n^2\Lambda(T)\, dV. \end{aligned} \tag{6.3}$$

Assuming that the surfaces at the top (S_0) and base (S_b) of the UTR lie in the x = constant plane (coordinate along the magnetic field) and that the net outward flux through the side of the closed surface is zero, it follows that,

$$\begin{aligned} \iiint_V \frac{\partial E}{\partial t}\, dx\, dy\, dz = &- \iint_{S_0} \left(\left(\frac{\gamma}{\gamma - 1} P + \frac{1}{2}\rho v^2 + \rho\Phi \right)\mathbf{v} + \mathbf{F}_c + \frac{\mathbf{E} \times \mathbf{B}}{\mu_0} \right) \cdot \hat{\mathbf{x}}\, dy\, dz \\ &+ \iint_{S_b} \left(\left(\frac{\gamma}{\gamma - 1} P + \frac{1}{2}\rho v^2 + \rho\Phi \right)\mathbf{v} + \mathbf{F}_c + \frac{\mathbf{E} \times \mathbf{B}}{\mu_0} \right) \cdot \hat{\mathbf{x}}\, dy\, dz \\ &+ \iiint_V Q - n^2\Lambda(T)\, dx\, dy\, dz. \end{aligned} \tag{6.4}$$

For the case of a locally uniform B_x magnetic field, the Poynting flux vector vanishes in the ideal MHD limit, which leaves,

$$N = -\iint_{S_0} \frac{\gamma}{\gamma-1} P_0 v_{x_0} + \frac{1}{2}\rho_0 v_{x_0}^3 + \rho_0 \Phi v_{x_0} + F_{c,x_0}\, dy\, dz + \iiint_V Q - n^2\Lambda(T)\, dx\, dy\, dz, \tag{6.5}$$

where N is defined as,

$$N \equiv \iiint_V \frac{\partial E}{\partial t}\, dx\, dy\, dz - \iint_{S_b} \frac{\gamma}{\gamma-1} P_b v_{x_b} + \frac{1}{2}\rho_b v_{x_b}^3 + \rho_b \Phi v_{x_b} + F_{c,x_b}\, dy\, dz. \tag{6.6}$$

We assume that the left-hand side of Eq. (6.5) can be neglected based on the arguments presented in Chapter 3. Under this assumption we obtain a simplified multi-dimensional jump condition,

$$\iint_{S_0} \frac{\gamma}{\gamma-1} P_0 v_{x_0} + \frac{1}{2}\rho_0 v_{x_0}^3 + \rho_0 \Phi v_{x_0}\, dy\, dz = -\iint_{S_0} F_{c,x_0}\, dy\, dz + \iiint_V Q - n^2\Lambda(T)\, dx\, dy\, dz, \tag{6.7}$$

which is valid for a locally uniform magnetic field.

Therefore, provided that $B_x >> B_y$ in the UTR, the multi-dimensional implementation of the jump condition (6.7) reduces to a series of field-aligned integrals in 2D, with the velocity corrections imposed in the direction along the magnetic field (x).

We also note that the thermal conduction model in Lare2D is based on the Braginskii heat flux in the presence of a magnetic field (Braginskii, 1965) and is of the form,

$$\begin{aligned}\rho\frac{\partial \epsilon}{\partial t} &= -\nabla\cdot\left(-\left(\frac{\kappa_0 T^{5/2}}{B^2+b_{\min}^2}\right)(\mathbf{B}\cdot\nabla T)\mathbf{B}\right) - \nabla\cdot\left(-\left(\frac{\kappa_0 T^{5/2}}{B^2+b_{\min}^2}\right) b_{\min}^2 \nabla T\right), \\ &= -\nabla\cdot(\mathbf{F}_c),\end{aligned} \tag{6.8}$$

where the heat flux vector,

$$\mathbf{F}_c = -\frac{\kappa_0 T^{5/2}}{B^2+b_{\min}^2}\left((\mathbf{B}\cdot\nabla T)\mathbf{B} + b_{\min}^2\nabla T\right), \tag{6.9}$$

recovers the Braginskii parallel thermal conductivity in the limit as $b_{\min} \to 0$. However, note that finite $b_{\min}$ is used to make the conductivity isotropic when $\mathbf{B} = \mathbf{0}$. Thus, the heat flux in the x direction is now given by,

$$F_{c,x} = -\frac{\kappa_0 T^{5/2}}{B^2+b_{\min}^2}\left(\left(B_x\frac{\partial T}{\partial x} + B_y\frac{\partial T}{\partial y}\right)B_x + b_{\min}^2\frac{\partial T}{\partial x}\right), \tag{6.10}$$

and the remaining quantities in Eq. (6.7) can be equated with those from the one-dimensional jump condition (3.10).

Furthermore, interpolation methods are now used to resolve the UTR in the calculation of $\mathcal{R}_{utr}$, enabling the direct integration of the radiative losses and efficient parallelisation of the method. In particular, we specify five points across the UTR (x_{b-1}, x_b, x_0, x_{0+1}, x_{0+2} where x_b and x_0 are the base and top of the UTR respectively) through which a cubic spline is fitted in $T^{7/2}$ space. The density profile is determined under the assumption of constant pressure (taken as the pressure at the top of the UTR). $\mathcal{R}_{utr}$ is then calculated by numerically integrating the radiative losses in the UTR, between x_b and x_0, based on the spline approximations for the temperature and density.

6.3 Uniform Heating

We start by considering the case of uniform heating throughout a 2D domain, which has a length of 60Mm along the loop and a width of 0.6Mm across the field. The numerical resolution used in this simulation is 512×32 grid points ($N_x \times N_y$). For this experiment, we repeat the Case 3 uniform heating event that was considered previously in Chapter 3. As described in Table 3.1, this is an impulsive heating event that lasts 60s with a peak heating rate of $Q_{H_0} = 8 \times 10^{-2} \mathrm{J\,m^{-3}\,s^{-1}}$. The spatial profile of the heating is adjusted here to be uniform both along and across the loop while the temporal profile is a triangular pulse.

Figure 6.1 shows the time evolution and spatial variation of the temperature response to the Case 3 uniform heating event, for a loop computed with the jump condition (LareJ). The coronal temperature increases rapidly, peaking after 30s at the time of maximum heating. Hence, it is predominantly the cooling phase that is seen in the time ordered contour plots. On the other hand, the initial downward movement of the TR during the evaporation phase (0–400s) and the subsequent movement back upwards in the atmosphere, during the draining phase (400–2000s), can still be tracked in these temperature plots. We note that the transportation of mass to and from the corona is controlled by the energy balance in the TR. Therefore, this observed movement of the TR highlights the importance of using a dynamic definition for the UTR as part of the implementation of the jump condition method. It is also clear from the contour plots that the coronal temperature cools globally below the equilibrium value during the draining phase (e.g. see the snapshots at $t = 1500$s and $t = 2000$s). The initial condition is then recovered only as a consequence of the background heating between 2000–4000s.

The evolution of the LareJ denisty and v_x velocity component are shown in Figures 6.2 & 6.3, respectively. In response to the heating, the coronal density increases as a material front that is driven by the field-aligned flows propagates upwards. After 50s, the strong e-

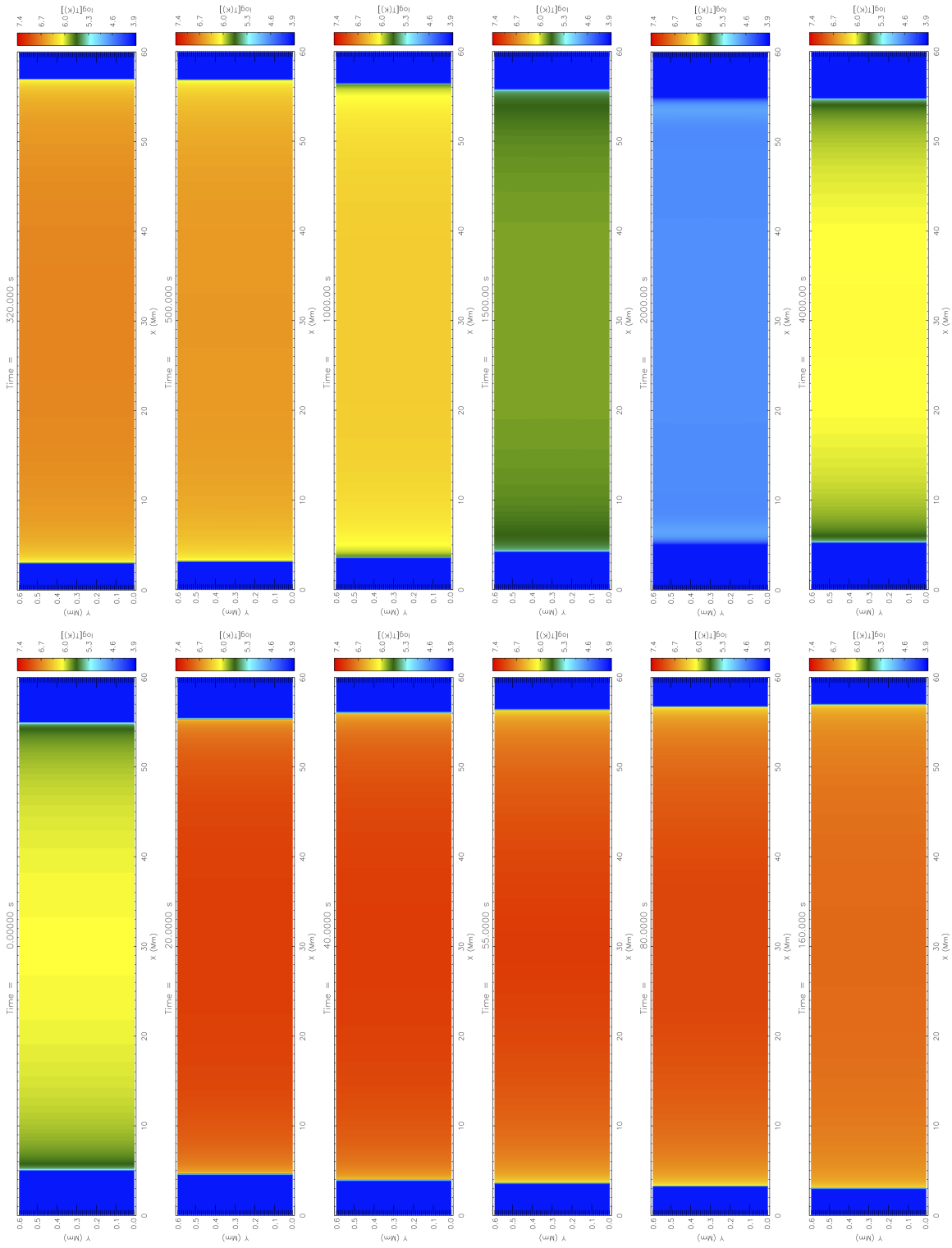

Figure 6.1: Results for uniform heating Case 3. The panels show time ordered contours of the LareJ temperature as a function of the field-aligned (x) and cross-field (y) directions.

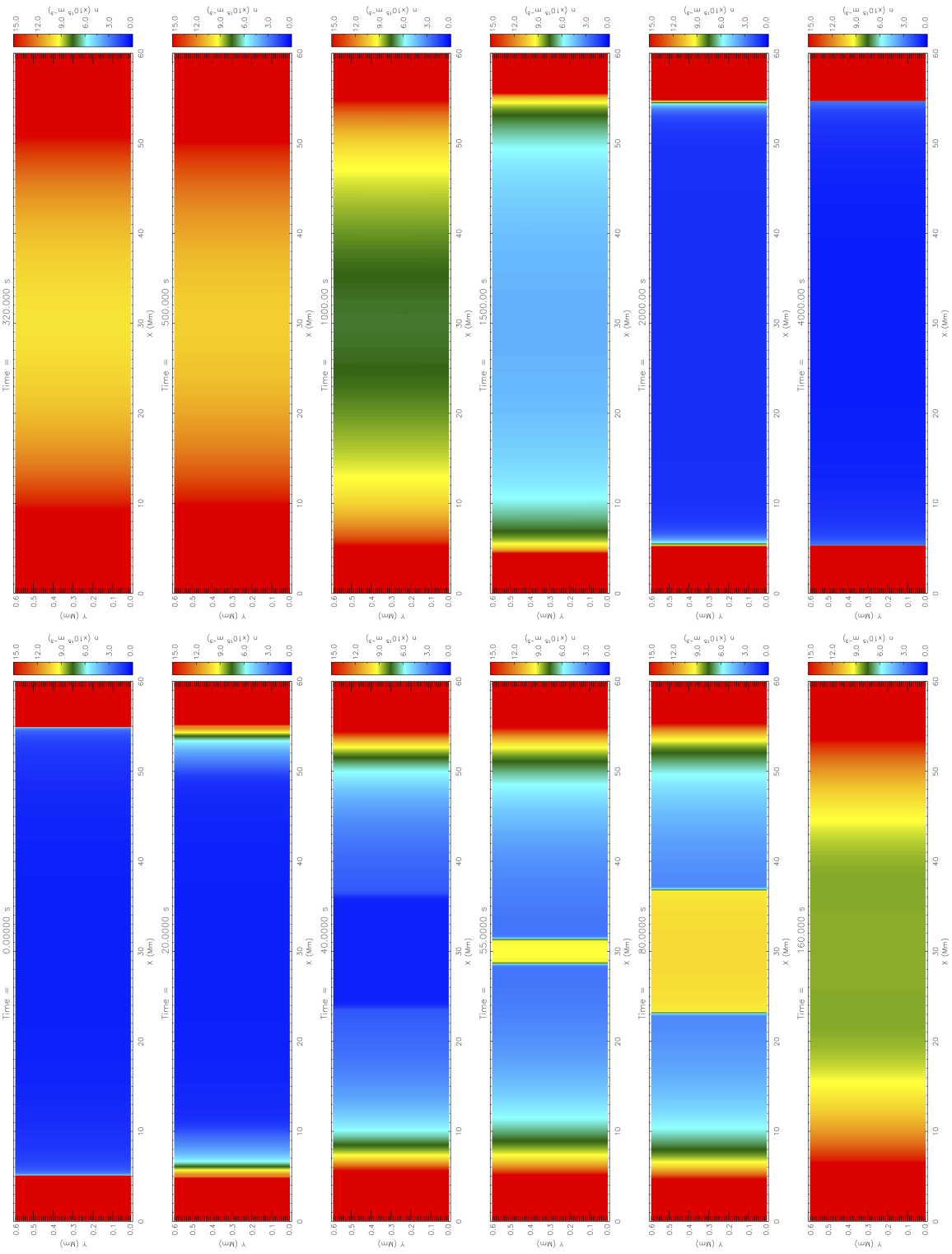

Figure 6.2: Results for uniform heating Case 3. The panels show time ordered contours of the LareJ density as a function of the field-aligned (x) and cross-field (y) directions.

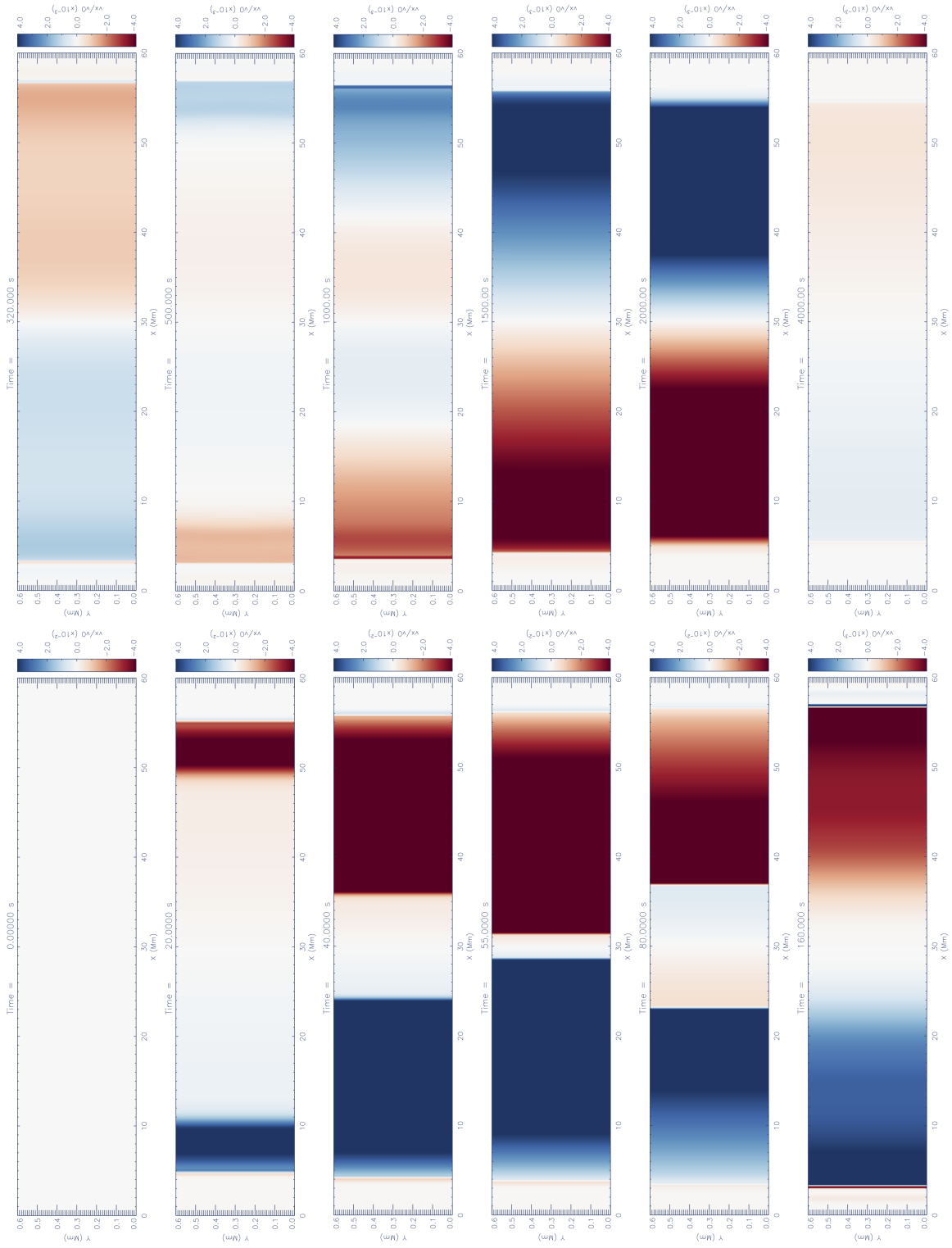

Figure 6.3: Results for uniform heating Case 3. The panels show time ordered contours of the LareJ v_x velocity component as a function of the field-aligned (x) and cross-field (y) directions. The colourbar has been saturated at $\pm$ 275 km/s for snapshots up until $t = 80$s but note that the v_x range is reduced by an order of magnitude in snapshots thereafter.

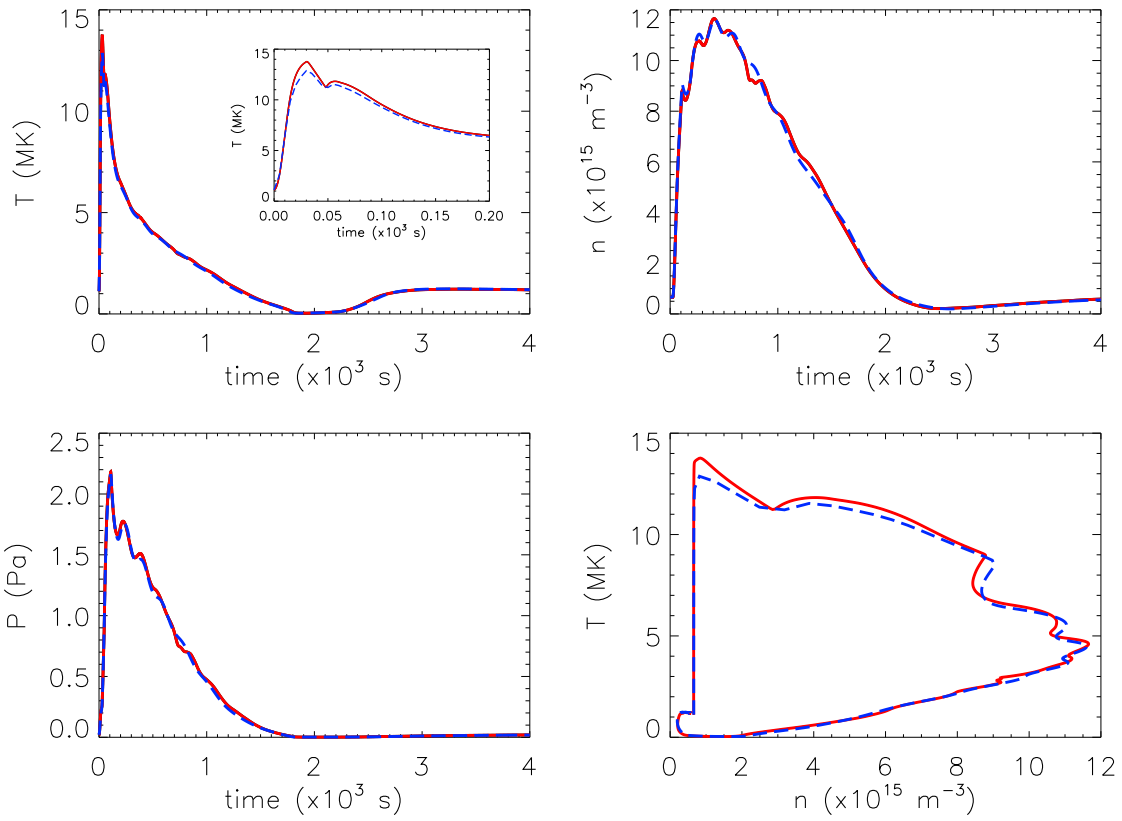

Figure 6.4: Results for uniform heating Case 3. The panels show the coronal averaged temperature, density and pressure as functions of time, and the temperature versus density phase space plot. The solid red line represents the two-dimensional LareJ solution and the dot-dashed blue line corresponds to the one-dimensional LareJ solution that was presented previously in Figure 3.8.

vaporative upflows (v_x velocity component) from each loop leg collide at the loop apex. It is striking that the loop then appears to fill from the apex rather than from the chromosphere when the material fronts rebound and return, propagating downwards along the magnetic field in the direction of the TR. This phenomena is particularly prominent in the snapshots at $t = 55$s and $t = 80$s. Thereafter, the density continues to increase up until the peak at around 400s, with weaker evaporative upflows sustaining the supply of dense material upwards into the corona. The loop then starts to drain globally with downflows that are about an order of magnitude smaller than the strong initial upflows, returning towards the equilibrium.

As a basic check of consistency against the one-dimensional implementation (for the case of uniform heating), coronal averaged quantities are computed from the two dimensional simulation and compared with the 1D results. In a similar manner as Chapter 3, the coronal averages are calculated by spatially averaging over the width and uppermost 50% of the loop length. For example, the coronal averaged temperature from the 2D domain

is defined as,

$$\bar{T} = \frac{1}{L_y}\frac{1}{L_x}\int_0^{L_y}\int_{x_a-L_x/2}^{x_a+L_x/2} T\,dx\,dy, \tag{6.11}$$

where L_y is the width of the loop, L_x is the loop half-length and x_a is the loop apex.

Figure 6.4 shows the time evolution of the coronal averaged temperature (T), density (n), pressure (P) and the corresponding temperature versus density phase space plot. The solid red lines represent coronal averaged quantities that are obtained from the two-dimensional LareJ simulation (Lare2D with the jump condition) while the dashed blue lines correspond to the one-dimensional LareJ solution that was discussed previously in Chapter 3. On one hand, there are differences between the one and two-dimensional LareJ simulations: (i) the maximum averaged temperature reached by the 2D solution is fractionally higher than the 1D result, and (ii) the density oscillations (seen as the plasma sloshes to and fro within the loop) are damped slightly faster in the 1D solution. On the other hand, these differences are sufficiently small enough so that any conclusions yielded are consistent between the two implementations. Indeed, the general level of agreement is excellent. This coherence (i) establishes confidence in the multi-dimensional implementation, and (ii) demonstrates that we are capable of reproducing the 1D results presented in Chapters 3–5. Therefore, we can now proceed to considering simulations where two-dimensional effects start to influence the evolution.

6.4 Non-Uniform Cross-field Heating

Next, we investigate the case of spatially non-uniform heating, with the energy deposition localised centrally in the cross-field direction, relative to the initial magnetic field. For this experiment, we extend the 2D computational domain by a factor of ten in the direction perpendicular to the magnetic field, to obtain a simulation box of length 60Mm and width 6Mm. The spatial resolution is kept constant by using an increased number of grid points, requiring a numerical resolution of 512×320 ($N_x \times N_y$). In this model the cross-field heating profile is of the form,

$$Q(y) = Q_{bg} + Q_{H_0}\exp\left(\frac{-(y-y_0)^2}{2y_H^2}\right), \tag{6.12}$$

where y_0 is the location of maximum heating, y_H is the length scale of heat deposition and Q_{H_0} is the maximum heating rate. We relate the results to Section 6.3 by releasing the same total amount of energy along the field line at $y_0 = 3$Mm as was released on average, along the magnetic field, in the uniform heating case presented above (i.e. $Q_{H_0} = 8 \times 10^{-2}\,\mathrm{J\,m^{-3}\,s^{-1}}$). Moving outwards from the centre of the box width at $y = 3$Mm, the

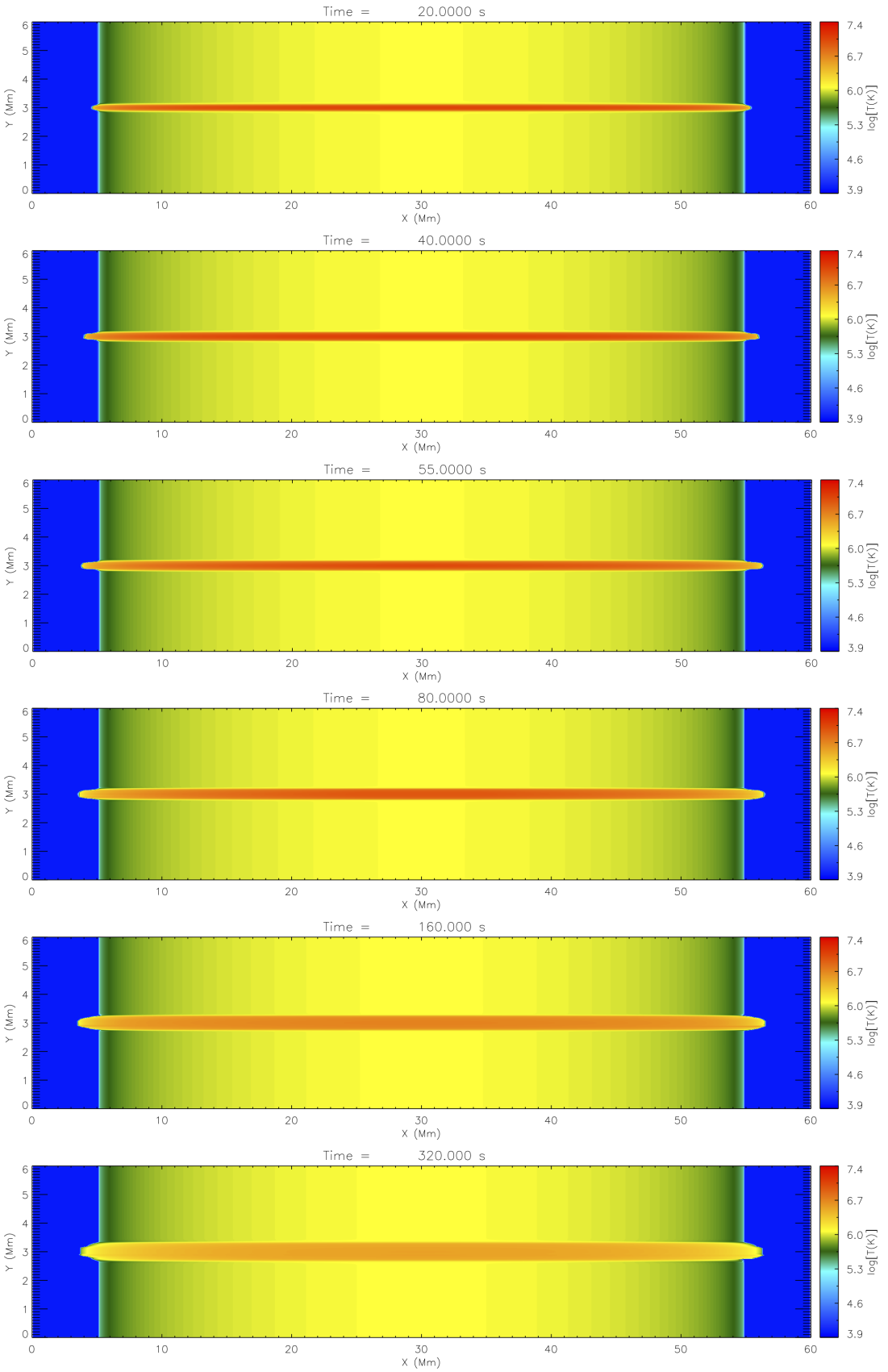

Figure 6.5: Results for the non-uniform cross-field heating event. The panels show time ordered contours of the LareJ temperature as a function of the field-aligned (x) and cross-field (y) directions, for times during the evaporation phase up until the peak density.

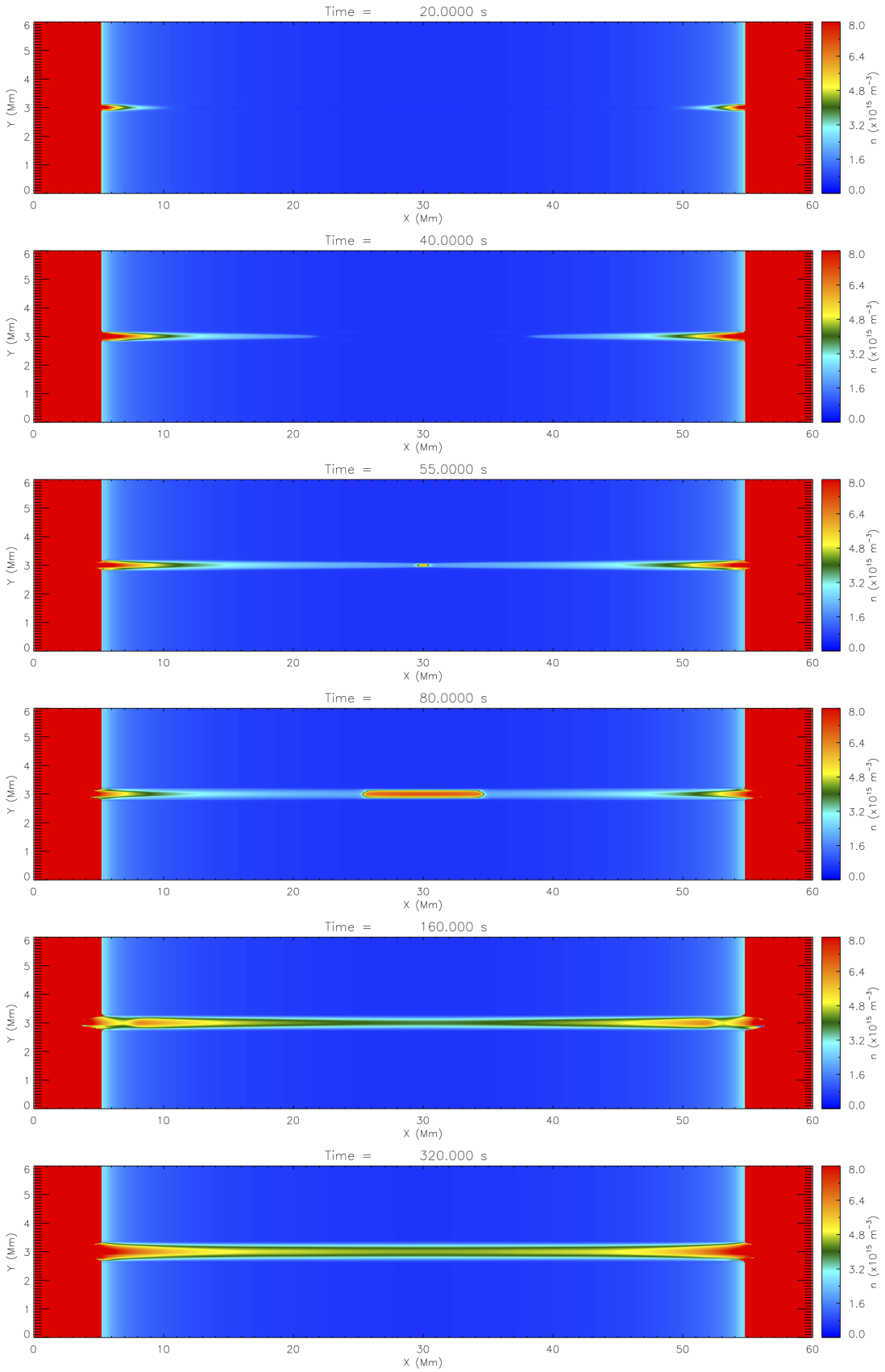

Figure 6.6: Results for the non-uniform cross-field heating event. The panels show time ordered contours of the LareJ density as a function of the field-aligned (x) and cross-field (y) directions, for times during the evaporation phase up until the peak density.

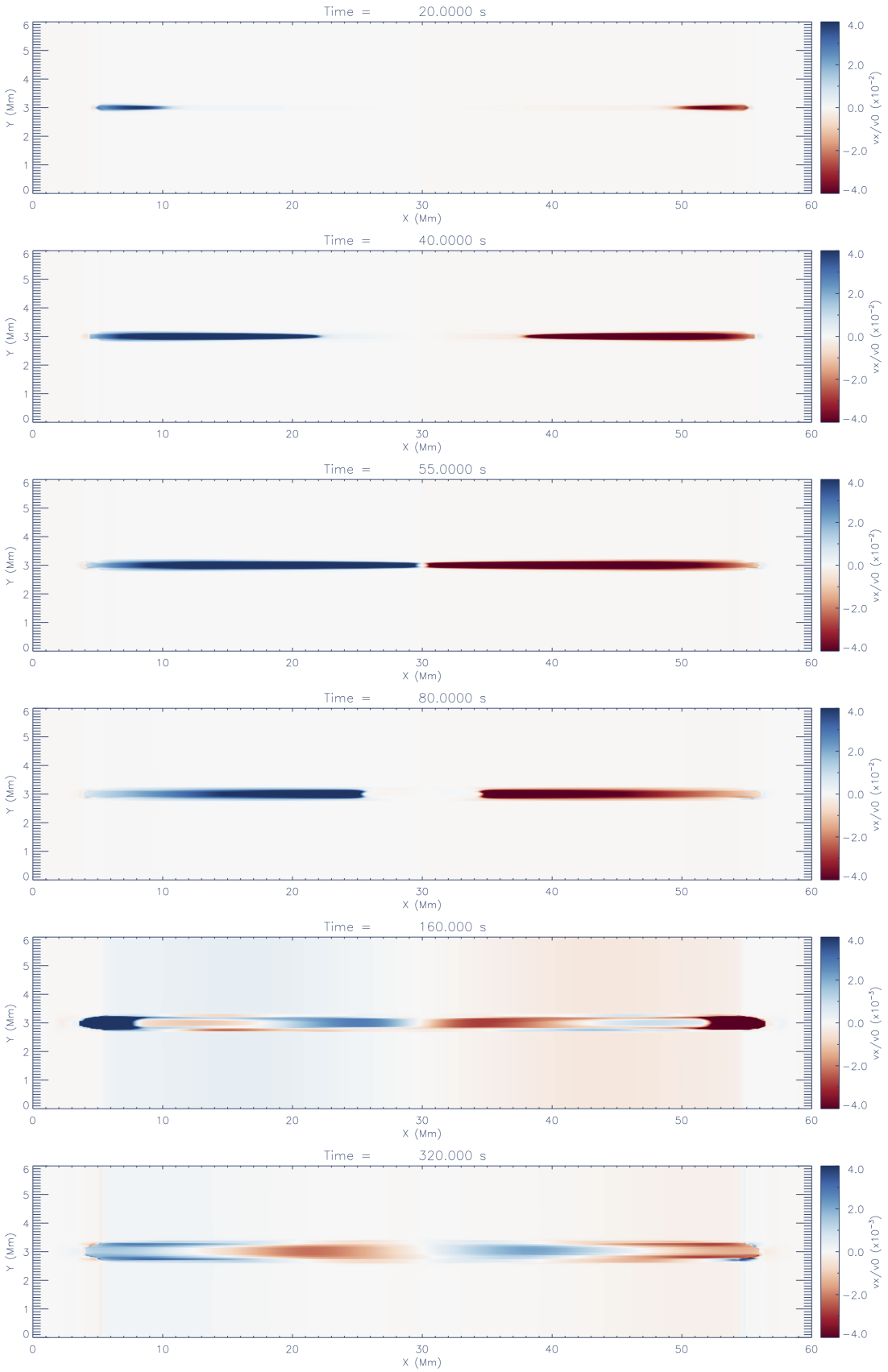

Figure 6.7: Results for the non-uniform cross-field heating event. The panels show time ordered contours of the LareJ v_x velocity component. The colourbar has been saturated at $\pm$ 275 km/s for snapshots up until $t = 80$s but note that the v_x range is reduced by an order of magnitude in snapshots thereafter.

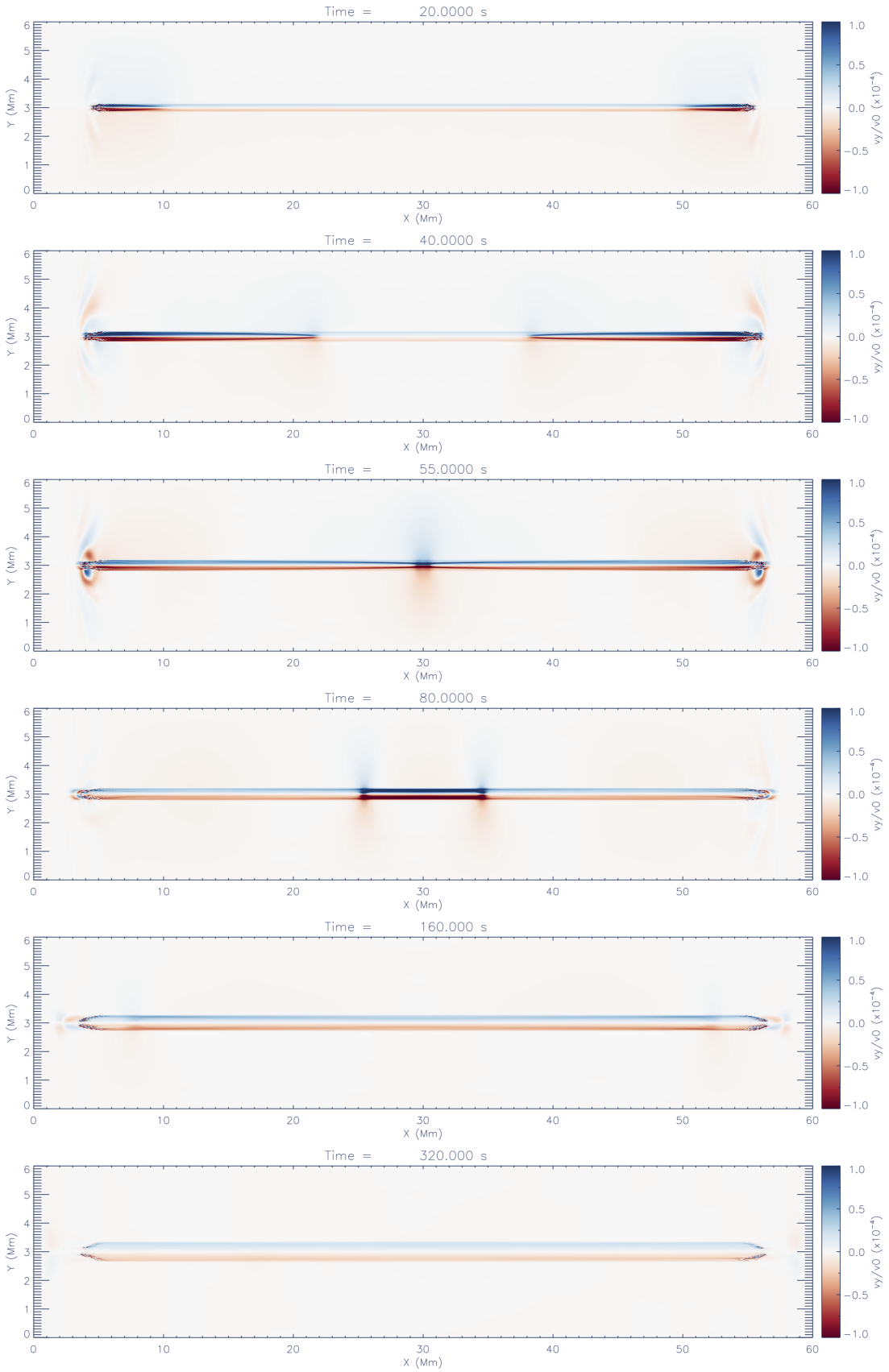

Figure 6.8: Results for the non-uniform cross-field heating event. The panels show time ordered contours of the LareJ v_y velocity component. The colourbar has been saturated at $\pm$ 2.75 km/s (two orders of magnitude smaller than the v_x range).

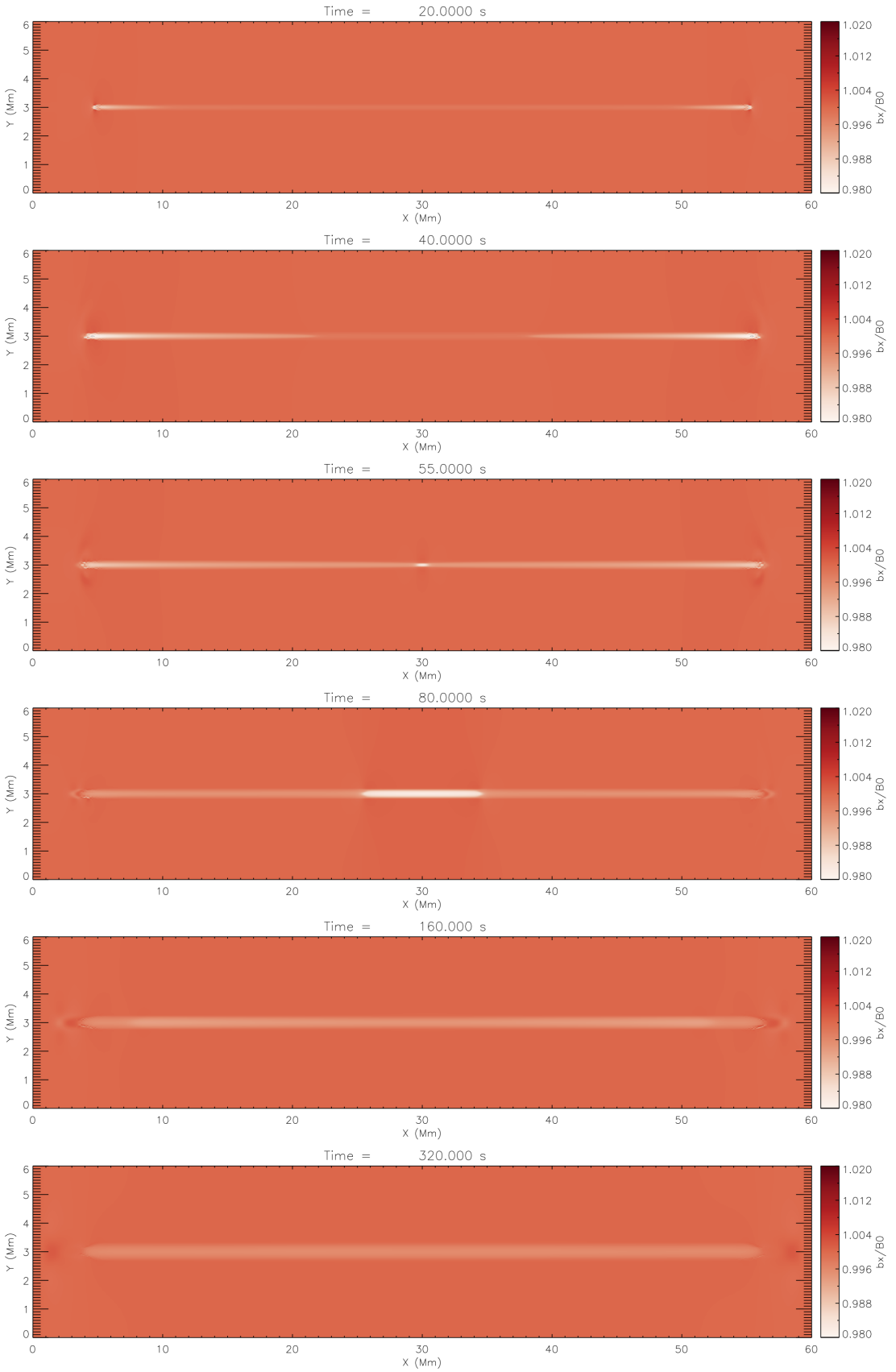

Figure 6.9: Results for the non-uniform cross-field heating event. The panels show time ordered contours of the LareJ B_x magnetic field component as a function of the field-aligned (x) and cross-field (y) directions.

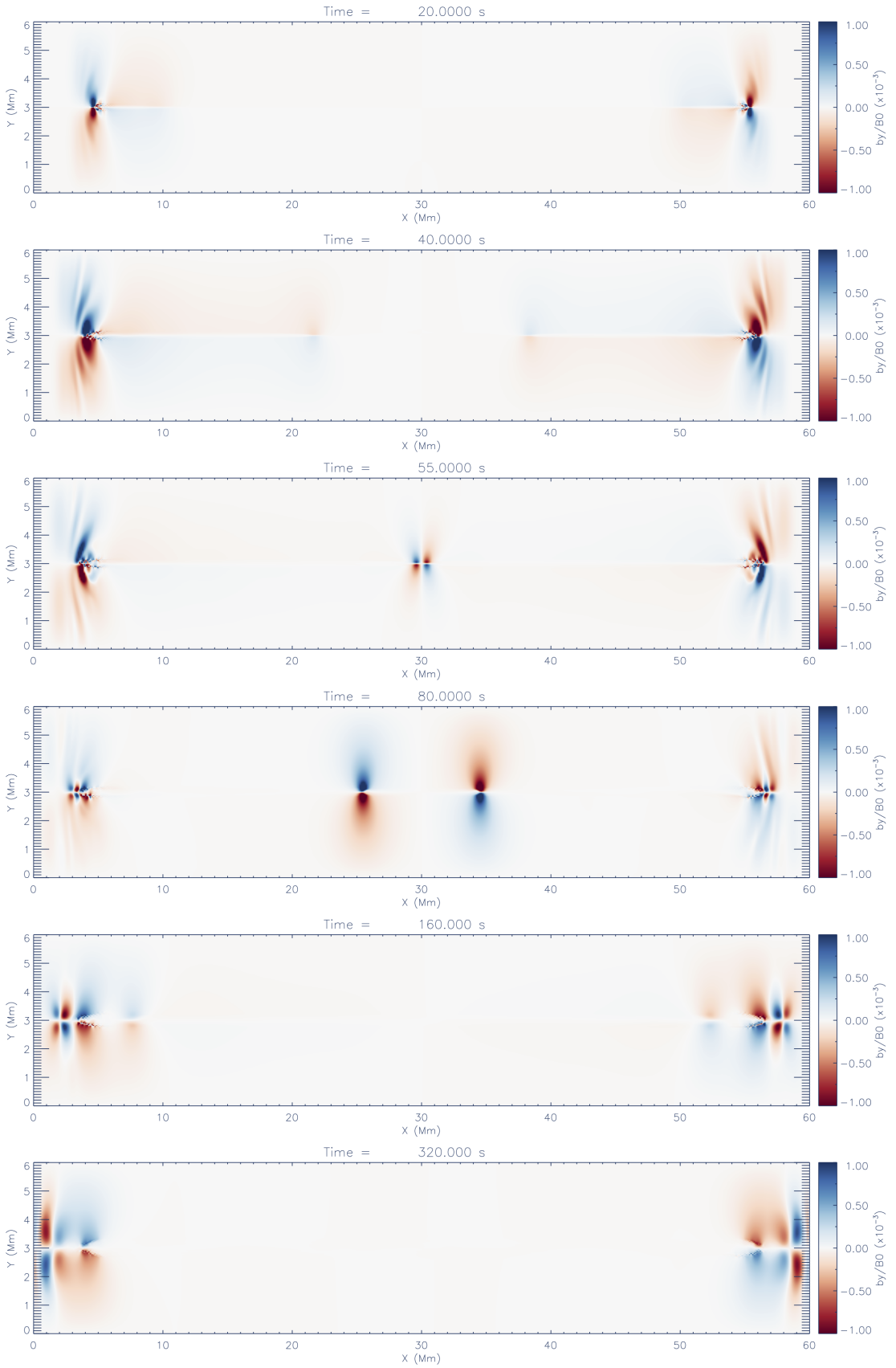

Figure 6.10: Results for the non-uniform cross-field heating event. The panels show time ordered contours of the LareJ B_y magnetic field component as a function of the field-aligned (x) and cross-field (y) directions.

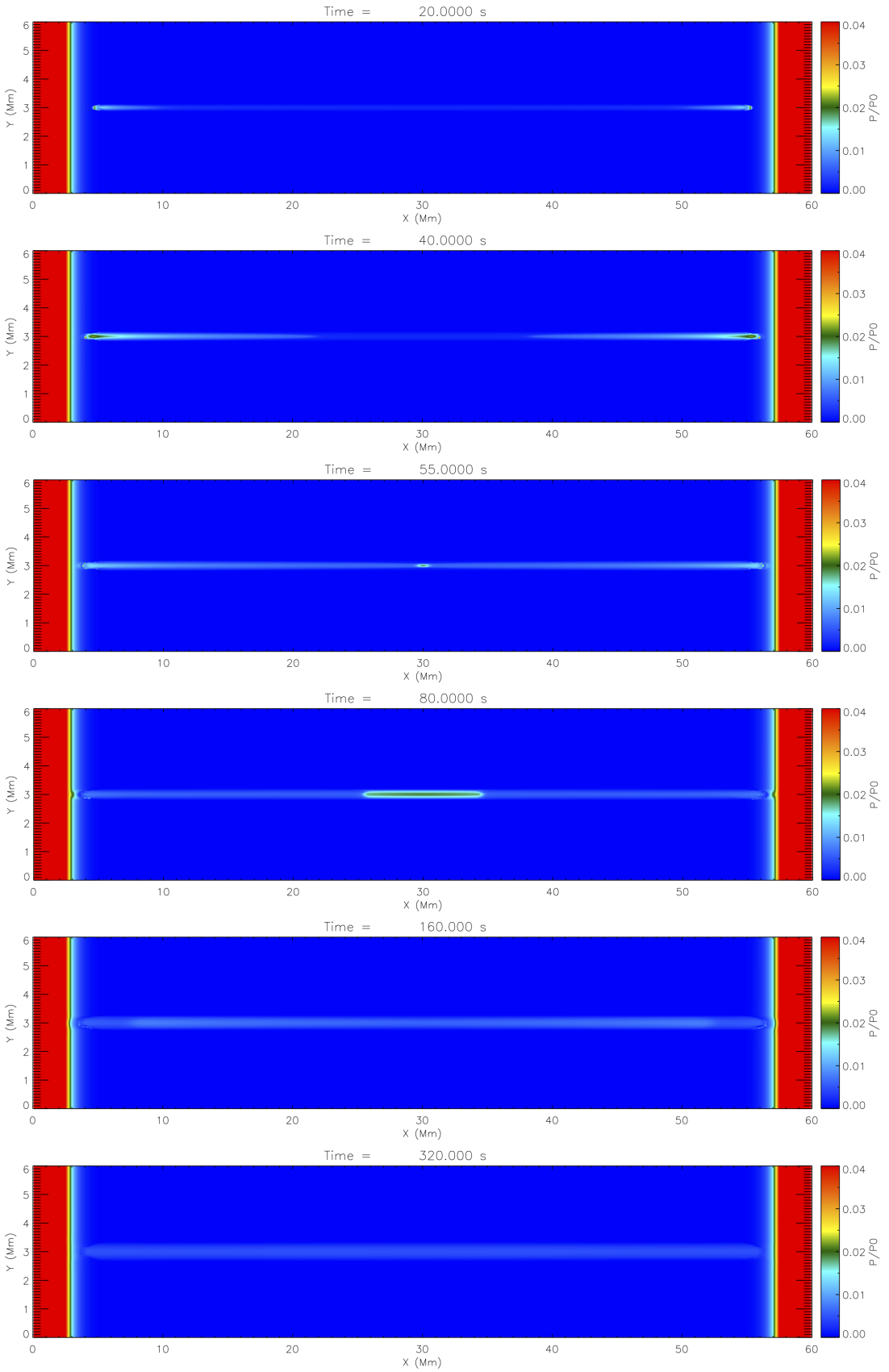

Figure 6.11: Results for the non-uniform cross-field heating event. The panels show time ordered contours of the LareJ gas pressure as a function of the field-aligned (x) and cross-field (y) directions.

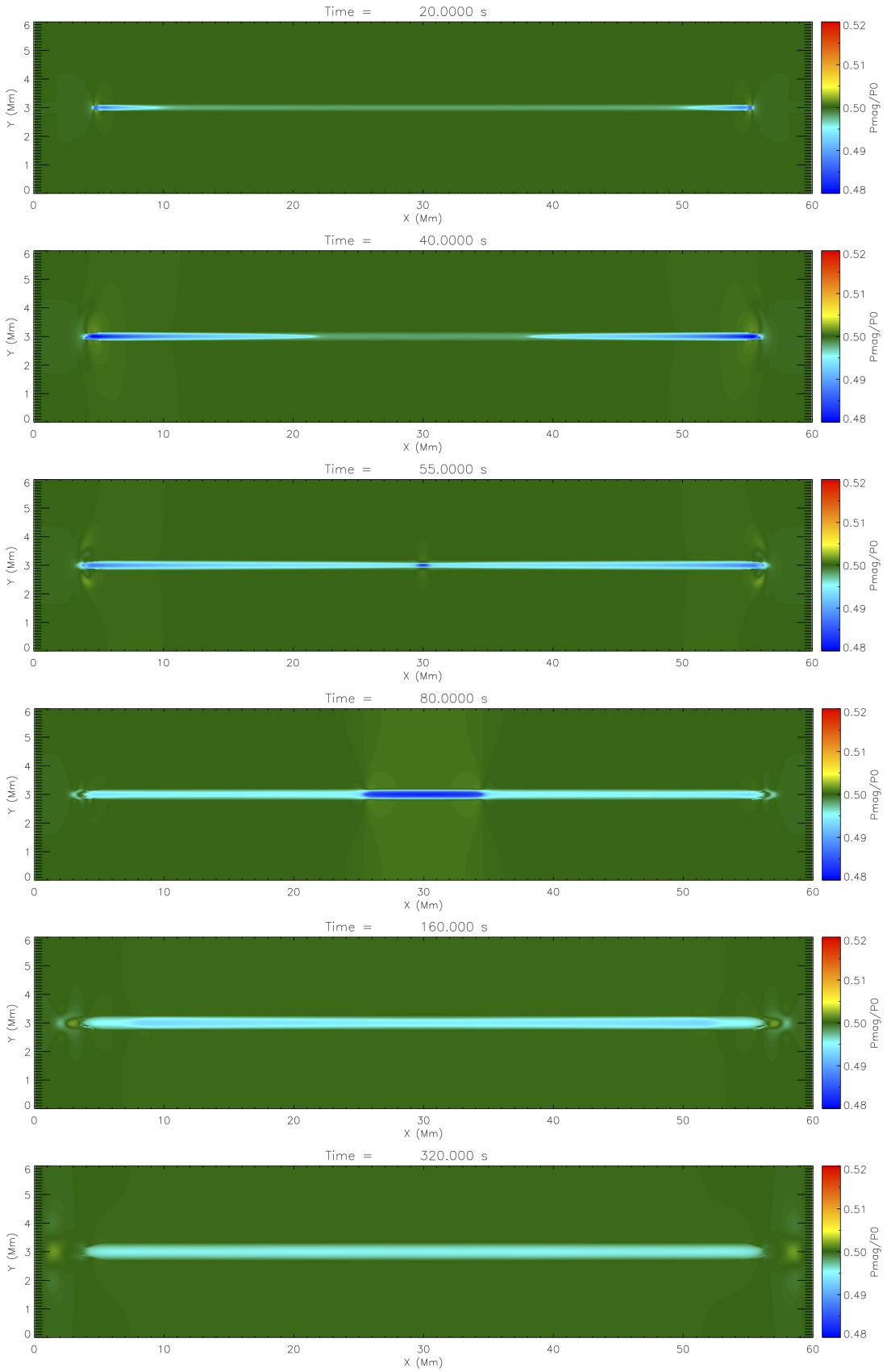

Figure 6.12: Results for the non-uniform cross-field heating event. The panels show time ordered contours of the LareJ magnetic pressure as a function of the field-aligned (x) and cross-field (y) directions.

cross-field heating profile decreases exponentially with $y_H = 0.05$Mm as shown in Figure 6.13 ($Q(y)/Q_{H_0}$ is displayed in the panels as the dashed red curve). Consistent with the uniform heating event described above, the temporal profile of the heating is a 60s triangular pulse while the spatial profile of the energy release is uniform along the loop.

Figures 6.5 – 6.12 show the temporal response of selected key variables, to the non-uniform cross-field heating event, for the simulation computed with the jump condition (LareJ). The quantities presented include the temperature, density, v_x, v_y, B_x, B_y, and the gas and magnetic pressures, respectively. The details of the field-aligned evolution show the same fundamental properties as those discussed above for the uniform heating case. Thus, here we focus just on the two-dimensional effects that are introduced by the localised cross-field energy deposition.

Firstly, the fast wave now acts to equalise cross-field pressure gradients. This equalisation is highly efficient, keeping the total pressure across the magnetic field approximately constant throughout the majority of the computational domain. Defining the total pressure as the sum of the gas and magnetic pressures, this means that during the simulation,

$$\frac{\partial}{\partial y}\left(P + \frac{B^2}{2}\right) \approx 0, \tag{6.13}$$

which requires that increases in the gas pressure are roughly balanced by decreases in the magnetic pressure. Figure 6.11 shows that increases in the gas pressure are principally associated with increases in the coronal density. Therefore, there is a coupling between the reductions observed in the dominant B_x component of the magnetic field and the propagation of the material fronts that increase the coronal density. However, throughout the simulation we find that on the boundary, between the interior and exterior of the loop, that enhancements in the gas pressure marginally exceed the reductions in the magnetic pressure. This perturbation to the cross-field pressure balance manifests itself as the small outflows that persist perpendicular to the magnetic field (v_y velocity component).

Secondly, the effect of these weak v_y flows is to cause the magnetic field to expand, reducing the magnetic pressure as the plasma tries to reach transverse pressure balance. The outcome is that the loop broadens in the y direction beyond the spatial scale of the energy deposition. Figure 6.13 uses a series of snapshots to show this y expansion of the loop via the time evolution of the temperature, pressure, density and density squared at the loop apex ($x = 30$Mm). At early times, during the heating the event, the temperature profile initially traces out the cross-field heating profile (e.g. see the snapshot at $t = 20$s). Significant broadening is then observed as the loop cools by heat conduction. Similarly, at first, when the material fronts collide at the loop apex, the length scale of the y increase in coronal density matches the width of the heating profile. However, once these field-aligned fronts have rebounded, the v_y velocity component then starts to become important, expanding the observable loop. Thereafter, the expansion of the coronal density is partic-

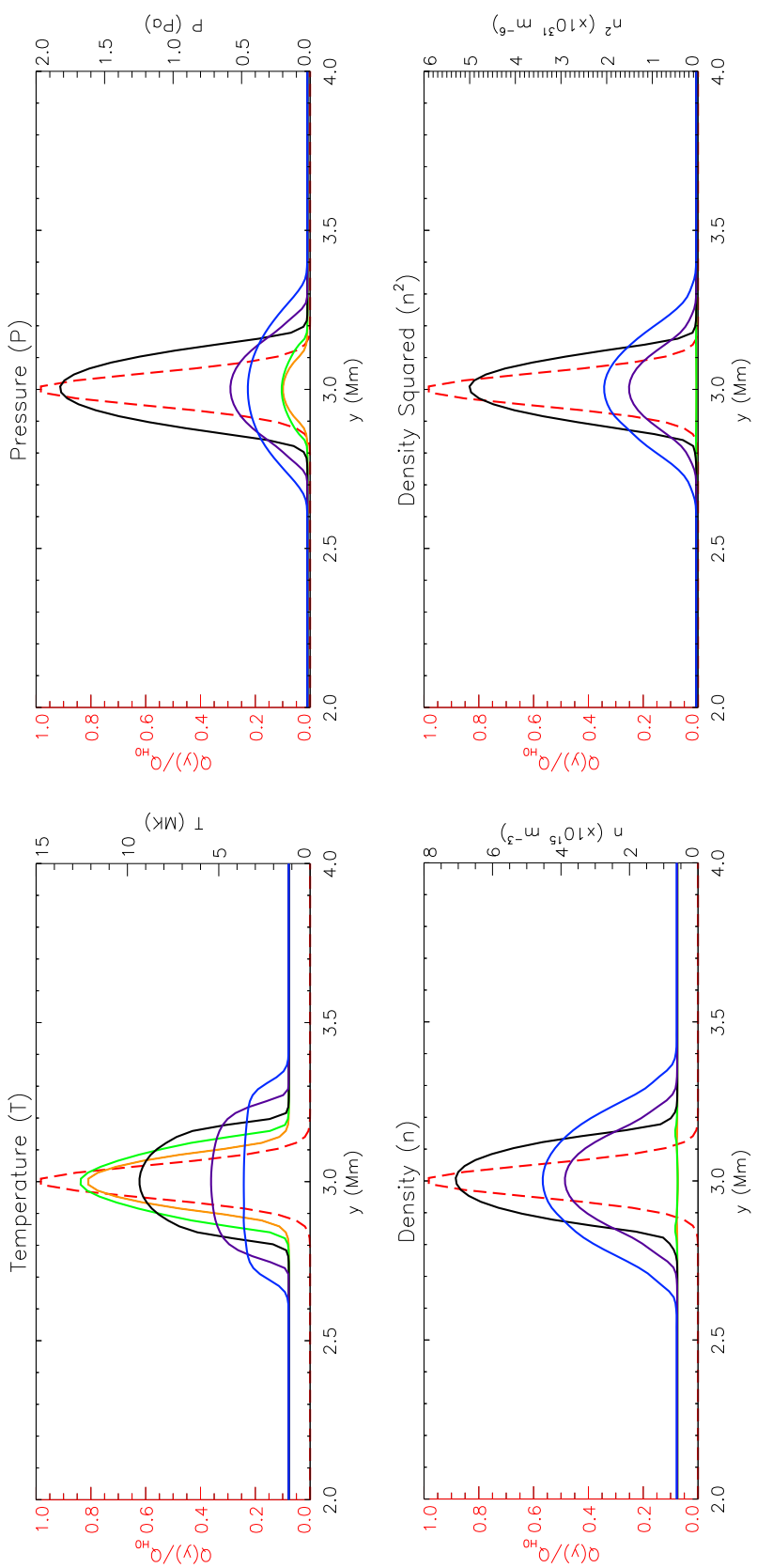

Figure 6.13: Results for the non-uniform cross-field heating event. The panels show the temperature, pressure, density and density squared (n^2) for temperatures at or above one million degrees ($T \geq 1$MK) obtained in the LareJ simulation (Lare2D with the jump condition), as functions of position across the loop (solid lines, right-hand axis) at the loop apex ($x = 30$Mm) for times during the evaporation phase up until the peak density, imposed on top of the cross-field heating profile $Q(y)/Q_{H_0}$ (dashed red line, left hand axis). The solid lines represent time ordered snapshots from orange ($t = 20$s) through to green ($t = 40$s), black ($t = 80$s), purple ($t = 160$s), and blue ($t = 320$s).

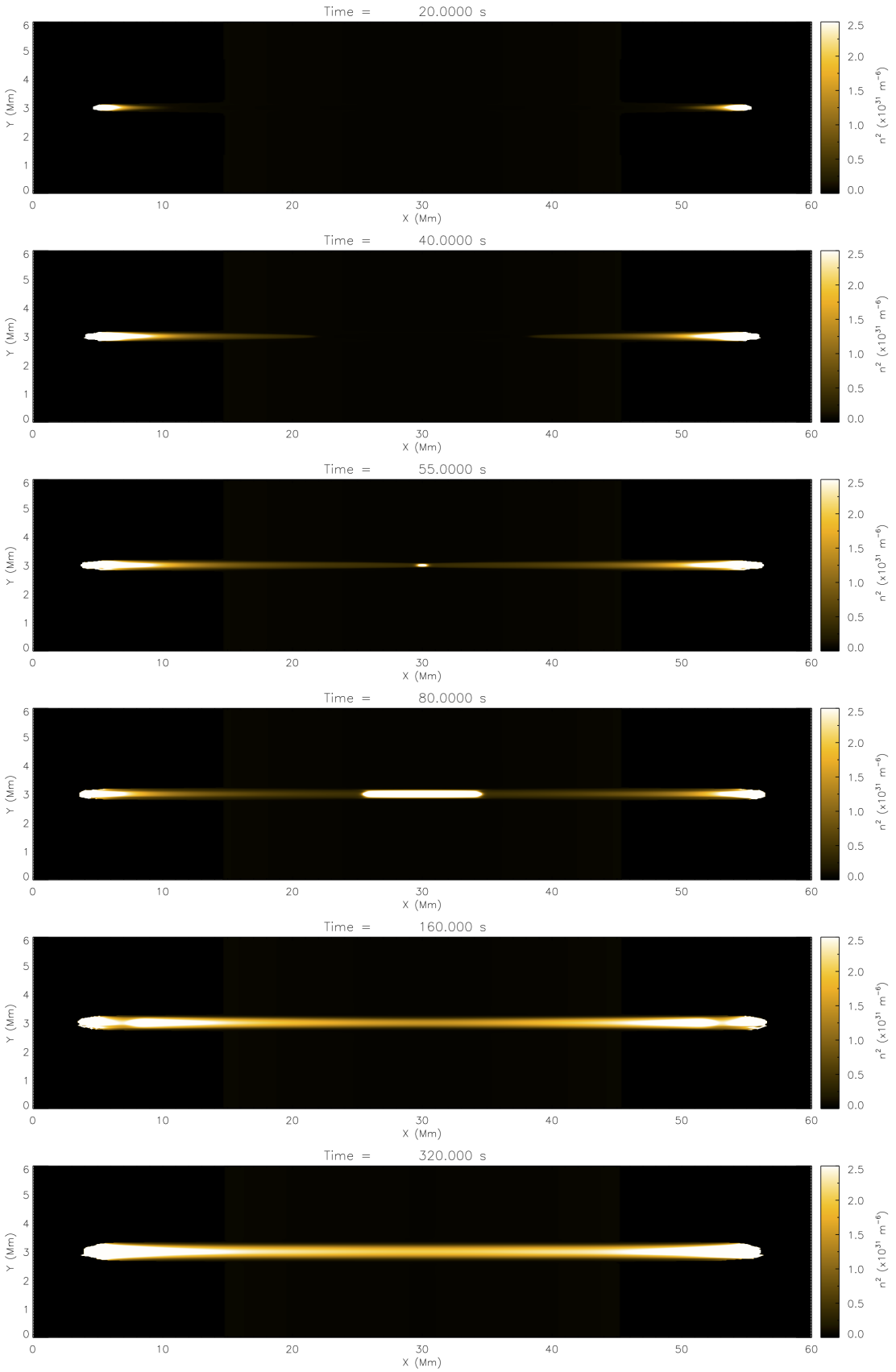

Figure 6.14: Results for the non-uniform cross-field heating event. The panels show time ordered contours of the density squared (n^2) for temperatures at or above one million degrees ($T \geq 1$MK), obtained in the LareJ simulation (Lare2D with the jump condition).

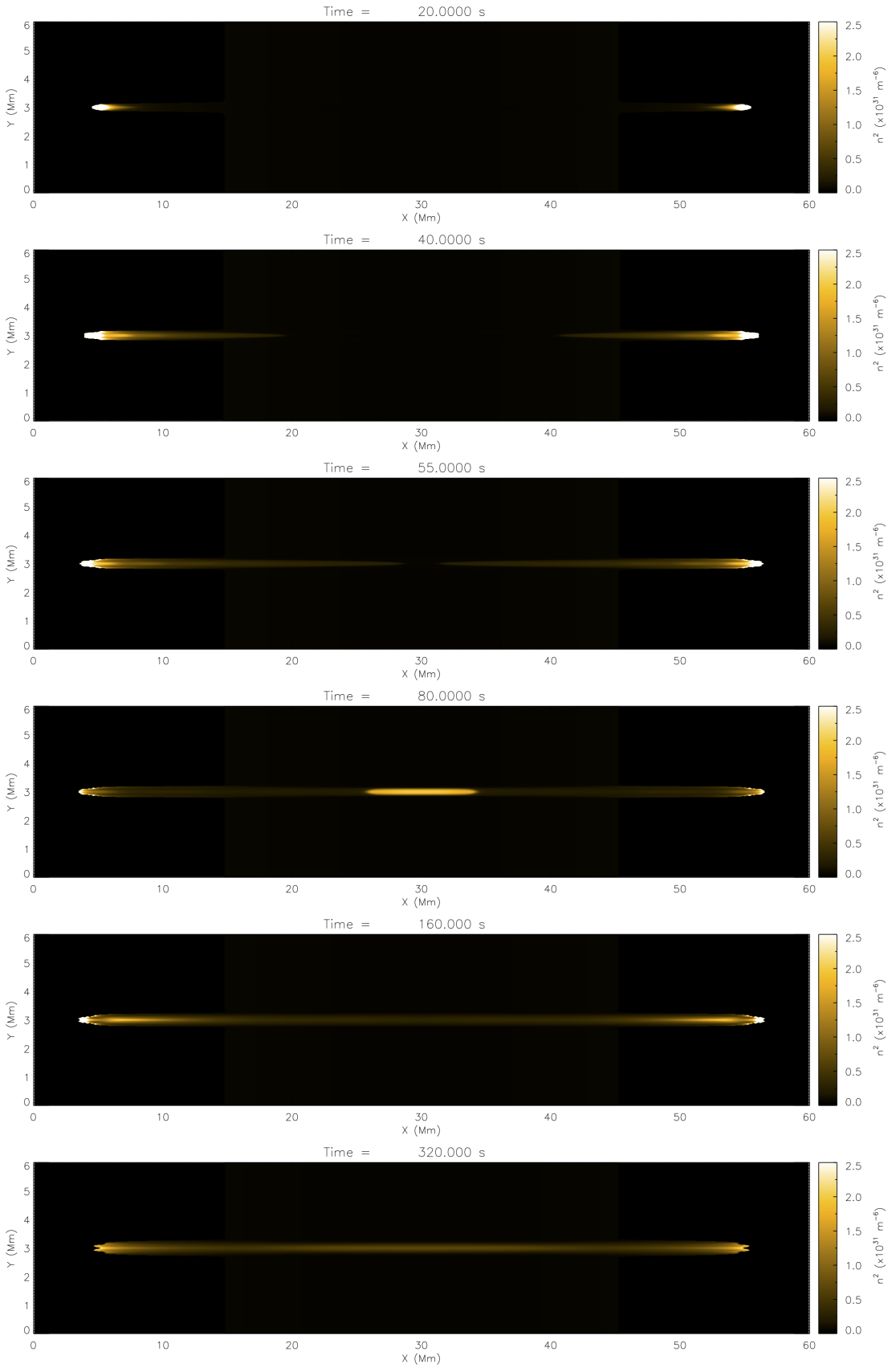

Figure 6.15: Results for the non-uniform cross-field heating event. The panels show time ordered contours of the density squared (n^2) for temperatures at or above one million degrees ($T \geq 1$MK), obtained in the Lare2D simulation without the jump condition.

ularly prominent. The broadening of the pressure and density squared show similar properties. Therefore, we can conclude that the length scales identified with the formation of coronal loops may not necessarily resolve the length scales associated with the physical heating mechanism.

An additional subtlety is that since increases in the gas pressure are primarily due to the evaporative response, which is intrinsically non-uniform along the loop, the reductions in the B_x component of the magnetic field that we described above, also show spatial variations along the loop. This non-uniform behaviour gives rise to gradients in B_x along the magnetic field (i.e $\partial B_x/\partial x$). Hence, satisfying the solenoidal constraint requires the generation of a small B_y magnetic field component which has gradients across the loop (i.e $\partial B_y/\partial y$). However, note that the B_y field generated is 3 orders of magnitude smaller than B_x and so the magnetic field remains predominantly uniform. Verifying our use of the simplified jump condition.

As a basic proxy of the coronal emission, we now show the temporal evolution and spatial variation of the density squared for temperatures at or above 1MK, in response to the non-uniform cross-field heating event in Figure 6.14, for the simulation computed with the jump condition (LareJ). The initial brightenings seen at the footpoints of the loop are associated with downward movements of the TR to denser regions of the atmosphere, while the tails (which are the gradual dimmings observed on the coronal side of the brightenings) trace the upward propagation of the material fronts. These tails become increasingly elongated as time evolves (e.g. see the snapshot at $t = 40$s) up until the point when the material fronts collide at the loop apex. At this stage, the material fronts superimpose, resulting in the significant brightening observed at the loop apex. The strong evaporative flows (v_x velocity component) that transported the material fronts upwards then rebound and return. As they propagate back downwards along the loop these flows redistribute the ablated material. The outcome is that the loop appears to fill from the apex rather than from the chromosphere (e.g. see the evolution between the snapshots at $t = 55$s and $t = 80$s), a result which may have observational implications. The coronal structure (i.e. the coronal loop) is fully formed once the material fronts arrive back at the footpoints of the loop ($t = 160$s), with significant broadening of the width observed. Regions previously characterised as gradual dimmings (the tails) now exhibit visible emission, peaking at the density maximum.

In order to contrast the formation of coronal loops computed with (LareJ) and without the jump condition (Lare2D) when subjected to the same heating, we show the time evolution of the coronal emission proxy obtained from the Lare2D simulation in Figure 6.15. Comparing the behaviour observed in the two simulations uncovers compelling differences. When computed without the jump condition (Lare2D) the main errors are that: (i) the brightenings at the footpoints of the loop are short lived, (ii) the emission at the loop apex when the material fronts collide is significantly underestimated, (iii) the coronal

structure never fully forms resulting in (iv) interpretations of the coronal loop's lifetime being completely meaningless, and (v) no cross-field expansion. Therefore, this comparison demonstrates (i) the potential for simulations to produce spurious conclusions when the number of grid points used is insufficient to fully resolve the TR, and (ii) advantages of using the jump condition approach in such multi-dimensional simulations.

6.5 Chapter Summary

We have demonstrated the simple extension of the jump condition method to two-dimensional models where the magnetic field remains predominantly uniform. Furthermore, the MHD simulations considered, revealed two results of observational significance. Specifically, that coronal loops can (i) appear to fill from the loop apex rather than from the chromosphere and (ii) broaden in the cross-field direction beyond the spatial scale of the heating mechanism. Advantages of using the jump condition method in multi-dimensional simulations have also been highlighted, through comparison of a proxy for the resulting coronal emission.

Chapter 7

Conclusions & Future Work

This thesis has presented a new computational approach for modelling chromospheric evaporation in response to coronal heating. In particular, the method developed has been shown to be successful in dealing with the difficulty of obtaining the correct interaction between a downward conductive flux from the corona and the resulting upflow from the TR, when the TR is under-resolved. Thus, the use of this new method makes it possible to model the evaporative response to coronal heating correctly without fully resolving the TR. To that end, we have demonstrated that this new approach (i) ensures accuracy when simulating the coronal density evolution and (ii) significantly reduces the computation time when used in 1D hydrodynamic and multi-dimensional MHD models.

To begin, in Chapter 2, we outlined the numerical methods, which have been used throughout, to solve the hydrodynamic and magnetohydrodynamic equations in models of coronal loops. Particular focus was given to introducing super time stepping (STS) methods to treat thermal conduction. The derivation of the second-order accurate Runge-Kutta Legendre (RKL2) method was presented and we tested this method for consistency and stability in coronal plasma conditions. Through a series of model problems, we demonstrated that the RKL2 method achieves the correct temporal evolution when integrating with an increased conductive time step, facilitating substantial computational gains. However, we note that care should be taken to ensure this time accuracy of the accelerated internal stages.

The unresolved transition region (UTR) jump condition was derived from an integrated form of energy conservation in Chapter 3, where the implementation of the method was also described for 1D hydrodynamic models. The method treats the unresolved region of the lower TR as a discontinuity that responds to changing coronal conditions through the imposition of a local velocity correction, which is implied by the jump condition. This approach was benchmarked against a fully resolved 1D model (HYDRAD) by considering a wide range of impulsive, spatially uniform heating events. Using the jump condition

approach in simulations with coarse resolutions that do not resolve the lower transition region, we were able to demonstrate that the method leads to (i) coronal densities comparable to fully resolved 1D models but with significantly faster computation times (the speed up was between one and two orders of magnitude), and (ii) significant improvements in the accuracy of both the coronal density and temperature temporal evolution when compared to the equivalent simulations run without the jump condition.

Further examples and analysis of the jump condition method were presented in Chapter 4. In particular, we considered how the jump condition performed for different spatially non-uniform heating functions and initial plasma conditions. This involved studying highly localised heating pulses and nanoflare trains. It was demonstrated that the overall behaviour of the coronal density and temperature showed good agreement with a fully resolved 1D model in all of the experiments considered. Therefore, the application of the jump condition method, to model the evaporative response of the TR, was not affected by introducing non-uniform complexities in the coronal heating.

In many cases, we noticed that the coronal density was slightly higher than the fully resolved results. To understand the cause of this difference, we undertook a detailed analysis of the terms both retained and neglected from the jump condition. This revealed that the causes of discrepancy with the fully resolved model are the influence of terms neglected from the jump condition, at the very start of the heating phase. In particular, it can be attributed to the neglect of terms corresponding to the rate of change of total energy in the unresolved atmosphere and mass motions at the base of the TR.

Therefore, one possible area of future work arising from this thesis is to formulate approximations to include these terms in the jump condition, in order to remove the premature enthalpy flux and over-evaporation. Another is to use interpolation methods to resolve the UTR in the calculation of R_{utr}, with the view of replacing the simple model used throughout which does underestimate the true value of the integrated radiative losses. The work presented in this thesis has also adopted a simple model for the chromosphere (the density increases exponentially with depth for an isothermal temperature) that provides a mass reservoir to allow plasma to flow upwards into the corona, in response to heating by thermal conduction. However, we note that the formulation of the jump condition method is also compatible with models that use a more accurate description of the chromosphere.

Mikić et al. (2013) have also proposed a method to sidestep the need for high spatial resolution in the TR. Their approach artificially broadens the TR by increasing the parallel thermal conductivity $\kappa_{\parallel}(T)$ and decreasing the radiative loss rate $\Lambda(T)$, at temperatures below a fixed cut off T_c, to preserve the product $\kappa_{\parallel}(T)\Lambda(T) = M_c$. They claim that with this modification, the solution at coronal temperatures remains unchanged. However, this method clearly assumes an energy balance in the TR between the downward heat flux and the radiative losses. Thus, since the evaporative response to coronal heating is driven by a

lack of energy balance in the TR between these quantities, it remains unclear how well this modification to the thermal energy equation deals with dynamic evolution. Furthermore, the selection of the cut off temperature is also unclear because the temperature of the TR can change significantly when the plasma is subjected to heating and cooling. It is not difficult to identify the potential problem that occurs when the TR is heated to temperatures above T_c. Therefore, it would be informative to benchmark this approximation against the jump condition approach.

In Chapter 5, we presented the application of the jump condition approach to coronal loop models with steady footpoint heating and thermal non-equilibrium (TNE). The effects of numerical resolution, background heating and adjusting the heating parameters were investigated to establish their influence on TNE limit cycles. We demonstrated that (i) inadequate spatial resolution prevents the onset of TNE, (ii) the use of a background heating term can significantly influence both the existence and period of TNE limit cycles, and (iii) the mapping between the period of the obtained TNE limit cycles and the imposed heating function is not necessarily one-to-one. Therefore, to gain confidence in results obtained, we recommend that researchers using 1D hydrodynamic and multi-dimensional MHD simulations to study footpoint heating and TNE undertake a series of resolution and background heating tests, to determine if the evolution of the loop changes significantly as a result of sensitivity to these parameters. The short computation time of the jump condition means that simulations with steady footpoint heating in coronal loop models can be run quickly, permitting extensive surveys of the large parameter space. Therefore, the jump condition method can be used, in future, to characterise the onset criteria for TNE and understand what defines the period of TNE limit cycles, for example. We considered loops with the simplest possible configuration but other factors such as the loop geometry, area expansion and stochastic heating (e.g. Mikić et al., 2013; Froment et al., 2018, Antolin et al., in preparation) also play an important role. These additional effects should be taken into consideration when investigating the link between coronal heating and TNE limit cycles.

Finally, in Chapter 6 we presented a first, basic extension of the jump condition method to two-dimensional MHD models where the magnetic field remains locally uniform in the UTR. The computational speed up of the jump condition over a fully resolved 2D code is now at the order of 10^4. One surprising result is that the apparent observable width of a heated loop is much wider than the width of the heated region. Further development of the method, for use in multi-dimensional MHD models which have more complex magnetic field configurations, requires the derivation of a more generalised jump condition and features of the computational implementation to be resolved and extended. Thereafter, it is important to consider how the jump condition performs in simulations with various different magnetic field structures (e.g. arcade structures with curvature in the magnetic field, null points and anti-parallel fields) in order for future users to have confidence in

the model.

Bibliography

S. K. Antiochos and J. A. Klimchuk. A model for the formation of solar prominences. ApJ, 378:372–377, September 1991. doi: 10.1086/170437.

S. K. Antiochos and P. A. Sturrock. Evaporative cooling of flare plasma. ApJ, 220: 1137–1143, March 1978. doi: 10.1086/155999.

S. K. Antiochos, P. J. MacNeice, D. S. Spicer, and J. A. Klimchuk. The Dynamic Formation of Prominence Condensations. ApJ, 512:985–991, February 1999. doi: 10.1086/306804.

P. Antolin, K. Shibata, and G. Vissers. Coronal Rain as a Marker for Coronal Heating Mechanisms. ApJ, 716:154–166, June 2010. doi: 10.1088/0004-637X/716/1/154.

P. Antolin, G. Vissers, T. M. D. Pereira, L. Rouppe van der Voort, and E. Scullion. The Multithermal and Multi-stranded Nature of Coronal Rain. ApJ, 806:81, June 2015. doi: 10.1088/0004-637X/806/1/81.

T. D. Arber, A. W. Longbottom, C. L. Gerrard, and A. M. Milne. A Staggered Grid, Lagrangian-Eulerian Remap Code for 3-D MHD Simulations. *Journal of Computational Physics*, 171:151–181, July 2001. doi: 10.1006/jcph.2001.6780.

F. Auchère, K. Bocchialini, J. Solomon, and E. Tison. Long-period intensity pulsations in the solar corona during activity cycle 23. A&A, 563:A8, March 2014. doi: 10.1051/0004-6361/201322572.

W. T. Barnes, P. J. Cargill, and S. J. Bradshaw. Inference of Heating Properties from "Hot" Non-flaring Plasmas in Active Region Cores. II. Nanoflare Trains. ApJ, 833:217, December 2016. doi: 10.3847/1538-4357/833/2/217.

R. Betta, G. Peres, F. Reale, and S. Serio. An adaptive grid code for high resolution 1-D hydrodynamics of the solar and stellar transition region and corona. A&AS, 122, May 1997. doi: 10.1051/aas:1997157.

P.-A. Bourdin, S. Bingert, and H. Peter. Observationally driven 3D magnetohydrodynamics model of the solar corona above an active region. A&A, 555:A123, July 2013. doi: 10.1051/0004-6361/201321185.

S. J. Bradshaw and P. J. Cargill. Explosive heating of low-density coronal plasma. A&A, 458:987–995, November 2006. doi: 10.1051/0004-6361:20065691.

S. J. Bradshaw and P. J. Cargill. A New Enthalpy-Based Approach to the Transition Region in an Impulsively Heated Corona. ApJ, 710:L39–L43, February 2010a. doi: 10.1088/2041-8205/710/1/L39.

S. J. Bradshaw and P. J. Cargill. The Cooling of Coronal Plasmas. III. Enthalpy Transfer as a Mechanism for Energy Loss. ApJ, 717:163–174, July 2010b. doi: 10.1088/0004-637X/717/1/163.

S. J. Bradshaw and P. J. Cargill. The Influence of Numerical Resolution on Coronal Density in Hydrodynamic Models of Impulsive Heating. ApJ, 770:12, June 2013. doi: 10.1088/0004-637X/770/1/12.

S. J. Bradshaw and H. E. Mason. The radiative response of solar loop plasma subject to transient heating. A&A, 407:1127–1138, September 2003. doi: 10.1051/0004-6361:20030986.

S. J. Bradshaw and N. M. Viall. Patterns of Activity in a Global Model of a Solar Active Region. ApJ, 821:63, April 2016. doi: 10.3847/0004-637X/821/1/63.

S. I. Braginskii. Transport Processes in a Plasma. *Reviews of Plasma Physics*, 1:205, 1965.

P. J. Cargill, S. J. Bradshaw, and J. A. Klimchuk. Enthalpy-based Thermal Evolution of Loops. II. Improvements to the Model. ApJ, 752:161, June 2012a. doi: 10.1088/0004-637X/752/2/161.

P. J. Cargill, S. J. Bradshaw, and J. A. Klimchuk. Enthalpy-based Thermal Evolution of Loops. III. Comparison of Zero-dimensional Models. ApJ, 758:5, October 2012b. doi: 10.1088/0004-637X/758/1/5.

P. J. Cargill, H. P. Warren, and S. J. Bradshaw. Modelling nanoflares in active regions and implications for coronal heating mechanisms. *Philosophical Transactions of the Royal Society of London Series A*, 373:20140260–20140260, April 2015. doi: 10.1098/rsta.2014.0260.

P. J. Cargill, I. De Moortel, and G. Kiddie. Coronal Density Structure and its Role in

Wave Damping in Loops. ApJ, 823:31, May 2016. doi: 10.3847/0004-637X/823/1/31.

R. B. Dahlburg, G. Einaudi, B. D. Taylor, I. Ugarte-Urra, H. P. Warren, A. F. Rappazzo, and M. Velli. Observational Signatures of Coronal Loop Heating and Cooling Driven by Footpoint Shuffling. ApJ, 817:47, January 2016. doi: 10.3847/0004-637X/817/1/47.

G. B. Field. Thermal Instability. ApJ, 142:531, August 1965. doi: 10.1086/148317.

L. Fletcher and B. De Pontieu. Plasma Diagnostics of Transition Region "Moss" using SOHO/CDS and TRACE. ApJ, 520:L135–L138, August 1999. doi: 10.1086/312157.

C. Froment, F. Auchère, K. Bocchialini, E. Buchlin, C. Guennou, and J. Solomon. Evidence for Evaporation-incomplete Condensation Cycles in Warm Solar Coronal Loops. ApJ, 807:158, July 2015. doi: 10.1088/0004-637X/807/2/158.

C. Froment, F. Auchère, G. Aulanier, Z. Mikić, K. Bocchialini, E. Buchlin, and J. Solomon. Long-period Intensity Pulsations in Coronal Loops Explained by Thermal Non-equilibrium Cycles. ApJ, 835:272, February 2017. doi: 10.3847/1538-4357/835/2/272.

C. Froment, F. Auchère, Z. Mikić, G. Aulanier, K. Bocchialini, E. Buchlin, J. Solomon, and E. Soubrié. On the Occurrence of Thermal Nonequilibrium in Coronal Loops. ApJ, 855:52, March 2018. doi: 10.3847/1538-4357/aaaf1d.

V. Hansteen, N. Guerreiro, B. De Pontieu, and M. Carlsson. Numerical Simulations of Coronal Heating through Footpoint Braiding. ApJ, 811:106, October 2015. doi: 10.1088/0004-637X/811/2/106.

E. Hildner. The Formation of Solar Quiescent Prominences by Condensation. Sol. Phys., 35:123–136, March 1974. doi: 10.1007/BF00156962.

A. W. Hood, P. J. Cargill, P. K. Browning, and K. V. Tam. An MHD Avalanche in a Multi-threaded Coronal Loop. ApJ, 817:5, January 2016. doi: 10.3847/0004-637X/817/1/5.

C. D. Johnston, A. W. Hood, P. J. Cargill, and I. De Moortel. A new approach for modelling chromospheric evaporation in response to enhanced coronal heating. I. The method. A&A, 597:A81, January 2017a. doi: 10.1051/0004-6361/201629153.

C. D. Johnston, A. W. Hood, P. J. Cargill, and I. De Moortel. A new approach for modelling chromospheric evaporation in response to enhanced coronal heating. II. Non-uniform heating. A&A, 605:A8, August 2017b. doi: 10.1051/0004-6361/201730486.

J. A. Klimchuk. On Solving the Coronal Heating Problem. Sol. Phys., 234:41–77, March

2006. doi: 10.1007/s11207-006-0055-z.

J. A. Klimchuk, S. K. Antiochos, and J. T. Mariska. A numerical study of the nonlinear thermal stability of solar loops. ApJ, 320:409–417, September 1987. doi: 10.1086/165554.

J. A. Klimchuk, S. Patsourakos, and P. J. Cargill. Highly Efficient Modeling of Dynamic Coronal Loops. ApJ, 682:1351–1362, August 2008. doi: 10.1086/589426.

N. P. M. Kuin and P. C. H. Martens. On the thermal stability of hot coronal loops - The coupling between chromosphere and corona. A&A, 108:L1–L4, April 1982.

R. Lionello, J. A. Linker, and Z. Mikić. Multispectral Emission of the Sun During the First Whole Sun Month: Magnetohydrodynamic Simulations. ApJ, 690:902–912, January 2009. doi: 10.1088/0004-637X/690/1/902.

R. Lionello, A. R. Winebarger, Y. Mok, J. A. Linker, and Z. Mikić. Thermal Nonequilibrium Revisited: A Heating Model for Coronal Loops. ApJ, 773:134, August 2013. doi: 10.1088/0004-637X/773/2/134.

C. D. Meyer, D. S. Balsara, and T. D. Aslam. A second-order accurate Super TimeStepping formulation for anisotropic thermal conduction. MNRAS, 422:2102–2115, May 2012. doi: 10.1111/j.1365-2966.2012.20744.x.

C. D. Meyer, D. S. Balsara, and T. D. Aslam. A stabilized Runge-Kutta-Legendre method for explicit super-time-stepping of parabolic and mixed equations. *Journal of Computational Physics*, 257:594–626, January 2014. doi: 10.1016/j.jcp.2013.08.021.

Z. Mikić, R. Lionello, Y. Mok, J. A. Linker, and A. R. Winebarger. The Importance of Geometric Effects in Coronal Loop Models. ApJ, 773:94, August 2013. doi: 10.1088/0004-637X/773/2/94.

Y. Mok, J. F. Drake, D. D. Schnack, and G. van Hoven. Prominence formation in a coronal loop. ApJ, 359:228–231, August 1990. doi: 10.1086/169053.

Y. Mok, Z. Mikić, R. Lionello, and J. A. Linker. The Formation of Coronal Loops by Thermal Instability in Three Dimensions. ApJ, 679:L161, June 2008. doi: 10.1086/589440.

Y. Mok, Z. Mikić, R. Lionello, C. Downs, and J. A. Linker. A Three-dimensional Model of Active Region 7986: Comparison of Simulations with Observations. ApJ, 817:15, January 2016. doi: 10.3847/0004-637X/817/1/15.

D. A. N. Müller, V. H. Hansteen, and H. Peter. Dynamics of solar coronal loops. I.

Condensation in cool loops and its effect on transition region lines. A&A, 411:605–613, December 2003. doi: 10.1051/0004-6361:20031328.

D. A. N. Müller, H. Peter, and V. H. Hansteen. Dynamics of solar coronal loops. II. Catastrophic cooling and high-speed downflows. A&A, 424:289–300, September 2004. doi: 10.1051/0004-6361:20040403.

D. A. N. Müller, A. De Groof, V. H. Hansteen, and H. Peter. High-speed coronal rain. A&A, 436:1067–1074, June 2005. doi: 10.1051/0004-6361:20042141.

J. P. O'Hara and I. De Moortel. Impact of flux distribution on elementary heating events. A&A, 594:A67, October 2016. doi: 10.1051/0004-6361/201628913.

E. N. Parker. Instability of Thermal Fields. ApJ, 117:431, May 1953. doi: 10.1086/145707.

C. E. Parnell and I. De Moortel. A contemporary view of coronal heating. *Philosophical Transactions of the Royal Society of London Series A*, 370:3217–3240, July 2012. doi: 10.1098/rsta.2012.0113.

H. Peter, S. Bingert, and S. Kamio. Catastrophic cooling and cessation of heating in the solar corona. A&A, 537:A152, January 2012. doi: 10.1051/0004-6361/201117889.

E. Priest. *Magnetohydrodynamics of the Sun*. May 2014.

F. Reale. Diagnostics of stellar flares from X-ray observations: from the decay to the rise phase. A&A, 471:271–279, August 2007. doi: 10.1051/0004-6361:20077223.

F. Reale. Coronal Loops: Observations and Modeling of Confined Plasma. *Living Reviews in Solar Physics*, 11, July 2014. doi: 10.12942/lrsp-2014-4.

F. Reale. Plasma Sloshing in Pulse-heated Solar and Stellar Coronal Loops. ApJ, 826: L20, August 2016. doi: 10.3847/2041-8205/826/2/L20.

F. Reale, S. Orlando, M. Guarrasi, A. Mignone, G. Peres, A. W. Hood, and E. R. Priest. 3D MHD modeling of twisted coronal loops. ApJ, 830:21, October 2016. doi: 10.3847/0004-637X/830/1/21.

J. W. Reep, S. J. Bradshaw, and J. A. Klimchuk. Diagnosing the Time Dependence of Active Region Core Heating from the Emission Measure. II. Nanoflare Trains. ApJ, 764:193, February 2013a. doi: 10.1088/0004-637X/764/2/193.

J. W. Reep, S. J. Bradshaw, and R. T. J. McAteer. On the Sensitivity of the GOES Flare Classification to Properties of the Electron Beam in the Thick-target Model. ApJ, 778:

76, November 2013b. doi: 10.1088/0004-637X/778/1/76.

L. Spitzer. *Physics of Fully Ionised Gases*. 1962.

R. Susino, A. C. Lanzafame, A. F. Lanza, and D. Spadaro. Signatures of Impulsive Localized Heating in the Temperature Distribution of Multi-Stranded Coronal Loops. ApJ, 709:499–506, January 2010. doi: 10.1088/0004-637X/709/1/499.

R. Susino, D. Spadaro, A. C. Lanzafame, and A. F. Lanza. Properties of multistranded, impulsively heated hydrodynamic loop models. A&A, 552:A17, April 2013. doi: 10.1051/0004-6361/201116542.

R. H. D. Townsend. An Exact Integration Scheme for Radiative Cooling in Hydrodynamical Simulations. ApJS, 181:391–397, April 2009. doi: 10.1088/0067-0049/181/2/391.

J. F. Vesecky, S. K. Antiochos, and J. H. Underwood. Numerical modeling of quasi-static coronal loops. I - Uniform energy input. ApJ, 233:987–997, November 1979. doi: 10.1086/157462.

H. P. Warren, D. H. Brooks, and A. R. Winebarger. Constraints on the Heating of High-temperature Active Region Loops: Observations from Hinode and the Solar Dynamics Observatory. ApJ, 734:90, June 2011. doi: 10.1088/0004-637X/734/2/90.

H. P. Warren, A. R. Winebarger, and D. H. Brooks. A Systematic Survey of High-temperature Emission in Solar Active Regions. ApJ, 759:141, November 2012. doi: 10.1088/0004-637X/759/2/141.

P. Zacharias, H. Peter, and S. Bingert. Investigation of mass flows in the transition region and corona in a three-dimensional numerical model approach. A&A, 531:A97, July 2011. doi: 10.1051/0004-6361/201016047.

Y. B. Zel'dovich and Y. P. Raizer. *Physics of shock waves and high-temperature hydrodynamic phenomena*. 1967.